



UNIL | Université de Lausanne

Unicentre

CH-1015 Lausanne

<http://serval.unil.ch>

Year : 2023

Evaluating Environmental Drivers of Late Permian to Early Triassic Marine Biotic Events Using Multiple Geochemical and Isotopic Proxies

Edward Oluwaseun Okorie

Edward Oluwaseun Okorie, 2023, Evaluating Environmental Drivers of Late Permian to Early Triassic Marine Biotic Events Using Multiple Geochemical and Isotopic Proxies

Originally published at : Thesis, University of Lausanne

Posted at the University of Lausanne Open Archive <http://serval.unil.ch>

Document URN : urn:nbn:ch:serval-BIB_C1BA0019932E7

Droits d'auteur

L'Université de Lausanne attire expressément l'attention des utilisateurs sur le fait que tous les documents publiés dans l'Archive SERVAL sont protégés par le droit d'auteur, conformément à la loi fédérale sur le droit d'auteur et les droits voisins (LDA). A ce titre, il est indispensable d'obtenir le consentement préalable de l'auteur et/ou de l'éditeur avant toute utilisation d'une oeuvre ou d'une partie d'une oeuvre ne relevant pas d'une utilisation à des fins personnelles au sens de la LDA (art. 19, al. 1 lettre a). A défaut, tout contrevenant s'expose aux sanctions prévues par cette loi. Nous déclinons toute responsabilité en la matière.

Copyright

The University of Lausanne expressly draws the attention of users to the fact that all documents published in the SERVAL Archive are protected by copyright in accordance with federal law on copyright and similar rights (LDA). Accordingly it is indispensable to obtain prior consent from the author and/or publisher before any use of a work or part of a work for purposes other than personal use within the meaning of LDA (art. 19, para. 1 letter a). Failure to do so will expose offenders to the sanctions laid down by this law. We accept no liability in this respect.



UNIL | Université de Lausanne

Faculty of Geosciences and Environment
Institute of Earth Surface Dynamics
University of Lausanne

**Evaluating Environmental Drivers of Late Permian to Early Triassic
Marine Biotic Events Using Multiple Geochemical and Isotopic Proxies**

Doctoral thesis

Presented at the

Faculty of Geosciences and Environment of the University of Lausanne

To obtain the grade of
Ph.D in Earth Sciences

by

Oluwaseun Okorie EDWARD

MSc. Geoscience, University of Copenhagen

Thesis director

Prof. Dr. Torsten Vennemann

Jury

Prof. Dr. Torsten Vennemann
Prof. Dr. Marie-Elodie Perga
Dr. László Kocsis
Prof. Dr. Stefano Bernasconi
Prof. Dr. Michael Joachimski
Prof. Dr. Jeroen Sonke

Director
President of the Jury
Internal Expert
External Expert
External Expert
External Expert

University of Lausanne
2023

IMPRIMATUR

Vu le rapport présenté par le jury d'examen, composé de

Présidente de la séance publique :	Mme la Professeure Marie-Elodie Perga
Présidente du colloque :	Mme la Professeure Marie-Elodie Perga
Directeur de thèse :	M. le Professeur Torsten Vennemann
Expert interne :	M. le Docteur Laszlo Kocsis
Expert externe :	M. le Professeur Stefano Bernasconi
Expert externe :	M. le Professeur Michael Joachimski
Expert externe :	M. le Professeur Jeroen Sonke

Le Doyen de la Faculté des géosciences et de l'environnement autorise l'impression de la thèse de

Monsieur Oluwaseun EDWARD

*Titulaire d'un
Master of Geology-Geosciences
de l'Université de Copenhague*

intitulée

**EVALUATING ENVIRONMENTAL DRIVERS OF LATE PERMIAN TO
EARLY TRIASSIC MARINE BIOTIC EVENTS USING MULTIPLE
GEOCHEMICAL AND ISOTOPIC PROXIES**

Lausanne, le 29 novembre 2023

Pour le Doyen de la Faculté des géosciences et de
l'environnement



Professeure Marie-Elodie Perga



UNIL | Université de Lausanne

Faculté de Géosciences et de l'Environnement
Institut des Dynamiques de la Surface Terrestre
Université de Lausanne

**Evaluating Environmental Drivers of Late Permian to Early Triassic
Marine Biotic Events Using Multiple Geochemical and Isotopic Proxies**

Thèse de Doctorat

Présentée à la

Faculté de Géosciences et de l'Environnement de l'Université de Lausanne

Pour l'obtention du grade de
Docteur en Sciences de la Terre

par

Oluwaseun Okorie EDWARD

MSc. Geoscience à Københavns Universitet (KU)

Directeur de thèse

Prof. Dr. Torsten Vennemann

Jury

Prof. Dr. Torsten Vennemann
Prof. Dr. Marie-Elodie Perga
Dr. László Kocsis
Prof. Dr. Stefano Bernasconi
Prof. Dr. Michael Joachimski
Prof. Dr. Jeroen Sonke

Directeur
Président/Rapporteur
Expert (interne)
Expert (externe)
Expert (externe)
Expert (externe)

Université de Lausanne
2023



UNIL | Université de Lausanne

Unicentre

CH-1015 Lausanne

<http://serval.unil.ch>

2023

Evaluating Environmental Drivers of Late Permian to Early Triassic Marine Biotic Events Using Multiple Geochemical and Isotopic Proxies

Oluwaseun Okorie EDWARD

Oluwaseun O. Edward, 2023, "Evaluating Environmental Drivers of Late Permian to Early Triassic Marine Biotic Events Using Multiple Geochemical and Isotopic Proxies"

Originally published at: Thesis, University of Lausanne

Posted at the University of Lausanne Open Archive <http://serval.unil.ch>

Document URN:

Droits d'auteur

L'Université de Lausanne attire expressément l'attention des utilisateurs sur le fait que tous les documents publiés dans l'Archive SERVAL sont protégés par le droit d'auteur, conformément à la loi fédérale sur le droit d'auteur et les droits voisins (LDA). A ce titre, il est indispensable d'obtenir le consentement préalable de l'auteur et/ou de l'éditeur avant toute utilisation d'une oeuvre ou d'une partie d'une oeuvre ne relevant pas d'une utilisation à des fins personnelles au sens de la LDA (art. 19, al. 1 lettre a). A défaut, tout contrevenant s'expose aux sanctions prévues par cette loi. Nous déclinons toute responsabilité en la matière.

Copyright

The University of Lausanne expressly draws the attention of users to the fact that all documents published in the SERVAL Archive are protected by copyright in accordance with federal law on copyright and similar rights (LDA). Accordingly, it is mandatory to obtain prior consent from the author and/or publisher before any use of a work or part of a work for purposes other than personal use within the meaning of LDA (art. 19, para. 1 letter a). Failure to do so will expose offenders to the sanctions laid down by this law. We accept no liability in this respect.

Table of Contents

Table of Contents	1
Acknowledgements	4
Abstract	5
Abstract Scientifique	7
INTRODUCTION	9
Objectives and Thesis Overview	11
References	14
CHAPTER 1	18
Timing and Provenance of Volcanic Fluxes Around the Permian-Triassic Boundary Mass Extinction in South China: U-Pb Zircon Geochronology, Volcanic Ash Geochemistry and Mercury Isotopes	19
Abstract	20
1. Introduction	21
2. Materials and Methods	25
3. Results	29
4. Discussion	35
5. Conclusions	49
References	51
CHAPTER 2	61
Evidence for Variable Provenance of Mercury Anomalies During the Smithian – Spathian (Olenekian)	62
Abstract	63
1. Introduction	64
2. Geological setting	65
3. Materials and Methods	68
4. Results	71
5. Discussion	79
6. Conclusion	90
References	92
CHAPTER 3	103
Olenekian sulfur isotope records: Deciphering global trends, links to marine redox changes and faunal evolution	104
Abstract	105
1. Introduction	106
2. Sample Localities	109

3. Methods.....	111
4 Results	116
5 Discussion.....	118
6. Conclusions.....	132
References.....	134
CHAPTER 4.....	142
Carbonate Clumped Isotope Constraints on Early Triassic NeoTethyan Seawater Oxygen Isotope Compositions and Temperatures.....	143
Abstract.....	144
1. Introduction.....	145
2. Sample localities	146
3. Methods.....	149
4. Results	151
5. Discussion.....	156
6. Conclusions.....	161
References.....	163
General Conclusions and Recommendations	170
APPENDIX A	172
Supplementary information for Chapter 2:	173
References.....	181
APPENDIX B	182
Supplementary information for Chapter 3:	183
APPENDIX C	199
Supplementary information for Chapter 4:	200
APPENDIX D.....	206
Curriculum Vitae	207

Evaluating Environmental Drivers of Late Permian to Early Triassic Marine Biotic Events Using Multiple Geochemical and Isotopic Proxies

Keywords: Permian-Triassic boundary, mass extinction, Early Triassic, volcanism, mercury enrichment, carbonate associated sulfate, marine redox, clumped isotopes, seawater temperatures

Acknowledgements

The Swiss National Science Foundation and the University of Lausanne are gratefully acknowledged for providing financial support for this thesis, as well as for scientific conference participation and continuing education over the course of the Doctoral research.

I would like to express my utmost gratitude to my thesis director, Professor Torsten Vennemann, for entrusting me with this work, for his professional and personal support and guidance throughout these years. Most especially with initial settling in Switzerland, being supportive of my evolving family situation and for just being the all-round great person that I have had the privilege of having as my supervisor. Thank you (and Cora) for everything!

I would also like to thank Professor Hugo Bucher for his role in the Sinergia Project which the research conducted in this thesis is a part of. Thank you for the invaluable scientific input and for fostering collaboration within the Sinergia Group.

I say thank you to all members of the Sinergia group for the scientific discussions, collaboration, and input over these years, especially Dr. Aymon Baud, Dr. Christian V  rard, Dr. Andr   N. Paul, Professor Urs Schaltegger and Charline Ragon. My gratitude also goes to Dr. Marc Leu, Dr. Thomas Br  hwiler, and Louis Dudit for assistance over the years with samples from the Paleontological Museum of the University of Zurich, as well as to Dr. Lara Locatelli for the constant encouragement and kindness over the years.

I am grateful to Dr. Laszlo Kocsis, Professor Micheal Joachimski, Professor Stefano Bernasconi and Professor Jeroen Sonke for helping to evaluate the thesis and for their constructive comments on the contents of this work.

Special thanks to my research partner and friend, Franziska Blattmann, for her support and friendship throughout this journey. You made the ups and downs more enjoyable! My gratitude also goes to present and past members of the IDYST IsoLab group, including Dr. Ana  l Lehmann and Dr. Zoneibe Luz for their assistance when I started at UNIL. Also, thanks to Laetitia Monbaron, Dr. Claudia Baumgartner, Dr. Benita Putlitz, and Dr. Jorge Spangenberg for laboratory assistance. My gratitude also goes to my colleagues at IDYST and ISTE, both past and present, for their moral support over the years. Special thanks to Floriane Tisserand for helping with French translations of parts of this thesis.

I am deeply grateful to my Swiss parents: Gerrit and Karin Spalteholz, for their love and support since the beginning of my journey in Switzerland. Thank you for your kindness, the discussions, jokes, and laughter throughout the years.

Finally, my deepest gratitude goes to my family: my wife, Jeanette, for her love, understanding, for being my biggest supporter, and for taking care of our son, Theo. You inspire me every day! To my Mum and Dad, thank you for your love and sacrifices for me, without which I would not be here today.

To everyone who has helped me along my journey so far, I say thank you!

Abstract

Periods of significant environmental and climatic upheavals throughout Earth's history are usually associated with increased faunal extinction rates. Therefore, these time intervals present unique opportunities to further our understanding of the link between environmental changes and the evolution of life on Earth. The latest Permian to Early Triassic (ca. 252 – 247.2 Ma) was one such interval, being characterized by significant environmental and climatic disturbances, as well as the largest mass extinction of the Phanerozoic, which was accompanied by several diversification and extinction cycles of marine faunas. While still the subject of much scientific debate, the environmental and climatic perturbations of this time are most attributed to Siberian Traps Large Igneous Province (STLIP) magmatism. This thesis aims to further our understanding of the causes, timing, and spatial distribution of marine environmental changes associated with the biotic events of the latest Permian to Early Triassic. This objective is approached using temporally calibrated geochemical and isotopic records from continental shelf and offshore marine sedimentary successions deposited in the Tethys Ocean and which are currently situated in South China and Oman, respectively. The results from this thesis indicate that mercury (Hg) concentration anomalies (a proxy for volcanism) associated with the Permian–Triassic boundary (PTB) in South China post-date the PTB mass extinction event in the studied sections and can be explained by regional subduction-related arc volcanism. Similarly, Hg concentration anomalies recorded in Smithian to Spathian (Olenekian, Early Triassic) strata vary in magnitude and age across different localities. These Hg anomalies derive from a combination of enhanced terrestrial Hg input to marine depositional environments, subduction-related arc volcanism and hydrothermal fluid activity in the Tethys region during the Early Triassic. An investigation of marine sulfur (S) cycle changes (a proxy for ocean-atmosphere oxygenation) across the Smithian – Spathian interval (ca. 251.2 – 247.2 Ma) indicates that the global ocean was characterized by relatively low dissolved oxygen levels between the middle and latest Smithian (ca. 250.4 – 249.3 Ma). This dissolved oxygen depletion, coupled with a low seawater sulfate reservoir, permitted geologically rapid sulfur cycle perturbations across the Smithian – Spathian interval. The oxygen depletion coincided with both climatic warming and cooling, as well as with increased faunal diversification and extinction alike. However, the Smithian–Spathian boundary (SSB, ca. 249.29 – 249.1 Ma) was associated with cooler seawater temperatures and water column oxygenation. Finally, NeoTethyan seawater likely had oxygen isotope compositions of around -1 ‰ VSMOW during the Early Triassic. Based on these results, it is concluded that Hg concentration anomalies associated with the PTB in South China cannot be unequivocally linked to STLIP magmatism, and that evidence for renewed STLIP magmatism during the Smithian – Spathian transition remains elusive. As such, subduction-related felsic and intermediate arc volcanism in the Tethys region likely played a bigger role in driving environmental changes during the studied interval than previously thought. Furthermore, the results argue against a direct causal link between marine redox or seawater temperature changes and faunal diversification/extinction during the middle

Smithian to early Spathian. Consequently, Early Triassic marine biotic events were likely driven by a combination of various biotic and abiotic factors, and not by environmental changes alone.

Abstract Scientifique

Les périodes significatives de bouleversements environnementaux et climatiques tout au long de l'histoire de la Terre sont généralement associées à des taux accrus d'extinction faunique. Par conséquent, ces intervalles temporels offrent des opportunités uniques pour approfondir notre compréhension du lien entre les changements environnementaux et l'évolution de la vie sur Terre. L'intervalle entre le Permien supérieur jusqu'au début du Trias (environ 252 à 247,2 Ma) a été caractérisé par d'importants troubles environnementaux et climatiques. Ce qui correspond aussi à la plus grande extinction de masse du Phanérozoïque, accompagnée de plusieurs cycles de diversification et d'extinction de la faune marine. Bien que ce sujet est toujours confronté à de vifs débats scientifiques, les perturbations environnementales et climatiques de cette époque sont principalement attribuées au magmatisme de la Province Igneuse des Trapps de Sibérie (STLIP). Ainsi les travaux de recherches de cette thèse visent à approfondir notre compréhension des causes, de la chronologie et de la répartition spatiale des changements environnementaux marins associés aux événements biotiques du Permien supérieur jusqu'au début du Trias. Cet objectif est abordé en utilisant des enregistrements géochimiques et isotopiques calibrés dans le temps provenant des successions sédimentaires marines déposées sur le plateau continental et au large de l'océan Téthys, actuellement situées respectivement en Chine du Sud et à Oman. Les résultats de cette thèse indiquent que les anomalies de concentration en mercure (Hg) (un indicateur du volcanisme) associées à la limite Permien-Trias (PTB) en Chine du Sud sont postérieures à l'événement d'extinction massive de la PTB dans les sections étudiées et peuvent être expliquées par un arc volcanique lié à la subduction régionale. De même, ces anomalies de concentration de Hg enregistrées dans les strates du Smithien jusqu'au Spathien (Olenekien, Trias inférieur) varient en amplitude et en âge selon les localités. Ces anomalies de Hg résultent d'une combinaison de l'apport accru de Hg terrestre dans les environnements de dépôt marins, de l'arc volcanique lié à la subduction et de l'activité des fluides hydrothermaux dans la région de Téthys au cours du Trias inférieur. Une étude des changements du cycle du soufre (S) marin (un indicateur de l'oxygénation océan-atmosphère) à travers l'intervalle Smithien-Spathien (env. 251,2 – 247,2 Ma) indique que l'océan mondial était caractérisé par des niveaux d'oxygène dissous relativement faibles entre le Smithien moyen et le Smithien récent (env. 250,4 – 249,3 Ma). Cet appauvrissement en oxygène dissous, associé à un faible réservoir de sulfate d'eau de mer, a permis des perturbations géologiquement rapides du cycle du soufre à travers l'intervalle Smithien-Spathien. La diminution du taux d'oxygène coïncide avec le réchauffement et le refroidissement climatique, ainsi qu'avec la diminution de la diversification de la faune et son extinction. En revanche, la limite Smithien - Spathien (SSB, 249.29 – 249.1Ma) a été associée à des températures de l'eau de mer plus fraîches et à l'oxygénation de la colonne d'eau. Finalement, l'eau de mer néotéthysienne avait probablement une composition isotopique en oxygène d'environ -1 ‰ VSMOW au cours du Trias inférieur. Sur la base de ces résultats, la conclusion est que les anomalies de concentration de Hg associées à la limite Permien-Trias en Chine méridionale ne peuvent pas être incontestablement liées au magmatisme de la province magmatique des Trapps

sibériens (STLIP), et que la preuve d'un magmatisme STLIP renouvelé pendant la transition Smithien-Spathien reste insaisissable. Ainsi, l'arc volcanique felsiques et intermédiaires liés à la subduction dans la région de Téthys a probablement joué un rôle plus important dans les changements environnementaux survenus au cours de l'intervalle étudié que précédemment envisagé. De plus, les résultats plaident contre un lien de causalité direct entre les changements de rédox marin ou de température de l'eau de mer et la diversification/extinction faunique au cours du milieu du Smithien jusqu'à la début du Spathien. Par conséquent, les événements biotiques marins du Trias inférieur ont peut-être été influencés par une combinaison de divers facteurs biotiques et abiotiques, et non pas par les seuls changements environnementaux marins.

INTRODUCTION

The evolution of life and the natural environment throughout Earth's history is an important aspect of scientific research perhaps best understood from the standpoint of uniformitarianism as proposed by James Hutton (1788). That is, in the same way that the present is the key to the past, reconstructing the evolution of natural environments and life throughout Earth's history is the key to predicting the future of Earth's current environments, flora and faunas. In the geologic record, the most significant and abrupt environmental changes are linked to major faunal extinctions (Ernst and Youbi, 2017). Therefore, reconstructing the magnitude, timing, spatial distribution, and duration of paleoenvironmental changes associated with mass extinctions in the geologic record is important. Much so because this knowledge offers important insights into how faunas and flora, in both terrestrial and marine environments, respond to adverse environmental change brought about by external forcings. Environmental and climatic changes in the geologic record are usually studied using geochemical (and isotopic) proxies (Higginson, 2009; Chagué, 2020). The utility of geochemical proxies is based on the understanding that the concentration and isotopic composition of chemical elements change due to physical, chemical, or biological processes in the environment. These concentrations and isotopic compositions can then be analyzed in geological materials such as rocks and sediments, to infer changes in past environmental conditions and climate (Higginson, 2009).

The most extreme faunal extinction on record during the last 540 million years is the Permian – Triassic boundary mass extinction event (PTBME), which occurred about 251.9 million years ago (Ma) (Raup and Sepkoski Jr, 1982; Erwin, 1998; Erwin et al., 2002; Burgess et al., 2014). Like other mass extinction events, the PTBME occurred against the background of significant environmental changes and has been the subject of much study. In fact, it is the most widely-studied extinction event (see reviews by Pruss et al., 2006; Chen et al., 2014; Algeo et al., 2015; Cui and Kump, 2015; Dal Corso et al., 2022). The cause(s) of the PTBME is(are) still debated. However, the most popular view is that it was triggered by environmental deterioration related to the emplacement of the Siberian Traps Large Igneous Province (STLIP) (Campbell et al., 1992; Renne et al., 1995). However, despite much progress over the years, establishing causal links between STLIP magmatism, environmental deterioration, and the faunal extinction remains challenged by an incomplete knowledge of the high-resolution timing of environmental perturbations associated with the extinction event (e.g., Davydov et al., 2019; Davydov, 2021). Thus, it is apparent that precise and high-resolution absolute age calibration of Permian-Triassic boundary (PTB) geochemical records, such as that offered by U-Pb zircon geochronology, is required to better evaluate causal links between STLIP magmatism, environmental perturbations, and mass extinction during the Permian-Triassic transition (see review by Dal Corso et al., 2022).

Following the PTBME, the subsequent Early Triassic interval (ca. 251.9 – 247.2 Ma) was also marked by environmental perturbations associated with biotic upheavals (Payne et al., 2004; Orchard, 2007; Sun et al., 2012; Romano et al., 2013), the most significant of which was during the Smithian – Spathian

transition (ca. 249.29 Ma; [Widmann et al., 2020](#)) (see reviews by [Algeo et al., 2019](#); [Zhang et al., 2019b](#)). Similar to the PTB, it has been proposed that environmental perturbations at this time were caused by (latter phases of) STLIP magmatism ([Shen et al., 2019](#); [Du et al., 2022](#)). Notably, large carbon isotope excursions (CIEs) throughout the Early Triassic have been documented from different localities globally ([Baud et al., 1996](#); [Payne et al., 2004](#); [Horacek et al., 2007](#)), indicative of frequent environmental perturbations during this 4.7-million-year interval. These perturbations to the Early Triassic global carbon cycle have been interpreted in terms of recurrent volcanic CO₂ degassing ([Payne and Kump, 2007](#)). However, STLIP magmatism is currently only documented up until 250.5 Ma based on U-Pb zircon ages from STLIP rocks ([Burgess et al., 2017](#); [Augland et al., 2019](#)). As such, the role of STLIP volcanism in causing environmental upheavals during the Smithian – Spathian transition remains uncertain.

Relatively high mercury (Hg) concentrations (usually > 50 ppb) in strata within sedimentary sequences are widely used as a proxy for ancient volcanic activity (e.g., [Sanei et al., 2012](#); [Grasby et al., 2019](#); [Percival et al., 2021](#)). Also, Hg isotopes have the potential to track the sources of Hg deposition to rocks ([Biswas et al., 2008](#); [Blum et al., 2014](#)). Hence, the relative variations in Hg concentrations and isotopic compositions in latest Permian to Early Triassic sedimentary successions have been used to evaluate the role of volcanism in causing environmental changes during the Permian – Triassic and Smithian – Spathian transitions (e.g., [Grasby et al., 2017](#); [Shen et al., 2019](#)). Nevertheless, questions remain regarding the fidelity of Hg as a proxy for volcanic activity in the geologic record, as well as the temporal consistency of sedimentary Hg records ([Hammer et al., 2019](#)). Chapters 1 and 2 of this thesis focus on the Hg record across the PTBME and Smithian – Spathian transition, and discuss the issues raised above.

In addition to massive volcanism, other causal mechanisms have been suggested to explain the marine environmental and biotic events of the Smithian – Spathian transition including: oceanic anoxia ([Clarkson et al., 2016](#); [Zhang et al., 2018](#); [Zhang et al., 2019a](#)) and seawater temperature changes ([Sun et al., 2012](#); [Romano et al., 2013](#)). However, the latter suggestion is based on oxygen isotope ($\delta^{18}\text{O}$) records, which require an assumption of seawater $\delta^{18}\text{O}$ to derive absolute temperatures. Furthermore, most Early Triassic geochemical records are from shelf sections which are susceptible to continental fluxes and thus, may not be representative of the open ocean. Hence, geochemical records from offshore marine successions are necessary in order to evaluate/validate the global significance of existing geochemical records from continental shelf successions. In addition, offshore geochemical records enable an evaluation of the spatial distribution of marine environmental events (such as oceanic anoxia) previously interpreted from Early Triassic continental shelf geochemical records.

An additional challenge with regards to high-resolution Early Triassic marine paleoenvironmental reconstruction has been the dating and correlation of geochemical records between different localities.

This is due to ambiguity regarding the placement of the Smithian-Spathian boundary (SSB) and low stratigraphic resolution of some Smithian – Spathian successions (see review by Zhang et al., 2019b). Significant progress has recently been made on this front, however. Widmann et al. (2020) established a high-resolution temporal calibration of three Smithian – Spathian successions deposited in South China, as well as an absolute age for the SSB, using U-Pb zircon geochronology. The temporal calibration by these authors thus enables Smithian – Spathian geochemical records to be reliably placed within an absolute time framework. Furthermore, Leu et al. (2022; 2023) produced a high-resolution biochronological framework for the Smithian and Spathian of South China and Oman based on conodont unitary association zones (UAZs). These UAZs were further intercalibrated with carbon isotope stratigraphy and the U-Pb zircon ages by Widmann et al. (2020), enabling high-resolution correlation of Smithian – Spathian successions between South China and Oman (Leu et al., 2023). The research in this thesis builds on these recent advances in temporal calibration of Smithian – Spathian marine successions to provide absolute time-constrained geochemical records from South China and Oman (Fig. 1) and reconstruct marine environmental changes during this interval.

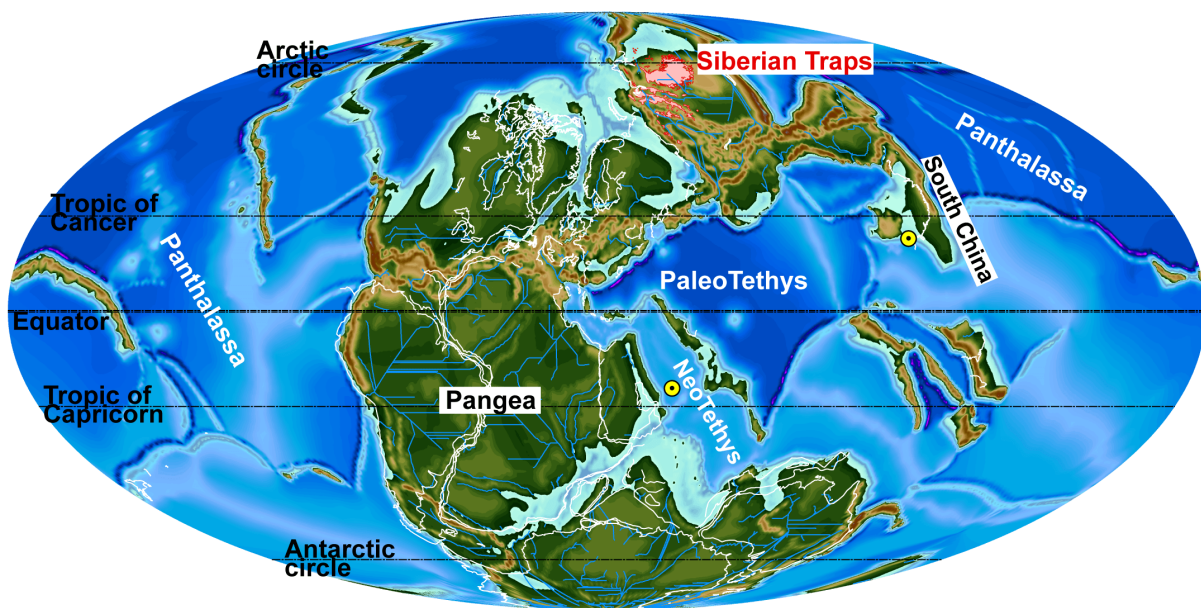


Figure 1. Global paleogeographical map of the latest Permian to Early Triassic world after the Panalexis model (Vérard, 2019). Yellow circles show the paleo location of the marine sedimentary successions, deposited in the Paleotethys (South China) and Neotethys (Oman), studied during this research.

Objectives and Thesis Overview

The scientific challenges discussed above form the basis for the research in this thesis. The research was conducted within the framework of a Swiss National Science Foundation Sinergia project (Project number: CRSII5_180253), drawing expertise from research groups of the University of Zurich and the University of Geneva. This thesis contains four research papers outlined in Chapters 1 to 4.

The main objective of this thesis is to improve our understanding of marine environmental changes associated with biotic events across the Permian – Triassic and Smithian – Spathian transitions, with a focus on their timing and spatial distribution. This objective is approached by producing geochemical and isotopic records tied to a precise high-resolution chronostratigraphic framework to explore three main themes as follows:

- 1) The timing and provenance of volcanic fluxes to Tethyan depositional environments across the PTB and Smithian – Spathian intervals.
- 2) Global marine sulfur cycle trends and links to faunal diversification/extinction over the Smithian – Spathian interval.
- 3) The record of seawater ^{18}O composition during the Early Triassic.

The geochemical records are produced from the same sedimentary successions from which U-Pb zircon ages and/or conodont UAZs were determined. Hence, allowing for temporally consistent interpretation of marine environmental changes in the studied interval, as well as precise correlation of geochemical records across different localities.

Chapter 1 focuses on the record of volcanic activity associated with the PTB mass extinction by using Hg as a geochemical proxy for volcanism. The aim of the study was to constrain the timing and the provenance of volcanic fluxes to South China during the Permian – Triassic transition. Using new precise and accurate U-Pb zircon ages determined from the two investigated deep-water marine sections, the age of the Hg concentration peak associated with the PTB in the studied sections was determined. This enabled an evaluation of the temporal relationship between volcanism and the PTB mass extinction in the studied sections. The study combined Hg isotopic compositions and volcanic ash trace element contents, with published data from other studies, to interpret the likeliest source of volcanic fluxes to South China. The study has been published in the journal *Geochemistry, Geophysics, Geosystems*.

Chapter 2 follows a similar theme to Chapter 1 but focuses on the Smithian and Spathian substages of the Early Triassic. This study builds on the high-resolution chronological framework previously established for continental shelf sections from South China and offshore marine sections from Oman (Widmann et al., 2020; Leu, 2022; 2023) to investigate the temporal distribution and provenance of Hg in Smithian – Spathian marine depositional environments. In this study, Hg concentration and isotopic data, Sr- and Nd-isotopic data, as well as bulk mineralogy, major and trace element concentration data are generated. Based on a compilation of previously published Hg concentration and isotopic records globally, as well as the new data, the evidence for a singular source of Hg to marine environments during the Smithian – Spathian, such as renewed STLIP volcanism, is evaluated. The manuscript has been published in the journal *Global and Planetary Change*.

Chapter 3 focuses on the Smithian – Spathian marine sulfur cycle with the aim of discerning global marine sulfur cycle trends and thus, changes in marine redox conditions during this interval. This study used sulfur and oxygen isotope compositions of carbonate associated sulfate (CAS) extracted from carbonates from shelf successions from South China and offshore successions from Oman. The marine sulfur isotope records from the offshore carbonate successions enabled an evaluation of sulfur cycle trends in the open ocean during the studied interval. Using the new absolute time-calibrated CAS isotopic records in conjunction with simple sulfur cycle box modeling, sulfur isotope trends were discussed in the context of prevailing global paleoenvironmental conditions. Also, the seawater sulfate inventory of the Tethys Ocean during the Smithian – Spathian was quantitatively estimated. Furthermore, this study compared the record of marine S-isotope changes, interpreted in terms of marine redox, with changes in conodont diversity as recorded in the studied sections to evaluate the possibility of a causal link between marine environmental changes and marine faunal diversity. This chapter has been published in the journal *Chemical Geology*.

Chapter 4 addresses a major challenge of oxygen isotope paleothermometry, which is the need to assume the oxygen isotope composition of seawater to calculate absolute temperatures from oxygen isotope compositions of marine fossils (e.g., conodonts). Carbonate clumped isotope thermometry was employed to tackle this challenge. Articulate brachiopod fossils and micritic carbonates from offshore marine sections of Oman were analyzed. Using the clumped isotope (Δ_{47}) and oxygen isotope compositions of the analyzed samples, this study discusses the probable seawater $\delta^{18}\text{O}$ values for NeoTethyan seawater, as well as seawater temperature variations during the Early Triassic. The study will be submitted for publication in an international journal.

References

- Algeo, T.J., Brayard, A., Richoz, S., 2019. The Smithian-Spathian boundary: A critical juncture in the Early Triassic recovery of marine ecosystems. *Earth-Science Reviews* 195, 1-6 DOI: <https://doi.org/10.1016/j.earscirev.2019.102877>.
- Algeo, T.J., Chen, Z.-Q., Bottjer, D.J., 2015. Global review of the Permian–Triassic mass extinction and subsequent recovery: Part II. *Earth-Science Reviews* 149, 1-4 DOI: <https://doi.org/10.1016/j.earscirev.2015.09.007>.
- Augland, L.E., Ryabov, V.V., Vernikovskiy, V.A., Planke, S., Polozov, A., Callegaro, S., Jerram, D.A., Svensen, H., 2019. The main pulse of the Siberian Traps expanded in size and composition. *Scientific Reports* 9, 1-12 DOI: 10.1038/s41598-019-54023-2.
- Baud, A., Atudorei, V., Sharp, Z., 1996. Late Permian and early Triassic evolution of the Northern Indian margin: Carbon isotope and sequence stratigraphy. *Geodinamica Acta* 9, 57-77 DOI: 10.1080/09853111.1996.11105278.
- Biswas, A., Blum, J.D., Bergquist, B.A., Keeler, G.J., Xie, Z., 2008. Natural mercury isotope variation in coal deposits and organic soils. *Environ Sci Technol* 42, 8303-8309 DOI: 10.1021/es801444b.
- Blum, J.D., Sherman, L.S., Johnson, M.W., 2014. Mercury Isotopes in Earth and Environmental Sciences. *Annual Review of Earth and Planetary Sciences*, Vol 42 42, 249-269 DOI: 10.1146/annurev-earth-050212-124107.
- Burgess, S.D., Bowring, S., Shen, S.Z., 2014. High-precision timeline for Earth's most severe extinction. *Proc Natl Acad Sci U S A* 111, 3316-3321 DOI: 10.1073/pnas.1317692111.
- Burgess, S.D., Muirhead, J.D., Bowring, S.A., 2017. Initial pulse of Siberian Traps sills as the trigger of the end-Permian mass extinction. *Nat Commun* 8, 164 DOI: 10.1038/s41467-017-00083-9.
- Campbell, I.H., Czamanske, G.K., Fedorenko, V.A., Hill, R.I., Stepanov, V., 1992. Synchronism of the Siberian Traps and the Permian-Triassic Boundary. *Science* 258, 1760-1763 DOI: doi:10.1126/science.258.5089.1760.
- Chagué, C., 2020. Chapter 18 - Applications of geochemical proxies in paleotsunami research, in: Engel, M., Pilarczyk, J., May, S.M., Brill, D., Garrett, E. (Eds.), *Geological Records of Tsunamis and Other Extreme Waves*. Elsevier, pp. 381-401.
- Chen, Z.-Q., Algeo, T.J., Bottjer, D.J., 2014. Global review of the Permian–Triassic mass extinction and subsequent recovery: Part I. *Earth-Science Reviews* 137, 1-5 DOI: <https://doi.org/10.1016/j.earscirev.2014.05.007>.
- Clarkson, M.O., Wood, R.A., Poulton, S.W., Richoz, S., Newton, R.J., Kasemann, S.A., Bowyer, F., Krystyn, L., 2016. Dynamic anoxic ferruginous conditions during the end-Permian mass extinction and recovery. *Nature Communications* 7, 12236 DOI: 10.1038/ncomms12236.
- Cui, Y., Kump, L.R., 2015. Global warming and the end-Permian extinction event: Proxy and modeling perspectives. *Earth-Science Reviews* 149, 5-22 DOI: <https://doi.org/10.1016/j.earscirev.2014.04.007>.
- Dal Corso, J., Song, H., Callegaro, S., Chu, D., Sun, Y., Hilton, J., Grasby, S.E., Joachimski, M.M., Wignall, P.B., 2022. Environmental crises at the Permian–Triassic mass extinction. *Nat Rev Earth Env* 3, 197-214 DOI: 10.1038/s43017-021-00259-4.

Davydov, V., 2021. Tunguska coals, Siberian sills and the Permian-Triassic extinction. *Earth-Science Reviews* 212, 103438 DOI: [10.1016/j.earscirev.2020.103438](https://doi.org/10.1016/j.earscirev.2020.103438).

Davydov, V.I., Karasev, E.V., Schmitz, M.D., Nurgalieva, N.G., Silantiev, V.V., Kuzina, D., Biakov, A.S., Gareev, B.I., Vasilenko, D.V., Zorina, S.O., 2019. Were the Siberian Traps a trigger for the global Permo-Triassic extinction?, Late Paleozoic Sedimentary Earth Systems: Stratigraphy, Geochronology, Petroleum Resources: Abstract Volume of Kazan Golovkinsky Stratigraphic Meeting, pp. 87-88.

Du, Y., Zhu, Y., Corso, J.D., Huang, J., Qiu, H., Song, H., Tian, L., Chu, D., Tong, J., Song, H., 2022. New Early Triassic marine $\delta^{13}\text{C}$ record from the northeastern Yangtze Platform: Implications for contemporaneous temperature changes and volcanic eruptions. *Palaeogeography, Palaeoclimatology, Palaeoecology* 607, 111270 DOI: <https://doi.org/10.1016/j.palaeo.2022.111270>.

Ernst, R.E., Youbi, N., 2017. How Large Igneous Provinces affect global climate, sometimes cause mass extinctions, and represent natural markers in the geological record. *Palaeogeography, Palaeoclimatology, Palaeoecology* 478, 30-52 DOI: <https://doi.org/10.1016/j.palaeo.2017.03.014>.

Erwin, D.H., 1998. The end and the beginning: recoveries from mass extinctions. *Trends in Ecology & Evolution* 13, 344-349 DOI: [https://doi.org/10.1016/S0169-5347\(98\)01436-0](https://doi.org/10.1016/S0169-5347(98)01436-0).

Erwin, D.H., Bowring, S.A., Yogan, J., 2002. End-Permian mass extinctions: A review, in: Koeberl, C., MacLeod, K.G. (Eds.), *Catastrophic events and mass extinctions: impacts and beyond*. Geological Society of America, p. 0.

Grasby, S.E., Shen, W., Yin, R., Gleason, J.D., Blum, J.D., Lepak, R.F., Hurley, J.P., Beauchamp, B., 2017. Isotopic signatures of mercury contamination in latest Permian oceans. *Geology* 45, 55-58.

Grasby, S.E., Them II, T.R., Chen, Z., Yin, R., Ardakani, O.H., 2019. Mercury as a proxy for volcanic emissions in the geologic record. *Earth-Science Reviews*, 102880 DOI: <https://doi.org/10.1016/j.earscirev.2019.102880>.

Hammer, Ø., Jones, M.T., Schneebeil-Hermann, E., Hansen, B.B., Bucher, H., 2019. Are Early Triassic extinction events associated with mercury anomalies? A reassessment of the Smithian/Spathian boundary extinction. *Earth-Science Reviews* 195, 179-190 DOI: [10.1016/j.earscirev.2019.04.016](https://doi.org/10.1016/j.earscirev.2019.04.016).

Higginson, M.J., 2009. Geochemical Proxies (Non-Isotopic), in: Gornitz, V. (Ed.), *Encyclopedia of Paleoclimatology and Ancient Environments*. Springer Netherlands, Dordrecht, pp. 341-354.

Horacek, M., Brandner, R., Abart, R., 2007. Carbon isotope record of the P/T boundary and the Lower Triassic in the Southern Alps: Evidence for rapid changes in storage of organic carbon. *Palaeogeography, Palaeoclimatology, Palaeoecology* 252, 347-354 DOI: <https://doi.org/10.1016/j.palaeo.2006.11.049>.

Hutton, J., 1788. *Theory of the Earth; or an Investigation of the Laws observable in the Composition, Dissolution, and Restoration of Land upon the Globe*. *Earth and Environmental Science Transactions of The Royal Society of Edinburgh* 1, 209-304.

Leu, M., Bucher, H., Baud, A., Vennemann, T., Luz, Z., Hautmann, M., Goudemand, N., 2023. An expanded Smithian–Spathian (Lower Triassic) boundary from a reefal build-up record in Oman: implications for conodont taxonomy, high-resolution biochronology and the carbon isotope record. *Papers in Palaeontology* 9, e1481 DOI: <https://doi.org/10.1002/spp2.1481>.

Leu, M., Bucher, H., Vennemann, T., Bagherpour, B., Ji, C., Brosse, M., Goudemand, N., 2022. A Unitary Association-based conodont biozonation of the Smithian–Spathian boundary (Early Triassic) and associated biotic crisis from South China. *Swiss Journal of Palaeontology* 141, 19 DOI: 10.1186/s13358-022-00259-x.

Orchard, M.J., 2007. Conodont diversity and evolution through the latest Permian and Early Triassic upheavals. *Palaeogeography, Palaeoclimatology, Palaeoecology* 252, 93-117 DOI: <https://doi.org/10.1016/j.palaeo.2006.11.037>.

Payne, J.L., Kump, L.R., 2007. Evidence for recurrent Early Triassic massive volcanism from quantitative interpretation of carbon isotope fluctuations. *Earth and Planetary Science Letters* 256, 264-277 DOI: <https://doi.org/10.1016/j.epsl.2007.01.034>.

Payne, J.L., Lehrmann, D.J., Wei, J., Orchard, M.J., Schrag, D.P., Knoll, A.H., 2004. Large Perturbations of the Carbon Cycle During Recovery from the End-Permian Extinction. *Science* 305, 506-509 DOI: 10.1126/science.1097023.

Percival, L.M.E., Bergquist, B.A., Mather, T.A., Sanei, H., 2021. Sedimentary Mercury Enrichments as a Tracer of Large Igneous Province Volcanism, in: Richard E. Ernst, Alexander J. Dickson, Bekker, A. (Eds.), *Large Igneous Provinces*. John Wiley and Sons, Inc., pp. 247-262.

Pruss, S.B., Bottjer, D.J., Corsetti, F.A., Baud, A., 2006. A global marine sedimentary response to the end-Permian mass extinction: Examples from southern Turkey and the western United States. *Earth-Science Reviews* 78, 193-206 DOI: <https://doi.org/10.1016/j.earscirev.2006.05.002>.

Raup, D.M., Sepkoski Jr, J.J., 1982. Mass extinctions in the marine fossil record. *Science* 215, 1501-1503 DOI: 10.1126/science.215.4539.1501.

Renne, P.R., Black, M.T., Zichao, Z., Richards, M.A., Basu, A.R., 1995. Synchrony and Causal Relations Between Permian-Triassic Boundary Crises and Siberian Flood Volcanism. *Science* 269, 1413-1416 DOI: 10.1126/science.269.5229.1413.

Romano, C., Goudemand, N., Vennemann, T.W., Ware, D., Schneebeli-Hermann, E., Hochuli, P.A., Brühwiler, T., Brinkmann, W., Bucher, H., 2013. Climatic and biotic upheavals following the end-Permian mass extinction. *Nature Geoscience* 6, 57-60 DOI: 10.1038/ngeo1667.

Sanei, H., Grasby, S.E., Beauchamp, B., 2012. Latest Permian mercury anomalies. *Geology* 40, 63-66 DOI: 10.1130/G32596.1.

Shen, J., Algeo, T.J., Planaysky, N.J., Yu, J.X., Feng, Q.L., Song, H.J., Song, H.Y., Rowe, H., Zhou, L., Chen, J.B., 2019. Mercury enrichments provide evidence of Early Triassic volcanism following the end-Permian mass extinction. *Earth-Science Reviews* 195, 191-212 DOI: 10.1016/j.earscirev.2019.05.010.

Sun, Y., Joachimski, M.M., Wignall, P.B., Yan, C., Chen, Y., Jiang, H., Wang, L., Lai, X., 2012. Lethally Hot Temperatures During the Early Triassic Greenhouse. *Science* 338, 366-370 DOI: 10.1126/science.1224126.

Vérard, C., 2019. Panalexis: towards global synthetic palaeogeographies using integration and coupling of manifold models. *Geological Magazine* 156, 320-330 DOI: 10.1017/S0016756817001042.

Widmann, P., Bucher, H., Leu, M., Vennemann, T., Bagherpour, B., Schneebeli-Hermann, E., Goudemand, N., Schaltegger, U., 2020. Dynamics of the largest carbon isotope excursion during the

Early Triassic biotic recovery. *Front Earth Sc-Switz*, 196 DOI:
<https://doi.org/10.3389/feart.2020.00196>.

Zhang, F., Algeo, T.J., Cui, Y., Shen, J., Song, H., Sano, H., Rowe, H.D., Anbar, A.D., 2019a. Global-ocean redox variations across the Smithian-Spathian boundary linked to concurrent climatic and biotic changes. *Earth-Science Reviews* 195, 147-168.

Zhang, F., Romaniello, S.J., Algeo, T.J., Lau, K.V., Clapham, M.E., Richoz, S., Herrmann, A.D., Smith, H., Horacek, M., Anbar, A.D., 2018. Multiple episodes of extensive marine anoxia linked to global warming and continental weathering following the latest Permian mass extinction. *Science Advances* 4, e1602921 DOI: doi:10.1126/sciadv.1602921.

Zhang, L., Orchard, M.J., Brayard, A., Algeo, T.J., Zhao, L., Chen, Z.-Q., Lyu, Z., 2019b. The Smithian/Spathian boundary (late Early Triassic): a review of ammonoid, conodont, and carbon-isotopic criteria. *Earth-Science Reviews*.

CHAPTER 1

Author contributions

Oluwaseun Edward: Conceptualization, Formal analysis, Data curation, Investigation, Data Analysis, Data visualization, Writing - original draft, Writing - review and editing.

André N. Paul: Formal Analysis, Investigation, Data Visualization, Writing - original draft (U-Pb geochronology), Writing - review and editing.

Hugo Bucher: Conceptualization, Funding Acquisition, Investigation, Project Administration, Resources, Supervision, Writing - review and editing.

Christian V erard: Formal analysis, Data Visualization, Resources, Writing - review and editing.

Thierry Adatte: Investigation, Formal analysis, Resources, Writing - review and editing.

Jeroen Sonke: Investigation, Resources, Data curation, Writing - review and editing.

Urs Schaltegger: Conceptualization, Funding Acquisition, Project Administration, Resources, Writing - review and editing.

Torsten Vennemann: Conceptualization, Funding Acquisition, Project Administration, Resources, Supervision, Writing - review and editing.

**Timing and Provenance of Volcanic Fluxes Around the Permian-Triassic Boundary
Mass Extinction in South China: U-Pb Zircon Geochronology, Volcanic Ash
Geochemistry and Mercury Isotopes**

Oluwaseun Edward¹, André Navin Paul², Hugo Bucher³, Christian Vérard², Thierry Adatte⁴, Jeroen E. Sonke⁵, Urs Schaltegger², Torsten Vennemann¹

¹Institute of Earth Surface Dynamics, Géopolis, University of Lausanne, CH-1015 Lausanne, Switzerland

²Department of Earth Sciences, Université de Genève, Rue des Maraîchers 13, CH-1205 Genève

³Paläontologisches Institut der Universität Zürich, Karl-Schmid-Strasse 4, 8006 Zürich, Switzerland

⁴Institute of Earth Sciences, Géopolis, University of Lausanne, CH-1015 Lausanne, Switzerland

⁵Observatoire Midi-Pyrénées, Géosciences Environnement Toulouse, Université Paul Sabatier Toulouse 3, 14 Avenue Edouard Belin, 31400 Toulouse, France

Corresponding author: Oluwaseun Edward (oluwaseun.edward@unil.ch)

Key Points:

- Mercury concentrations show elevated volcanic fluxes to South China before and after the Permian-Triassic boundary.
- The recorded mercury anomalies are attributed primarily to regional subduction-related arc volcanism, not the Siberian Traps.
- Mercury anomalies close to the Permian-Triassic boundary are not a reliable stratigraphic marker for the mass extinction event.

Abstract

Anomalous mercury (Hg) contents recorded near the Permian-Triassic boundary (PTB) are often linked to Siberian Traps Large Igneous Province (STLIP) volcanism and the Permian-Triassic boundary mass extinction (PTBME). However, mounting evidence indicates that the relation between STLIP volcanism and Hg “anomalies” is not straightforward. This study focuses on the timing and provenance of volcanic fluxes around the PTBME in South China. We constrain carbon isotope ($\delta^{13}\text{C}$) and Hg concentration and isotope records by utilizing high-precision U-Pb zircon ages from two expanded deep-water marine sections spanning the Late Permian to Early Triassic in the Nanpanjiang Basin. Results reveal two episodes of Hg enrichment. The oldest episode predates the onset of a large negative $\delta^{13}\text{C}$ excursion, which is documented to be older than 252.07 ± 0.130 Ma. The second episode occurred between 251.822 ± 0.060 Ma and 251.589 ± 0.062 Ma, coinciding with the nadir of the $\delta^{13}\text{C}$ excursion. Volcanic ash geochemistry and Hg isotope compositions suggest that mercury was mainly sourced from subduction-related volcanic arc magmatism in the Tethys region, which peaked between 251.668 ± 0.079 Ma and 251.589 ± 0.052 Ma. These results are compatible with suggestions that regional arc volcanism contributed to the causes of the PTBME in South China and provide evidence that Hg anomalies close to the PTB are not a reliable stratigraphic marker for the PTB extinction event. This study demonstrates that relations between volcanism, environmental perturbations and mass extinction during the Permian-Triassic transition are better resolved with the aid of high-precision U-Pb zircon ages.

Plain Language Summary

Unusually high mercury contents in sedimentary rock sequences and the mass extinction of organisms during the transition from the Permian–Triassic Period are often linked to Siberian Traps volcanism. However, results from several studies indicate that the relationship between this massive volcanism and mercury peaks in Permian- to Triassic-aged rocks in the South China region is complex. This study combines the geochemical and isotopic records of carbon and mercury from Late Permian to Early Triassic sedimentary rocks, with absolute ages determined from interlayered volcanic ashes, to investigate the presence, timing, and source of volcanic inputs to these rock successions in South China. Results show higher mercury concentrations in two intervals, one before and after the Permian-Triassic boundary. Absolute age results indicate that the mercury peak closest to the Permian-Triassic boundary occurred around 300,000 years after the mass extinction. We attribute the mercury peaks to more local volcanic activity than the far away Siberian Traps and suggest that this regional-scale volcanic activity began shortly before 252 million years ago (Ma) and peaked around 251.6 Ma.

1. Introduction

The Paleozoic – Mesozoic transition (ca. 252 million years ago) was characterized by the largest mass extinction event in the Phanerozoic – the Permian-Triassic boundary mass extinction (PTBME) (Erwin, 1998; Stanley, 2016). This event paved the way for the faunal transition from the Paleozoic evolutionary fauna to the modern fauna (Dal Corso et al., 2022). Furthermore, major perturbations of the global carbon and mercury cycles (expressed as negative carbon (C) isotope excursions and mercury (Hg) concentration spikes, respectively) are documented for sedimentary successions straddling the Permian-Triassic boundary (PTB) in several spatially disparate localities (e.g., Baud et al., 1989; 1996; Grasby et al., 2013; Korte & Kozur, 2010; Sanei et al., 2012; J. Shen et al., 2019; S. Shen et al., 2013; Sial et al., 2020). Causal mechanisms for the extinction are still debated. However, the most popular trigger suggested by researchers is volcanic activity of the Siberian Large Igneous Province (STLIP), based on a temporal overlap between U-Pb ages of STLIP rocks and those of volcanic ash beds in the Meishan Global Stratotype Section and Point (GSSP) (Burgess & Bowring, 2015; Burgess et al., 2017).

The connection between volcanic activity and Hg concentration spikes in sedimentary successions is founded on the understanding that volcanoes are a dominant natural source of Hg to the environment (Pyle & Mather, 2003). As such, LIP volcanism could result in the emission and sequestration of high levels of Hg in the environment. Consequently, mercury “anomalies” – relatively high Hg concentrations or Hg/TOC ratios in a portion of strata within a given sedimentary succession – are used to trace the timing of Large Igneous Province (LIP) magmatism in the geological record (Grasby et al., 2019; Percival et al., 2021; Yager et al., 2021). In the case of the $\delta^{13}\text{C}$ record, previous studies have interpreted the negative C isotope excursion associated with the PTB as the result of the intrusion of magma into surrounding organic-rich country rocks (e.g., coal, shale) and petroleum-rich evaporites in the Tunguska Basin, Siberia (Broadley et al., 2018; Payne & Kump, 2007; Svensen et al., 2009). Thus, Hg anomalies and negative $\delta^{13}\text{C}$ excursions recorded close to the PTB are usually interpreted in the context of STLIP volcanism and its associated deleterious environmental effects leading to faunal extinction.

However, our understanding of the links between STLIP volcanism, carbon cycle perturbations and mass extinction during the Permian-Triassic (P-T) transition are still complicated by several factors. First, Hg and Hg/TOC content vary significantly near the PTB between different localities and the relative timing of Hg anomalies with regards to the PTBME horizon is inconsistent (e.g., J. Shen et al., 2019; Sial et al., 2020; Wang et al., 2018). In addition, Hg anomalies can also be influenced by factors other than direct volcanic emissions. For instance, Hg anomalies can arise from increased input of Hg remobilized from soils to marine sediments due to increased erosion and continental weathering rates (Them II et al., 2019), as well as enhanced sequestration by sulfides in euxinic depositional environments (J. Shen et al., 2020). In addition, sedimentary Hg records can be distorted by post-depositional weathering, erosion, and thermal alteration (Charbonnier et al., 2020; Chen et al., 2022).

Second, the correlation of geochemical records between different localities is fraught with uncertainty because the position of the PTB in many successions remains uncertain (e.g., Johnson et al., 2021; J. Shen et al., 2019; Sial et al., 2020). Also, sedimentary and volcanic successions straddling the Permian and Triassic are often characterized by an unconformity at the PTB (Burgess & Bowring, 2015; Davydov, 2021; Yin et al., 2014), which for South China has been estimated to represent a time gap of about 89 ± 38 kyr for the Permian part (Baresel et al., 2017a). Third, it has become apparent that several paleocontinents, including South China, experienced extensive regional intermediate to felsic volcanism during the P-T transition (Gao et al., 2013; J. Shen et al., 2021; Vajda et al., 2020; Yin et al., 1992; H. Zhang et al., 2021), increasing the potential sources of volcanic Hg input to PTB marine records at these localities. Fourth, absolute time calibration of the eruptive history of the STLIP remains coarse, limiting precise temporal correlations between STLIP magmatism and mass extinction (Dal Corso et al., 2022), although, U-Pb geochronologic evidence suggests that the PTBME may have been limited to only a short period of STLIP magmatism (Burgess et al., 2017). Consequently, considering the complex biogeochemical cycling of Hg, the widespread incompleteness of the PTB rock record (which limits the accuracy of chemostratigraphic and biostratigraphic correlations and the placement of the PTB), and the occurrence of more proximal regional volcanic activity capable of locally supplying Hg, links between Hg anomalies around the PTB and STLIP magmatism cannot be unequivocally inferred without a thorough assessment of the provenance of the recorded Hg anomalies and their timing relative to the PTBME using precise and accurate geochronology.

Hg isotopes are widely used to trace the sources of Hg anomalies in ancient sedimentary successions, as different transformations during the biogeochemical cycling of Hg can induce mass-dependent (MDF) and/or mass-independent fractionation (MIF) of Hg isotopes (Blum et al., 2014; Thibodeau & Bergquist, 2017). Previous studies have applied Hg isotopes in investigating the source of Hg anomalies and its relationship to the PTBME in P-T successions of South China and elsewhere (Grasby et al., 2017; J. Shen et al., 2021; J. Shen et al., 2019; Wang et al., 2019a; Wang et al., 2018). However, these studies have provided mixed results, with Hg MIF data from nearshore depositional settings reflecting a dominant terrestrial Hg source and those from deeper-water depositional settings being congruent with atmospheric volcanic Hg input (Grasby et al., 2017; J. Shen et al., 2023; Wang et al., 2018). Hence, it has been suggested that the Hg isotope record for these successions mostly reflects their depositional setting (Yager et al., 2021) and that distal/deep-water marine sections, being less vulnerable to terrestrial Hg inputs, may be better suited for investigations of volcanic Hg input sources (Grasby et al., 2017; Thibodeau & Bergquist, 2017; Wang et al., 2018).

The Upper Permian to Lower Triassic of South China is characterized by the widespread occurrence of volcanic ash layers (Gao et al., 2013; He et al., 2014; Yang et al., 2012; Yin et al., 1992), permitting precise and accurate U-Pb zircon geochronological calibrations of P-T successions (e.g., Baresel et al., 2017a, 2017b; Burgess et al., 2014; Lehrmann et al., 2015; S. Shen et al. 2019), as well as providing a

means of evaluating the provenance of volcanic products (e.g. zircon) to sedimentary successions in South China (e.g., Jiao et al., 2022; Zhao et al., 2019). However, except for the Shangsi section (with published U-Pb zircon ages, S. Shen et al., 2011), Hg anomalies recorded near the PTB from deep-water marine successions in South China (e.g., Wang et al., 2018; J. Shen et al., 2019) lack U-Pb zircon age calibration. Also, the published U-Pb zircon ages for Shangsi were not obtained with the most recent EARTHTIME spike (S. Shen et al., 2011; Yuan et al., 2019), making a direct comparison with ages obtained using this spike problematic at high temporal resolution. The EARTHTIME spike is an isotopic tracer solution that has been precisely calibrated, and which enables the direct measurement of U and Pb fractionation during analysis (see Condon et al., 2015). To accurately account for spike composition effects on the weighted mean U-Pb age when comparing ages determined using different spikes, the tracer and analytical uncertainty needs to be propagated (i.e., Y uncertainty, see section 2.5, not reported in Shen et al. (2011)).

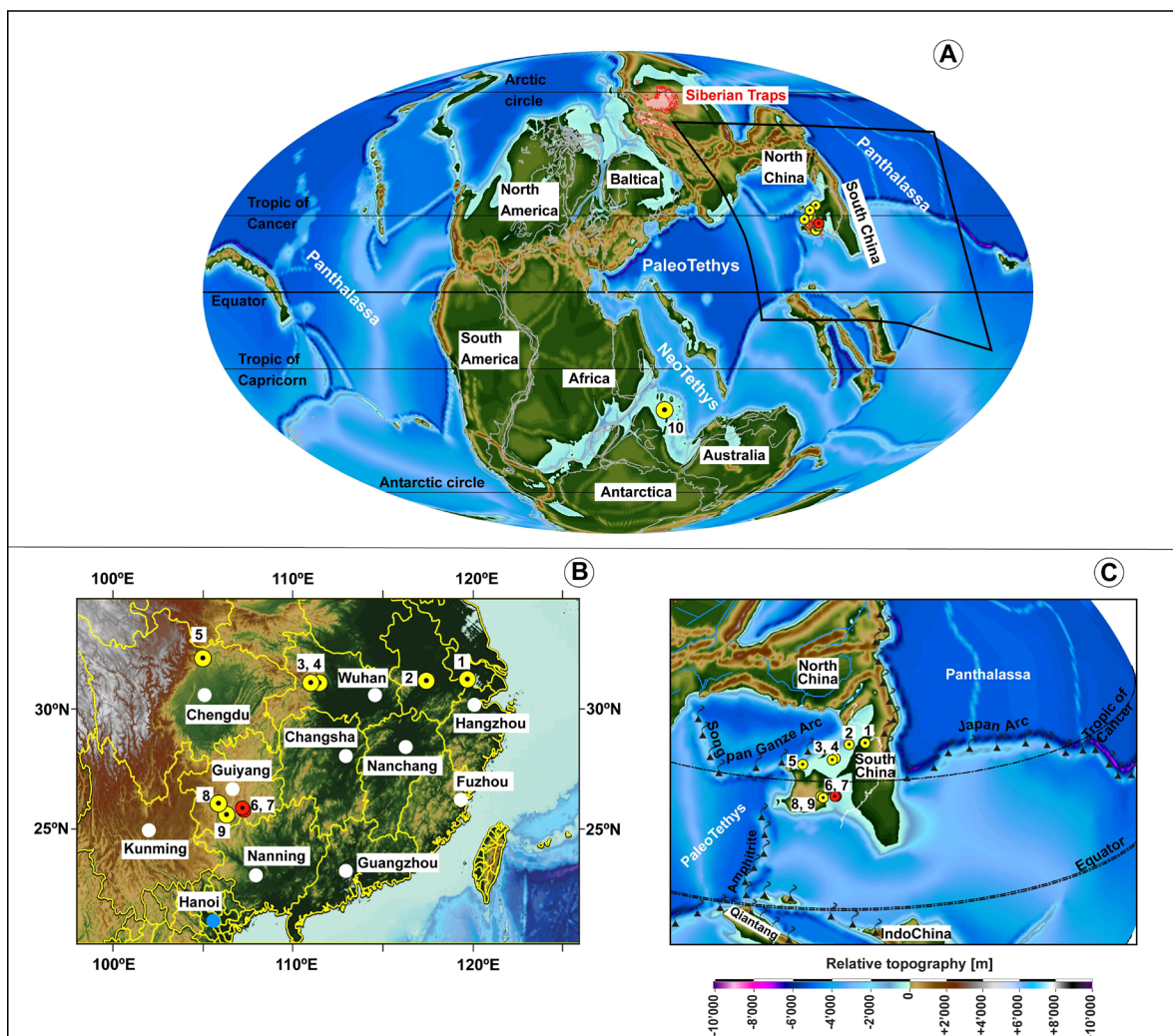


Figure 1. Maps showing the location of the studied successions, as well as other marine successions in the Tethys region from which Permian-Triassic (P-T) transition mercury records have been published. a) Global paleogeographic map at the P-T transition after the Panalexis model (Vérard, 2019). Locality

marked '10' represents the paleo-location of Guryul Ravine, northern India. b) Map showing the present-day location of the studied sections (red circles) and other deep-water marine sections in South China (yellow circles); white circles show the main cities. The sections are represented by numbers as follows: 1 – Meishan, 2 – Majiashan, 3 – Daxiakou, 4 – Xiakou. 5 – Shangsi, 6 – Laxian, 7 – Potuo, 8 – Xinmin, 9 – Kejiao. c) Detailed map of the South China area (orthogonal projection) with the paleo-location of the discussed sections.

This $\delta^{13}\text{C}$ uncertainty propagation results in less-precise ages, inhibiting age comparison at high temporal resolution. In addition to enabling precise geochronology, volcanic ashes provide an archive for the assessment of magmatic sources, as their geochemical compositions reflect those of the source magma (e.g., He et al., 2014; Song et al., 2022; Yang et al., 2012). This study presents, for the first time, a paired $\delta^{13}\text{C}$ and Hg (concentration and isotope) record calibrated by precise and accurate U-Pb zircon ages from two sections (Laxian and Potuo) representing deep-water marine depositional environments in the Nanpanjiang Basin, South China. The aim of the study is to assess the occurrence, timing, and provenance of volcanic fluxes during the P-T transition in South China.

1.1 Geological Context

The Potuo and Laxian sections (Fig. 1) are situated in the NE-SW trending Pingtang syncline, which in the present-day, is in the northern part of the Nanpanjiang Basin, South China (Bagherpour et al. 2020). The Changhsingian (Late Permian) sedimentary succession in Potuo is characterized by thin-bedded siliceous mudstones interbedded with volcanic ash layers: the Talung/Dalong Formation (Bagherpour et al., 2020; Baresel et al. 2017b). The Griesbachian (Induan, Early Triassic) consists of laminated black shales with interbedded concretionary micritic limestones and occasional ash beds representing the Daye/Ziyun Formation (Bagherpour et al., 2020). The Changhsingian to Griesbachian sedimentary succession for Laxian is similar to that of Potuo except that there are no concretionary micritic limestone beds interbedded with the Griesbachian shale units (Bagherpour et al., 2020). The Late Permian to Early Triassic sedimentary sequence in these localities is interpreted to have been deposited as a continuous section in a deep-water basin paleoenvironment (Bagherpour et al., 2020). Furthermore, there is no field evidence for an unconformity between the Talung and Daye formations in Laxian, consistent with similar observations for other sections in the Nanpanjiang Basin (Bagherpour et al., 2020; Baresel et al., 2017b; Dai et al., 2019). In addition, the presence of volcanic ashes in these sections enables studies of latest Permian to earliest Triassic volcanic fluxes to the Nanpanjiang Basin of South China. As such, these sections are ideally suited for our combined geochronologic and geochemical study, having been deposited in troughs within a horst-and-graben paleotopography (Bagherpour et al., 2020). Samples spanning the Upper Permian to Lower Triassic used for this study are the same as those analyzed by Bagherpour et al. (2020) and details on the geological setting, lithostratigraphy, biostratigraphy, as well as $\delta^{13}\text{C}$ record for these sections are given in that study. A sampling gap between upper Changhsingian to lower Griesbachian strata hinders the documentation of a continuous Upper Permian to Lower

Triassic record for Potuo (Bagherpour et al., 2020). Nevertheless, the combination of geochemical data with high-precision U-Pb zircon ages from both sections makes geochemical records from these sections valuable.

2. Materials and Methods

For this study, measurements of the Hg concentrations (n=70) and isotopic compositions (n=22), total organic carbon (TOC) contents (n=60), major and trace element concentrations for sedimentary rocks and interbedded volcanic ash beds (n=55) were made. These data are complemented by U-Pb zircon geochronology based on single zircon grains from five volcanic ash beds in the two sections (Table S1, supplementary information).

2.1 Stratigraphical correlation of the study sections

Stratigraphical correlation between the two sections studied – Laxian (25.78880°N, 107.29750°E) and Potuo (25.82638°N, 107.24861°E) follows Bagherpour et al. (2020). The PTB is delineated based on the lithostratigraphic boundary between the Talung and Daye formations, which for deep-water sections of the Nanpanjiang Basin, has been shown to be equivalent to the PTB as defined at the Meishan D GSSP based on U-Pb zircon ages (Burgess et al., 2014; Baresel et al., 2017b). Furthermore, the transition from the Talung/Dalong Fm. to Daye Fm. is considered to correspond to the mass extinction interval in the Nanpanjiang Basin (J. Shen et al., 2019). The stratigraphical correlation of the Laxian and Potuo sections, which is based on lithostratigraphy (Bagherpour et al. 2020), is congruent with the similarity of the Hg trends for Potuo and Laxian and is consistent with our new U-Pb zircon ages (see section 3).

2.2 Mercury concentration and isotopic composition

Mercury concentration was measured using a Zeeman R-915F high-frequency atomic absorption spectrometer at the University of Lausanne, Switzerland. Samples (sedimentary rocks, including volcanic ashes) were analyzed in triplicates to ensure analytical precision and the reference material – GSD-11, Chinese alluvium (Hg concentration of 72 ± 9 ppb; Zintwana et al., 2012) was used to monitor accuracy of the measurements (correlation coefficient = 0.99, standard residual deviation = 5 %).

Twenty-two samples (Potuo = 11, Laxian = 11) with sufficiently high Hg concentrations (≥ 9 ppb) were selected for Hg isotopic analysis at the Observatoire Midi-Pyrénées, Toulouse, France. Mercury was preconcentrated using a double-stage tube furnace – acid-trapping protocol as detailed by Sun et al. (2013). Powdered samples were loaded in quartz tubes (pre-cleaned at 550 °C), capped at both ends with quartz wool and heated in a combustion furnace connected to a flow of Hg-free oxygen and set to ramp up from room temperature to 900 °C within 6 hours. Liberated gaseous Hg⁰ was then purged into a decomposition oven, held at 1000 °C, using a continuous flow of oxygen. Subsequently, the Hg⁰ was collected by oxidation to Hg^{II} in a trapping solution of 40 % (v/v) inverse aqua regia (iAR, 2HNO₃/1HCl), which was then diluted at the end of the 6 h pre-concentration to 20 % (v/v) iAR and

stored at 4 °C in the dark before Hg isotopic measurements (Sun et al., 2013). Two certified reference materials, NIST 1632D (bituminous coal, n=2) and MESS3 (Arctic marine sediment, n=2) were processed along with the samples. Hg isotope compositions were subsequently measured in duplicate over two analytical sessions by cold vapor multi-collector inductively coupled plasma mass spectrometry (CV-MC-ICP-MS) following analytical procedures detailed by Sonke et al., 2010; Sun et al., 2013 and Jiskra et al., 2021. Briefly, the Hg^{II} in the iAR trap solution was reduced to Hg⁰ vapor using SnCl₂ solution (3 %, w/v, in 1 M HCl) and then analyzed for Hg stable isotopes using an online CETAC HGX-200 cold vapor generator coupled to a Thermo-Scientific Neptune PLUSTM equipped with a 10¹² Ω resistor on the ¹⁹⁸Hg isotope. The MC-ICP-MS instrumental mass bias was corrected by sample-standard bracketing using the NIST 3133 standard at matching standard and sample concentrations (0.71 ppb and 2.1 ppb). Long-term instrumental precision was monitored by repeated analysis of the ETH-Fluka (n = 6) and UM-Almaden (n = 3) Hg standard solutions at Hg concentrations corresponding to the samples (i.e., 0.71 ng/g and 2.1 ng/g). Procedural blanks had an average Hg concentration of ~ 0.01 ng/g (n=3). Mass-dependent fractionation (MDF) of Hg isotopes is reported in small delta notation (δ) as δ²⁰²Hg in permil (‰) relative to the bracketing NIST 3133 standard:

$$\delta^{202}\text{Hg} = \left[\left(\frac{{}^{202}\text{Hg}/{}^{198}\text{Hg}}{({}^{202}\text{Hg}/{}^{198}\text{Hg})_{\text{NIST3133}}} - 1 \right) \times 10^3 \right] \quad (1)$$

Mass independent fractionation (MIF) values are denoted using capital delta (Δ) notation and are defined as the difference between the measured values of δ¹⁹⁹Hg, δ²⁰⁰Hg, δ²⁰¹Hg, δ²⁰⁴Hg and those predicted for MDF with respect to δ²⁰²Hg using the kinetic MDF law as follows:

$$\Delta^{\text{xxx}}\text{Hg} = \delta^{\text{xxx}}\text{Hg} - K_{\text{xxx}} \times \delta^{202}\text{Hg} \quad (2)$$

where xxx refers to Hg isotope masses 199, 200, 201, and 204, and K_{xxx} refers to the constants that are used to calculate values for Δ^{xxx}Hg, which are: 0.2520, 0.5024, 0.7520 and 1.4930 for δ¹⁹⁹Hg, δ²⁰⁰Hg, δ²⁰¹Hg and δ²⁰⁴Hg respectively (Blum & Bergquist, 2007). Hg isotopic compositions are reported as the mean of duplicate measurements and analytical uncertainty of isotopic analysis are reported conservatively, as either the 2σ (2 × standard deviation) of the replicate sample measurements or that of the standard with the largest 2σ, whichever was larger. ETH-Fluka and UM-Almaden standard solutions yielded mean values (± 2σ) of -1.48 ± 0.14 ‰, 0.09 ± 0.03 ‰, 0.04 ± 0.03 ‰, 0.04 ± 0.07 ‰; and -0.59 ± 0.09 ‰, -0.03 ± 0.10 ‰, 0.02 ± 0.06 ‰ and -0.05 ± 0.07 ‰ for δ²⁰²Hg, Δ¹⁹⁹Hg, Δ²⁰⁰Hg, and Δ²⁰¹Hg respectively. NIST 1632D and MESS-3 had mean values of -1.93 ± 0.32 ‰, -0.01 ± 0.05 ‰, -0.06 ± 0.08 ‰, -0.06 ± 0.01 ‰; and -2.25 ± 0.02 ‰, 0 ± 0.04 ‰, 0.04 ± 0.03 ‰ and -0.14 ± 0.14 ‰ for δ²⁰²Hg, Δ¹⁹⁹Hg, Δ²⁰⁰Hg, and Δ²⁰¹Hg respectively. These mean values are comparable with reported values for these standard solutions and certified reference materials (Jiskra et al., 2019; Kwon et al., 2015; Sun et al., 2013).

2.3 Organic carbon content

All total organic carbon (TOC) content data for Laxian (n=26) were acquired during the present study. For the Potuo section, 10 data points are from Bagherpour et al. (2020) and an additional 28 samples

have been analyzed for this study. Organic matter content and preservation was assessed by Rock-Eval pyrolysis using a Rock EvalTM 6 with the analytical procedures described by Behar et al. (2001). This included measurement of total organic carbon (TOC) content, pyrolysis temperature (T_{max}), hydrogen index (HI) and oxygen index (OI). The standard IFP160000 was used for calibration of the samples and instrumental precision was about 0.1 wt.% for TOC, 10 mg HC/g for HI and 10 mg CO₂/g for OI.

2.4 Major and trace element analysis

Major and trace element concentrations were analyzed by X-ray fluorescence (XRF) spectrometry on glass discs and pressed tablets, respectively, using a PANalytical PW2400 XRF spectrometer at the University of Lausanne, Switzerland. The standard reference materials: JLS-1, JDO-1 and BHVO were used for assessment of analytical accuracy. External reproducibility (1σ) is between 0.5 % and 5 % depending on the element, and detection limit for major elements is ca. 0.01 % and between 1 and 7 ppm for trace elements.

2.5 U-Pb zircon geochronology

In total, nine volcanic ash layers from the Talung (Late Permian) and Daye (Early Triassic) formations at Potuo (POT66T, POT67T, and POT68T) and Laxian (LAX8T, LAX9T, LAX10T, LAX11T, LAX13T and LAX14T) were processed for U-Pb zircon dating. Of these, seven ash layers yielded sufficient zircon crystals for CA ID-TIMS U-Pb analyses. Zircon U-Pb isotopic compositions were determined by chemical abrasion, isotope dilution, thermal ionization mass spectrometry (CA-ID-TIMS) at the University of Geneva, Switzerland, following the procedure described by Widmann et al. (2019). Zircons were extracted from ash beds by conventional methods (crushing, milling, sieving, magnetic and density separation), including hand-picking of high aspect ratio grains free of visible inclusions. The zircon grains were thermally treated at 900 °C for 48 h to stimulate self-annealing prior to partial dissolution in concentrated hydrofluoric acid (HF_{conc}), to remove structurally damaged domains that may have suffered lead (Pb) loss (see Widmann et al. (2019) for the detailed procedure). The partially dissolved grains were then extracted and washed in 6N HCl in 3 ml Savillex beakers overnight (min. 12 h), at 80 °C. Further cleaning steps involve cycling of 7N HNO₃ and ultra-sonic bathing prior to loading into 200 µl capsules for dissolution in 2 to 3 drops of HF_{conc} for 48 h at 210 °C in pressurized ParrTM vessels. A ²⁰²Pb-²⁰⁵Pb-²³³U-²³⁵U tracer solution: ET2535 (EARTH TIME 2535, Condon et al., 2015) was added prior to dissolution, and Pb and U were isolated using ion exchange resin chromatography. Uranium and Pb isotopic compositions were measured on an IsotopX Phoenix TIMS at the University of Geneva. Pb was measured using a dynamic peak jumping routine on a Daly ion counting system, while uranium was measured as UO₂ in static mode using 10¹² Ω resistor Faraday amplifiers for samples POT66T, POT67T, POT68T, and using ATONA Faraday amplifiers (with a 30 s integration time) for samples LAX8T and LAX10T. The measured isotopic ratios were corrected for interferences of ²³⁸U¹⁸O¹⁶O on ²³⁵U¹⁶O₂ using a ¹⁸O/¹⁶O composition of 0.00205 based on repeat measurements of the U500 standard. Mass fractionation of U was corrected using a double isotope

tracer with a $^{235}\text{U}/^{233}\text{U}$ of 0.99506 ± 0.005 . The Pb blank isotopic composition is $^{206}\text{Pb}/^{204}\text{Pb} = 17.43 \pm 0.71$ (1σ), $^{207}\text{Pb}/^{204}\text{Pb} = 14.73 \pm 0.38$ (1σ) and $^{208}\text{Pb}/^{204}\text{Pb} = 35.58 \pm 1.04$ (1σ), based on total procedural blank measurements.

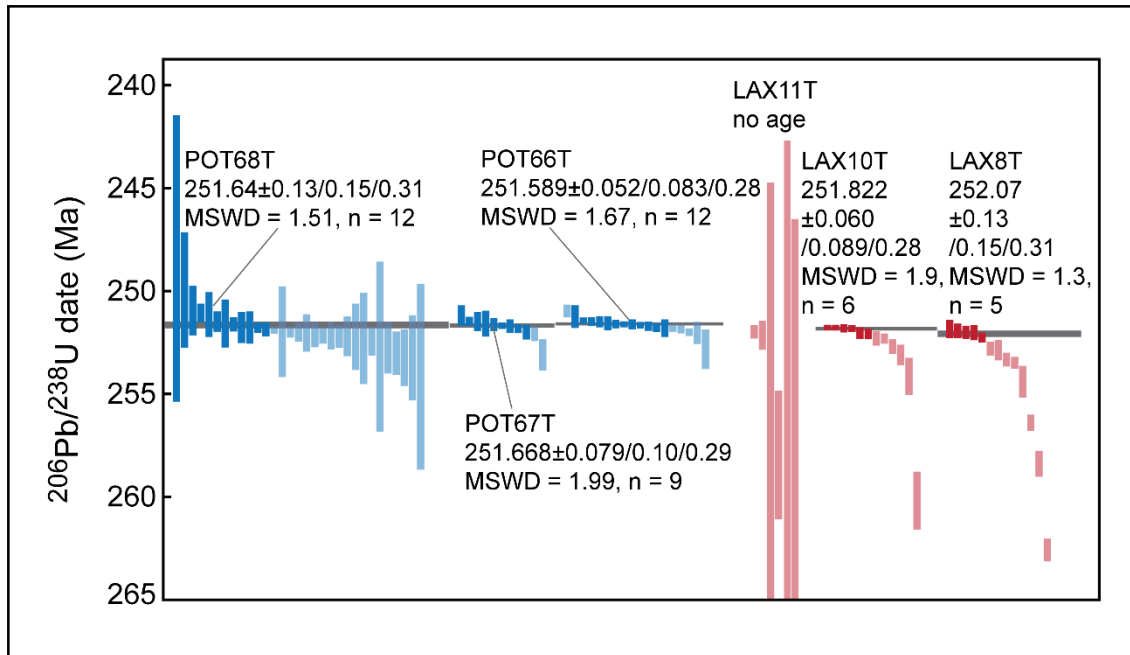


Figure 2. Single-grain zircon analyses and $^{206}\text{Pb}/^{238}\text{U}$ weighted mean dates for volcanic ash beds from Potuo and Laxian. Bars represent single grain zircon U-Pb dates and their uncertainty. Transparent bars are rejected for interpretation (Pb-loss, inheritance, antecrystic).

U-Pb dates of zircons were calculated using data reduction software Tripoli and ETRedux (Bowring et al., 2011; McLean et al., 2011), and all uncertainties are reported at the 95 % confidence interval. The interpreted weighted mean age is reported in the format: “weighted mean” \pm /X/Y/Z, where X corresponds to analytical uncertainty, Y to analytical + tracer uncertainty and Z to analytical, tracer and decay constant uncertainty (Schoene et al., 2006). All zircon $^{206}\text{Pb}/^{238}\text{U}$ dates were corrected for ^{230}Th - ^{238}U disequilibrium using a $\text{Th}/\text{U}_{\text{magma}}$ of 3.5 ± 1.0 . We discuss dates at the precision level of analytical uncertainty (X), since most U-Pb data in the relevant literature were obtained using the same isotope tracer (ET2535) and mode of analysis (ID-TIMS), effectively eliminating inter-lab uncertainty. Repeat analyses of the ET100 solution ($^{206}\text{Pb}/^{238}\text{U}$ age: 100.173 ± 0.003 Ma; Schaltegger et al., 2021) yielded a value of 100.1678 ± 0.0046 Ma (mean square weighted deviation (MSWD) = 3.2, n = 32/40). One batch comprising 8 ET100 samples was rejected due to an anomalous young average age (this batch is internally consistent). Similarly young, anomalous ET100 ages observed in Schaltegger et al. (2021) were explained by fractionation effects during the sample preparation process. Inclusion of this rejected batch would result in an average ET100 age of 100.1639 ± 0.0039 Ma (MSWD = 3.8, n = 39/40). Excess scatter is indicated by the elevated MSWD value and is commonly observed for the synthetic ET100

solution. This is potentially derived from instrument instability and from the sample preparation process (Schaltegger et al., 2021).

3. Results

Results of all geochemical analyses are given in the supplementary information and presented in figures 2 to 5.

3.1 U-Pb zircon geochronology

A total of 98 zircons from 7 volcanic ash beds were analyzed. Zircon U and Pb data are presented in the supplementary information and interpreted U-Pb dates are illustrated in Fig. 2. For each volcanic ash bed, the U-Pb weighted mean date is interpreted on the following basis: i) not rejecting any analyses that are concordant, ii) the youngest cluster of interpreted concordant zircons consists of ≥ 3 analyses and iii) assuming that all Pb-loss is effectively removed by the chemical abrasion procedure. This data reduction strategy is in line with previous U-Pb ID-TIMS studies concerning volcanic ash beds straddling the Permian-Triassic Boundary and the Early Triassic (e.g., Augland et al., 2019; Baresel et al., 2017b; Burgess et al., 2014; Widmann et al., 2020), making all of these previous ID-TIMS ages directly comparable.

Only in one sample (POT 66T) do we reject one younger, concordant analysis, as it is younger than the statistically significant, slightly older age plateau of 12 analyses (Fig. 2). We assume that this deviation is due to unresolved, residual lead loss not mitigated by the chemical abrasion procedure. Analyses that are older than the youngest, statistically valid, date plateau are considered detrital or due to inherited or antecrystic cores. The principal guideline for the youngest weighted mean age determination is a statistically valid MSWD for the chosen age cluster. Applying this strategy, volcanic ash beds LAX8T, LAX10T, POT66T, POT67T and POT68T have statistically significant $^{206}\text{Pb}/^{238}\text{U}$ weighted mean ages of $252.07 \pm 0.13/0.15/0.31$ Ma (Mean Square Weighted Deviation (MSWD) = 1.3, n = 5), $251.822 \pm 0.060/0.089/0.28$ Ma (MSWD = 1.9, n = 6), $251.589 \pm 0.052/0.083/0.28$ Ma (MSWD = 1.67, n = 12), $251.668 \pm 0.079/0.10/0.29$ Ma (MSWD = 1.99, n = 9) and $251.64 \pm 0.13/0.15/0.31$ Ma (MSWD = 1.5, n = 12), respectively (Fig. 2). Ash beds LAX14T and LAX11T (Table S1) did not satisfy the data reduction criteria outlined above and are thus not interpreted.

3.2 TOC contents and Hg concentrations

TOC content is stratigraphically variable and generally low for Laxian relative to Potuo with a range between $< 0.1 - 0.3$ wt.% and $0.1 - 2.9$ wt.% respectively (Fig. 3). TOC generally shows moderate correlation with Hg for Laxian ($r^2 = 0.36$) and Potuo ($r^2 = 0.50$) (Fig. 4). Only 3 samples for Laxian have TOC content above 0.2 wt.%, a suggested threshold for robust Hg/TOC normalization (Grasby et al., 2016). In contrast, only 6 out of 38 samples for Potuo have TOC values < 0.2 wt.%. Therefore, Hg data for Laxian are not normalized to TOC. OI values for Laxian are high and have a range between 69 and 1386 mg CO_2/g TOC. OI values are between 3 and 334 mg CO_2/g TOC for Potuo, except for

volcanic ash samples with values between 64 and 967 mg CO₂/g TOC. HI values are between 19 and 283 mg HC/g TOC and between 17 and 229 mg HC/g TOC for Potuo and Laxian respectively.

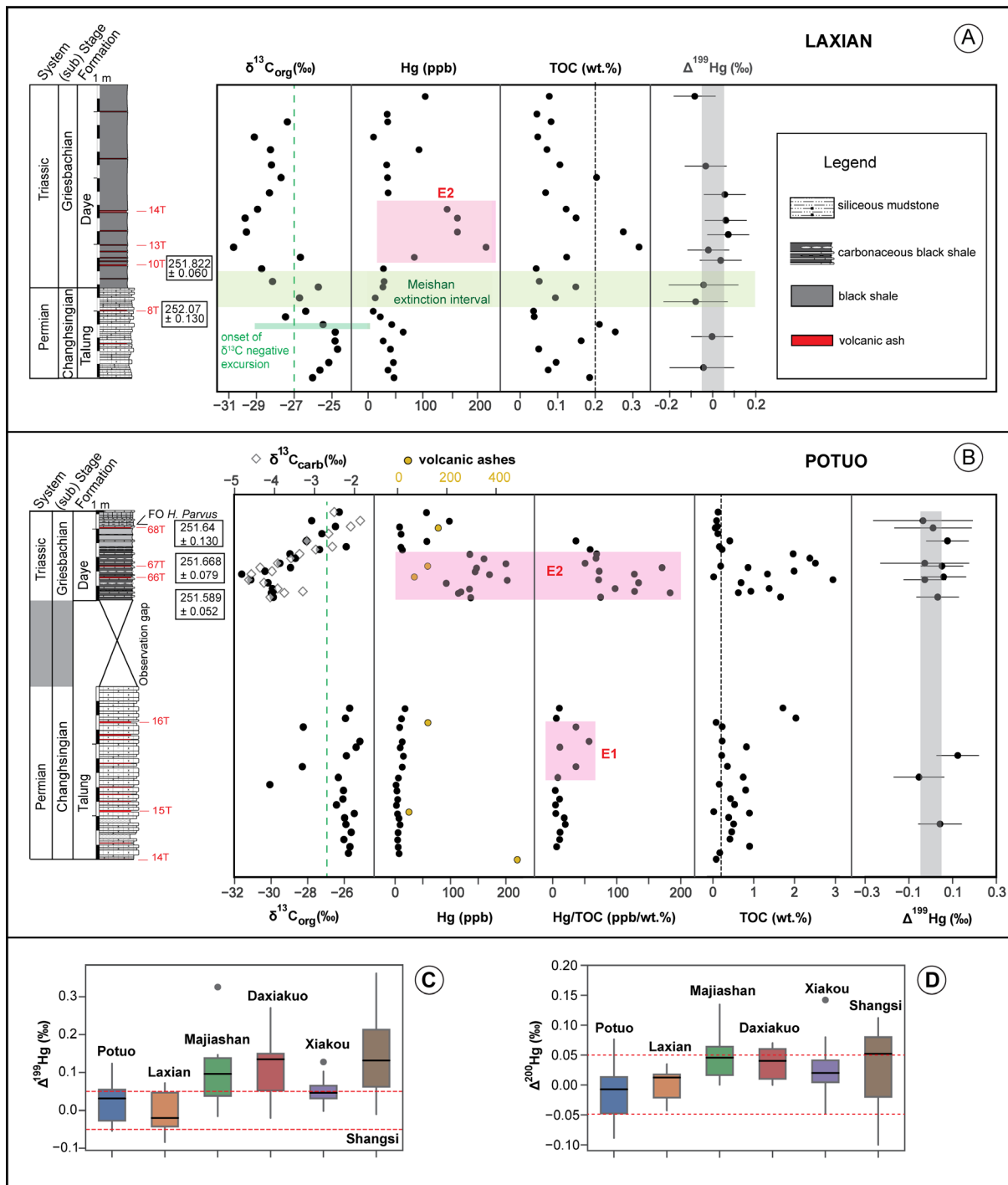


Figure 3. Carbon isotope values, Hg concentrations, Hg/TOC ratios, TOC contents and Δ¹⁹⁹Hg values from a) Laxian, b) Potuo. The gap between the Talung and Daye formations in the Potuo stratigraphic log is an observation gap due to coverage by alluvium (Bagherpour et al., 2020). Note that the x-axis for volcanic ash Hg concentrations in B is at the top. Black dashed lines represent the 0.2 wt.% TOC limit for Hg/TOC normalization (Grasby et al., 2016) and green dashed lines represent background δ¹³C_{org} values (-27 ‰). Box and whisker plots of c) Δ¹⁹⁹Hg values and d) Δ²⁰⁰Hg values for Potuo and

Laxian compared to those previously documented for other deep-water marine sections in South China. Grey shaded rectangle (in a, b) and red dashed lines (in c, d) represent the interval of no measurable Hg isotope mass independent fractionation (MIF, $0 \pm 0.05 \text{ ‰}$). Data sources are as follows: Majiashan - Wang et al.(2019a), Daxiakou - Wang et al. (2018), Xiakou - J. Shen et al. (2019), Shangsi - J. Shen et al. (2021).

Hg concentrations of samples from the Talung Fm. in Potuo are between 2 ppb and 18 ppb and are generally lower than for Laxian, which have a range between 9 ppb and 64 ppb. The main feature of the latest Permian Hg record for Potuo is a minor Hg/TOC excursion (referred to as E1 here) with a peak Hg/TOC value of 70 ppb/wt.%. In the Daye Fm., a significant Hg concentration increase (here labelled as E2) is recorded in the lower part of the successions at both sections. This Hg excursion is simultaneously expressed by the Hg and Hg/TOC records for Potuo (Fig. 3). Peak Hg concentrations within E2 Hg anomaly (Laxian = 251 ppb, Potuo = 203 ppb) are higher than the mean so far reported (62 ppb) for sedimentary rocks (Grasby et al., 2019).

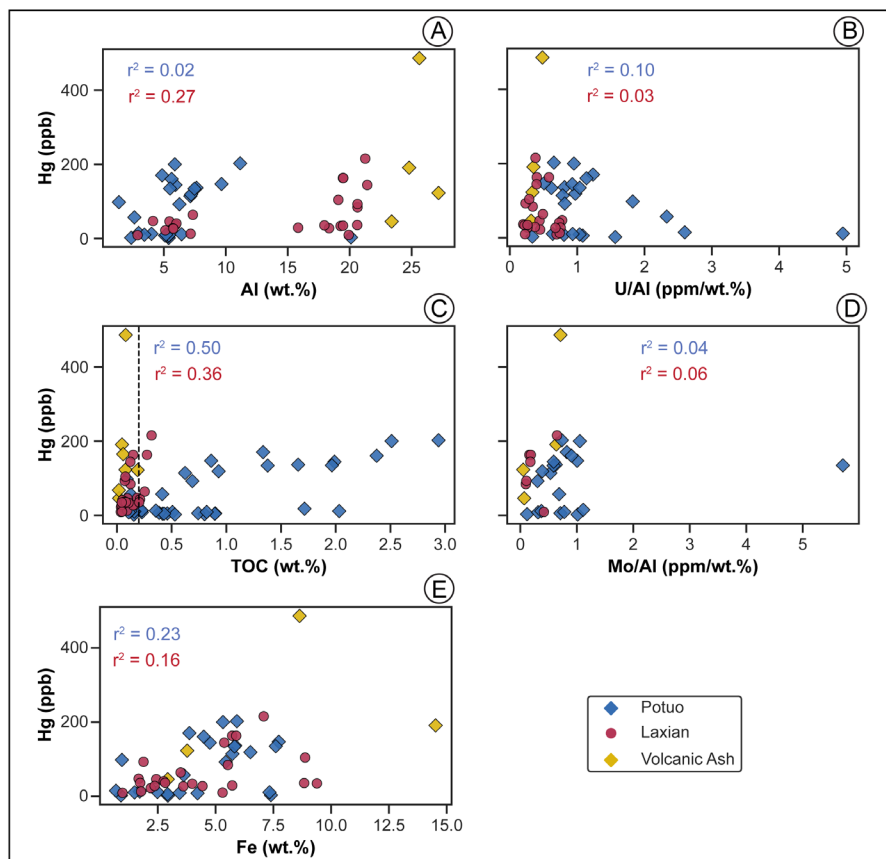


Figure 4. Scatter plot showing the relationship between Hg and a) Al, b) U/Al, c) TOC, d) Mo/Al and e) Fe in the Pingtang syncline sections. Black dashed line represents 0.2 wt.% TOC limit (Grasby et al., 2016). Volcanic ash samples are not included in the calculation of the correlation coefficient squared (r^2).

Volcanic ashes from the Talung Fm. at Potuo have Hg concentrations that are at least one order of magnitude higher than for interbedded siliceous mudstones. This difference does not hold in the Daye Fm., where Hg concentration values range between 68 ppb and 165 ppb for volcanic ashes and between 84 ppb and 203 for interbedded rocks within the E2 Hg anomaly interval (Fig. 3b).

3.3 Mercury isotopes

Mass dependent fractionation of Hg isotopes ($\delta^{202}\text{Hg}$) shows near-zero to negative values for both sections throughout the studied interval (range: $+0.23 \pm 0.32 \text{ ‰}$ to $-1.75 \pm 0.32 \text{ ‰}$; mean = $-1.13 \pm 1.02 \text{ ‰}$), except for 2 volcanic ash samples from Potuo with more negative values (Fig. 5, POT66T: $-2.49 \pm 0.32 \text{ ‰}$ and POT67T: $-2.29 \pm 0.32 \text{ ‰}$).

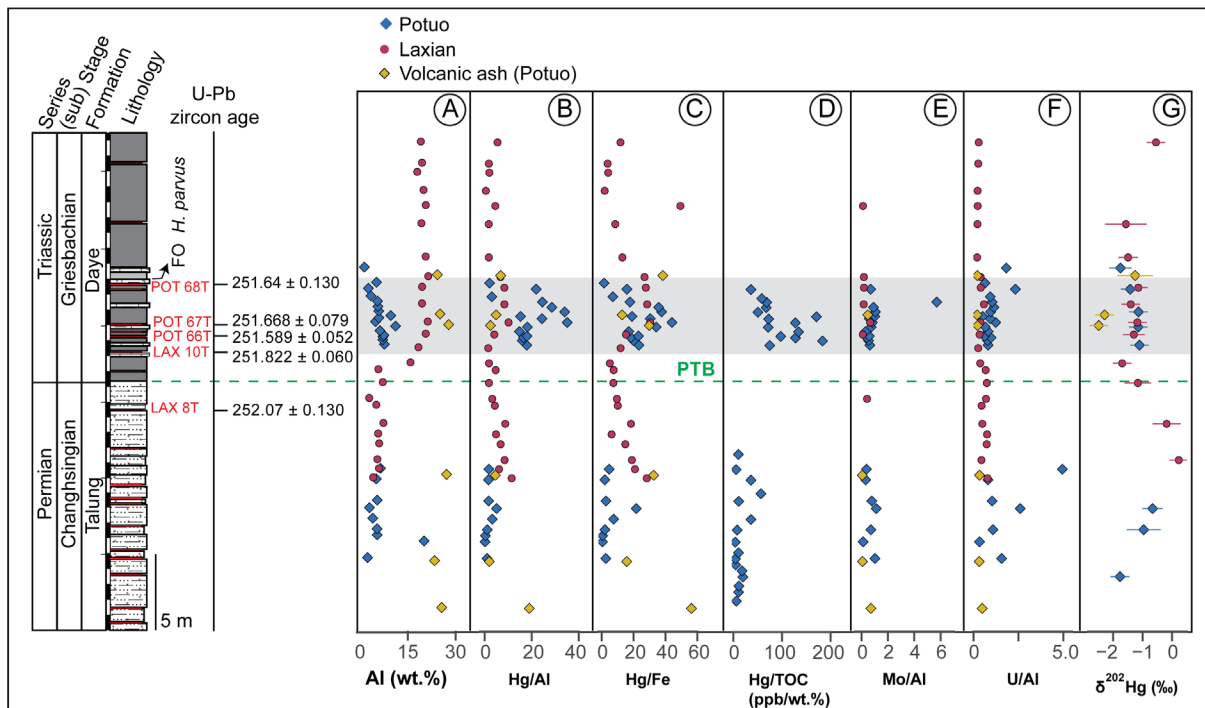


Figure 5. Composite plot of Hg/element ratios and Hg isotope mass dependent fractionation values for Potuo and Laxian. a) Al, b) Hg/Al, c) Hg/Fe, d) Hg/TOC, e) Mo/Al, f) U/Al, g) $\delta^{202}\text{Hg}$. Symbols of lithological log are identical to those of Fig. 3. The composite section is based on lithological comparison of the Potuo and Laxian sections (Bagherpour et al., 2020) and assumes similar sedimentation rates for both sections. Note that the Potuo and Laxian sections are only 6.4 km apart and both belong to the Pingtang syncline of the Nanpanjiang Basin, recording laterally continuous basinal facies belonging to the Talung Fm. and Daye Fm. (Bagherpour et al., 2020).

Hg isotope MIF ($\Delta^{199}\text{Hg}$ and $\Delta^{200}\text{Hg}$) values for both sections are near-zero throughout the studied interval (i.e., $0.1 \text{ ‰} > z > -0.1 \text{ ‰}$, where z = sample Hg MIF value), except for sample POT 59, which has a $\Delta^{199}\text{Hg}$ value of $0.12 \pm 0.11 \text{ ‰}$. Mean ($\pm 2\sigma$) $\Delta^{199}\text{Hg}$ values are $0.02 \pm 0.11 \text{ ‰}$ and $-0.01 \pm 0.11 \text{ ‰}$ for Potuo and Laxian respectively. For Potuo, the mean $\Delta^{200}\text{Hg}$ value is $-0.01 \pm 0.10 \text{ ‰}$ and for Laxian, it is $0.00 \pm 0.05 \text{ ‰}$. Hence, the Pingtang syncline sections record no measurable mass

independent fractionation of Hg isotopes, in contrast to Hg isotope records for deep-water marine sections outside the Nanpanjiang Basin in South China (Fig. 3c).

3.4 Major and Trace Elements

Al₂O₃ concentrations for both sections show similar patterns, having lower values in the Talung Fm. (with a range of 2 to 4 wt.%, except for 1 Potuo sample) relative to the Daye Fm. For Laxian, Al₂O₃ values in the Daye Fm. are 3× higher (range: 15 – 22 wt.%) than those of the Talung Fm. Fe₂O₃ concentrations show a similar trend to Al₂O₃, with lower values in the Talung Fm. (1 to 5 wt.%) relative to the Daye Fm. for both localities. However, unlike Al₂O₃, values in the Daye Fm. for both localities are identical (between 2 and 9 wt.%). Al and Fe (proxied by Al₂O₃ and Fe₂O₃) show little to no correlation with Hg for both Potuo (Al: $r^2=0.02$, Fe: $r^2=0.23$) and Laxian (Al: $r^2=0.27$, Fe: $r^2=0.16$). Mo and U are redox-sensitive trace elements used to track redox variations in sedimentary environments (Algeo & Maynard, 2004; Hardisty et al. 2018; Tribovillard et al., 2006). Redox-sensitive trace element concentrations are usually normalized to Al to account for variations that may be unrelated to changes in redox conditions, such as changes in sediment input or authigenic mineral formation (e.g., Algeo & Maynard, 2004; Grasby et al., 2013; Rolison et al., 2017). For Laxian, 73 % of samples analyzed have Mo contents lower than the lower limit of detection (LLD) of the XRF spectrometer (i.e., 1 ppm). Mo/Al values show no stratigraphic trend for either studied locality (Fig. 5e) and have no correlation with Hg contents (Potuo: $r^2 = 0.04$, Laxian: $r^2 = 0.06$; Fig. 4D). Laxian samples with measurable Mo (n = 7) have Mo/Al values between 0.1 and 0.6 ppm/wt.%. Mo/Al values for Potuo are slightly higher and range between 0.1 and 1.1 ppm/wt.%, except for sample POT 80 with a value of 5.7 ppm/wt.%. Potuo U/Al values range between 0.2 and 2.3 ppm/wt.%, except for sample POT 63 (U/Al = 4.9 ppm/wt.%). For Laxian, U/Al ranges between 0.2 and 0.8 ppm/wt.%. As with Mo/Al, no correlation is observed between Hg and U/Al (Potuo: $r^2 = 0.10$, Laxian: $r^2 = 0.03$; Fig. 4b).

Volcanic ash samples have high LOI (loss on ignition) values between 9 to 14 wt.%, consistent with results from contemporaneous ash layers in South China (He et al., 2014). The ash samples have LOI-corrected mean ($\pm 1\sigma$) concentrations of 58 ± 5 wt.%, 25 ± 2 wt.% and 5 ± 3 wt.% for SiO₂, Al₂O₃ and total alkali (Na₂O+K₂O) respectively (Table S2, supplementary information). To mitigate the chemical effects of secondary alteration of the volcanic ashes, only immobile elements (such as Th, Nb, Ta, Zr, Hf, Ti, Y), known to be unaffected by post-depositional alteration (Portnyagin et al., 2020), are utilized for subsequent chemical classification and tectonic interpretation (Fig. 6). The ashes mainly plot within the fields of rhyodacite/dacite, andesite and trachyandesite on the Nb/Y vs. Zr/Ti diagram (Winchester and Floyd, 1977), separate from STLIP volcanic rocks, except for 1 sample: POT 14T (Fig. 6a). Incompatible trace elements normalized against primitive mantle values (Sun and McDonough, 1989) show that the volcanic ashes are characterized by pronounced negative Nb, Ta and Ti anomalies (Fig. 6d), similar to the trace element pattern for volcanic ashes from other localities in South China (He et al., 2014; Yang et al., 2012).

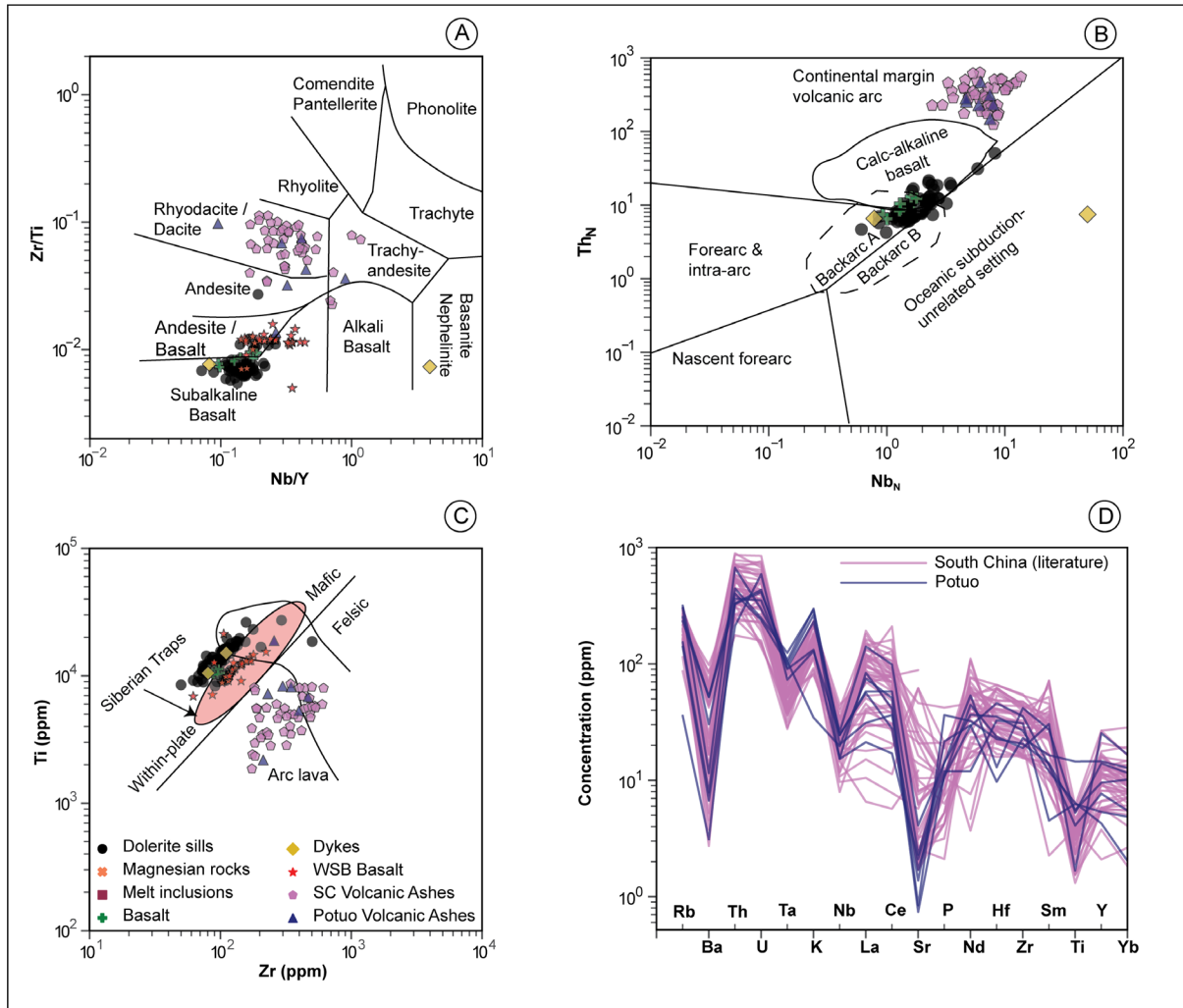


Figure 6: Major and trace element geochemistry results for volcanic ash samples from the Pingtang syncline. A) Zr/Ti vs Nb/Y classification diagram (Winchester & Floyd, 1977) for volcanic ashes from South China plotted along with volcanic rocks from the Siberian Traps Large Igneous Province (STLIP) B) N-MORB-normalized Th vs. Nb discriminant plot, with tectonic setting interpretation after Saccani et al. (2015, 2018) for volcanic ashes from South China, together with data from dolerite sills, dykes and basalts from the STLIP (Tunguska Basin) plotted for comparison. N-MORB: normal-type mid-oceanic ridge basalt. C) Ti vs Zr classification diagram after Pearce (1982). The field illustrating typical Siberian Traps volcanic rock compositions is after He et al. (2014). D) Primitive mantle-normalized spider diagram for Changhsingian and Griesbachian volcanic ashes from Potuo and other localities (Meishan, Chaotian, Jianshi, Rencunping, Shangsi and Dongpan) in South China. Data for South China localities other than Potuo are from He et al. (2014), Song et al. (2022) and Wang et al. (2019b). Normalization values for N-MORB and primitive mantle are from Sun & McDonough (1989). Data for volcanic rocks from the STLIP are from several sources as follows: basalt flows, dolerite sills, dykes: Sibik et al. (2015); Callegaro et al. (2021); magnesian rocks, melt inclusions: Sobolev et al. (2009); West Siberia Basin (WSB) basalts: Reichow et al. (2005). WSB: West Siberia Basin, SC: South China.

4. Discussion

4.1 Sedimentary hosts of Hg and interpretation of the Hg anomalies

4.1.1 Hosts of Hg

Hg enrichment in sediments may reflect enhanced Hg sequestration related to increased abundance of its sedimentary host phase(s) or enhanced Hg input fluxes during sediment deposition (Grasby et al., 2019; J. Shen et al., 2020). Due to the high affinity of Hg for organic matter (OM), Hg concentration is usually normalized to TOC content to account for any OM increases that could have preferentially enhanced Hg sequestration in sediments (e.g., Sanei et al., 2012; Grasby et al., 2017, 2019). However, in samples with low OM content (< 0.2 wt.% TOC), the Hg/TOC ratio is deemed unreliable as the Hg/TOC values become exaggerated, potentially producing false Hg/TOC peaks (Grasby et al., 2016; 2019; but see Yager et al., 2021). In addition to TOC variations, Hg sequestration in sedimentary rocks can be influenced by other sedimentary host phases such as clay minerals, iron oxides and sulfides (Charbonnier et al., 2017; J. Shen et al., 2020).

Based on cross plots of Hg vs. TOC, Al, Fe, Mo/Al and U/Al values for both sections, Hg is best correlated to TOC (r^2 : Potuo = 0.50 and Laxian = 0.36, Fig. 4c). This correlation suggests that Hg sequestration in the studied sites was partially controlled by organic matter availability and may explain the more efficient sequestration of Hg in the black shales of the Daye Formation relative to the siliceous mudstones of the Talung Formation. Nevertheless, plots of Hg/Al and Hg/Fe ratios for both localities, including Hg/TOC for Potuo (Fig. 3; Fig 5) show similar trends of peak Hg contents in the lower part of the Griesbachian record, suggesting that the Hg anomaly in this interval cannot be explained by TOC variability or clay mineral inputs alone. Furthermore, lithological changes are unlikely to control the Hg concentration spike as increases in Hg concentration do not coincide with the change in lithology in either of the two sections. Moreover, relatively high, and low Hg concentrations alike are measured for the Talung and Daye formations where Hg and Hg/TOC anomalies are recorded (Fig. 3; Fig. 8).

4.1.2 Evaluation of Hg preservation

As OM is the dominant host of Hg in the studied successions, the potential impact of post-depositional OM degradation on the Hg record warrants evaluation. Rock-Eval TOC data cross plots (HI, OI, T_{\max}) (Fig. 7) are routinely used to evaluate the type and maturity of preserved OM in sedimentary successions (e.g., Charbonnier et al., 2020; Espitalié et al., 1985; Fantasia et al., 2018). The low HI and OI values of many of the samples with enough OM for Rock-Eval data interpretation (i.e., TOC > 0.2 wt.%, Fig. 7a) may indicate diagenetic alteration of marine OM (altered type II) and/or high input of terrestrial OM (type III) (Charbonnier et al., 2020; Fantasia et al., 2018). The range of T_{\max} values (400 – 525 °C) suggests that some of the OM in the studied successions are thermally mature and have undergone post-depositional oxidation (Fig. 7b; Espitalié et al., 1985). The thermal maturity of preserved OM in some strata of the studied successions suggests that original Hg contents may have been diagenetically

modified due to OM loss (Charbonnier et al., 2020). Consequently, the Hg content measured for strata characterized by thermally mature OM may be a minimum estimate of the original Hg content of these rocks.

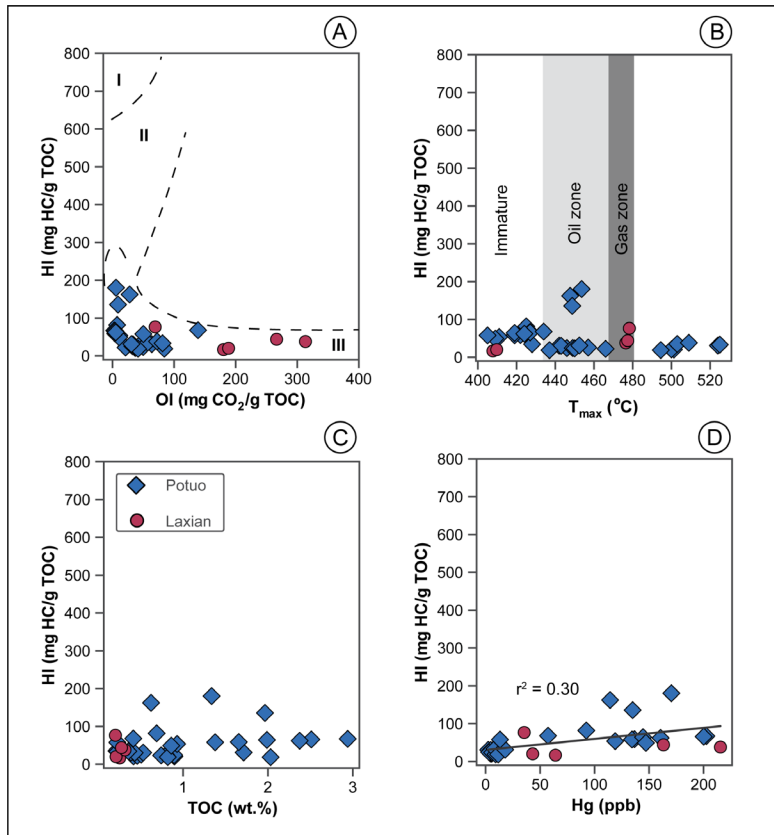


Figure 7. Cross plots of Rock-Eval TOC data for samples with TOC > 0.2 wt.% to assess the type and quality of preserved organic matter in Potuo and Laxian (modified after Charbonnier et al., 2020). A) HI vs OI, b) HI vs T_{max}, c) HI vs TOC, d) HI vs Hg.

Despite the probable partial loss of the original Hg content for some samples, several points argue in favor of the reliability of the general Hg trend documented in the present study. The global negative $\delta^{13}\text{C}$ excursion characteristic of the PTB is recorded in both successions, and for Potuo is recorded both for organic and carbonate carbon, similar to the Meishan GSSP (Fig. 9). The Changhsingian to Griesbachian Hg trend for both localities is similar despite the vast difference in OM content (Fig. 3). The lack (or loss) of OM is more prevalent in the Laxian succession, yet the background Hg content in this succession is 3× that of Potuo. Also, volcanic ashes mostly have similar Hg content in the Talung and Daye Fm. In contrast, interbedded rocks differ strongly in Hg content between these rock formations (Fig. 3). The much higher Hg content of volcanic ashes despite their higher susceptibility to weathering (e.g., Jiao et al. 2022) and as such, Hg loss, suggests that: i) Hg is reasonably well preserved in these strata, and ii) that the disparity in Hg content between volcanic ashes and interbedded rocks is primary.

Furthermore, both sections record the E2 Hg anomaly, and with a similar excursion magnitude (Fig. 3, Fig. 8). Similar Hg trends are documented for coeval strata within the Nanpanjiang Basin i.e., Kejiao and Xinmin (J. Shen et al., 2019). Specifically, the Hg anomaly associated with the PTB in these Nanpanjiang Basin sections is recorded in Griesbachian strata (Fig. 9; see also figures 2, S6, and S7 of J. Shen et al. 2019). This similarity between the Changhsingian to Griesbachian Hg trends and hence, their spatial reproducibility across the Nanpanjiang Basin indicates that primary Hg concentration trends are preserved in Potuo and Laxian. In addition, there is no correlation between HI and TOC (Fig. 7c) and little correlation ($r^2 = 0.30$) between HI and Hg values (Fig. 7d), suggesting that OM maturity does not influence Hg trends to any large degree in these successions. Also, the E2 Hg anomaly coincides with the climax of the negative $\delta^{13}\text{C}$ excursion at the P-T transition (Fig. 3, Fig. 8), suggesting that the Hg trend is controlled by environmental perturbations (as indicated by the $\delta^{13}\text{C}$ excursion), and not diagenetic alteration. Finally, Charbonnier et al. (2020) noted that despite the oxidative weathering of OM observed for weathered rock samples, there were no significant changes in Hg/TOC ratios, suggesting that the Hg/TOC ratio is less susceptible to the effects of post-depositional OM degradation. In the present study, both Hg anomalies reported are present in the Hg/TOC record and more significantly, the main excursion (E2) is present in both the Hg and Hg/TOC record, suggesting that these Hg trends are primary.

4.1.3 Hg isotopes

Hg isotopes are used to trace the source(s) and depositional pathway(s) of Hg to natural environments, as Hg isotope mass-dependent fractionation ($\delta^{202}\text{Hg}$) and mass-independent fractionation (MIF, $\Delta^{199}\text{Hg}$ and $\Delta^{200}\text{Hg}$) compositions vary across Earth surface reservoirs and transport mechanisms (Bergquist & Blum, 2007; Blum et al., 2014; Fu et al., 2021). Here, we focus on Hg isotope MIF, as this occurs via fewer processes compared to MDF (Blum et al., 2014). Also, $\delta^{202}\text{Hg}$ values of direct volcanic emissions overlap with those of terrestrial runoff and atmospheric Hg^{II} deposition (Yager et al., 2021), making them less diagnostic than Hg isotope MIF values.

Hg isotope MIF values are considered to be resistant to diagenetic alteration (e.g., Grasby et al. 2017; Thibodeau et al., 2016). This view was recently strengthened by the experimental study of Chen et al. (2022), who documented that high-temperature or high-pressure alteration of rocks does not result in alteration of $\Delta^{199}\text{Hg}$ and $\Delta^{200}\text{Hg}$ values. $\Delta^{199}\text{Hg}$ is commonly used to interpret the sources and pathways of Hg deposition (Thibodeau & Bergquist, 2017; Yager et al., 2021) and recently, $\Delta^{200}\text{Hg}$ has been proposed as a complementary tracer of Hg sources to land and oceans (Jiskra et al., 2021). This proposition is because even number-Hg isotope MIF (e.g., $\Delta^{200}\text{Hg}$) only occurs via upper atmospheric oxidation-reduction pathways and thus, Hg transformations near Earth's surface yield no measurable even number-Hg isotope MIF (Chen et al., 2012; Fu et al., 2021). Hg from terrestrial biomass usually has negative $\Delta^{199}\text{Hg}$ values while oceanic reservoirs (e.g., marine sediments and seawater) are characterized by near-zero to positive $\Delta^{199}\text{Hg}$ values (Blum et al., 2014; Yin et al., 2022). Furthermore,

Hg released to the atmosphere may undergo MIF via photochemical reactions during its cycling, acquiring positive or negative MIF values (Blum et al., 2014) before long-term burial in marine sediments (Thibodeau et al., 2016). Hg derived from direct volcanic emission is thought to have no measurable MIF (i.e., $\Delta^{199}\text{Hg}$, $\Delta^{200}\text{Hg} = \sim 0 \text{ ‰}$, Thibodeau & Bergquist, 2017; Zambardi et al., 2009), consistent with a recent estimate of the $\Delta^{199}\text{Hg}$ value of the primitive mantle ($0.00 \pm 0.10 \text{ ‰}$, Moynier et al., 2021). Therefore, near-zero $\Delta^{199}\text{Hg}$ values recorded for rock samples in the geologic record have been interpreted as reflecting unaltered volcanic Hg input to the depositional environment (e.g., Font et al., 2021; Thibodeau et al., 2016; Yager et al., 2021; H. Zhang et al., 2021). Alternatively, near-zero $\Delta^{199}\text{Hg}$ values have also been interpreted as reflecting Hg contributions from a combination of terrestrial and oceanic Hg reservoirs (e.g., J. Shen et al., 2019; 2021; Wang et al., 2019a).

The near-zero and invariant $\Delta^{199}\text{Hg}$ and $\Delta^{200}\text{Hg}$ values throughout our studied interval (Fig. 8) are consistent with direct volcanic Hg input from a volcanic center close to the Nanpanjiang Basin, or a mixture of terrestrial and atmospheric/volcanic Hg sources. Several lines of evidence, however, argue in favor of a dominantly atmospheric volcanic Hg source to the studied successions. First, the lack of correlation between Hg and Al suggests that Hg sequestration was unrelated to terrestrial input to the Pingtang syncline. As terrestrial input is characterized by negative Hg isotope MIF values (Thibodeau & Bergquist, 2017; Yager et al., 2021; Yin et al., 2022), enhanced clastic input during the Griesbachian (as evidenced by dominantly shale lithology and increase in Al content, Fig. 5) is expected to have resulted in more negative $\Delta^{199}\text{Hg}$ values. However, $\Delta^{199}\text{Hg}$ values immediately after the PTB are near-zero to slightly positive for both sites (Fig. 3), suggesting that atmospheric volcanic Hg input was the dominant source of Hg to the Nanpanjiang Basin even with potentially higher terrestrial Hg delivery to the basin during the Griesbachian. Second, the Nanpanjiang Basin was situated close to a volcanic center during the P-T transition. This proximity is evidenced by the occurrence of thicker volcanic ash beds in coeval marine successions in southwest South China (i.e., in the Nanpanjiang Basin) relative to the rest of South China (He et al., 2014; Zhao et al., 2019), the occurrence of coeval acidic-intermediate volcanic and intrusive rocks in southwestern South China and northern Vietnam, as well as copper concentration and isotope excursions linked to felsic “super-eruptions” in South China during the Changhsingian (H. Zhang et al., 2021 and references therein). The paleo-location of the Nanpanjiang Basin may, therefore, also explain the disparity between the Pingtang syncline Hg MIF record and those previously published for other parts of South China (e.g., J. Shen et al., 2021; Wang et al., 2019a; Fig. 3c) (discussed in section 4.4). Third, the Hg isotope MIF values for volcanic ash samples are indistinguishable from those of overlying and underlying strata, suggesting that the source of Hg for volcanic ashes (TOC = ~ 0) and interbedded rocks (TOC = 0 – 3 wt.%) were the same. Consequently, the Hg and Hg/TOC anomalies recorded for both localities are interpreted as dominantly reflective of pulses of elevated atmospheric volcanic Hg input to these deep-water marine depositional sites.

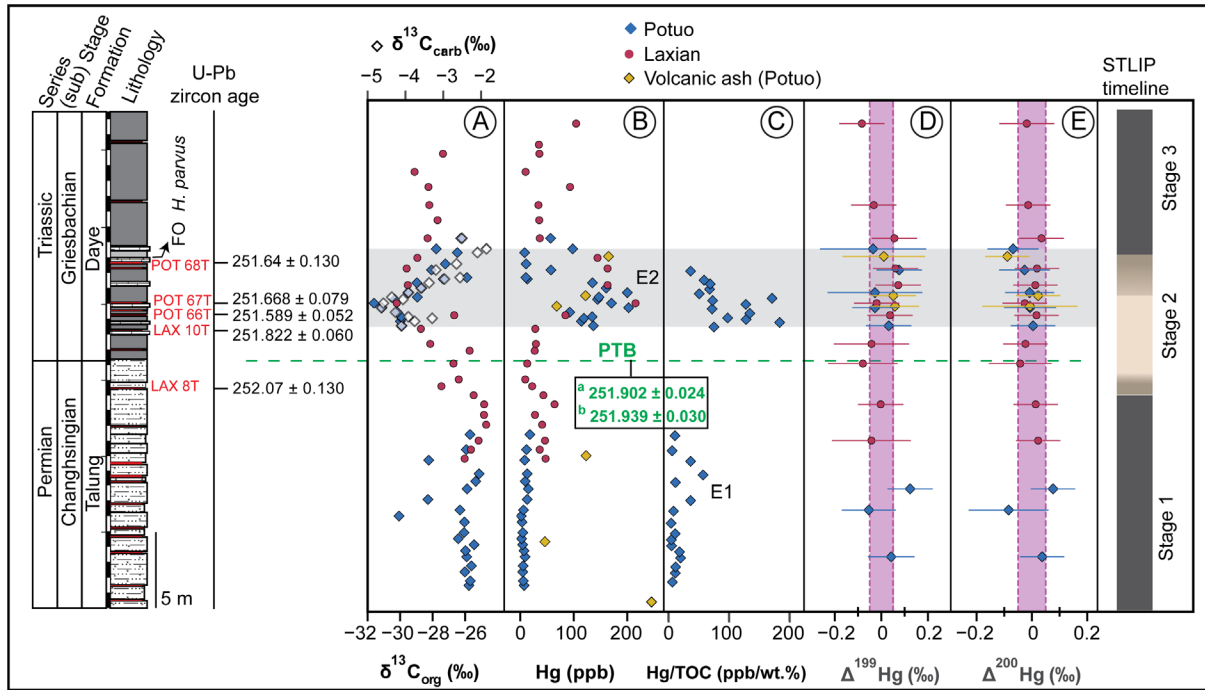


Figure 8. Composite profiles for a) $\delta^{13}\text{C}$, b) Hg concentration, c) Hg/TOC ratios, d) $\Delta^{199}\text{Hg}$, e) $\Delta^{200}\text{Hg}$ records from the Potuo and Laxian sections. $\delta^{13}\text{C}$ values are from Bagherpour et al. (2020). The horizontal gray band marks the interval of Hg concentration spike (E2) and nadir of the negative $\delta^{13}\text{C}$ excursion, and the vertical pink bands depict near-zero Hg isotope MIF (0 ± 0.05 ‰, Thibodeau et al., 2016). The dashed green line represents the Talung-Daye formational boundary and the PTB. The Siberian Traps magmatism timeline is after Burgess et al. (2017) and the color gradient between the stages depicts the uncertainty in the timing of the transition between different stages. The PTB on the composite log is defined from the Laxian section as this interval at Potuo is covered by recent alluvial deposits (Bagherpour et al., 2020). U-Pb zircon ages for the PTB (in green) are from (a) Burgess et al. (2014) and (b) Baresel et al. (2017b). FO – first occurrence.

4.2 U-Pb zircon age constraints on the Hg anomaly and C isotope excursion

Although previous works (Grasby et al., 2017; J. Shen et al., 2019; Sial et al., 2020) indicated a coeval global occurrence of Hg anomalies around the PTBME, the majority of sections with defined Hg anomalies around the P-T transition lack high-resolution, high-precision geochronology. Our study attempts to specifically bracket the age of a well-defined Hg anomaly in the Early Triassic via dating of under and overlying ash beds in expanded deep-water marine records. The new U-Pb zircon ages from the Pingtang syncline span the onset of the latest Permian negative $\delta^{13}\text{C}$ excursion, ca. 252.07 ± 0.130 Ma and brackets a Griesbachian Hg anomaly. The two ash layers analyzed from Laxian straddle the PTB and the U-Pb ages are consistent with the stratigraphy, yielding U-Pb weighted mean ages of 252.07 ± 0.13 Ma (LAX8T, latest Permian) and 251.822 ± 0.060 Ma (LAX10T, Griesbachian) respectively. These U-Pb zircon ages overlap, within analytical error, with the ages of Bed 25 (251.941 ± 0.037 Ma) and Bed 28 (251.880 ± 0.031 Ma) of the very condensed Meishan Global Stratotype

Section and Point (GSSP) (Burgess et al., 2014). Thus, the interval between LAX8T and LAX10T includes the PTBME interval at Meishan and agrees with previous suggestions that the conformable lithological boundary between the Talung/Dalong and Daye/Ziyun formations accurately delineates the PTB in deep-water marine successions in the Nanpanjiang Basin (Bagherpour et al., 2020; Baresel et al., 2017b). Based on lithological comparisons between Potuo and Laxian, the E1 anomaly in Potuo is stratigraphically below LAX 8T (Bagherpour et al., 2020) and as such, likely predates the mass extinction interval. However, the lack of U-Pb ages in the strata spanning E1 makes quantitative comparisons to LAX 8T uncertain.

The overlap between the $^{206}\text{Pb}/^{238}\text{U}$ weighted mean ages of ash beds POT 66T, 67T and 68T suggests the occurrence of several successive volcanic eruptions (within the time covered by these volcanic ash layers) at intervals shorter than the resolving power of our ID-TIMS U-Pb geochronology at the given quality of zircon available for this study. Nevertheless, as these volcanic ash layers from Potuo straddle both the Hg anomaly recorded in the Daye Fm., as well as the coeval nadir of the negative $\delta^{13}\text{C}$ excursion (Fig. 8), the age of both the Hg anomaly (E2) and peak C-cycle perturbation during the P-T transition can be determined. The youngest age for both the peak of the E2 Hg anomaly and the nadir of the $\delta^{13}\text{C}$ excursion is 251.589 ± 0.052 Ma (POT66T, Fig. 8), while the oldest age estimate is 251.668 ± 0.079 Ma (POT67T). These two ages are identical within the analytical (X) uncertainty, precluding an estimation of the duration of the Hg anomaly. Despite these uncertainties, we can establish with confidence that the post-PTB Hg anomaly peak observed in Potuo is ca. 300 kyr younger (largely outside of analytical uncertainty) than the Meishan PTBME interval (Burgess et al., 2014; Burgess and Bowring, 2015), as well as the extinction horizon in Penglaitan (251.939 ± 0.031 Ma; S. Shen et al., 2019).

4.2.1 Hg anomalies as a PTBME correlation tool

A negative $\delta^{13}\text{C}$ excursion at the P-T transition together with a Hg anomaly are common features of many PTB-straddling sedimentary successions (Fig. 9). As such, the peak of the Hg anomaly and/or the nadir of the negative $\delta^{13}\text{C}$ excursion associated with the PTB are often considered to be stratigraphic markers for the PTB extinction interval (e.g., Grasby et al., 2017; Sial et al. 2020; J. Shen et al. 2019, 2023; Wignall et al., 1998). Although some sedimentary successions, especially in high latitudes, show Hg excursions coincident with both the negative $\delta^{13}\text{C}$ excursion and mass extinction (e.g., Sanei et al., 2012; Grasby et al., 2013), it is apparent that Hg excursions in several other successions straddling the PTB vary in expression, timing, and vertical stratigraphic extent (Fig. 9). Furthermore, local post-depositional processes (e.g., weathering and burial diagenesis) may lead to the loss of Hg sequestered in rocks, altering the Hg record of these successions (Charbonnier et al., 2020). As such, Hg loss due to post-depositional alteration may partly explain the locally variable expression of Hg anomalies observed for many PTB successions (Fig. 9). However, a thorough assessment of the degree of preservation of rock successions from which P-T transition Hg records have been published would be

required to fully explore this possibility. Therefore, the variability of PTB Hg records across different localities questions the reliability of these Hg anomalies for positioning the PTBME, as well as the use of Hg anomalies as a stratigraphic correlation tool in general.

In the case of the Pingtang syncline record, neither Hg excursion (E1 nor E2) temporally corresponds to the extinction interval as calibrated in the Meishan GSSP (Fig. 3; Fig. 8). Also, no Hg anomaly is recorded at the PTBME extinction interval in Laxian (i.e., between LAX 8T and 10T, Fig. 3), although the equivalent stratigraphical interval in Potuo is a visibility gap (Bagherpour et al., 2020). As such, the presence of a Hg anomaly there cannot be formally excluded. Nevertheless, our U-Pb zircon ages show that both the nadir of the PTB negative $\delta^{13}\text{C}$ excursion and the peak of the stratigraphically nearest Hg anomaly to the PTB (E2) are of Griesbachian age (between 251.589 ± 0.052 Ma and 251.668 ± 0.079 Ma). The peak of these excursions therefore, correlate with Bed 33 of the Meishan GSSP (251.583 ± 0.086 Ma, Burgess et al., 2014), which is much younger than the PTB. Thus, these data provide evidence that although Hg anomalies may coincide with the nadir of the PTB negative $\delta^{13}\text{C}$ excursion (Fig. 9), this correspondence cannot be reliably used as a stratigraphic marker for the PTBME in a single section or between different sections (and/or different basins). Similar conclusions were reached for the end-Triassic extinction (ETE) event by Yager et al. (2021), who documented “mismatches in timing” between Triassic-Jurassic boundary Hg anomalies and Central Atlantic Magmatic Province (CAMP) magmatism, which is purported to have triggered the ETE event. The validity of Hg anomalies as a stratigraphic correlation tool has also been questioned for other intervals of the geologic record, including the Toarcian (Them II et al., 2019), Cretaceous – Paleogene (Fendley et al., 2019; Percival et al., 2018) and the Late Devonian (Liu et al., 2021; Zhao et al., 2022). Hence, positioning the PTB extinction event by means of and/or correlation based on Hg chemostratigraphy should be treated with extreme caution. Nevertheless, the PTB (as determined for the individual sections), appears to approximately correspond to the midpoint, not the nadir, of the negative $\delta^{13}\text{C}$ excursion in successions not affected by stratigraphic condensation (e.g., Meishan) or a PTB hiatus (Fig. 9).

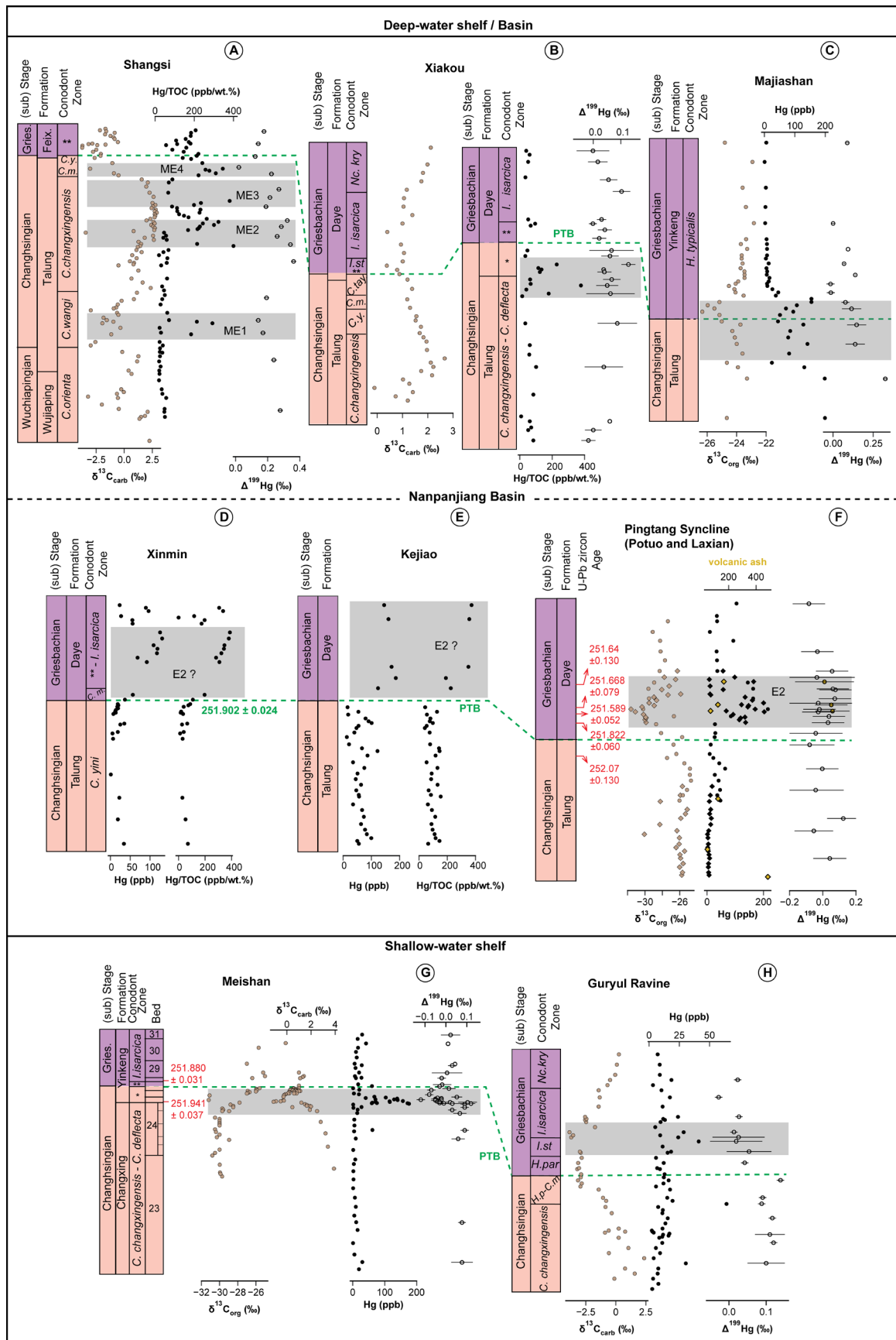


Figure 9. Compilation of carbon (organic and carbonate) isotope, mercury (Hg) concentration, Hg/TOC and Hg isotope ($\Delta^{199}Hg$) records for marine depositional environments in the Tethys region: South

China and northern India. Hg/TOC ratios are shown only for localities and stratigraphic intervals where TOC content is > 0.2 wt.%. a) Shangsi, b) Xiakou, c) Majiashan, d) Daxiakou, e) Xinmin, f) Kejiao, g) Pingtang syncline (composite of the Potuo and Laxian sections), h) Meishan. U-Pb zircon ages are from Burgess et al. (2014), i) Guryul Ravine, northern India. The different profiles are correlated using the Permian-Triassic boundary as placed by the authors of the original data sources. Data sources are as follows: Meishan: Cao et al. (2002); Grasby et al. (2017) and J. Shen et al. (2019); Guryul Ravine and Majiashan: Wang et al. (2019a); Shangsi: J. Shen et al. (2021); Xiakou: J. Shen et al. (2019); G.J. Zhang et al. (2021); Xinmin, Kejiao: J. Shen et al. (2019); Daxiakou: Wang et al. (2018); Pingtang syncline (Potuo, Laxian): this study. U-Pb zircon age for the Permian-Triassic boundary (in green) is from Burgess et al. (2014). Abbreviations: Gries.: Griesbachian; *: *Hindeodus latidentatus*; C.m.: *Clarkina meishanensis*; **: *Hindeodus parvus*; H.p.: *Hindeodus praeparvus*; I.st.: *Isarcicella staeschei*; Nc.kry.: *Neoclarkina krystyni*; C.y.: *Clarkina yini*; C.tay.: *Clarkina taylorae*.

The $\delta^{13}\text{C}$ record from Tethyan marine successions (Fig. 9) indicates that the expression of the PTB $\delta^{13}\text{C}$ excursion varies between different sections (as previously alluded to by S. Shen et al., 2019). Therefore, it is suggested that in the absence of high-resolution U-Pb zircon age calibration, an approximate correlation of the PTB extinction interval could be achieved using the midpoint of the PTB negative $\delta^{13}\text{C}$ excursion. This correlation strategy could be most effective for sections lacking robust biochronology and where the P-T transition $\delta^{13}\text{C}$ record is not truncated by a hiatus.

4.3 Does the E2 Hg anomaly of Griesbachian age coincide with a 2nd extinction event?

The onset of the Griesbachian Hg anomaly as recorded from the Laxian section (Fig. 3) postdates LAX 10T, which is dated at 251.822 ± 0.060 Ma. This age coincides, within analytical uncertainty, with that determined for Bed 28 at the Meishan GSSP (251.880 ± 0.031 Ma; Burgess et al., 2014). Because a second step of the PTB mass extinction has been postulated to have occurred within Bed 28 in Meishan (Song et al., 2013), it is pertinent to consider whether the E2 Hg anomaly is associated with this proposed second extinction step.

Conodont biozones around the PTB are usually interval zones (IZs), with the base of each IZ being defined by the first occurrence (FO) of an index species and the top defined by the base of the next overlying IZ. However, this biostratigraphical correlation technique often leads to diachronous correlations because the relative stratigraphic order of FOs of index species is not constant across space, as demonstrated by Brosse et al. (2016) for conodonts around the PTB in South China (see also Ellwood et al., 2017). Reasons for diachronous IZs include ecological control over the distribution of species in time and space, sampling effort, selective preservation, and hiatuses in the sedimentary record (Guex, 1991; Holland & Patzkowsky, 2015; Leu et al., 2022). However, following this approach, the “legal”

base Triassic was defined by the FO of *Hindeodus parvus* in the very condensed Meishan section (Yin et al., 2001).

Song et al. (2013) compiled FOs and LOs (last local occurrences) for conodonts and benthic taxa from seven South Chinese PTB sections (including Meishan and Shangsi), which led the authors to propose two extinction steps. The main and older event was placed at the base of the *C. meishanensis* IZ, the antepenultimate IZ below the FO of *H. parvus*. The proposed second extinction step, of lesser magnitude, was found at the base of the *I. isarcica* IZ, which is the third Triassic IZ above the spatially variable FO of *H. parvus*. However, a recent thorough re-investigation of Late Permian conodont IZs in the more expanded Shangsi section (Yuan et al., 2019) led to a revision of the basal Triassic into the *C. meishanensis* IZ. This new placement of the base of the Triassic (Yuan et al. 2019; written comm. 2022) in the *C. meishanensis* IZ in Shangsi and Meishan has the intrinsic benefit of coinciding with both the main extinction event and the lithostratigraphic boundary between Permian and Triassic rock units, which is marked by a hiatus in outer shelves and shallower depositional settings in South China and elsewhere (Bagherpour et al., 2017; Yin et al., 2014). Close examination of the raw biostratigraphic data (Table S2 of Song et al. 2013) from which a second extinction step was postulated shows no consistent extinction in the relative timing of the different species across the data set. Extinction of a given clade occurs in a single section, or pair of sections at the very best, thus undermining arguments in favor of a second extinction event of global significance. For instance, only the condensed Meishan section displays an apparent second step for benthic foraminifers and bivalves. In Shangsi, no second extinction emerges for any benthic clade around the base of *the I. isarcica* IZ.

Furthermore, the compositing of local extinctions patterns (Song et al. 2013) relies on the implicit assumption of synchronous conodont IZs. However, as the seven sections of this data set cover a very broad range of water depths, ranging from lagoon-shoals to lower slope-basin (Table S1 of Song et al. 2013), the assumption of synchronous conodont IZs becomes untenable. It is also at variance with the fact that the respective bathymetric distribution of segminate and segminiplate conodonts, both involved as index species of IZs, is known to be spatially controlled by temperature – i.e., depth of water masses (Joachimski et al., 2012; Leu et al., 2019). Moreover, the general development of a hiatus spanning approximately the entire *C. meishanensis* IZ in shallower depositional settings as clearly established by Yin et al. (2014) automatically excludes any synchronicity of the neighboring IZ when comparing to hiatus-free deep-water sections.

Consequently, because (i) the presence of a stratigraphic hiatus in some sections will inevitably generate a spurious extinction event and (ii) conodont IZs across a depth gradient ranging from lagoonal to basinal depositional settings can hardly be synchronous, there is insufficient biostratigraphic evidence to support a second extinction event in South China. Consequently, it is concluded that the E2 Griesbachian Hg anomaly reported here is not associated with a second extinction pulse in South China.

4.4 Provenance of volcanic Hg input

Our U-Pb geochronological results allow us to place the Pingtang syncline Hg record within the temporal framework of Siberian Traps Large Igneous Province magmatism (Burgess & Bowring, 2015; Burgess et al., 2017), a prominently discussed source of volatiles and toxic elements (such as Hg) during the P-T transition (Black et al., 2012; Broadley et al., 2018; Sibik et al., 2021; Svensen et al., 2018). A maximum duration for intrusive and extrusive magmatic STLIP activity is given by the bracketing ages of 252.27 ± 0.11 Ma (Burgess & Bowring, 2015) to 250.60 ± 0.22 Ma (Augland et al., 2019), the latter from syenitic intrusions with an uncertain relationship to the STLIP. Therefore, STLIP magmatism, being active during the studied interval, is a potential source of volcanic Hg input to South China during the P-T transition.

However, several studies have demonstrated that more proximal regional volcanic activity related to convergent plate tectonism and subduction magmatism occurred during the P-T transition, which led to elevated Hg concentrations and may have contributed to the PTBME in South China (Gao et al., 2013; He et al., 2014; Jiao et al., 2022; H. Zhang et al., 2021; Zhao et al., 2019; Zheng et al., 2020). In addition to Hg/TOC anomalies close to the PTBME horizon, Hg/TOC excursions and corresponding Hg isotope compositions have been documented for the earliest Triassic (Griesbachian) from South China and northern India (Wang et al., 2019a, 2018). Wang et al. (2019a) documented a pair of Hg/TOC anomalies in the latest Permian and earliest Triassic respectively, accompanied by a decreasing trend of $\Delta^{199}\text{Hg}$ values from the Changhsingian to the Griesbachian. Based on this $\Delta^{199}\text{Hg}$ trend, they interpreted their Griesbachian Hg/TOC excursion as having resulted from terrestrial Hg input due to elevated Early Triassic continental weathering. Recently, J. Shen et al. (2021) reported several Hg enrichment intervals predating the PTBME (named ME1-ME3), as well as one interval coeval with the PTBME (ME4), from three marine sections in South China. These authors reported the same pattern of decreasing $\Delta^{199}\text{Hg}$ values from the Changhsingian to Griesbachian. The Hg anomalies preceding the PTBME were interpreted to reflect regional subduction-related volcanism due to their spatial restriction to the Tethys region, the occurrence of numerous volcanic ash layers in Upper Permian rocks across South China, and the geochemical composition of zircons in these ash layers supporting a subduction-zone volcanic arc origin.

In contrast with previous studies, the $\Delta^{199}\text{Hg}$ values in the current study remain near-zero throughout the studied interval and are slightly positive within the Griesbachian E2 anomaly (Fig. 8). This $\Delta^{199}\text{Hg}$ trend, despite variations in OM content and detrital flux, is consistent with a constant, dominantly atmospheric volcanic Hg source relatively close to the Nanpanjiang Basin during the studied interval. The disparity between the Hg isotope MIF record of the Pingtang syncline and other deep-water marine records in South China (e.g., Wang et al., 2019a; J. Shen et al., 2021) (Fig. 9), however, suggests that: 1) Hg sequestered in PTB-straddling marine successions in different parts of South China do not have the same source/depositional pathway, and 2) Hg isotope compositions alone may not be sufficient for

discriminating between different potential volcanic sources of Hg (e.g., Siberian Traps volcanism or regional arc volcanism) to deep-water depositional sites during the P-T transition in South China.

Given that i) Hg excursions in the Pingtang syncline successions are recorded in strata with numerous interbedded volcanic ash layers (which have high Hg content throughout the studied interval, Fig. 3), ii) the $\Delta^{199}\text{Hg}$ values of these ashes are indistinguishable from those of interbedded rocks, and iii) the Nanpanjiang Basin was situated close to a volcanic center during the P-T transition, we postulate that the major and trace element geochemical properties of these volcanic ashes can be used to trace the origin of volcanic Hg inputs to these successions. The analyzed volcanic ash beds from Potuo have major and trace element characteristics similar to previously studied volcanic ashes from South China (Fig. 6) (He et al., 2014; Wang et al., 2019b). Their primitive mantle-normalized trace element compositions (Sun & McDonough, 1989) are characterized by depletions in Ta, Nb, Sr and Ti, similar to rocks from subduction settings (Pearce et al., 1995). The ashes show intermediate to acidic chemical compositions, plotting in the field of basaltic andesite, trachy-andesite and rhyolite/dacite (Fig. 6a), and are chemically distinct from volcanic rocks originating from the STLIP (Callegaro et al., 2021; Reichow et al., 2005; Sibik et al., 2015; Sobolev et al., 2009). In addition, a mid-oceanic ridge basalt (MORB)-normalized trace element (Th vs. Nb) discriminant plot (Saccani et al., 2015, 2018) of the volcanic ashes from the Pingtang syncline suggests that they originate from a continental margin volcanic arc tectonic setting (Fig. 6b). Similar conclusions were reached for other volcanic ashes from successions straddling the PTB in South China, in that these ashes have no genetic link to the Siberian Traps, but instead derived from subduction zone arc volcanism in the Tethys region (Gao et al., 2013; He et al., 2014; Jiao et al., 2022; Song et al., 2022; Zhao et al., 2019).

Consequently, we conclude that episodic regional arc volcanism associated with convergent plate tectonics in the Tethys region best explains the elevated Hg input to the Nanpanjiang Basin as recorded in the Pingtang syncline during Changhsingian to Griesbachian times. Furthermore, based on general atmospheric circulation models, previous studies have suggested that the Canadian Arctic was favorably positioned to receive volatiles (including volcanic ash) from the STLIP during the Permian to Triassic because it was situated downwind relative to the location of the STLIP eruptions (Dal Corso et al., 2022; Grasby et al., 2011, 2013). In this scenario, the South China region, being located towards the southeast and several thousands of kilometers away from Siberia, would have been poorly situated to receive volatiles from the STLIP. Nevertheless, STLIP Hg contributions to South China cannot be ruled out. Finally, as noted by J. Shen et al. (2023), volcanic arc magmatism was especially active along the eastern margin of the PaleoTethys during the Permian to Triassic. This can be inferred from abundant volcanic ash beds in coeval strata, the distribution of volcanic rocks, as well as a number of associated Hg anomalies across the PTB in this region (Fig. 9).

4.5 Hg anomalies, $\delta^{13}\text{C}$ excursions and volcanism during the P-T transition

Owing to the paucity of U-Pb zircon ages for deep-water sections from which Hg anomalies have been reported in South China, it is difficult to confidently correlate our recorded Hg anomalies with those reported for other localities in the Tethys region. However, the E1 anomaly recorded from the studied successions together with ME2 and ME3 episodes of J. Shen et al. (2021), indicate that Hg anomalies preceding the PTB extinction are recorded in both shallow and deep-marine settings in South China. In contrast, the E2 Griesbachian Hg anomaly is not recorded from any shallow-water marine section nor deep-water sections in South China, except for deep-water sections in the Nanpanjiang Basin (e.g., Xinmin, Kejiao; Fig. 9). Nevertheless, E2 may be coeval with the Hg anomaly recorded between the *I. staeschei* and *I. isarcica* conodont zones (Wang et al., 2019a), which also coincides with the nadir of the PTB-straddling negative $\delta^{13}\text{C}$ excursion in the southwestern Tethys Guryul Ravine section (Fig. 9). However, further work from other marine successions with precise U-Pb zircon ages is required to confirm the spatial extent of the Griesbachian Hg anomaly.

The (stratigraphically variable) coincidence of the nadir of $\delta^{13}\text{C}$ excursions with Hg anomalies in the Pingtang syncline and other Tethyan localities (Fig. 9) hints at a common driving factor – volcanism. The global distribution of $\delta^{13}\text{C}$ excursions and Hg anomalies close to the PTB in Permian-Triassic successions (Baud et al., 1996; Grasby et al., 2013; Korte & Kozur, 2010; Sanei et al., 2012; J. Shen et al., 2019) argues in favor of a large-scale volcanic degassing episode, such as that of the STLIP, as the ultimate cause of drastic environmental changes of global extent. The onset of the negative $\delta^{13}\text{C}$ excursion in the Pingtang syncline starts just before deposition of the ash layer (LAX8T) at 252.07 ± 0.130 Ma (Fig. 8) and is characterized by an initial 2 ‰ decrease in $\delta^{13}\text{C}$ values in the upper Changhsingian followed by a further 3 ‰ decrease in the lower Griesbachian. This onset of $\delta^{13}\text{C}$ excursion may temporally overlap with the transition from the extrusive Stage 1 to intrusive Stage 2 of STLIP magmatism, proposed to have occurred at about 251.9 Ma (Burgess et al., 2017). Stage 2 STLIP magmatism was characterized by intrusion of dykes and sills into country rocks in the Tunguska Basin (Burgess & Bowring, 2015; Burgess et al., 2017). The intrusions, and subsequent sill complex formation, are proposed to have caused injection of massive amounts of both CO_2 and CH_4 into the atmosphere via contact metamorphism of coal beds, shales and petroleum-bearing evaporites (Burgess et al., 2017; Svensen et al., 2009, 2018), which collectively are thought to result in a > 5 ‰ negative $\delta^{13}\text{C}$ excursion.

However, Davydov (2021) recently questioned the validity of this sill-rock thermal interaction model, pointing out that there is no correlation between coal metamorphism and the distribution of sills in the Tunguska Basin. This author also argued that the role of contact metamorphism by undifferentiated intrusions, which constitute > 95 % of the Tunguska Basin intrusions, was limited and insignificant to the general coal metamorphism in the Tunguska Basin; and that coal metamorphism in the Tunguska Basin was probably related to regional tectonic deformation instead of magmatism. Furthermore, the

role of intrusive STLIP magmatism as a potential driver of the global carbon cycle perturbations and mass extinction during the P-T transition is questioned. This stems from the uncertainty regarding the age of the explosion pipes in the Tunguska Basin (which could have transported CO₂ and other gases such as Hg to the atmosphere), as well as the U-Pb ages of the sill intrusions that violate stratigraphic superposition (Davydov, 2021). Consequently, additional U-Pb zircon geochronologic calibrations of STLIP intrusive rocks are required to resolve these questions.

Pending the resolution of these questions, an additional but not mutually exclusive explanation that could reconcile the coincidence of negative $\delta^{13}\text{C}$ excursions and Hg anomalies recorded at a global scale during the P-T transition can be considered. This is that concurrent regional arc volcanism in different paleocontinents was responsible for both CO₂ and Hg release resulting in the $\delta^{13}\text{C}$ excursions and Hg anomalies. In addition to South China, extensive regional arc volcanism during the P-T transition has been documented for many spatially disparate localities. Some of these include: the northern Patagonian Massif, Argentina (Luppo et al., 2018), Antarctica (Nelson & Cottle, 2019), Australia (Chapman et al., 2022; Metcalfe et al., 2015), Karoo Basin, South Africa (Gastaldo et al., 2020), with coeval Hg anomalies also recently documented for the latter two (J. Shen et al., 2023). The suggestion of concurrent regional arc volcanism in several paleocontinents during the P-T transition is congruent with recent suggestions of a Pangean ‘ring of fire’ (subduction-related volcanism along the convergent Panthalassan margin of Pangea) as an explanation for marine and terrestrial environmental perturbations during the latest Permian (Vajda et al., 2020).

Reasons for a global increase in regional arc volcanism concurrent with STLIP volcanism are still uncertain. Jiao et al. (2022) recently suggested that the ascent of the STLIP mantle plume may have triggered volcanic activity in several subduction zone systems. While the effect of a large mantle plume on global plate tectonics is highly debatable, STLIP volcanism occurred in a context of global increase of accretion and subduction rates from the Permian to Triassic (Vérard et al. 2015a, their Fig. 11a), which has also been linked with Early Triassic sea-level rise (Vérard et al., 2015b, their Fig.17). However, such global increase in subduction rates is likely to occur over tens of millions of years. Hence, increased regional arc volcanism over hundreds of thousands of years between the latest Permian to earliest Triassic may be totally disconnected from global tectonics. Irrespective of the reasons for this global increase in arc volcanism over the P-T transition, our results from the Pingtang syncline suggest that volcanic activity linked to Hg anomalies and C-isotope excursion probably peaked between 251.589 ± 0.052 Ma and 251.668 ± 0.079 Ma in the Nanpanjiang Basin, South China (Fig. 8).

4.6 Implications for the PTBME

While it is generally accepted that STLIP magmatism exerted a major control on the global carbon budget and mercury cycle during the Paleozoic to Mesozoic transition, it is clear that South China was substantially influenced by nearby volcanic centers throughout the Late Permian to Triassic (He et al.,

2014; H. Zhang et al., 2021). This is evident from the older and well-known Emeishan LIP (Huang et al., 2022), the occurrence of Permian-Triassic volcanic rocks especially in southwest South China (Gao et al., 2013), the abundant volcanic ash layers within Permian-Triassic marine sedimentary successions, shown to be genetically distinct from STLIP rocks (Gao et al., 2013; He et al., 2014; Yang et al., 2012), as well as Changhsingian Hg/TOC anomalies restricted to the Tethys region (J. Shen et al., 2021; this study). In addition, regional arc volcanism has been linked to notably decreased carbonate and biogenic silica production, as well as decreased water column oxygenation in South China (J. Shen et al., 2013). The temporal overlap between regional intermediate to felsic volcanism and the basaltic volcanism from the STLIP, thus supports a scenario in which STLIP magmatism and concurrent subduction-related regional arc volcanism in the Tethys region may have acted in concert to generate pernicious environmental conditions for marine and terrestrial faunas in South China during the Late Permian (J. Shen et al., 2013, 2021; S. Shen et al., 2019).

The finding of several sudden increases in mercury concentration that both predate and post-date the PTBME event is significant. This is because these Hg enrichments suggest that elevated volcanic activity, which is thought to have triggered the PTBME in South China, was not restricted only to a short interval e.g., within Stage 2 STLIP magmatism (Burgess et al., 2017), but rather, took place over several thousands of years during the P-T transition. Thus, repeated bursts of regional felsic and intermediate volcanism (and resulting increases in mercury concentration) could have had a cumulative adverse effect on the environment and the species that lived at the time, making them more vulnerable to extinction (J. Shen et al., 2013; 2021; S. Shen et al., 2019). Subsequently, significant environmental stresses resulting from STLIP magmatism would have quite easily pushed faunas in South China “over the edge” to bring about the mass extinction at the Paleozoic-Mesozoic transition. This scenario is similar to that proposed by Racki (2020) for the Late Devonian Kellwasser Crisis.

5. Conclusions

The present study establishes the Hg record of two deep-water marine successions in the Nanpanjiang Basin, South China, spanning the Changhsingian to Griesbachian. U-Pb zircon ages and Hg/TOC ratios indicate elevated volcanic activity before 252.07 ± 0.130 Ma (preceding the PTBME) and during several episodes in the Griesbachian, peaking between 251.589 ± 0.052 Ma and 251.668 ± 0.079 Ma. The latter range in ages is coeval with the nadir of a large negative C isotope excursion, similar in magnitude to the global excursion at the PTB. Based on evidence from the coupled $\delta^{13}\text{C}$ and Hg records, major and trace element geochemistry of volcanic ashes, and the U-Pb zircon age constraints, we conclude that the recorded Hg enrichments are primarily sourced from subduction-related arc volcanism in the Tethys region. Consequently, our Hg record together with recent results from South China documenting several episodes of Hg enrichment during the P-T transition, are compatible with previous suggestions that arc volcanism contributed to environmental deterioration and biodiversity decline in South China leading up to the PTBME, which was triggered by STLIP magmatism. Our study provides an absolute

timeframe within which Late Permian to Early Triassic Hg and $\delta^{13}\text{C}$ records from different deep-water successions (which are less likely to contain stratigraphic gaps) in South China can be calibrated. This precise, radioisotopic timeframe allows for a more in-depth assessment of the relation between volcanism, environmental changes, and the mass extinction event at the P-T transition.

Acknowledgements

This research was supported by a Swiss NSF Sinergia grant (project nr. CRSII5_180253). We thank Olivier Reubi, Edson Ramudzuli and Jérôme Chmeleff for analytical assistance. Special thanks to Borhan Bagherpour and Marc Leu for providing logs for the study sections, and to members of the Sinergia PaleoC4 team for discussions during the development of this manuscript. The authors also thank Kuang Guodong (Geological survey of Guanxi), Ji Cheng (NIGPAS), Shen Shuzhong (University of Nanjing) for their help related to fieldwork and for scientific discussions. Three anonymous reviewers are also thanked for their comments, which helped improve the manuscript.

Data availability Statement

The dataset associated with the current study is available on the open-source online data repository – Zenodo – at “<https://doi.org/10.5281/zenodo.7972240>”. Figure 1 was made based on the Panalysis model (Vérard, 2019) using ArcGIS®. Figures 2-8 were made with Matplotlib version 3.5.2 (Caswell et al., 2022), available under the Matplotlib license at <https://matplotlib.org>, and seaborn version 0.11.2 (Waskom, 2021) available at <https://pypi.org/project/seaborn/>. All figures were edited using Adobe Illustrator©.

References

- Algeo, T.J., Maynard, J.B., 2004. Trace-element behavior and redox facies in core shales of Upper Pennsylvanian Kansas-type cyclothems. *Chemical Geology* 206, 289-318 DOI: <https://doi.org/10.1016/j.chemgeo.2003.12.009>.
- Augland, L. E., Ryabov, V. V., Vernikovskiy, V. A., Planke, S., Polozov, A., Callegaro, S., et al. (2019). The main pulse of the Siberian Traps expanded in size and composition. *Scientific reports*, 9(1), 1-12. <https://doi.org/10.1038/s41598-019-54023-2>
- Bagherpour, B., Bucher, H., Baud, A., Brosse, M., Vennemann, T., Martini, R., & Guodun, K. (2017). Onset, development, and cessation of basal Early Triassic microbialites (BETM) in the Nanpanjiang pull-apart Basin, South China Block. *Gondwana Research*, 44, 178-204. <https://doi.org/10.1016/j.gr.2016.11.013>
- Bagherpour, B., Bucher, H., Vennemann, T., Schneebeli-Hermann, E., Yuan, D. X., Leu, M., et al. (2020). Are Late Permian carbon isotope excursions of local or of global significance? *Geological Society of America Bulletin*, 132(3-4), 521-544. <https://doi.org/10.1130/B31996.1>
- Baresel, B., Bucher, H., Bagherpour, B., Brosse, M., Guodun, K., & Schaltegger, U. (2017a). Timing of global regression and microbial bloom linked with the Permian-Triassic boundary mass extinction: implications for driving mechanisms. *Sci Rep*, 7, 43630. <https://doi.org/10.1038/srep43630>
- Baresel, B., Bucher, H., Brosse, M., Cordey, F., Kuang, G. D., & Schaltegger, U. (2017b). Precise age for the Permian-Triassic boundary in South China from high-precision U-Pb geochronology and Bayesian age-depth modeling. *Solid Earth*, 8(2), 361-378. <https://doi.org/10.5194/se-8-361-2017>
- Baud, A., Atudorei, V., & Sharp, Z. (1996). Late Permian and early Triassic evolution of the Northern Indian margin: Carbon isotope and sequence stratigraphy. *Geodinamica acta*, 9(2-3), 57-77. <https://doi.org/10.1080/09853111.1996.11105278>
- Baud, A., Magaritz, M., & Holser, W. T. (1989). Permian-Triassic of the Tethys: Carbon isotope studies. *Geologische Rundschau*, 78, 649-677. <https://doi.org/10.1007/BF01776196>
- Behar, F., Beaumont, V., & Penteado, H. L. D. (2001). Rock-Eval 6 technology: Performances and developments. *Oil & Gas Science and Technology-Revue D Ifp Energies Nouvelles*, 56(2), 111-134. <https://doi.org/10.2516/ogst:2001013>
- Bergquist, B. A., & Blum, J. D. (2007). Mass-dependent and -independent fractionation of Hg isotopes by photoreduction in aquatic systems. *Science*, 318(5849), 417-420. <https://doi.org/10.1126/science.1148050>
- Black, B. A., Elkins-Tanton, L. T., Rowe, M. C., & Peate, I. U. (2012). Magnitude and consequences of volatile release from the Siberian Traps. *Earth and Planetary Science Letters*, 317, 363-373. <https://doi.org/10.1016/j.epsl.2011.12.001>
- Black, B. A., Neely, R. R., Lamarque, J.-F., Elkins-Tanton, L. T., Kiehl, J. T., Shields, C. A., et al. (2018). Systemic swings in end-Permian climate from Siberian Traps carbon and sulfur outgassing. *Nature Geoscience*, 11(12), 949-954. <https://doi.org/10.1038/s41561-018-0261-y>
- Blum, J. D., & Bergquist, B. A. (2007). Reporting of variations in the natural isotopic composition of mercury. *Anal Bioanal Chem*, 388(2), 353-359. <https://doi.org/10.1007/s00216-007-1236-9>
- Blum, J. D., Sherman, L. S., & Johnson, M. W. (2014). Mercury Isotopes in Earth and Environmental Sciences. *Annual Review of Earth and Planetary Sciences*, Vol 42, 42, 249-269. <https://doi.org/10.1146/annurev-earth-050212-124107>

- Bowring, J. F., McLean, N. M., & Bowring, S. A. (2011). Engineering cyber infrastructure for U-Pb geochronology: Tripoli and U-Pb_Redux. *Geochemistry Geophysics Geosystems*, *12*(6). <https://doi.org/10.1029/2010gc003479>
- Broadley, M. W., Barry, P. H., Ballentine, C. J., Taylor, L. A., & Burgess, R. (2018). End-Permian extinction amplified by plume-induced release of recycled lithospheric volatiles. *Nature Geoscience*, *11*(9), 682-687. <https://doi.org/10.1038/s41561-018-0215-4>
- Brosse, M., Bucher, H., & Goudemand, N. (2016). Quantitative biochronology of the Permian-Triassic boundary in South China based on conodont unitary associations. *Earth-Science Reviews*, *155*, 153-171. <https://doi.org/10.1016/j.earscirev.2016.02.003>
- Burgess, S. D., Bowring, S., & Shen, S. Z. (2014). High-precision timeline for Earth's most severe extinction. *Proc Natl Acad Sci U S A*, *111*(9), 3316-3321. <https://doi.org/10.1073/pnas.1317692111>
- Burgess, S. D., & Bowring, S. A. (2015). High-precision geochronology confirms voluminous magmatism before, during, and after Earth's most severe extinction. *Science advances*, *1*(7), e1500470. <https://doi.org/10.1126/sciadv.1500470>
- Burgess, S. D., Muirhead, J. D., & Bowring, S. A. (2017). Initial pulse of Siberian Traps sills as the trigger of the end-Permian mass extinction. *Nat Commun*, *8*(1), 164. <https://doi.org/10.1038/s41467-017-00083-9>
- Callegaro, S., Svensen, H. H., Neumann, E. R., Polozov, A., Jerram, D. A., Deegan, F., et al. (2021). Geochemistry of deep Tunguska Basin sills, Siberian Traps: correlations and potential implications for the end-Permian environmental crisis. *Contributions to Mineralogy and Petrology*, *176*(7), 1-30. <https://doi.org/10.1007/s00410-021-01807-3>
- Cao, C., Wang, W., & Jin, Y. (2002). Carbon isotope excursions across the Permian-Triassic boundary in the Meishan section, Zhejiang Province, China. *Chinese Science Bulletin*, *47*(13), 1125-1129. <https://doi.org/10.1360/02fb9252>
- Caswell, T. A., Droettboom, M., Lee, A., Sales De Andrade, E., Hoffmann, T., Klymak, J., et al. (2022). *Matplotlib v3.5.2*. [Software]. In Zenodo. <https://doi.org/10.5281/zenodo.6513224>
- Chapman, T., Milan, L.A., Metcalfe, I., Blevin, P.L., Crowley, J., 2022. Pulses in silicic arc magmatism initiate end-Permian climate instability and extinction. *Nature Geoscience* *15*, 411-416 DOI: 10.1038/s41561-022-00934-1.
- Charbonnier, G., Adatte, T., Föllmi, K. B., & Suan, G. (2020). Effect of Intense Weathering and Postdepositional Degradation of Organic Matter on Hg/TOC Proxy in Organic-rich Sediments and its Implications for Deep-Time Investigations. *Geochemistry Geophysics Geosystems*, *21*(2), e2019GC008707. <https://doi.org/10.1029/2019GC008707>
- Charbonnier, G., Morales, C., Duchamp-Alphonse, S., Westermann, S., Adatte, T., & Föllmi, K. B. (2017). Mercury enrichment indicates volcanic triggering of Valanginian environmental change. *Scientific reports*, *7*(1), 1-6. <https://doi.org/10.1038/srep40808>
- Chen, D., Ren, D., Deng, C., Tian, Z., & Yin, R. (2022). Mercury loss and isotope fractionation during high-pressure and high-temperature processing of sediments: Implication for the behaviors of mercury during metamorphism. *Geochimica et Cosmochimica Acta*, *334*, 231-240. <https://doi.org/10.1016/j.gca.2022.08.010>
- Chen, J., Hintelmann, H., Feng, X., & Dimock, B. (2012). Unusual fractionation of both odd and even mercury isotopes in precipitation from Peterborough, ON, Canada. *Geochimica et Cosmochimica Acta*, *90*, 33-46. <https://doi.org/10.1016/j.gca.2012.05.005>

- Condon, D. J., Schoene, B., McLean, N. M., Bowring, S. A., & Parrish, R. R. (2015). Metrology and traceability of U-Pb isotope dilution geochronology (EARTHTIME Tracer Calibration Part I). *Geochimica et Cosmochimica Acta*, *164*, 464-480. <https://doi.org/10.1016/j.gca.2015.05.026>
- Dai, X., Song, H., Brayard, A., Ware, D., 2019. A new Griesbachian–Dienerian (Induan, Early Triassic) ammonoid fauna from Gujiao, South China. *Journal of Paleontology* *93*, 48-71 DOI: 10.1017/jpa.2018.46.
- Dal Corso, J., Song, H., Callegaro, S., Chu, D., Sun, Y., Hilton, J., et al. (2022). Environmental crises at the Permian–Triassic mass extinction. *Nature Reviews Earth & Environment*, *3*(3), 197-214. <https://doi.org/10.1038/s43017-021-00259-4>
- Davydov, V. (2021). Tunguska coals, Siberian sills and the Permian-Triassic extinction. *Earth-Science Reviews*, *212*, 103438. <https://doi.org/10.1016/j.earscirev.2020.103438>
- Ellwood, B.B., Wardlaw, B.R., Nestell, M.K., Nestell, G.P., Lan, L.T.P., 2017. Identifying globally synchronous Permian–Triassic boundary levels in successions in China and Vietnam using Graphic Correlation. *Palaeogeography, Palaeoclimatology, Palaeoecology* *485*, 561-571 DOI: <https://doi.org/10.1016/j.palaeo.2017.07.012>.
- Erwin, D.H., 1998. The end and the beginning: recoveries from mass extinctions. *Trends in Ecology & Evolution* *13*, 344-349 DOI: [https://doi.org/10.1016/S0169-5347\(98\)01436-0](https://doi.org/10.1016/S0169-5347(98)01436-0).
- Espitalié, J., Deroo, G., Marquis, F., 1985. La pyrolyse Rock-Eval et ses applications. *Rev. Inst. Fr. Pétr* *40*, 563-579 DOI: <https://doi.org/10.2516/ogst:1985035>.
- Fantasia, A., Föllmi, K.B., Adatte, T., Bernárdez, E., Spangenberg, J.E., Mattioli, E., 2018. The Toarcian Oceanic Anoxic Event in southwestern Gondwana: an example from the Andean Basin, northern Chile. *Journal of the Geological Society* *175*, 883-902 DOI: 10.1144/jgs2018-008.
- Fendley, I.M., Mittal, T., Sprain, C.J., Marvin-DiPasquale, M., Tobin, T.S., Renne, P.R., 2019. Constraints on the volume and rate of Deccan Traps flood basalt eruptions using a combination of high-resolution terrestrial mercury records and geochemical box models. *Earth and Planetary Science Letters* *524*, 115721 DOI: <https://doi.org/10.1016/j.epsl.2019.115721>.
- Font, E., Chen, J., Regelous, M., Regelous, A., Adatte, T., 2021. Volcanic origin of the mercury anomalies at the Cretaceous–Paleogene transition of Bidart, France. *Geology* *50*, 142-146 DOI: 10.1130/G49458.1.
- Fu, X., Jiskra, M., Yang, X., Maruszczak, N., Enrico, M., Chmeleff, J., et al. (2021). Mass-Independent Fractionation of Even and Odd Mercury Isotopes during Atmospheric Mercury Redox Reactions. *Environ Sci Technol*, *55*(14), 10164-10174. <https://doi.org/10.1021/acs.est.1c02568>
- Gao, Q., Zhang, N., Xia, W., Feng, Q., Chen, Z.-Q., Zheng, J., et al. (2013). Origin of volcanic ash beds across the Permian–Triassic boundary, Daxiakou, South China: petrology and U–Pb age, trace elements and Hf-isotope composition of zircon. *Chemical Geology*, *360*, 41-53. <https://doi.org/10.1016/j.chemgeo.2013.09.020>
- Gastaldo, R. A., Kamo, S. L., Neveling, J., Geissman, J. W., Looy, C. V., & Martini, A. M. (2020). The base of the Lystrosaurus Assemblage Zone, Karoo Basin, predates the end-Permian marine extinction. *Nature Communications*, *11*(1), 1-8. <https://doi.org/10.1038/s41467-020-15243-7>
- Grasby, S. E., Sanei, H., & Beauchamp, B. (2011). Catastrophic dispersion of coal fly ash into oceans during the latest Permian extinction. *Nature Geoscience*, *4*(2), 104-107. <https://doi.org/10.1038/ngeo1069>

- Grasby, S. E., Sanei, H., Beauchamp, B., & Chen, Z. H. (2013). Mercury deposition through the Permo-Triassic Biotic Crisis. *Chemical Geology*, *351*, 209-216. <https://doi.org/10.1016/j.chemgeo.2013.05.022>
- Grasby, S.E., Beauchamp, B., Bond, D.P., Wignall, P.B., Sanei, H., 2016. Mercury anomalies associated with three extinction events (Capitanian crisis, latest Permian extinction and the Smithian/Spathian extinction) in NW Pangea. *Geological magazine* *153*, 285-297.
- Grasby, S. E., Shen, W. J., Yin, R. S., Gleason, J. D., Blum, J. D., Lepak, R. F., et al. (2017). Isotopic signatures of mercury contamination in latest Permian oceans. *Geology*, *45*(1), 55-58. <https://doi.org/10.1130/G38487.1>
- Grasby, S. E., Them, T. R., Chen, Z. H., Yin, R. S., & Ardakani, O. H. (2019). Mercury as a proxy for volcanic emissions in the geologic record. *Earth-Science Reviews*, *196*, 102880. <https://doi.org/10.1016/j.earscirev.2019.102880>
- Guex, J. (1991). *Biochronological correlations* (1 ed., Vol. 250). Springer Berlin, Heidelberg. 978-3-540-53937-7
- Hardisty, D.S., Lyons, T.W., Riedinger, N., Isson, T.T., Owens, J.D., Aller, R.C., Rye, D.M., Planavsky, N.J., Reinhard, C.T., Gill, B.C., 2018. An evaluation of sedimentary molybdenum and iron as proxies for pore fluid paleoredox conditions. *Am J Sci* *318*, 527-556 DOI: <https://doi.org/10.2475/05.2018.04>.
- He, B., Zhong, Y. T., Xu, Y. G., & Li, X. H. (2014). Triggers of Permo-Triassic boundary mass extinction in South China: The Siberian Traps or Paleo-Tethys ignimbrite flare-up? *Lithos*, *204*, 258-267. <https://doi.org/10.1016/j.lithos.2014.05.011>
- Holland, S. M., & Patzkowsky, M. E. (2015). The stratigraphy of mass extinction. *Palaeontology*, *58*(5), 903-924. <https://doi.org/10.1111/pala.12188>
- Huang, H., Huyskens, M. H., Yin, Q.-Z., Cawood, P. A., Hou, M., Yang, J., et al. (2022). Eruptive tempo of Emeishan large igneous province, southwestern China and northern Vietnam: Relations to biotic crises and paleoclimate changes around the Guadalupian-Lopingian boundary. *Geology*, *50*(9), 1083-1087. <https://doi.org/10.1130/G50183.1>
- Jiao, Y., Zhou, L., Algeo, T. J., Shen, J., Feng, L., Hu, Y., et al. (2022). Zirconium isotopes track volcanic inputs during the Permian-Triassic transition in South China. *Chemical Geology*, *610*, 121074. <https://doi.org/10.1016/j.chemgeo.2022.121074>
- Jiskra, M., Heimbürger-Boavida, L. E., Desgranges, M. M., Petrova, M. V., Dufour, A., Ferreira-Araujo, B., et al. (2021). Mercury stable isotopes constrain atmospheric sources to the ocean. *Nature*, *597*(7878), 678-682. <https://doi.org/10.1038/s41586-021-03859-8>
- Jiskra, M., Sonke, J. E., Agnan, Y., Helmig, D., & Obrist, D. (2019). Insights from mercury stable isotopes on terrestrial-atmosphere exchange of Hg(0) in the Arctic tundra. *Biogeosciences*, *16*(20), 4051-4064. <https://doi.org/10.5194/bg-16-4051-2019>
- Joachimski, M. M., Lai, X., Shen, S., Jiang, H., Luo, G., Chen, B., et al. (2012). Climate warming in the latest Permian and the Permian–Triassic mass extinction. *Geology*, *40*(3), 195-198. <https://doi.org/10.1130/G32707.1>
- Johnson, D. L., Present, T. M., Li, M., Shen, Y., & Adkins, J. F. (2021). Carbonate associated sulfate (CAS) $\delta^{34}\text{S}$ heterogeneity across the End-Permian Mass Extinction in South China. *Earth and Planetary Science Letters*, *574*, 117172. <https://doi.org/10.1016/j.epsl.2021.117172>

- Korte, C., & Kozur, H. W. (2010). Carbon-isotope stratigraphy across the Permian-Triassic boundary: A review. *Journal of Asian Earth Sciences*, 39(4), 215-235. <https://doi.org/10.1016/j.jseaes.2010.01.005>
- Kwon, S. Y., Blum, J. D., Nadelhoffer, K. J., Dvonch, J. T., & Tsui, M. T.-K. (2015). Isotopic study of mercury sources and transfer between a freshwater lake and adjacent forest food web. *Science of the Total Environment*, 532, 220-229. <https://doi.org/10.1016/j.scitotenv.2015.06.012>
- Lehrmann, D. J., Stepchinski, L., Altiner, D., Orchard, M. J., Montgomery, P., Enos, P., et al. (2015). An integrated biostratigraphy (conodonts and foraminifers) and chronostratigraphy (paleomagnetic reversals, magnetic susceptibility, elemental chemistry, carbon isotopes and geochronology) for the Permian–Upper Triassic strata of Guandao section, Nanpanjiang Basin, south China. *Journal of Asian Earth Sciences*, 108, 117-135. <https://doi.org/10.1016/j.jseaes.2015.04.030>
- Leu, M., Bucher, H., & Goudemand, N. (2019). Clade-dependent size response of conodonts to environmental changes during the late Smithian extinction. *Earth-Science Reviews*, 195, 52-67. <https://doi.org/10.1016/j.earscirev.2018.11.003>
- Leu, M., Bucher, H., Vennemann, T., Bagherpour, B., Ji, C., Brosse, M., & Goudemand, N. (2022). A Unitary Association-based conodont biozonation of the Smithian–Spathian boundary (Early Triassic) and associated biotic crisis from South China. *Swiss Journal of Palaeontology*, 141(1), 19. <https://doi.org/10.1186/s13358-022-00259-x>
- Liu, Z., Percival, L.M.E., Vandeputte, D., Selby, D., Claeys, P., Over, D.J., Gao, Y., 2021. Upper Devonian mercury record from North America and its implications for the Frasnian–Famennian mass extinction. *Palaeogeography, Palaeoclimatology, Palaeoecology* 576, 110502 DOI: <https://doi.org/10.1016/j.palaeo.2021.110502>.
- Luppo, T., de Luchi, M. G. L., Rapalini, A. E., Dopico, C. I. M., & Fanning, C. M. (2018). Geochronologic evidence of a large magmatic province in northern Patagonia encompassing the Permian-Triassic boundary. *Journal of South American Earth Sciences*, 82, 346-355. <https://doi.org/10.1016/j.jsames.2018.01.003>
- McLean, N. M., Bowring, J. F., & Bowring, S. A. (2011). An algorithm for U-Pb isotope dilution data reduction and uncertainty propagation. *Geochemistry Geophysics Geosystems*, 12(6). <https://doi.org/10.1029/2010GC003478>
- Metcalf, I., Crowley, J., Nicoll, R., & Schmitz, M. (2015). High-precision U-Pb CA-TIMS calibration of Middle Permian to Lower Triassic sequences, mass extinction and extreme climate-change in eastern Australian Gondwana. *Gondwana Research*, 28(1), 61-81. <https://doi.org/10.1016/j.gr.2014.09.002>
- Moynier, F., Jackson, M.G., Zhang, K., Cai, H., Halldórsson, S.A., Pik, R., Day, J.M.D., Chen, J., 2021. The Mercury Isotopic Composition of Earth's Mantle and the Use of Mass Independently Fractionated Hg to Test for Recycled Crust. *Geophys Res Lett* 48, e2021GL094301 DOI: <https://doi.org/10.1029/2021GL094301>.
- Nelson, D. A., & Cottle, J. M. (2019). Tracking voluminous Permian volcanism of the Choiyoi Province into central Antarctica. *Lithosphere*, 11(3), 386-398. <https://doi.org/10.1130/11015.1>
- Payne, J.L., Kump, L.R., 2007. Evidence for recurrent Early Triassic massive volcanism from quantitative interpretation of carbon isotope fluctuations. *Earth and Planetary Science Letters* 256, 264-277 DOI: <https://doi.org/10.1016/j.epsl.2007.01.034>.

- Pearce, J. A. (1982). Trace element characteristics of lavas from destructive plate boundaries. In R. S. Thorpe (Ed.), *Orogenic andesites and related rocks* (pp. 528-548). John Wiley and Sons. 9780471280347
- Pearce, J. A., Baker, P. E., Harvey, P. K., & Luff, I. W. (1995). Geochemical evidence for subduction fluxes, mantle melting and fractional crystallization beneath the South Sandwich island arc. *Journal of Petrology*, 36(4), 1073-1109. <https://doi.org/10.1093/petrology/36.4.1073>
- Portnyagin, M. V., Ponomareva, V. V., Zelenin, E. A., Bazanova, L. I., Pevzner, M. M., Plechova, A. A., et al. (2020). TephraKam: geochemical database of glass compositions in tephra and welded tuffs from the Kamchatka volcanic arc (northwestern Pacific). *Earth System Science Data*, 12(1), 469-486. <https://doi.org/10.5194/essd-12-469-2020>
- Percival, L.M.E., Bergquist, B.A., Mather, T.A., Sanei, H., 2021. Sedimentary Mercury Enrichments as a Tracer of Large Igneous Province Volcanism, in: Richard E. Ernst, Alexander J. Dickson, Bekker, A. (Eds.), *Large Igneous Provinces*. John Wiley and Sons, Inc., pp. 247-262.
- Percival, L.M., Jenkyns, H.C., Mather, T.A., Dickson, A.J., Batenburg, S.J., Ruhl, M., Hesselbo, S.P., Barclay, R., Jarvis, I., Robinson, S.A., 2018. Does large igneous province volcanism always perturb the mercury cycle? Comparing the records of Oceanic Anoxic Event 2 and the end-Cretaceous to other Mesozoic events. *Am J Sci* 318, 799-860 DOI: <https://doi.org/10.2475/08.2018.01>
- Pyle, D. M., & Mather, T. A. (2003). The importance of volcanic emissions for the global atmospheric mercury cycle. *Atmospheric Environment*, 37(36), 5115-5124. <https://doi.org/10.1016/j.atmosenv.2003.07.011>
- Racki, G., 2020. A volcanic scenario for the Frasnian–Famennian major biotic crisis and other Late Devonian global changes: More answers than questions? *Global and Planetary Change* 189, 103174 DOI: <https://doi.org/10.1016/j.gloplacha.2020.103174>.
- Reichow, M. K., Saunders, A. D., White, R. V., Al'Mukhamedov, A. I., & Medvedev, A. Y. (2005). Geochemistry and petrogenesis of basalts from the West Siberian Basin: an extension of the Permo–Triassic Siberian Traps, Russia. *Lithos*, 79(3), 425-452. <https://doi.org/https://doi.org/10.1016/j.lithos.2004.09.011>
- Rolison, J.M., Stirling, C.H., Middag, R., Rijkenberg, M.J.A., 2017. Uranium stable isotope fractionation in the Black Sea: Modern calibration of the $^{238}\text{U}/^{235}\text{U}$ paleo-redox proxy. *Geochimica et Cosmochimica Acta* 203, 69-88 DOI: <https://doi.org/10.1016/j.gca.2016.12.014>.
- Saccani, E., Delavari, M., Dolati, A., Marroni, M., Pandolfi, L., Chiari, M., & Barbero, E. (2018). New insights into the geodynamics of Neo-Tethys in the Makran area: Evidence from age and petrology of ophiolites from the Coloured Mélange Complex (SE Iran). *Gondwana Research*, 62, 306-327. <https://doi.org/10.1016/j.gr.2017.07.013>
- Saccani, E., Dilek, Y., Marroni, M., & Pandolfi, L. (2015). Continental margin ophiolites of Neotethys: remnants of ancient Ocean–Continent Transition Zone (OCTZ) lithosphere and their geochemistry, mantle sources and melt evolution patterns. *Episodes Journal of International Geoscience*, 38(4), 230-249. <https://doi.org/10.18814/epiugs/2015/v38i4/82418>
- Sanei, H., Grasby, S. E., & Beauchamp, B. (2012). Latest Permian mercury anomalies. *Geology*, 40(1), 63-66. <https://doi.org/10.1130/G32596.1>
- Schaltegger, U., Ovtcharova, M., Gaynor, S. P., Schoene, B., Wotzlaw, J.-F., Davies, J. F., et al. (2021). Long-term repeatability and interlaboratory reproducibility of high-precision ID-TIMS U–Pb geochronology. *Journal of Analytical Atomic Spectrometry*, 36(7), 1466-1477. <https://doi.org/10.1039/D1JA00116G>

- Schoene, B., Crowley, J. L., Condon, D. J., Schmitz, M. D., & Bowring, S. A. (2006). Reassessing the uranium decay constants for geochronology using ID-TIMS U-Pb data. *Geochimica et Cosmochimica Acta*, 70(2), 426-445. <https://doi.org/10.1016/j.gca.2005.09.007>
- Shen, J., Algeo, T.J., Hu, Q., Xu, G., Zhou, L., Feng, Q., 2013. Volcanism in South China during the Late Permian and its relationship to marine ecosystem and environmental changes. *Global and Planetary Change* 105, 121-134 DOI: 10.1016/j.gloplacha.2012.02.011.
- Shen, J., Chen, J., Algeo, T. J., Feng, Q., Yu, J., Xu, Y.-G., et al. (2021). Mercury fluxes record regional volcanism in the South China craton prior to the end-Permian mass extinction. *Geology*, 49(4), 452-456. <https://doi.org/10.1130/G48501.1>
- Shen, J., Chen, J., Algeo, T. J., Yuan, S., Feng, Q., Yu, J., et al. (2019). Evidence for a prolonged Permian-Triassic extinction interval from global marine mercury records. *Nat Commun*, 10(1), 1563. <https://doi.org/10.1038/s41467-019-09620-0>
- Shen, J., Chen, J., Yu, J., Algeo, T. J., Smith, R. M. H., Botha, J., et al. (2023). Mercury evidence from southern Pangea terrestrial sections for end-Permian global volcanic effects. *Nature Communications*, 14(1), 6. <https://doi.org/10.1038/s41467-022-35272-8>
- Shen, J., Feng, Q. L., Algeo, T. J., Liu, J. L., Zhou, C. Y., Wei, W., et al. (2020). Sedimentary host phases of mercury (Hg) and implications for use of Hg as a volcanic proxy. *Earth and Planetary Science Letters*, 543, 116333. <https://doi.org/10.1016/j.epsl.2020.116333>
- Shen, S.-z., Cao, C.-q., Zhang, H., Bowring, S. A., Henderson, C. M., Payne, J. L., et al. (2013). High-resolution $\delta^{13}\text{C}_{\text{carb}}$ chemostratigraphy from latest Guadalupian through earliest Triassic in South China and Iran. *Earth and Planetary Science Letters*, 375, 156-165. <https://doi.org/10.1016/j.epsl.2013.05.020>
- Shen, S.Z., Crowley, J. L., Wang, Y., Bowring, S. A., Erwin, D. H., Sadler, P. M., et al. (2011). Calibrating the end-Permian mass extinction. *Science*, 334(6061), 1367-1372. <https://doi.org/10.1126/science.1213454>
- Shen, S.Z., Ramezani, J., Chen, J., Cao, C. Q., Erwin, D. H., Zhang, H., et al. (2019). A sudden end-Permian mass extinction in South China. *Geological Society of America Bulletin*, 131(1-2), 205-223. <https://doi.org/10.1130/B31909.1>
- Sial, A. N., Chen, J. B., Lacerda, L. D., Korte, C., Spangenberg, J. E., Silva-Tamayo, J. C., et al. (2020). Globally enhanced Hg deposition and Hg isotopes in sections straddling the Permian-Triassic boundary: Link to volcanism. *Palaeogeography Palaeoclimatology Palaeoecology*, 540, 109537. <https://doi.org/10.1016/j.palaeo.2019.109537>
- Sibik, S., Edmonds, M., Maclennan, J., & Svensen, H. (2015). Magmas erupted during the main pulse of Siberian Traps volcanism were volatile-poor. *Journal of Petrology*, 56(11), 2089-2116. <https://doi.org/10.1093/petrology/egv064>
- Sibik, S., Edmonds, M., Villemant, B., Svensen, H. H., Polozov, A. G., & Planke, S. (2021). Halogen enrichment of Siberian Traps magmas during interaction with evaporites. <https://doi.org/10.3389/feart.2021.741447>
- Sobolev, A. V., Krivolutskaya, N. A., & Kuzmin, D. V. (2009). Petrology of the parental melts and mantle sources of Siberian trap magmatism. *Petrology*, 17(3), 253-286. <https://doi.org/10.1134/S0869591109030047>
- Song, H., Wignall, P. B., Tong, J., & Yin, H. (2013). Two pulses of extinction during the Permian-Triassic crisis. *Nature Geoscience*, 6(1), 52-56. <https://doi.org/10.1038/ngeo1649>

- Song, Q., Hong, H., Algeo, T. J., Fang, Q., Zhao, C., Liu, C., & Xu, Y. (2022). Clay mineralogy mediated by pH and chemical weathering intensity of Permian–Triassic boundary K-bentonites at Dongpan (Guangxi, South China). *Chemical Geology*, 121262. <https://doi.org/10.1016/j.chemgeo.2022.121262>
- Sonke, J. E., Schafer, J., Chmeleff, J., Audry, S., Blanc, G., & Dupre, B. (2010). Sedimentary mercury stable isotope records of atmospheric and riverine pollution from two major European heavy metal refineries. *Chemical Geology*, 279(3-4), 90-100. <https://doi.org/10.1016/j.chemgeo.2010.09.017>
- Stanley, S.M., 2016. Estimates of the magnitudes of major marine mass extinctions in earth history. *Proceedings of the National Academy of Sciences* 113, E6325-E6334 DOI: 10.1073/pnas.1613094113.
- Sun, R., Enrico, M., Heimburger, L. E., Scott, C., & Sonke, J. E. (2013). A double-stage tube furnace-acid-trapping protocol for the pre-concentration of mercury from solid samples for isotopic analysis. *Anal Bioanal Chem*, 405(21), 6771-6781. <https://doi.org/10.1007/s00216-013-7152-2>
- Sun, S.-S., & McDonough, W. F. (1989). Chemical and isotopic systematics of oceanic basalts: implications for mantle composition and processes. *Geological Society, London, Special Publications*, 42(1), 313-345. <https://doi.org/10.1144/GSL.SP.1989.042.01.1>
- Svensen, H., Planke, S., Polozov, A. G., Schmidbauer, N., Corfu, F., Podladchikov, Y. Y., & Jamtveit, B. (2009). Siberian gas venting and the end-Permian environmental crisis. *Earth and Planetary Science Letters*, 277(3-4), 490-500. <https://doi.org/10.1016/j.epsl.2008.11.015>
- Svensen, H. H., Frolov, S., Akhmanov, G. G., Polozov, A. G., Jerram, D. A., Shiganova, O. V., et al. (2018). Sills and gas generation in the Siberian Traps. *Philos Trans A Math Phys Eng Sci*, 376(2130), 20170080. <https://doi.org/10.1098/rsta.2017.0080>
- Them II, T., Jagoe, C., Caruthers, A., Gill, B., Grasby, S., Gröcke, D., Yin, R., Owens, J., 2019. Terrestrial sources as the primary delivery mechanism of mercury to the oceans across the Toarcian Oceanic Anoxic Event (Early Jurassic). *Earth and Planetary Science Letters* 507, 62-72 DOI: <https://doi.org/10.1016/j.epsl.2018.11.029>.
- Thibodeau, A. M., & Bergquist, B. A. (2017). Do mercury isotopes record the signature of massive volcanism in marine sedimentary records? *Geology*, 45(1), 95-96. <https://doi.org/10.1130/focus012017.1>
- Thibodeau, A. M., Ritterbush, K., Yager, J. A., West, A. J., Ibarra, Y., Bottjer, D. J., et al. (2016). Mercury anomalies and the timing of biotic recovery following the end-Triassic mass extinction. *Nat Commun*, 7(1), 11147. <https://doi.org/10.1038/ncomms11147>
- Tribovillard, N., Algeo, T.J., Lyons, T., Riboulleau, A., 2006. Trace metals as paleoredox and paleoproductivity proxies: An update. *Chemical Geology* 232, 12-32 DOI: <https://doi.org/10.1016/j.chemgeo.2006.02.012>.
- Vajda, V., McLoughlin, S., Mays, C., Frank, T. D., Fielding, C. R., Tevyaw, A., et al. (2020). End-Permian (252 Mya) deforestation, wildfires and flooding—an ancient biotic crisis with lessons for the present. *Earth and Planetary Science Letters*, 529, 115875. <https://doi.org/10.1016/j.epsl.2019.115875>
- Vérard, C., Hochard, C., Baumgartner, P. O., Stampfli, G. M., & Liu, M. (2015a). Geodynamic evolution of the Earth over the Phanerozoic: Plate tectonic activity and palaeoclimatic indicators. *Journal of Palaeogeography*, 4(2), 167-188. <https://doi.org/10.3724/SP.J.1261.2015.00072>

- Vérard, C., Hochard, C., Baumgartner, P. O., Stampfli, G. M., & Liu, M. (2015b). 3D palaeogeographic reconstructions of the Phanerozoic versus sea-level and Sr-ratio variations. *Journal of Palaeogeography*, 4(1), 64-84. <https://doi.org/10.3724/SP.J.1261.2015.00068>
- Vérard, C. (2019). Panalexis: towards global synthetic palaeogeographies using integration and coupling of manifold models. *Geological Magazine*, 156(2), 320-330. <https://doi.org/10.1017/S0016756817001042>
- Wang, X., Cawood, P. A., Zhao, H., Zhao, L., Grasby, S. E., Chen, Z.-Q., & Zhang, L. (2019a). Global mercury cycle during the end-Permian mass extinction and subsequent Early Triassic recovery. *Earth and Planetary Science Letters*, 513, 144-155. <https://doi.org/10.1016/j.epsl.2019.02.026>
- Wang, X., Cawood, P. A., Zhao, L., Chen, Z.-Q., Lyu, Z., & Ma, B. (2019b). Convergent continental margin volcanic source for ash beds at the Permian-Triassic boundary, South China: Constraints from trace elements and Hf-isotopes. *Palaeogeography, Palaeoclimatology, Palaeoecology*, 519, 154-165. <https://doi.org/10.1016/j.palaeo.2018.02.011>
- Wang, X. D., Cawood, P. A., Zhao, H., Zhao, L. S., Grasby, S. E., Chen, Z. Q., et al. (2018). Mercury anomalies across the end Permian mass extinction in South China from shallow and deep water depositional environments. *Earth and Planetary Science Letters*, 496, 159-167. <https://doi.org/10.1016/j.epsl.2018.05.044>
- Waskom, M. L. (2021). Seaborn: statistical data visualization [Software]. *Journal of Open Source Software*, 6(60), 3021. <https://doi.org/10.21105/joss.03021>
- Widmann, P., Bucher, H., Leu, M., Vennemann, T., Bagherpour, B., Schneebeli-Hermann, E., Goudemand, N., Schaltegger, U., 2020. Dynamics of the largest carbon isotope excursion during the Early Triassic biotic recovery. *Front Earth Sc-Switz*, 196 DOI: <https://doi.org/10.3389/feart.2020.00196>.
- Widmann, P., Davies, J. H. F. L., & Schaltegger, U. (2019). Calibrating chemical abrasion: Its effects on zircon crystal structure, chemical composition and U Pb age. *Chemical Geology*, 511, 1-10. <https://doi.org/10.1016/j.chemgeo.2019.02.026>
- Wignall, P.B., Morante, R., Newton, R., 1998. The Permo-Triassic transition in Spitsbergen: $\delta^{13}\text{C}_{\text{org}}$ chemostratigraphy, Fe and S geochemistry, facies, fauna and trace fossils. *Geological Magazine* 135, 47-62 DOI: 10.1017/S0016756897008121.
- Winchester, J. A., & Floyd, P. A. (1977). Geochemical discrimination of different magma series and their differentiation products using immobile elements. *Chemical Geology*, 20, 325-343. [https://doi.org/10.1016/0009-2541\(77\)90057-2](https://doi.org/10.1016/0009-2541(77)90057-2)
- Yager, J. A., West, A. J., Thibodeau, A. M., Corsetti, F. A., Rigo, M., Berelson, W. M., et al. (2021). Mercury contents and isotope ratios from diverse depositional environments across the Triassic-Jurassic Boundary: Towards a more robust mercury proxy for large igneous province magmatism. *Earth-Science Reviews*, 223, 103775. <https://doi.org/10.1016/j.earscirev.2021.103775>
- Yang, J., Cawood, P. A., Du, Y., Huang, H., Huang, H., & Tao, P. (2012). Large Igneous Province and magmatic arc sourced Permian-Triassic volcanogenic sediments in China. *Sedimentary Geology*, 261, 120-131. <https://doi.org/10.1016/j.sedgeo.2012.03.018>
- Yin, H., Jiang, H., Xia, W., Feng, Q., Zhang, N., & Shen, J. (2014). The end-Permian regression in South China and its implication on mass extinction. *Earth-Science Reviews*, 137, 19-33. <https://doi.org/10.1016/j.earscirev.2013.06.003>

- Yin, H., Siji, H., Kexing, Z., H.J, H., Fengqing, Y., Meihua, D., Xianmei, B., 1992. The effects of volcanism on the Permo-Triassic mass extinction in South China, in: Dickins, J.M., Sweet, W.C., Zunyi, Y., Hongfu, Y. (Eds.), *Permo-Triassic Events in the Eastern Tethys: Stratigraphy Classification and Relations with the Western Tethys*. Cambridge University Press, Cambridge, pp. 146-157.
- Yin, R., Chen, D., Pan, X., Deng, C., Chen, L., Song, X., Yu, S., Zhu, C., Wei, X., Xu, Y., Feng, X., Blum, J.D., Lehmann, B., 2022. Mantle Hg isotopic heterogeneity and evidence of oceanic Hg recycling into the mantle. *Nature Communications* 13, 948 DOI: [10.1038/s41467-022-28577-1](https://doi.org/10.1038/s41467-022-28577-1).
- Yin, H., Zhang, K., Tong, J., Yang, Z., & Wu, S. (2001). The global stratotype section and point (GSSP) of the Permian-Triassic boundary. *Episodes*, 24(2), 102-114. <https://doi.org/10.18814/epiiugs/2001/v24i2/004>
- Yuan, D.-X., Shen, S.-z., Henderson, C. M., Chen, J., Zhang, H., Zheng, Q.-f., & Wu, H. (2019). Integrative timescale for the Lopingian (Late Permian): A review and update from Shangsi, South China. *Earth-Science Reviews*, 188, 190-209. <https://doi.org/10.1016/j.earscirev.2018.11.002>
- Zambardi, T., Sonke, J. E., Toutain, J. P., Sortino, F., & Shinohara, H. (2009). Mercury emissions and stable isotopic compositions at Vulcano Island (Italy). *Earth and Planetary Science Letters*, 277(1-2), 236-243. <https://doi.org/10.1016/j.epsl.2008.10.023>
- Zhang, G. J., Zhang, X. L., & Shen, Y. N. (2021). Quantitative constraints on carbon cycling and temporal changes in episodic euxinia during the end-Permian mass extinction in South China. *Chemical Geology*, 562, 120036. <https://doi.org/10.1016/j.chemgeo.2020.120036>
- Zhang, H., Zhang, F., Chen, J. B., Erwin, D. H., Syverson, D. D., Ni, P., et al. (2021). Felsic volcanism as a factor driving the end-Permian mass extinction. *Sci Adv*, 7(47), eabh1390. <https://doi.org/10.1126/sciadv.abh1390>
- Zhao, H., Shen, J., Algeo, T.J., Racki, G., Chen, J., Huang, C., Song, J., Qie, W., Gong, Y., 2022. Mercury isotope evidence for regional volcanism during the Frasnian-Famennian transition. *Earth and Planetary Science Letters* 581, 117412 DOI: <https://doi.org/10.1016/j.epsl.2022.117412>
- Zhao, T. Y., Algeo, T. J., Feng, Q. L., Zi, J. W., & Xu, G. Z. (2019). Tracing the provenance of volcanic ash in Permian-Triassic boundary strata, South China: Constraints from inherited and syn-depositional magmatic zircons. *Palaeogeography Palaeoclimatology Palaeoecology*, 516, 190-202. <https://doi.org/10.1016/j.palaeo.2018.12.002>
- Zheng, B. S., Mou, C. L., Zhou, R. J., Wang, X. P., Xiao, Z. H., & Chen, Y. (2020). Nature and origin of the volcanic ash beds near the Permian-Triassic boundary in South China: new data and their geological implications. *Geological Magazine*, 157(4), 677-689. <https://doi.org/10.1017/S001675681900133x>
- Zintwana, M. P., Cawthorn, R. G., Ashwal, L. D., Roelofse, F., & Cronwright, H. (2012). Mercury in the Bushveld Complex, South Africa, and the Skaergaard Intrusion, Greenland. *Chemical Geology*, 320, 147-155. <https://doi.org/10.1016/j.chemgeo.2012.06.001>

CHAPTER 2

Author contributions

Oluwaseun Edward: Conceptualization, Formal analysis, Data curation, Investigation, Data Analysis, Data visualization, Writing - original draft, Writing - review and editing.

Hugo Bucher: Conceptualization, Funding Acquisition, Investigation, Project Administration, Resources, Supervision, Writing - review and editing.

Sandrine Le Houedec: Investigation, Validation, Resources, Writing - review and editing.

Christian V  rard: Formal analysis, Data Visualization, Resources, Writing - review and editing.

Marc Leu: Validation, Data Curation, Writing - review and editing.

Aymon Baud: Resources, Validation, Writing - review and editing.

Jeroen Sonke: Investigation, Validation, Resources, Writing - review and editing.

Franziska Blattmann: Investigation, Validation, Writing - review and editing.

Thierry Adatte: Investigation, Validation, Resources, Writing - review and editing.

Torsten Vennemann: Conceptualization, Funding Acquisition, Project Administration, Resources, Supervision, Writing - review and editing.

Evidence for Variable Provenance of Mercury Anomalies During the Smithian – Spathian (Olenekian)

Oluwaseun Edward^{1*}, Hugo Bucher², Sandrine Le Houedec³, Christian V  rard³, Marc Leu², Aymon Baud⁴, Jeroen E. Sonke⁵, Franziska Blattmann¹, Thierry Adatte⁴, Torsten Vennemann¹

¹Institute of Earth Surface Dynamics, G  opolis, University of Lausanne, CH-1015 Lausanne, Switzerland

²Pal  ontologisches Institut der Universit  t Z  rich, Karl-Schmid-Strasse 4, 8006 Z  rich, Switzerland

³Department of Earth Sciences, Universit   de Gen  ve, Rue des Mara  chers 13, CH-1205 Gen  ve, Switzerland

⁴Institute of Earth Sciences, G  opolis, University of Lausanne, CH-1015 Lausanne, Switzerland

⁵Observatoire Midi-Pyr  n  es, G  osciences Environnement Toulouse, Universit   Paul Sabatier Toulouse 3, 14 Avenue Edouard Belin, 31400 Toulouse, France

*Corresponding author | E-mail: oluwaseun.edward@unil.ch

Keywords: Early Triassic, volcanism, Siberian Traps, mercury, Smithian-Spathian

Abstract

Mercury (Hg) enrichment recorded in Smithian to Spathian (Olenekian) marine sedimentary successions has been used to link putative renewed Siberian Traps Large Igneous Province (STLIP) magmatism to climatic and environmental perturbations during this interval. To assess the potential for massive volcanism as a trigger for marine environmental disturbances across the Smithian – Spathian boundary (SSB), the patterns and provenance of Hg sequestration in four Tethyan marine sedimentary successions are investigated in the current study. We present a diverse array of new, temporally calibrated geochemical data including Hg concentrations and isotopic compositions, strontium, and neodymium isotope records, as well as major and trace element concentrations from carbonate-poor and -rich strata alike, including volcanic ashes. Results indicate that Hg anomalies in middle to late Smithian strata vary in magnitude and age. Based on several lines of evidence, the Hg anomalies recorded for the investigated PaleoTethyan successions are interpreted to have been sourced from subduction-related arc volcanism, with potential contributions from terrestrial Hg reservoirs. In contrast, a low-magnitude mercury enrichment interval recorded for NeoTethyan late Smithian strata is attributed to hydrothermal fluid or submarine volcanic activity. These results, together with previously published Smithian to Spathian Hg records, provide evidence that Smithian Hg anomalies cannot be attributed to a singular source such as renewed STLIP activity. Instead, the stratigraphically variable mercury anomalies reflect local patterns of enhanced mercury sequestration from various sources during the middle Smithian to SSB. Consequently, evidence for STLIP magmatism during the Smithian – Spathian transition is still lacking, and regional volcanic activity may have been influential in causing marine environmental upheavals in the Tethys region across the SSB.

1. Introduction

The Early Triassic was an important interval in Earth's history, marked by the reorganization of marine and terrestrial ecosystems following the ecological devastations of the Permian-Triassic boundary mass extinction (PTBME) (Erwin et al., 2002; Hermann et al., 2012; Stanley, 2016). Studies show that biotic recovery during the Early Triassic was repeatedly interrupted by climatic, as well as marine and terrestrial environmental upheavals (e.g., Galfetti et al., 2007a; Orchard, 2007; Chen and Benton, 2012; Grasby et al., 2013a; Wei et al., 2015; Hochuli et al., 2016). The pattern of marine faunal recovery differed between nektonic and benthic organisms, with the former being characterized by a rapid Early Triassic recovery punctuated by intermittent extinctions (Orchard, 2007; Brayard and Bucher, 2015; Hautmann et al., 2015). In contrast, the main rediversification of the latter was delayed until the Middle Triassic (Foster and Sebe, 2017; Friesenbichler et al., 2021). Perhaps the most significant interval of the Early Triassic was the middle Smithian to earliest Spathian (ca. 249.9 – 249.1 Ma; Widmann et al., 2020). This interval was characterized by large carbon cycle perturbations (Payne et al., 2004; Galfetti et al., 2007b), significant changes in seawater temperatures (Sun et al., 2012; Romano et al., 2013), and the largest nektonic faunal extinction of the Early Triassic (Orchard, 2007; Stanley, 2009). Also, terrestrial ecosystems experienced a significant vegetation shift from lycophyte dominance in the middle Smithian to gymnosperm dominance in the early Spathian (Lindström et al., 2020 and references therein).

Causal relations between Early Triassic environmental perturbations, climatic changes and biotic turnover have been proposed and remain the subject of scientific debate (e.g., Brayard et al., 2009; Goudeband et al., 2019; Leu et al., 2019; Shen et al., 2019a; Dai et al., 2021). Notably, renewed Siberian Traps Large Igneous Province (STLIP) magmatism has been proposed as an explanation for Smithian to Spathian climatic and environmental disturbances, which have been causally related to contemporaneous biotic upheavals (Ovtcharova et al., 2006; Galfetti et al., 2007a; Payne and Kump, 2007; Sun et al., 2012; Shen et al., 2019a). However, there is currently no U-Pb zircon geochronology evidence for STLIP magmatism younger than 250.3 Ma (Augland et al., 2019; Widmann et al., 2020). Instead, mercury (Hg) enrichment intervals recorded in Smithian-Spathian marine strata from spatially disparate localities have been proposed as evidence of Smithian-Spathian transition STLIP volcanism (e.g., Grasby et al., 2016; Shen et al., 2019a).

Although generally successfully applied as a proxy for volcanism, several studies show that the biogeochemical cycling of Hg in the environment is complex and Hg anomalies can result from a variety of non-volcanic means (e.g., Grasby et al., 2019; Hammer et al., 2019; Them II et al., 2019; Shen et al., 2020; Percival et al., 2021; Yager et al., 2021). Also, the Hg content of ancient sedimentary rocks can be altered during late diagenesis (Charbonnier et al., 2020). Therefore, Hg isotopes are frequently used to constrain the provenance and trajectory of Hg deposition in both modern and ancient sediments (e.g., Rolison et al., 2013; Blum et al., 2014; Sun et al., 2014; Yin et al., 2016; Grasby et al., 2019).

Unfortunately, however, of all published Early Triassic Hg records, Hg isotope data are only available for two marine sections (i.e., Chaohu, South China and Guryul Ravine, India; Wang et al., 2019a). Furthermore, the precise stratigraphic relationship between published Smithian–Spathian Hg records for different basins remains uncertain (Hammer et al., 2019; Widmann et al., 2020). Consequently, high-resolution stratigraphic correlation of Smithian to Spathian Hg records between various sedimentary basins, an assessment of the preservation of Hg contents in investigated sedimentary successions, as well as a thorough evaluation of Hg sources to Smithian to Spathian-aged marine successions, are required to reliably infer a link between Smithian Hg anomalies and a potential middle to late Smithian reemergence of STLIP volcanism.

The current study investigates the occurrence and provenance of Hg concentration anomalies in middle Smithian to Spathian sedimentary successions, with the aim of assessing the putative role of STLIP volcanism in promoting marine environmental upheavals during the studied interval. The investigated successions include carbonate-poor and carbonate-rich strata deposited in shallow and deep-water environments of the Tethys Ocean, enabling an evaluation of the intensity of Hg release to Olenekian marine depositional environments. Our dataset includes Hg concentrations and isotope compositions, carbon isotope compositions of organic matter ($\delta^{13}\text{C}_{\text{org}}$), major and trace element concentrations, mineralogical compositions, total organic carbon (TOC) content, as well as strontium and neodymium isotope ratios. Combining precise and accurate U-Pb zircon ages and conodont biostratigraphy based on unitary association zones (UAZs) (Widmann et al., 2020; Leu et al., 2022; Leu et al., 2023), a high-resolution correlation of the geochemical records from our spatially dispersed study sections is achieved. Further, we compare our Hg records to previously published Smithian to Spathian Hg records for other localities to evaluate the evidence for a singular global source for Smithian-Spathian Hg anomalies (such as renewed STLIP volcanism).

2. Geological setting

The four studied sections are currently situated in Oman and China and comprise marine sedimentary successions which were deposited in the PaleoTethys (Qiakong, Shanggang) and NeoTethys oceans (Jebel Aweri, Wadi Musjah) during the Early Triassic.

2.1 Oman

By the Early Triassic, the majority of Earth's landmass had amalgamated, forming one supercontinent – Pangea, which was bordered by a super ocean – Panthalassa (Fig. 1a). On the southern half of Pangea, the Arabian Peninsula, together with Africa and India constituted part of the Gondwana continent (Baud et al., 2001; Baud et al., 2012; Stampfli et al., 2013). Oman was situated on the northern Gondwanan margin, mainly between 20°S and 30°S and bordered to the north and east by the NeoTethys (e.g., Smith et al., 2004; Richoz et al., 2010; Brühwiler et al., 2012). The geologic evolution of the Arabian passive margin (including Oman) during the Permian to Triassic is chronicled in several studies (e.g., Baud et

al., 1993; Pillevuit et al., 1997; Immenhauser et al., 1998; Baud et al., 2001; Hauser et al., 2002; Scharf et al., 2021). During the Permian, tectonic extension of the NeoTethys commenced in tandem with the northward drift of the Cimmerian Block (Şengör et al., 1984; Stampfli, 2000; Baud et al., 2012; Richoz et al., 2014), initiating the formation of offshore seamounts, which record the evolution of pelagic environments during the Triassic (Baud et al., 1993; Lapierre et al., 2004; Brosse et al., 2019). Afterwards in the Jurassic, the Triassic offshore seamounts and other Permian-Triassic rocks were redeposited within Jurassic sediments as olistostromes, which can be found in both the Hawasina Basin and Batain plain of Oman (Schreurs and Immenhauser, 1999; Brosse et al., 2019).

The Jebel Aweri (JA) outcrop (22.3556666667 °N, 59.7541944444 °E) is an exotic build-up block located in the Batain plain, northeastern Oman (Fig. 1f). Details of the geologic evolution of the Batain plains have been discussed in different studies (e.g., Immenhauser et al., 1998; Schreurs and Immenhauser, 1999; Hauser et al., 2002). The JA carbonate succession is situated about 30 km south of Ras al Hadd, Oman. It is located alongside successions of the Middle Jurassic Guwayza Formation and the Ad Daffah conglomerate in the Batain area. This exotic block comprises a 22 m-thick lower block and an 8 m-thick upper block and represents a Lower Triassic reefal succession consisting of shell-supported biostrome, cemented lime clasts and microbialite bioherm (dendrolitic stromatolite) of late Smithian to Spathian age (Leu et al., 2023). Thus, the JA exotic block constitutes an Early Triassic-aged offshore seamount carbonate succession, which has been redeposited as an olistostrome within Jurassic sediments (Schreurs and Immenhauser, 1999; Brosse et al., 2019).

The Wadi Musjah (WMJ) outcrop (22.9623611111 °N, 58.2670555556 °E) is a 4.6 m-thick, strongly condensed, red ammonoid limestone succession located about 75 km from Muscat, Oman (Fig. 1f). This succession was previously described by Baud et al. (2001), Brühwiler et al. (2012), and most recently by Leu et al. (2023). The WMJ section comprises Hallstatt-type limestones, which are pelagic carbonate deposits with near-zero terrigenous components and are known from several other Tethyan localities (Brühwiler et al., 2012). These Hallstatt-type limestones from the Arabian margin have been interpreted to represent isolated oceanic build-ups, i.e. seamounts, which have been transported on the Arabian margin during the Late Cretaceous obduction of oceanic crust (Brühwiler et al., 2012; Baud, 2013). Based on conodont biochronology, the WMJ succession covers the middle Smithian to Spathian (Leu et al. 2023). Thus, WMJ spans a longer time interval than the six-times thicker JA build up block, albeit having a lower (ca. 6× lower than JA) sedimentation rate. The lower 2.4 m of the succession consists of cemented bivalve coquina biostromes and peloidal grainstone with centimetre-sized bivalves in fibrous and blocky calcite cement. The upper 2.2 m of the section is characterized by a sudden appearance of crinoid ossicles, brachiopod shells, and echinoid spines, which form yellow to brown colored calcite cemented encrinites-brachiopod biostromes (Leu et al. 2023).

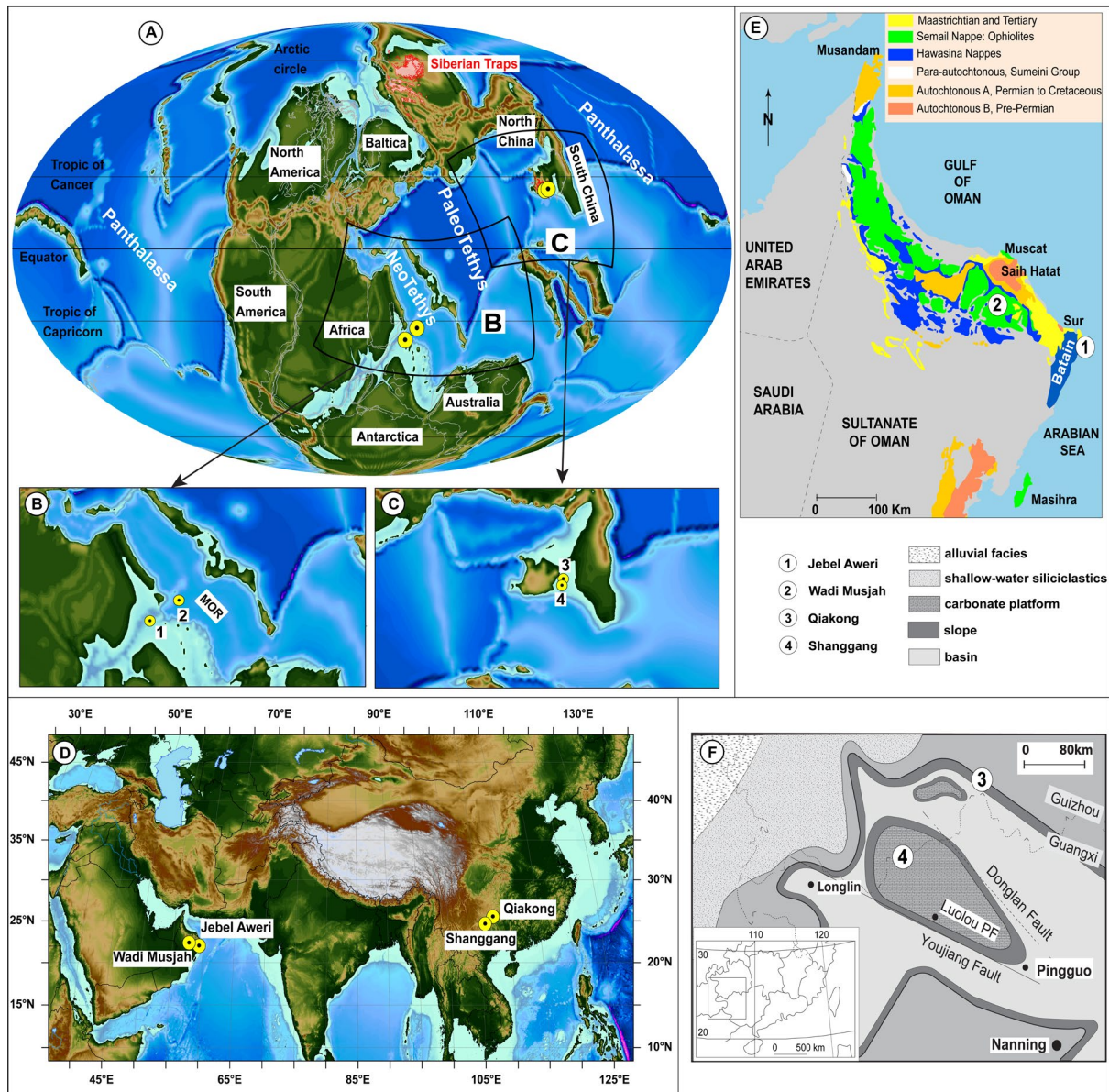


Figure 1. Paleogeographic, present-day and geologic maps of the study locations. A) Early Triassic paleogeographic map after the Panalexis model (Vérard, 2019) showing the location of the studied successions in the Paleotethys and Neotethys. Mollweide projection of the B) Oman (NeoTethys) and C) South China (PaleoTethys) areas during the Early Triassic from A. D) Map showing the present-day location of the studied successions. Geological map of E) Oman with the present-day locations of the exotic blocks modified after Baud et al. (2001), and F) the Nanpanjiang basin after Bagherpour et al. (2017) showing the studied sections. MOR: mid-oceanic ridge.

2.2 South China

The South China Block was situated along the eastern margin of the Paleotethys ocean and occupied equatorial to intertropical paleolatitudes in the Early Triassic (Fig. 1a). The studied sections in South China are situated in the Nanpanjiang Basin, which is in the present-day southern section of the South

China block (southern Guizhou and northwestern Guanxi provinces; (Enos et al., 2006)). During the Late Permian to Early Triassic, the Nanpanjiang Basin developed as an extensional to transtensional basin in a back-arc setting (Duan et al., 2020). Rock successions of this basin extend across southern China and northern Vietnam (Leu et al., 2022 and references therein) and include Early Triassic sedimentary deposits representing deep-water, slope/basinal settings and isolated shallow-water carbonate platforms (Lehrmann et al., 2007; Duan et al., 2020). The Nanpanjiang Basin is characterized by a fault-bounded (graben and horst) paleotopography (Bagherpour et al., 2020), with horsts consisting of carbonate platforms (such as the Great Bank of Guizhou (GBG) and Luolou platform (Lehrmann et al., 1998; Bagherpour et al., 2017)) and the grabens consisting of distal turbidites and slope to basin deposits (such as the Pingtang syncline (Bagherpour et al., 2020; Widmann et al., 2020)).

The Qiakong (QIA) section (25.8573277778°, 107.3089138889°) is situated in the Pingtang syncline, northern Nanpanjiang Basin and consists of Early Triassic sediments of the Daye and Luolou formations. The Smithian to Spathian succession in QIA comprises middle Smithian-aged thin-bedded limestone strata with volcanic ashes of the Daye Formation (Widmann et al., 2020; Leu et al., 2022). These are overlain by alternating beds of laminated black shale and thin-bedded limestone of late Smithian age, which accumulated in a slope/basin setting (Leu et al., 2022). The Spathian portion of the Luolou Formation in QIA was deposited in an outer platform setting (Galfetti et al., 2007a; Leu et al., 2022). It comprises conodont- and ammonoid-rich nodular limestone and marly limestone beds, as well as interbedded volcanic ash beds.

The Shanggang (SHA) succession (24.812333°, 106.542194°) is situated in the northern part of the Guangxi province, China and was deposited on the laterally extensive Luolou platform of the Nanpanjiang Basin (Fig. 1e). It consists of mixed siliciclastic and carbonate deposits in the Smithian interval and nodular limestone beds in the Spathian (Widmann et al., 2020; Leu et al., 2022). Several volcanic ash beds are intercalated within the Smithian-Spathian succession, which is subdivided into several lithological units ranging from the early Smithian thin-bedded 'Flemingites' limestone of Unit III to the Spathian cliff-forming nodular limestone beds of unit V (Galfetti et al., 2008; Leu et al., 2022).

3. Materials and Methods

Materials analyzed for this study – whole rock carbonates, shales, volcanic ashes, as well as fossil conodont and fish teeth samples – are from recent studies of the Nanpanjiang Basin (Widmann et al., 2020; Leu et al., 2022) and Oman exotic blocks (Leu et al., 2023). These recent studies provided detailed sedimentological descriptions and carbon isotope chemostratigraphy for the study sites. Furthermore, U-Pb zircon geochronology and conodont biochronology from these recent studies provide the correlation framework and absolute time constraint utilized in the current study. Whole rock samples from each of the localities were analyzed for Hg concentration and isotope composition, total organic carbon (TOC) content, major element, and trace element concentration, respectively. Conodont

elements and fossil fish teeth fragments from the Oman study sites (Leu et al., 2023) were analyzed for their Sr and Nd isotope compositions and volcanic ash samples from QIA and SHA were analyzed for their major and trace element concentrations, as well as Hg concentration and isotope compositions.

3.1 Mercury concentration and isotope composition

Mercury content of pulverized shales, carbonates and volcanic ashes was measured at the Institute of Earth Sciences (ISTE), University of Lausanne (UNIL) using a Zeeman R-915F high-frequency atomic absorption spectrometer. Analyses were made in duplicate for all samples. For the samples with outlier Hg concentrations in each of the studied sections, three extra measurements were done to ensure both the representativeness and analytical precision for the sample. The standard reference material – GSD-11 (Chinese alluvium) – was used to monitor accuracy of the measurements.

Hg isotope analyses were made at the Observatoire Midi-Pyrénées, Toulouse, France, following analytical procedures reported in Sun et al. (2013) and Jiskra et al. (2021). Briefly, Hg was preconcentrated as Hg^{II} from pulverized samples using the double-stage furnace – acid-trapping technique (Sun et al., 2013). Two reference materials, NIST SRM 1632D (bituminous coal, n=5) and NIST SRM 1944 (New Jersey sediment, n=4), were processed along with the samples. This was followed by Hg isotope analysis by cold vapor multi-collector inductively coupled plasma mass spectrometry (CV-MC-ICPMS). Measurements were carried out in duplicates over two analytical sessions following previously documented analytical procedures (Sonke et al., 2010; Jiskra et al., 2021). Sample-standard bracketing (Blum and Bergquist, 2007) using the NIST SRM 3133 standard at matching standard and sample concentrations (1 and 2.1 ng/g) was used to correct the MC-ICPMS instrumental mass bias. Repeated analysis of the UM-Almaden (n = 14) and ETH-Fluka (n = 14) Hg standard solutions at matching sample concentrations were used to monitor long term instrumental precision.

Hg isotope compositions are reported as the mean of duplicate measurements using the delta notation (δ) in permil (‰) relative to the bracketing NIST SRM 3133 standard (Blum and Bergquist, 2007). For mass dependent fractionation (MDF), this is expressed as $\delta^{202}\text{Hg}$ in permil (‰) and for mass independent fractionation (MIF), values as reported using the capital delta (Δ) notation:

$$\Delta^{\text{xxx}}\text{Hg} = \delta^{\text{xxx}}\text{Hg} - K_{\text{xxx}} \times \delta^{202}\text{Hg} \quad (1)$$

where xxx refers to Hg isotope mass, except ¹⁹⁸Hg, and K represents the mass-dependent scaling factor for the different Hg isotope masses. We report analytical uncertainty of Hg isotope values conservatively by using whichever is larger between the 2 × standard deviation (2σ) of the replicate measurements or that of the certified reference material with the largest 2σ.

3.2 Total organic carbon (TOC) content and carbon isotope analysis

TOC was measured at ISTE using two analytical methods: (i) Rock-Eval pyrolysis of bulk (non-decarbonated) sample material and (ii) TOC determination on decarbonated samples using an Elemental Analyzer. A Rock-Eval 6 was used to measure TOC content in volcanic ashes and a subset of limestone and shale samples following the procedure described by (Behar et al., 2001). The standard – IFP-160000 was used to monitor analytical quality and analytical error was < 0.1 %. Pulverized material from the remainder subset of shale and limestone samples was decarbonated by acid treatment overnight using 3 M HCl. The residues were then rinsed several times with deionized water and dried in an oven at 45 °C for three days. TOC content and carbon isotope compositions ($\delta^{13}\text{C}_{\text{org}}$) were measured on the acid treated samples using a Carlo Erba (CE 1100) Elemental Analyzer linked to a Thermo Fisher Delta V Plus isotope ratio mass spectrometer. $\delta^{13}\text{C}_{\text{org}}$ values were measured only for samples from QIA and SHA because the samples from the Oman exotics have too low organic matter (OM) contents. The internal standards: glycine, pyridene, urea and graphite used for $\delta^{13}\text{C}_{\text{org}}$ analysis are calibrated against IAEA standards: USGS-24 graphite ($\delta^{13}\text{C} = -15.9$ ‰) and NBS-22 oil ($\delta^{13}\text{C} = -29.7$ ‰) (Spangenberg and Herlec, 2006). Final TOC contents were calculated from the EA TOC yields and documented weights of the samples before and after acid treatment.

3.3 Major and Trace elements analysis

Major element (ME) and trace element (TE) concentrations were determined by X-ray fluorescence (XRF) spectrometry using a PANalytical Axios^{mAX} wavelength dispersive XRF spectrometer fitted with a 4.0 kW Rh X-ray tube at ISTE, UNIL. For ME analysis, about 1.2 g of calcined sample powder was mixed with 6 g of lithium tetraborate ($\text{Li}_2\text{B}_4\text{O}_7$) and heated to 1250 °C to make fused disks prior to analysis. For TE, measurements were conducted on pressed disks obtained by pressing a homogenized mixture of 12 g of sample powder and 3 g of Hoechst-C-wax. The detection limits are approximately 0.01 % for MEs and 1 to 7 ppm for TEs. The external reproducibility (1σ) varies between 0.5 and 5 % depending on the element. The accuracy of analyses was assessed using standard reference materials: JLS-1, JDO-1 and BHVO.

3.4 Strontium and Neodymium isotopes

Radiogenic isotope ratios of Sr ($^{87}\text{Sr}/^{86}\text{Sr}$) and Nd ($^{143}\text{Nd}/^{144}\text{Nd}$) in bioapatite material (conodont elements and fish teeth) from the Omani sections were measured at the Department of Earth Sciences, University of Geneva, Switzerland. Bioapatite samples were dissolved in a few drops of concentrated HNO_3 (16N) over night and brought to evaporation over a hot plate at 80 °C. Samples were re-dissolved in 1N HNO_3 and a sequential chromatographic column was used to separate Sr and Nd. Sr separation was done using Eichrom Sr Spec resin in a solution of 1N HNO_3 (Pin and Bassin, 1992). Neodymium was separated using two ion chromatography columns. Eichrom TRU-SpecTM resin (in solution of 1N HNO_3) was used during the first extraction step to remove the Rare Earth Elements (REE) from the

initial solution while the Eichrom LnSpec™ resin (in solution of 0.25N HCl) was used during the second step to separate Nd from other REE (Caro et al., 2006). The total procedural Nd blanks were smaller than 5 pg and thus is negligible compared to the Nd content of samples (> 200 ng). Nd and Sr isotope ratios were measured on a Neptune MC-ICP-MS (Thermo Finnigan) using an Apex Omega injection system. Nd isotope values were corrected for internal fractionation using $^{146}\text{Nd}/^{144}\text{Nd} = 0.7219$ and for external fractionation by multiple analyses ($n = 26$) of JNdi-1 standard at 25 ppb concentration ($^{143}\text{Nd}/^{144}\text{Nd} = 0.512115$, Tanaka et al. (2000); $2\sigma = 1.6 \times 10^{-5}$). The Rb content of the Sr purified samples was small ($^{85}\text{Rb}/^{86}\text{Sr} < 0.1 \%$) and thus, no Rb correction was applied to Sr measurements on the MC-ICP-MS. Kr interference was monitored by measurements of the $^{83}\text{Kr}/^{86}\text{Kr}$ and $^{83}\text{Kr}/^{84}\text{Kr}$ ratios. The accuracy and reproducibility of the Sr isotope measurements were checked with the NBS SRM 987 standard ($^{87}\text{Sr}/^{86}\text{Sr} = 0.710248$, McArthur et al. (2001); $2\sigma = 4.4 \times 10^{-6}$; $n = 25$). The Nd isotope values ($^{143}\text{Nd}/^{144}\text{Nd}_{(0)}$) were corrected for radiogenic production of ^{143}Nd (Martin and Macdougall, 1995) and expressed as $\epsilon_{\text{Nd}(t)}$ (see supplementary information).

3.5. Bulk rock mineralogical composition

Representative samples from both the Oman and South China successions were selected for analysis of their bulk rock mineralogy using X-ray diffraction (XRD) spectrometry. XRD analysis was conducted using a Thermo Scientific™ ARL™ X'TRA diffractometer fitted with a copper tube operating at 30 mA and 40 kV at ISTE following the procedure outlined in Adatte et al. (1996). Homogenous powdered samples, obtained by milling whole rocks (particle sizes < 40 μm), were pressed into a powder holder by using a glass slide and subsequently scanned from 2° to 65° two-theta in steps of 0.02° two theta using a one second per step counting time. Bulk mineralogy was determined semi-quantitatively based on XRD peak intensities of the main minerals relative to external standards (Kübler, 1983; Adatte et al., 1996). Uncertainty for grain minerals was about 5 wt.% and 5–10 wt.% for phyllosilicates.

4. Results

All the geochemical data generated for this study are provided in the supplementary files hosted on Mendeley data (Edward et al. 2023a) and are illustrated in Figures 2 to 6.

4.1 Mercury content and isotope composition

Hg concentrations have a range between 1 to 216 ppb, < lower level of detection (LLD) to 126 ppb, < LLD to 21 ppb and < LLD to 4 ppb for SHA, QIA, JA and WMJ, respectively. Background Hg contents are higher for South China (< 10 ppb) than for Oman successions (< 1 ppb; LLD). Except for the WMJ succession, Hg concentration anomalies (and Hg/TOC for samples with TOC > 0.2 wt.%) are recorded within the Smithian interval in all localities, albeit with different stratigraphic extent and magnitude. For QIA, a Hg anomaly is recorded for the upper middle Smithian to the latest Smithian (Fig. 2). The Smithian Hg anomaly for SHA appears to be pulsed, with an initial minor peak in the lower middle

Smithian and a main peak recorded between the upper middle Smithian to latest Smithian (Fig. 2). For JA, a low-magnitude Hg anomaly is recorded and is restricted to the upper late Smithian (Fig. 3A).

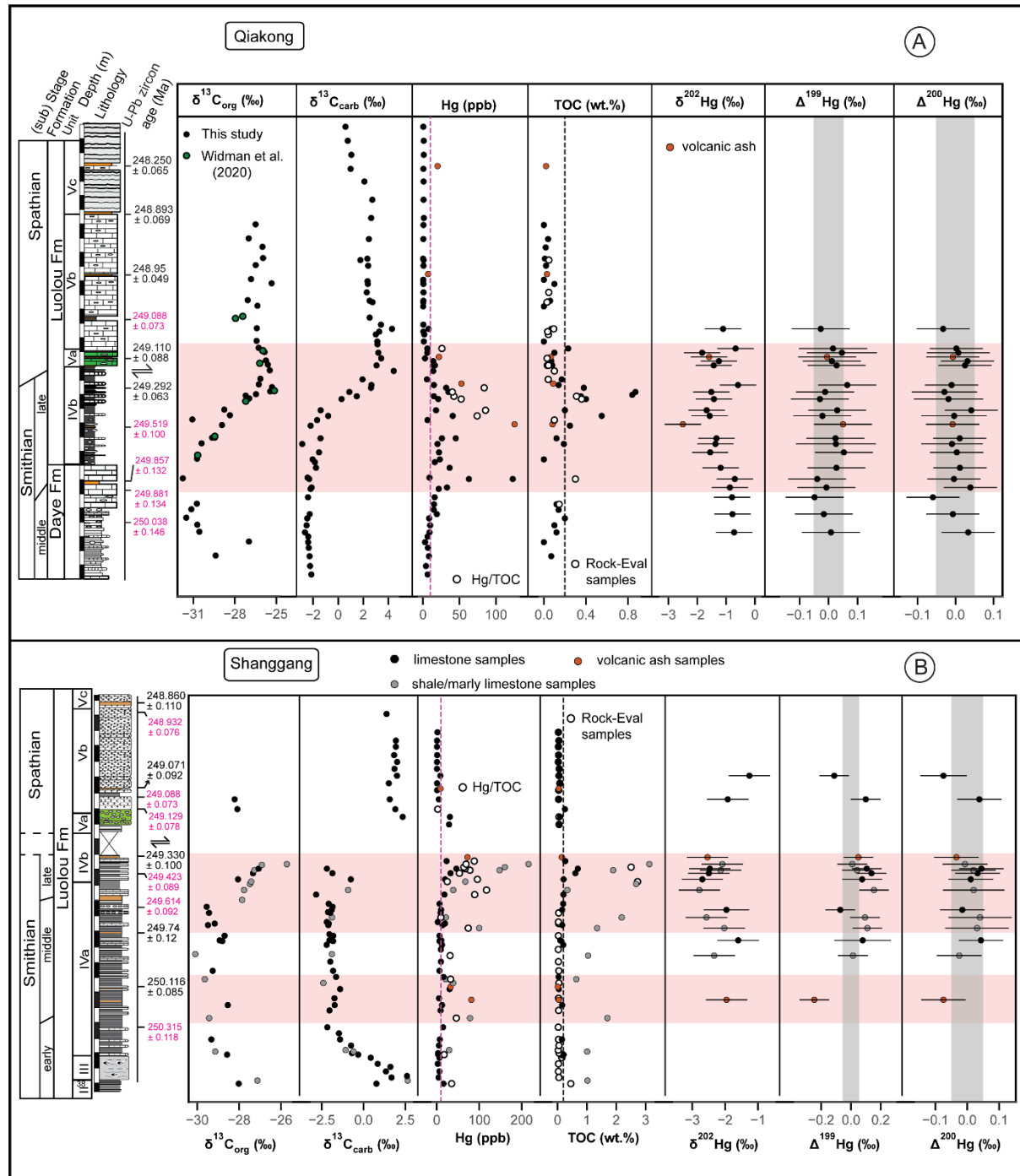


Figure 2. Geochemical profiles showing carbon isotope ($\delta^{13}C$), mercury (Hg) concentration and Hg/TOC ratios, TOC contents, Hg isotope mass-dependent fractionation (MDF, $\delta^{202}Hg$), and Hg isotope mass-independent fractionation (MIF) records ($\Delta^{199}Hg$, $\Delta^{200}Hg$) from A) Qiakong and B) Shanggong sections. $\delta^{13}C_{carb}$ data and U-Pb zircon ages are from Widmann et al. (2020). Absolute ages in pink color are derived by Bayesian age-depth modeling (Widmann et al., 2020). Dashed vertical black line on TOC plot depicts 0.2 wt.% TOC limit and pink vertical dashed line on Hg, Hg/TOC profiles represent

background Hg contents (10 ppb). Horizontal pink bands depict the intervals of Hg enrichment. Vertical gray bands on the Hg MIF records depicts the interval of near zero Hg isotope MIF ($0 \pm 0.05 \text{ ‰}$).

Hg isotope MDF ($\delta^{202}\text{Hg}$) values are generally higher for QIA (range: -2.5 to -0.58 ‰) compared to SHA (range: -2.78 to -1.26 ‰). In this study, we focus on Hg MIF values as these are more diagnostic of the sources and depositional pathways of Hg in the natural environment (Blum et al., 2014; Yin et al., 2014; Yager et al., 2021) and have been shown to be resistant towards post-depositional alteration (Chen et al., 2022). For QIA, $\Delta^{199}\text{Hg}$ and $\Delta^{200}\text{Hg}$ values are near zero ($0 \pm 0.05 \text{ ‰}$), with a median value of 0.01 ‰ and 0.00 ‰, respectively. Hg MIF values have a range between $-0.05 \pm 0.1 \text{ ‰}$ – $0.06 \pm 0.1 \text{ ‰}$ and $0.04 \pm 0.07 \text{ ‰}$ to $-0.06 \pm 0.07 \text{ ‰}$ for $\Delta^{199}\text{Hg}$ and $\Delta^{200}\text{Hg}$, respectively. SHA samples have slightly positive $\Delta^{199}\text{Hg}$ values (range: $0.01 \pm 0.1 \text{ ‰}$ to $0.16 \pm 0.1 \text{ ‰}$, median: 0.07 ‰), except for 1 volcanic ash sample ($-0.25 \pm 0.1 \text{ ‰}$) and 2 limestone samples ($-0.11 \pm 0.1 \text{ ‰}$ and $-0.07 \pm 0.1 \text{ ‰}$, respectively). Similar to QIA, $\Delta^{200}\text{Hg}$ values for SHA are near zero (median: 0.02 ‰), except for 1 limestone and volcanic ash sample that have slightly negative values ($-0.07 \pm 0.07 \text{ ‰}$). Secondary reference materials analyzed to monitor the external reproducibility of the Hg isotope measurements (NIST SRM 1632D and NIST SRM 1944) have Hg isotope MIF values (Table S6) consistent with those previously published for these materials (Sonke et al., 2010; Sun et al., 2013; Jiskra et al., 2019).

4.2 TOC contents and $\delta^{13}\text{C}_{\text{org}}$

TOC contents are higher for South China than Oman. All samples for both Oman successions have TOC content $< 0.1 \text{ wt.}\%$, except for sample C15 in JA with $0.16 \text{ wt.}\%$ TOC (Fig. 3). For South China, volcanic ash and limestone samples generally have TOC contents $< 0.2 \text{ wt.}\%$, except some samples within the late Smithian Hg enrichment interval and one early Smithian sample in SHA (Fig. 2). TOC content differs between different lithologies, as samples with TOC content $> 0.2 \text{ wt.}\%$ for SHA are predominantly dark mudstone or shale samples (Fig. 2B). No systematic difference in TOC content based on analytical technique (i.e., Rock-Eval vs. Elemental Analyzer, Fig. 2) is observed.

$\delta^{13}\text{C}_{\text{org}}$ values have a range from -31.8 ‰ to -26.2 ‰ for QIA and -30.1 ‰ and -25.7 ‰ for SHA. Both localities are characterized by a negative $\delta^{13}\text{C}_{\text{org}}$ excursion in the middle Smithian, which is succeeded by a late Smithian positive excursion, which peaks in the earliest Spathian (Fig. 2). This organic carbon $\delta^{13}\text{C}$ trend is similar to that of inorganic carbon $\delta^{13}\text{C}$, which was previously reported for these sections by Widmann et al. (2020) and Leu et al. (2022).

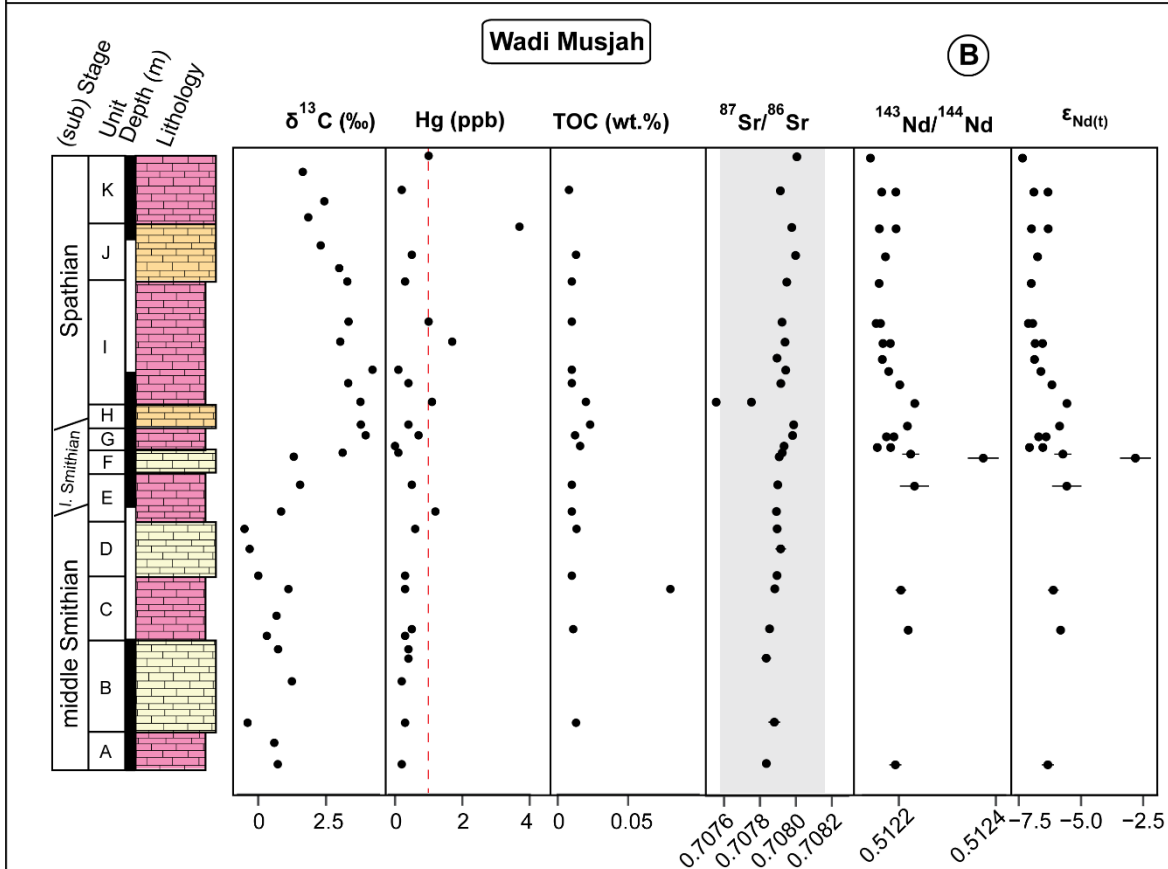
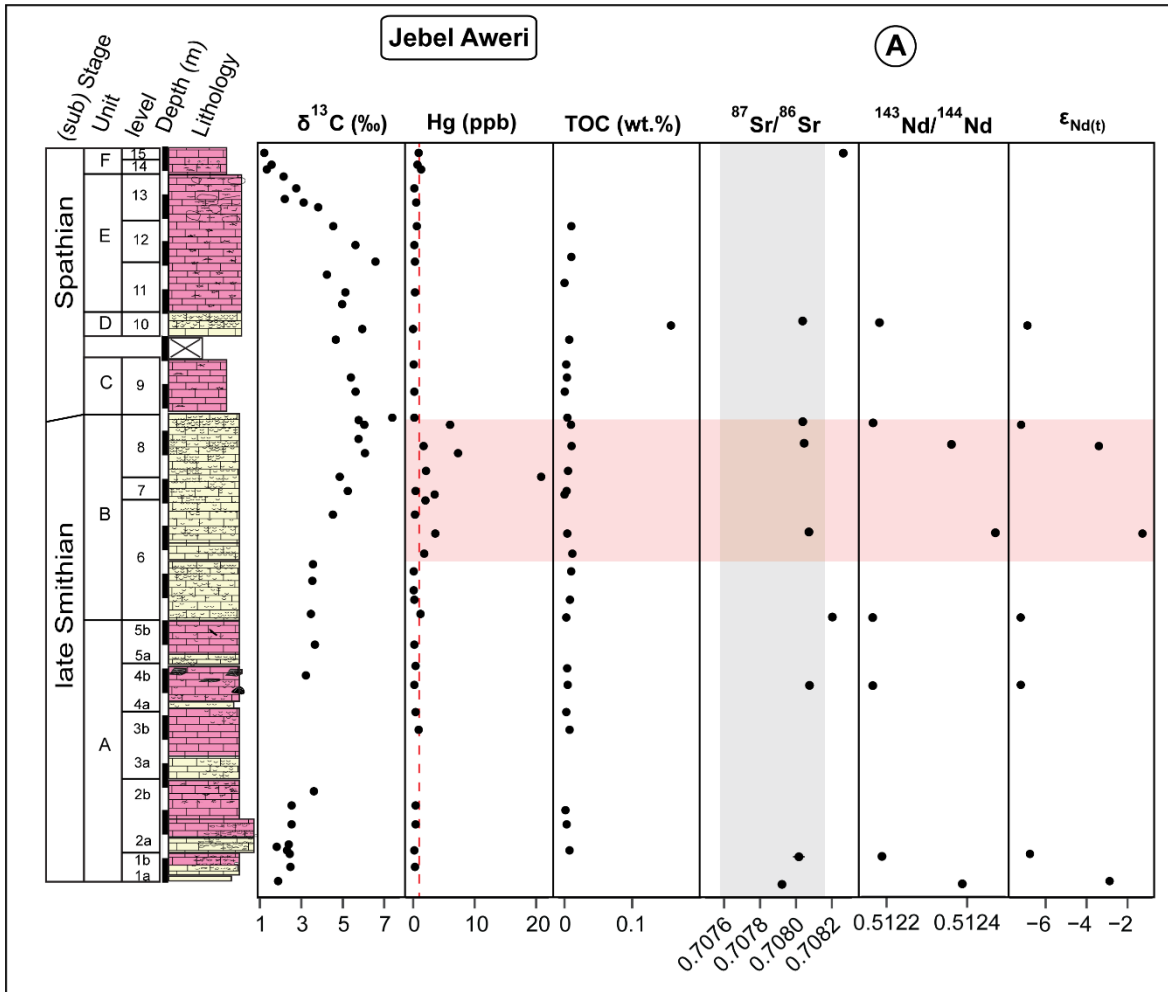


Figure 3. Carbon isotope ($\delta^{13}\text{C}_{\text{carb}}$), mercury concentration, TOC content, $^{87}\text{Sr}/^{86}\text{Sr}$ and $\epsilon_{\text{Nd}(t)}$ records for A) Jebel Aweri and B) Wadi Musjah. $\delta^{13}\text{C}$ values are from Leu et al. (2023). Vertical, red-colored dashed lines depict the background Hg concentrations (1 ppb). Grey rectangle in $^{87}\text{Sr}/^{86}\text{Sr}$ plot depicts the range of previously published Olenekian $^{87}\text{Sr}/^{86}\text{Sr}$ values for NeoTethyan samples (0.70759 – 0.70813; Sedlacek et al., 2014).

4.3 Major and Trace element concentration

In addition to OM, Hg sequestration can be influenced by the terrigenous input, as well as marine redox conditions (Grasby et al., 2019; Shen et al., 2020; Them II et al., 2019). Al, Fe, Mo and U contents are commonly evaluated together with Hg to assess whether variations in clay content, precipitation of pyrite or Fe (oxy) hydroxides resulting from marine redox changes is the main control on Hg sequestration (e.g., Charbonnier et al., 2017; Wang et al., 2019a, Shen et al., 2020). Spearman's rank correlation analysis is used to assess the strength (ρ) and significance (p) of potential statistical correlations between Hg and Al, Fe, Mo, and U contents in the studied sections. Spearman's rank correlation analysis is advantageous because it can be used to evaluate the statistical correlation between two variables which do not necessarily have a linear relationship (e.g., Vickers et al., 2023). Al content (Al_2O_3) is higher for South China (max: 28 wt.%) than for Oman (max: 3 wt. %) and varies according to lithology (Fig. S1) as follows: volcanic ashes > shales > carbonates. Al shows no statistical correlation to Hg in the studied sections, except for SHA samples which show a moderate but significant correlation ($\rho = 0.50$, $p = 0.03$). Fe_2O_3 concentrations range between 0.02 wt.% and 30.54 wt.%. Like Al, the highest Fe contents are measured in volcanic ashes. However, there is no correlation between Fe and Hg in any of the studied sections (Fig. 4). Mo contents are very low for all samples and have a range between < 1 ppm (i.e., below lower limit of detection (LLD) of the XRF spectrometer) and 5 ppm, except for sample Q3T with 30 ppm. Like Fe, Mo has no statistically significant correlation to Hg in any of the studied sections (Fig. 4). U contents range between 1 and 8 ppm for QIA and SHA but is much lower for JA (range = 1 – 2 ppm) and WMJ (< LLD) (Fig. S1). A moderate but significant correlation is recorded between Hg and U for both SHA and QIA but is absent for JA and WMJ.

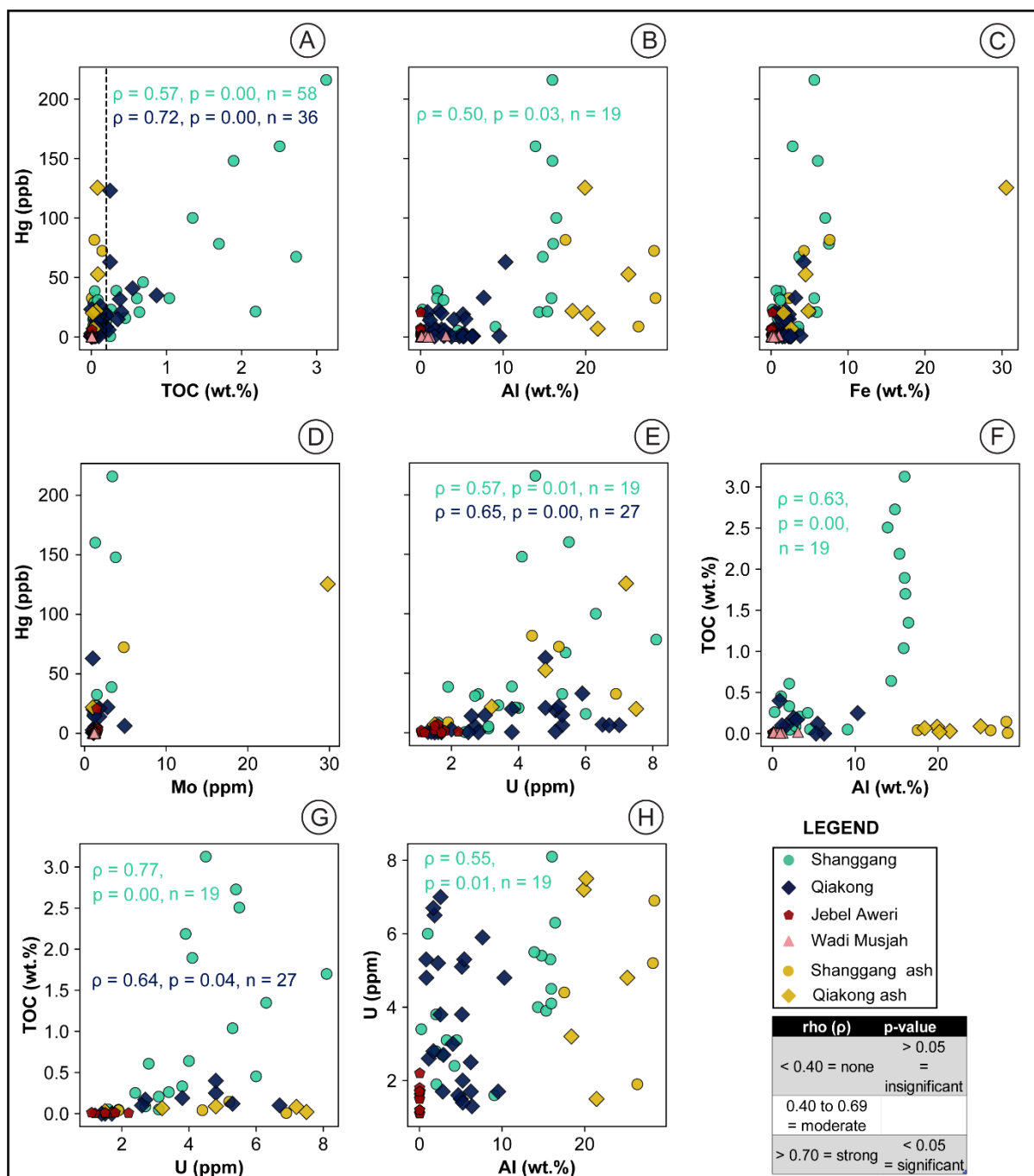


Figure 4. Cross plots showing the statistical relationship between mercury (Hg) and A) TOC. Black line represents the suggested 0.2 wt.% TOC limit for Hg/TOC normalization (Grasby et al., 2016), B) Al, C) Fe, D) Mo, E) U. Cross plots of F) TOC vs. Al, G) TOC vs. U, H) U vs Al. Spearman's correlation coefficient (ρ) and p-values (p) are given within individual cross plots only when a significant correlation is observed (i.e., p -value < 0.05). Volcanic ash samples were not included in the calculation of correlation coefficients.

Volcanic ash samples have high LOI values ($7.4 \leq \text{LOI} \leq 23.1$ wt.%), similar to other Permian-Triassic volcanic ashes from South China e.g., (He et al., 2014; Wang et al., 2019b; Edward et al., 2023b). LOI-corrected SiO_2 , Al_2O_3 and total alkali ($\text{Na}_2\text{O} + \text{K}_2\text{O}$) concentrations have a range between 38.6 and 67.9

wt.%, 17.5 and 28.4 wt.%, and 3.0 and 9.0 wt.%, respectively. $\text{TiO}_2/\text{Al}_2\text{O}_3$ ratios for all volcanic ash samples are generally < 0.055 (Table S5), suggesting that the ashes retain primary geochemical compositions (Hong et al., 2019). Nevertheless, only immobile elements, which are less susceptible to post-depositional alteration (Hong et al., 2019; Portnyagin et al., 2020), are utilized for subsequent interpretation of the tectonic provenance of the volcanic ashes. Primitive mantle-normalized trace element patterns (Sun and McDonough, 1989) indicate that ashes are characterized by conspicuous Ta, Nb, Sr and Ti negative anomalies (Fig. 5A, 5B), consistent with a subduction-related tectonic provenance (Pearce et al., 1995).

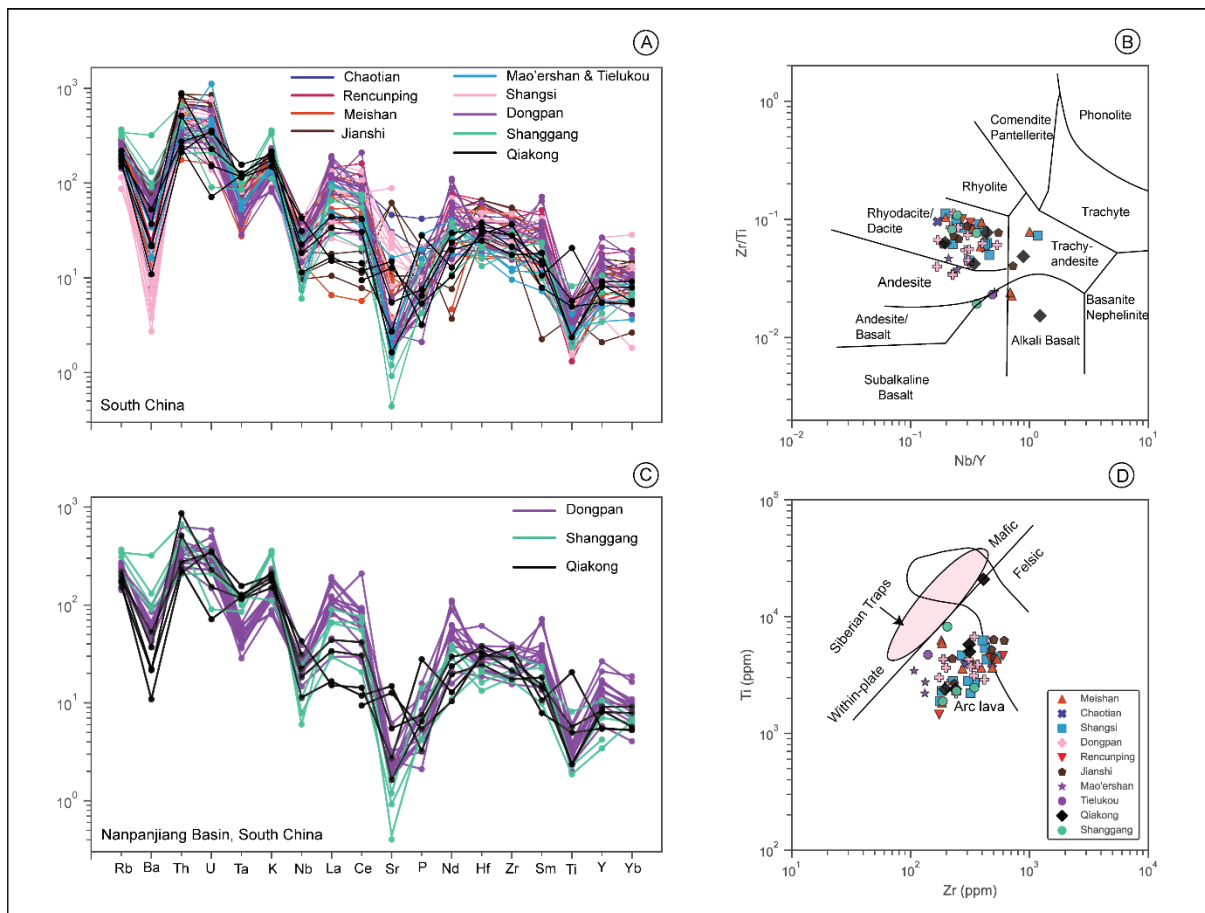


Figure 5. Major element and trace element composition of volcanic ash samples from Qiakong and Shanggang. A, B) Primitive mantle-normalized spider diagram comparing incompatible trace element concentrations for Olenekian (Smithian and Spathian) volcanic ashes from the studied sections compared with Changhsingian to Induan volcanic ashes from other localities in South China. Data for other sections in South China are from (He et al., 2014; Wang et al., 2019b; Zhao et al., 2021; Song et al., 2022). Primitive mantle normalization values are from (Sun and McDonough, 1989). C) Zr/Ti vs Nb/Y classification diagram (Winchester and Floyd, 1977) for volcanic ashes from the Nanpanjiang Basin and other localities in South China. D) Ti vs Zr tectonic setting classification diagram (Pearce,

1982) for the volcanic ash samples from the current study compared with other volcanic ash samples from South China. The field labelled Siberian Traps in D) is after He et al. (2014).

4.4 Strontium and Neodymium isotopes

Smithian to Spathian $^{87}\text{Sr}/^{86}\text{Sr}$ values for WMJ and JA fall within the global Olenekian range of $^{87}\text{Sr}/^{86}\text{Sr}$ values (i.e., 0.70759 – 0.70848, Martin and Macdougall, 1995; Sedlacek et al., 2014; Song et al., 2015). Values are generally lower for WMJ ($0.707556 \pm 6.0 \times 10^{-6}$ to $0.708005 \pm 7.1 \times 10^{-6}$) than JA ($0.707922 \pm 1.2 \times 10^{-5}$ to $0.708202 \pm 1.3 \times 10^{-5}$). For both JA and WMJ, $^{87}\text{Sr}/^{86}\text{Sr}$ values are generally characterized by an increasing trend between the Smithian and Spathian (from $0.707835 \pm 5.0 \times 10^{-6}$ to $0.708005 \pm 7.1 \times 10^{-6}$). However, this trend is punctuated by slightly lower values around the Smithian – Spathian boundary (SSB; Fig. 3). For WMJ, $\epsilon_{\text{Nd}(t)}$ values are between -7.5 ± 0 and -5.7 ± 0.6 except sample WMJ 1 which has a value of -3.0 ± 0.6 . $\epsilon_{\text{Nd}(t)}$ values for JA have a range between -7.0 ± 0.1 and -1.1 ± 0.1 , with the highest values recorded in the latest Smithian (Fig. 3). Notably, both WMJ and JA record an increase in $\epsilon_{\text{Nd}(t)}$ values in the latest Smithian, which for JA coincides with decreasing $^{87}\text{Sr}/^{86}\text{Sr}$ values (Fig. 3A).

4.5 Mineralogical compositions

XRD analyses indicate that QIA samples are predominantly composed of calcite, phyllosilicates, quartz, and plagioclase feldspar, with average proportions of 66 %, 16 %, 12 %, and 4 %, respectively. Rare occurrences of minerals such as pyrite, dolomite and ankerite are also recorded (Fig. 6). The mineralogical composition of QIA samples is consistent with the mixed carbonate and siliciclastic lithological make-up of this section. In contrast with QIA, samples from the Oman exotics contain about 95 % calcite. For JA, samples comprise on average 98 % calcite and variable proportions of quartz and phyllosilicates. WMJ samples contain, on average, 94 % calcite and variable proportions of quartz and phyllosilicates.

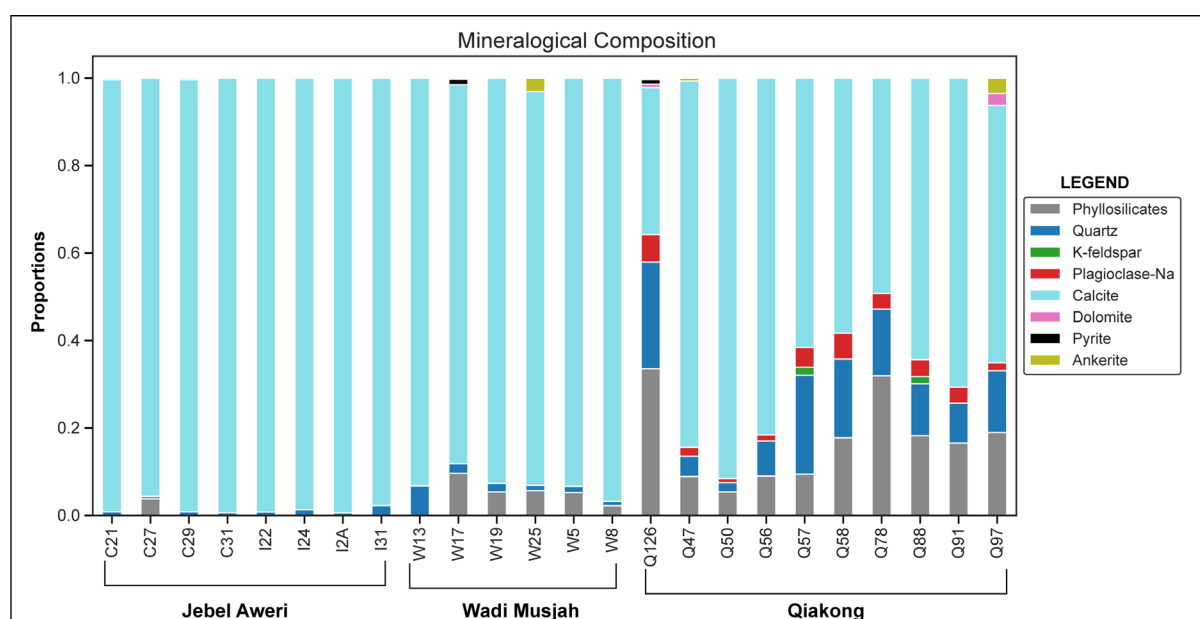


Figure 6. Semi-quantitative estimation of the main mineral constituents of rock samples from the studied successions in Jebel Aweri and Wadi Musjah (Oman) and Qiakong (South China).

5. Discussion

5.1 Assessing the preservation of the $\delta^{13}\text{C}$ and Hg records

The preservation of the rock successions in the studied sections are evaluated to assess the reliability of their Hg and $\delta^{13}\text{C}$ records. TOC measurements indicate that the majority of analyzed material is characterized by low OM content (section 4.2). Low TOC contents may be due to primary limited burial of organic matter in the sediments or may have resulted from post-depositional oxidation of OM in these successions. The Oman exotic block successions (i.e., WMJ and JA) were probably characterized by very limited initial terrestrial OM content owing to their offshore paleo-depositional environment. Hence, any OM in these successions would probably have been marine. For the Nanpanjiang Basin sections – QIA and SHA, the source and preservation of OM can be evaluated using the Rock-Eval pyrolysis data. Analyzed samples with high OM content plot within the field of kerogen type III, corresponding to a terrestrial OM source (Espitalié et al., 1985). However, the high T_{max} values for most samples ($n = 49/66$) suggests that OI and HI values have been altered by burial diagenesis (Fig. 7B), complicating the interpretation of OM source for these successions based on these values only. Nevertheless, the low HI values for samples with > 0.2 wt.% TOC (Fig. 7) may indicate that SHA and QIA are predominantly characterized by terrestrial OM, a mixture of terrestrial and oxidized marine OM or that these successions comprise completely reworked OM (Espitalié et al., 1985; Fantasia et al., 2018). Terrestrial OM contribution to the South China sections is supported by the presence of woody particles in QIA (Widmann et al., 2020). Also, the moderate but significant correlation between TOC and Al for SHA (Fig. 4F) supports terrestrial OM contribution to this succession. However, this correlation can also be explained by lithology (e.g., mudstone yielding higher TOC values). Thus, a dominant OM source for these successions cannot be confidently inferred.

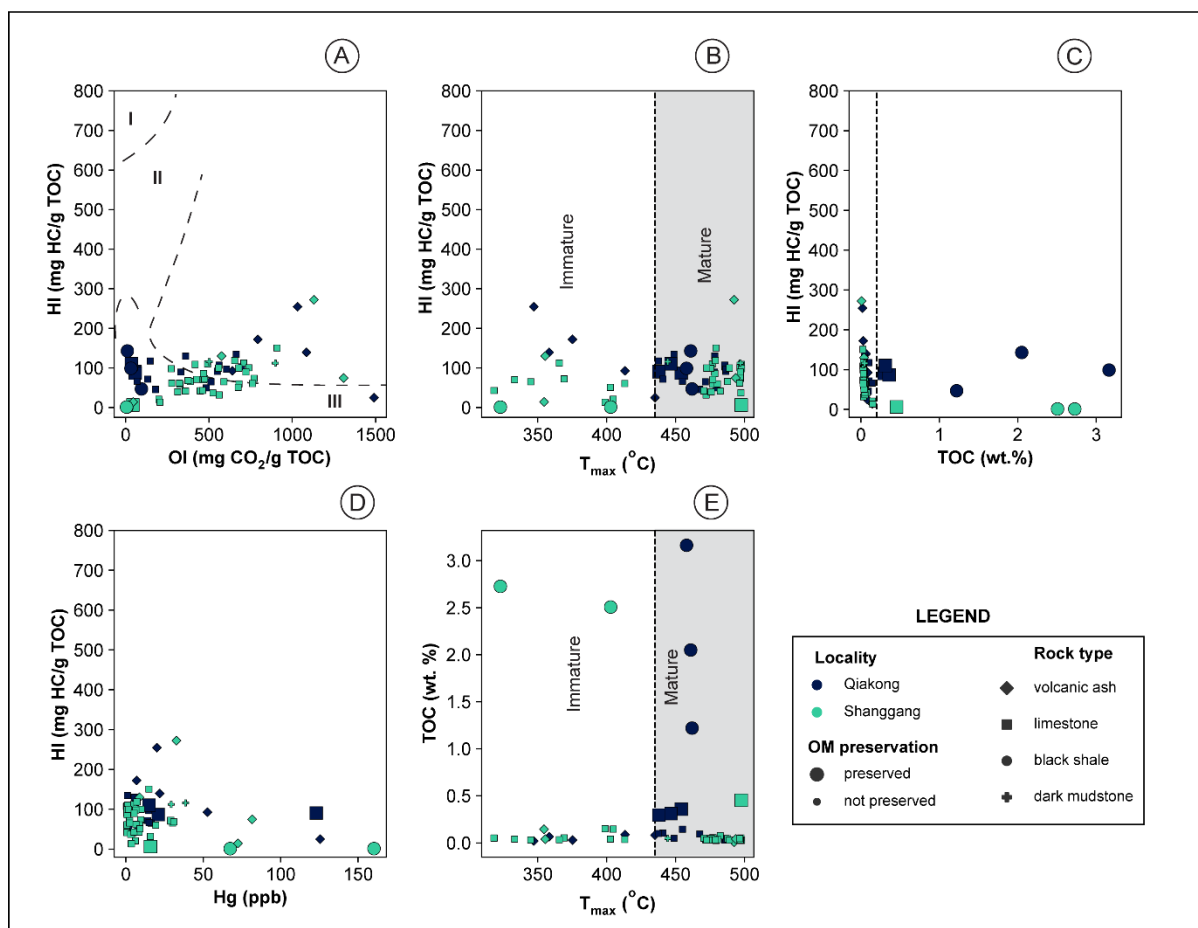


Figure 7. Scatterplot of Rock-Eval pyrolysis data for Qiakong and Shanggang. A) HI vs. OI, B) HI vs. T_{max}, C) HI vs. TOC. Dashed black line denotes the 0.2 wt.% TOC preservation limit (Grasby et al., 2016), D) HI vs. Hg, E) TOC vs. T_{max}. Samples interpreted to have preserved organic matter have TOC > 0.2 wt.%. OM = organic matter.

Despite the poor preservation (or lack) of OM in the studied sections, the $\delta^{13}\text{C}$ values and Hg concentrations from these sedimentary successions are interpreted to be primary. This is because the $\delta^{13}\text{C}$ trends (carbonate and organic carbon) and range in absolute values for the studied successions are consistent with those for other Tethyan Smithian to Spathian sedimentary successions (e.g., Tong et al., 2007; Song et al., 2013). Notably, we find that the global early to middle Smithian negative carbon isotope excursion (CIE) and the positive CIE characteristic of the SSB (N3 and P3, respectively; Song et al., 2013) are recorded in both organic carbon and carbonate carbon isotope records. The reproducibility of the Smithian $\delta^{13}\text{C}$ trends in both organic and carbonate carbon supports the argument that the documented geochemical records for these successions are primary.

Similar to the $\delta^{13}\text{C}$ record, Hg anomalies that variably span the middle Smithian to SSB are known from both Tethyan and Boreal sedimentary successions (e.g., Grasby et al., 2016; Hammer et al., 2019; Shen et al., 2019a; Wang et al., 2019a). Thus, the spatial reproducibility of Hg enrichment in Smithian rocks globally argues against the possibility that our documented Hg trends can be explained by diagenetic

alteration of the studied rocks. Furthermore, there is no correlation between HI and TOC or Hg (Fig. 7), suggesting that the Hg record is not affected to any significant degree by organic matter type or preservation. Therefore, both the CIEs and Hg anomalies recorded in these sections are interpreted as reflecting environmental perturbations that affected the carbon and mercury cycles during the Smithian-Spathian transition.

5.2 High-resolution correlation of the Tethyan Smithian-Spathian Hg records

Biostratigraphical correlations based on conodont unitary association zones (UAZ) for sections from Oman and South China recently published by Leu et al. (2022; 2023), together with precise and accurate U-Pb zircon ages for QIA and SHA (Widmann et al., 2020), enable a high-resolution correlation of the geochemical records presented in the current study (Fig. 8). For QIA, the Hg anomaly spans conodont UAZ 6 to UAZ 8, while the positive CIE spans UAZ 7 to UAZ 9. For SHA, the presence of a hiatus at the SSB precludes a determination of the precise onset of the SSB positive CIE (Fig. 8B). Nevertheless, it is apparent that the onset of the positive CIE is younger than UAZ 6 (ca. 249.330 ± 0.100 Ma) and that the CIE climaxes within UAZ 9 (ca. 249.088 ± 0.073 Ma), similar to QIA (Fig. 8). The SHA Hg record indicates that Hg peaks are recorded between UAZ 5 and UAZ 7 (i.e., between 250.116 ± 0.085 Ma and 249.330 ± 0.100 Ma, Widmann et al., 2020), indicating that the onset of Hg enrichment for SHA was earlier than for QIA (Fig. 8). Unlike the South China successions, the Hg enrichment interval recorded for JA is restricted to a brief stratigraphic interval, i.e., UAZ 3 of Oman, which corresponds to the interval of separation between UAZs 7 and 8 of South China (Fig. 8). The SSB positive CIE for JA, however, is stratigraphically extended, spanning UAZs 1 to 5 (which corresponds to UAZs 6 to 9 of South China; Leu et al., 2023). For both QIA and SHA, the onset of the Smithian Hg anomaly predates the onset of the global SSB positive CIE. However, the opposite is true for JA. Therefore, the Hg anomalies recorded for these Tethyan sites are temporally discordant, opening the possibility that they may derive from unrelated causes.

Divergence in onset between the SSB positive CIE and Smithian Hg anomalies is documented for other sections in the PaleoTethys (e.g., North Pingdingshan, Zuodeng), the NeoTethys (e.g., Guryul Ravine, Mud) and Panthalassa (e.g., Festningen, Jesmond, Smith Creek) (Fig. 9; see also Grasby et al., 2013b; Grasby et al., 2016; Shen et al., 2019a; Wang et al., 2019a). These observations indicate that the record of Hg anomalies in Smithian to Spathian marine successions is variable in both timing (onset) and duration. In the case of SHA, the offset between the onset of Smithian Hg anomalies and the SSB positive CIE is about 700 kyr (Fig. 8). Thus, the variability in the timing/stratigraphic occurrence of Smithian Hg anomalies contrasts with the carbon isotope record, for which the stratigraphic occurrence of Early Triassic excursions seems to match globally (Zhang et al., 2019). Consequently, Smithian Hg anomalies may be indicative of local patterns of Hg sequestration, which may be unrelated to the causes of the associated CIEs.

5.3 Hosts of Hg and interpretation of the Hg anomaly

5.3.1 Sedimentary hosts of Hg in QIA & SHA

Volcanic eruptions are recognized as the dominant natural source of Hg to the environment (Pyle and Mather, 2003). However, a direct link between volcanic activity and anomalous Hg content in sedimentary strata cannot be assumed. This is because enhanced Hg sequestration in rocks can also occur via non-volcanic means (e.g., Hammer et al., 2019; Them II et al., 2019; Shen et al., 2019b). Also, Hg enrichment in sedimentary successions may result from variations in the abundance of sedimentary host phases of Hg (Shen et al., 2019b; 2020). Spearman's rank correlation analysis indicates a moderate but significant correlation between Hg and TOC for both SHA and QIA (SHA: $\rho = 0.57$, $p = 0.00$, QIA: $\rho = 0.72$, $p = 0.00$), suggesting a significant influence of organic matter availability on Hg sequestration for both sites (Fig. 4A). In addition, a significant correlation between Hg and Al is noted for SHA, as well as between Hg and U for QIA and SHA (Fig. 4). These correlations suggest that both lithology and OM content modulated Hg sequestration for these successions. Nevertheless, the persistence of the Hg anomaly upon Hg/TOC normalization (where TOC > 0.2 wt.% for both QIA and SHA) suggests that Hg enrichment recorded for these successions cannot be explained by OM availability only. Furthermore, although amounts of Hg sequestered appears to be lower in carbonate-rich but OM-poor strata), the recorded Hg anomalies relative to background values are recorded in nodular limestone, shale, and volcanic ash samples alike, just to different degrees (Fig. 2, Fig. S4).

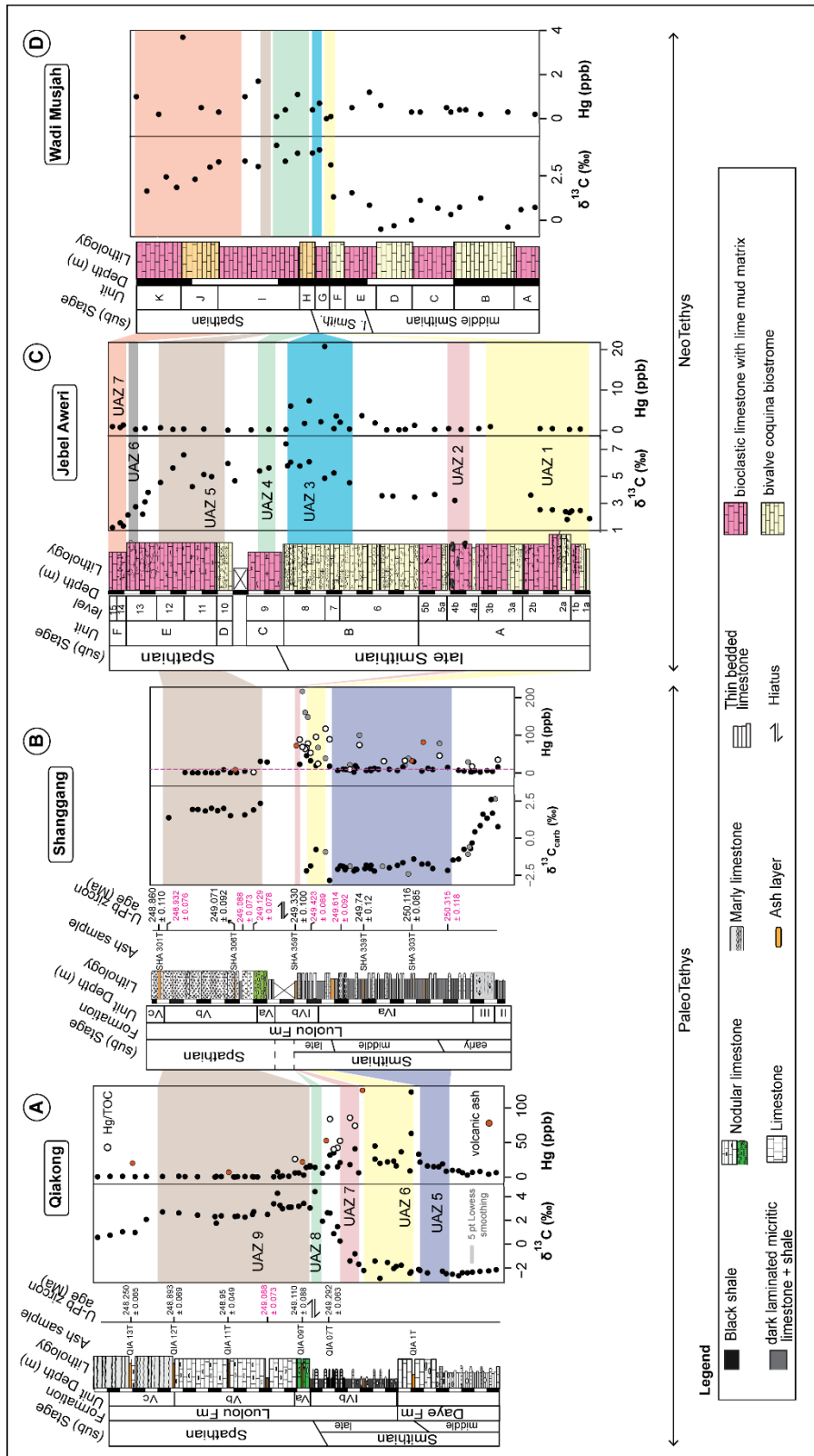


Figure 8. Carbon isotope ($\delta^{13}\text{C}$) and mercury records correlated across the studied sections. $\delta^{13}\text{C}$ data, stratigraphic log and U-Pb zircon ages for Qiakong and Shanggang are from Widmann et al. (2020). $\delta^{13}\text{C}$ data for Jebel Aweri and Wadi Musjah sections is from Leu et al. (2023). Correlation of the sections follows Leu et al. (2023) and is based on U-Pb zircon ages and conodont unitary association zones.

5.3.2 Interpretation of the South China Hg anomaly

Mercury has a complex biogeochemical cycle and can be deposited in the environment via several pathways (Selin, 2009). Different studies indicate that upon initial emission from volcanoes, Hg has no measurable MIF (Zambardi et al., 2009; Sun et al., 2016; Si et al., 2020), in agreement with estimates of the $\Delta^{199}\text{Hg}$ value of the primitive mantle (Moynier et al., 2021). However, during Hg biogeochemical cycling, diagnostic patterns of isotopic variation are imparted by different processes (such as volatilization, photoreduction and methylation), allowing for the use of Hg isotope ratios to decipher the sources and pathways of Hg deposition (Blum et al., 2014; Yin et al., 2014; but see also Grasby et al., 2019; Percival et al., 2021 and Yager et al., 2021 for a review). Hg in sedimentary rocks that are deposited in marine depositional environments far away from land (or with limited terrigenous input) are usually characterized by positive $\Delta^{199}\text{Hg}$ values, reflective of a dominantly atmospheric Hg input source (Blum et al., 2014; Sun et al., 2019; Yager et al., 2021). In contrast, marine successions deposited closer to land usually have Hg with negative $\Delta^{199}\text{Hg}$ values, which is consistent with Hg input from terrestrial biomass (Yager et al., 2021; Yin et al., 2022). Furthermore, a record of near zero Hg MIF in sedimentary successions may indicate that Hg in these rocks was sourced from different reservoirs having complementary MIF values that average to near zero (c.f. Blum et al., 2014).

Near zero $\Delta^{199}\text{Hg}$ values recorded for QIA and slightly positive values for SHA are consistent with direct volcanic Hg emissions and/or a mixture of Hg contributions from terrestrial biomass and atmospheric Hg inputs to the Nanpanjiang Basin during the studied interval. The late Smithian of the Nanpanjiang Basin is characterized by a 622 ± 137 kyr period of black shale deposition (Widmann et al., 2020), which suggests elevated terrigenous flux to the Nanpanjiang Basin during this interval. Owing to characteristically negative $\Delta^{199}\text{Hg}$ values for terrestrial biomass, it is reasonable to expect negative $\Delta^{199}\text{Hg}$ values (or a trend to less positive $\Delta^{199}\text{Hg}$ values) within the interval of black shale deposition. However, both SHA and QIA are characterized by near zero to slightly positive $\Delta^{199}\text{Hg}$ values during the Smithian (Fig. 2). In addition, volcanic ashes with no MIF, which show similar Hg concentration trends with interbedded rocks, occur within the late Smithian Hg enrichment interval (Fig. 2). These observations suggest that both QIA and SHA were characterized by atmospheric Hg input, probably from a proximal volcanic Hg source. Similar observations have recently been documented for Permian-Triassic boundary sections in South China (Edward et al., 2023b). Furthermore, an atmospheric volcanic Hg source to the Nanpanjiang Basin during the Smithian is supported by slightly negative $\Delta^{200}\text{Hg}$ values recorded for some samples from SHA (Fig. 2), which are comparable to those reported for gaseous elemental Hg^0 from atmospheric samples by Rolison et al. (2013). Consequently, the Hg isotope MIF record supports a scenario whereby Hg in these Nanpanjiang Basin sections was sourced from direct atmospheric deposition from volcanic emissions. The trend towards more positive $\Delta^{199}\text{Hg}$ values for SHA from the middle Smithian to early Spathian, despite

elevated late Smithian detrital flux further supports our inference that atmospherically cycled Hg from volcanic activity dominated Hg input to the Nanpanjiang Basin during this interval.

Potential candidates for volcanically sourced Hg to the Nanpanjiang Basin during the Olenekian include renewed STLIP volcanism and subduction-related arc volcanism in the Tethys region. Renewed volcanism of the STLIP has been suggested as an explanation for environmental and climatic perturbation during the Early Triassic (e.g., Payne and Kump, 2007; Paton et al., 2010; Grasby et al., 2013a), as well as for Hg anomalies recorded in Olenekian strata (Grasby et al., 2016; Shen et al., 2019a). However, no tangible proof of purported STLIP volcanism during the Smithian has been found so far (Grasby et al., 2013b; Hammer et al., 2019; Shen et al., 2019a; Widmann et al., 2020). Furthermore, U-Pb zircon age constraint for our Smithian-Spathian Hg records (Fig. 8; Widmann et al., 2020) indicates that the Smithian Hg anomalies recorded in the Nanpanjiang Basin post-date the youngest dated STLIP rocks (ca. 250.3 Ma; Augland et al., 2019). In contrast with renewed STLIP volcanism, direct evidence for near-field volcanic activity in the Tethys region is provided by abundant volcanic ash layers in Smithian to Spathian strata in South China (Galfetti et al., 2007b; Gilder et al., 2008; Ovtcharova et al., 2015; Widmann et al., 2020). These volcanic ashes have similar Hg concentration trends as interbedded Smithian rocks and are also characterized by near zero Hg isotope MIF (Fig. 2). Hence, it is reasonable to suggest that the volcanic effusions that supplied these volcanic ashes was the same as that supplying Hg to the Nanpanjiang Basin during the Smithian – Spathian.

Volcanic ash samples from QIA and SHA are geochemically distinct from STLIP rocks but similar to Permian to Triassic-aged volcanic ashes from other localities in South China (Fig. 5). These ashes plot within the field of rhyodacite/dacite and trachyandesite on a Zr/Ti vs Nb/Y discrimination diagram (Winchester and Floyd, 1977), consistent with the composition of Early Triassic volcanic rocks that outcrop in southern South China (Gilder et al., 2008). The ashes are characterized by notable negative Nb, Ta and Ti anomalies on the primitive mantle-normalized incompatible trace elements plot (Fig. 5A, 5B), consistent with a subduction zone provenance (Pearce et al., 1995). Also, these ash samples plot within the field of arc lavas on the Ti vs Zr diagram (Fig. 5D; Pearce, 1982). As such, QIA and SHA volcanic ashes derive from subduction-related arc volcanism (He et al., 2014), which is documented for the South China region during the Early Triassic (Zi et al., 2013; Duan et al., 2020; Duan et al., 2023). Subduction-related arc volcanism can result in the release of large amounts of volatiles, including Hg, into the atmosphere (Lu et al., 2021; Shen et al., 2021; Zhang et al., 2021), consistent with the frequent occurrence of volcanic ashes in Olenekian strata within South China (Ovtcharova et al., 2006; Widmann et al., 2020). Consequently, it is concluded that subduction-related arc volcanism in the Tethys region was the source of volcanic Hg to the Nanpanjiang Basin during the studied interval.

5.3.3 Interpretation of the Jebel Aweri Hg enrichment interval

Low amounts of OM and absence of a correlation between Hg and Al, as well as redox proxy elements such as Mo and U (Fig. 4), precludes an evaluation of the control of sedimentary Hg hosts on Hg sequestration in the JA succession. The late Smithian Hg enrichment interval for JA is presumably related to factors other than enhanced availability of sedimentary Hg host phases. Furthermore, Hg content in this carbonate succession is generally too low for Hg extraction for isotopic analysis. Despite the generally low Hg content in JA samples, a Hg enrichment interval is inferred because it is expected that this succession be characterized by near zero Hg content owing to its pure carbonate mineralogical composition and depositional environment. The JA succession was deposited on an offshore seamount (Leu et al., 2023), limiting the potential for terrestrial Hg input to this succession (also evidenced by near zero Al and TOC contents, Fig 4). Also, well-oxygenated depositional environments which are usually impoverished with regards to preserved organic matter and sulfides, and with low clay mineral content, can be expected to have limited Hg sequestration ability (Percival et al., 2018). Hence, considering the depositional setting and mineralogical composition of the JA succession, the Hg enrichment recorded in this succession is significant and unlikely to be sourced from terrestrial runoff. This inference is further compatible with relatively lower $^{87}\text{Sr}/^{86}\text{Sr}$ values across the interval of Hg enrichment (Fig. 3A), which is opposite of the trend expected during periods of enhanced continental weathering input to the oceans. Although considered only a minor source of Hg to the ocean, hydrothermal vents associated with mid-oceanic ridges may be locally important Hg sources to specific sites (Bowman et al., 2020; Racki, 2020; Sanei et al., 2021). Paleogeographic reconstructions for the Early Triassic after the Panalesis model (Fig. 1B; V  rard, 2019) suggest that the WMJ and JA successions were deposited along a hotspot track close to a mid-oceanic ridge. Also, the trend of higher (more radiogenic) $\epsilon_{\text{Nd}(t)}$ values recorded around the SSB for JA and WMJ (Fig. 3) is consistent with mantle fluxes to these NeoTethyan sites (Bizimis and Scher, 2016). Alternatively, Hg enrichment recorded for JA may be due to nearby submarine volcanic activity (e.g., Scaife et al., 2017; Jones et al., 2019; Racki, 2020). Hence, the latest Smithian Hg enrichment recorded for JA, and positive $\epsilon_{\text{Nd}(t)}$ excursions for WMJ and JA around the SSB (Fig. 3) are compatible with hydrothermal fluid or submarine volcanic Hg input to these offshore seamount carbonate depositional environments. Inferred hydrothermal/submarine volcanic Hg input to JA during the late Smithian is further supported by plume-related magmatic activity associated with late Paleozoic to Triassic rifting of the Gondwana and Cimmerian blocks (  ng  r et al., 1984; Stampfli et al., 1991; Chauvet et al., 2008), which was likely associated with hydrothermal fluid circulation in the NeoTethys. The absence of a corresponding Hg enrichment interval for WMJ may indicate that inferred hydrothermal Hg input to NeoTethyan offshore seamount depositional environments during the late Smithian was locally restricted. Alternatively, the existence of a late Smithian Hg enrichment interval for WMJ may be hidden due to the very condensed nature of this carbonate succession.

5.4 Correlation and provenance of global Smithian to Spathian Hg records

The $\delta^{13}\text{C}$ record of the middle Smithian to early Spathian interval is well constrained, in that several studies show that this interval is globally marked by a large negative excursion (N3, middle Smithian to early late Smithian), which is succeeded by a large positive excursion (P3) spanning the late Smithian to earliest Spathian (Galfetti et al., 2007b; Tong et al., 2007; Song et al., 2013; Zhang et al., 2019). Hence, the $\delta^{13}\text{C}$ trends may be used as a stratigraphic marker to evaluate the timing of other geochemical excursions that may be recorded in coeval strata. In expanded marine sections, the N3 and P3 excursions are usually separated by an interval of nearly uniform $\delta^{13}\text{C}$ values (Fig. 9), as can be observed from $\delta^{13}\text{C}$ records for Guryul Ravine (Wang et al., 2019a), Mud (Shen et al., 2019a), Yashan (Du et al., 2022), Laren, Qiakong, and Shanggang (Widmann et al., 2020; Dai et al., 2021; Leu et al., 2022). In sharp contrast, the N3 CIE abruptly grades into the late Smithian P3 CIE in some other marine sections such as the North Pingdingshan (Tong et al., 2007), Mingtang (Song et al., 2013), Festningen (Grasby et al., 2016), Wallenbergfjellet (Hammer et al., 2019), Wadi Musjah (Leu et al., 2023), Jesmond (Shen et al., 2019a), and Smith Creek sections (Grasby et al., 2013a), among others. This abrupt transition from N3 to P3 in many sections is strongly suggestive of a late Smithian hiatus (Hammer et al., 2019), a detail that is important when comparing geochemical records between spatially dispersed Smithian to Spathian-aged successions.

Mercury anomalies within Smithian to Spathian strata from both high and low-latitude marine successions have been documented by different workers (e.g., Grasby et al., 2013b; Grasby et al., 2016; Hammer et al., 2019; Shen et al., 2019a; Wang et al., 2019a) and are summarized in Figure 9. Shen et al. (2019) documented Smithian Hg anomalies from marine successions straddling the Smithian-Spathian boundary and found that these Hg enrichments coincide with a Smithian negative CIE (N3; Song et al., 2013). These authors argued that the recorded middle Smithian Hg anomalies resulted from STLIP volcanic activity during the Smithian, similar to previous suggestions by Grasby et al. (2013b; 2016) based on Hg records from the Festningen and Smith Creek sections. In contrast, Wang et al. (2019a) recorded a Hg anomaly (not reflected in Hg/TOC ratios) for both the middle Smithian and SSB for one (Chaohu section, South China) of two investigated sections, concluding that any potential renewed STLIP volcanism probably only affected the northern hemisphere. For the Chaohu section, Wang et al., (2019a) document elevated middle Smithian Hg/TOC ratios coincident with a negative CIE (N3) but also late Smithian enrichments coincident with the SSB positive CIE (P3). The global occurrence of Hg anomalies within middle and late Smithian strata, therefore, suggests that the middle to late Smithian interval was characterized by elevated Hg supply to and/or sequestration in Smithian oceans. Nevertheless, a comparison of these Hg records indicates that Smithian Hg anomalies vary in their stratigraphic occurrence between different sections (Fig. 9). Specifically, Smithian Hg anomalies variably correspond stratigraphically to the peak of the N3 CIE or the onset of the P3 CIE (Fig. 9), suggesting that the cause(s) of the global carbon cycle perturbations are not directly related to the

stratigraphically variable Hg anomalies. Despite the widespread occurrence of middle to late Smithian Hg anomalies, available evidence indicates that these Hg anomalies differ in provenance. For the South China region, our results, together with those from previous studies (e.g., Shen et al., 2019a; Wang et al., 2019a), suggest that middle to late Smithian Hg anomalies are most likely due to a combination of regional subduction-related volcanism and enhanced terrigenous flux to marine environments presumably due to elevated continental weathering.

Smithian to Spathian increase in continental weathering is supported by the bioapatite $^{87}\text{Sr}/^{86}\text{Sr}$ record for WMJ, which shows a secular increasing trend from the middle Smithian to Spathian (Fig. 3), consistent with previously published Early Triassic $^{87}\text{Sr}/^{86}\text{Sr}$ records (e.g., Sedlacek et al., 2014; Song et al., 2015). While there is direct evidence for Smithian volcanism in South China, the same cannot be said for other regions. Apart from the Guryul Ravine and West Pingdingshan (Chaohu) sections (Wang et al., 2019a), previously published Smithian–Spathian Hg records lack Hg isotope data, inhibiting more detailed investigation of the provenance of Smithian Hg anomalies documented for these sites. However, for the high-latitude Wallenbergfjellet section, Spitsbergen, Hammer et al. (2019) recently demonstrated that the middle to late Smithian Hg/TOC anomaly recorded for this section is attributable to a change in OM type from terrestrial to marine OM. Furthermore, based on the correlation between Hg and Al, as well as Hg isotope compositions, recorded increases in Smithian Hg/TOC ratios for Chaohu and Guryul Ravine sections were attributed to increased terrestrial Hg flux to Tethyan marine depositional environments during the Early Triassic (Wang et al., 2019a). Variable provenance for Smithian Hg anomalies is further supported by the Smithian Hg enrichment recorded for JA, which can be attributed to submarine volcanic or hydrothermal fluid activity. Therefore, the causes of Hg anomalies recorded during the Smithian vary for different localities. This view is further strengthened by the variability in onset, duration, and magnitude of recorded Smithian Hg anomalies (Fig. 9; Widmann et al., 2020).

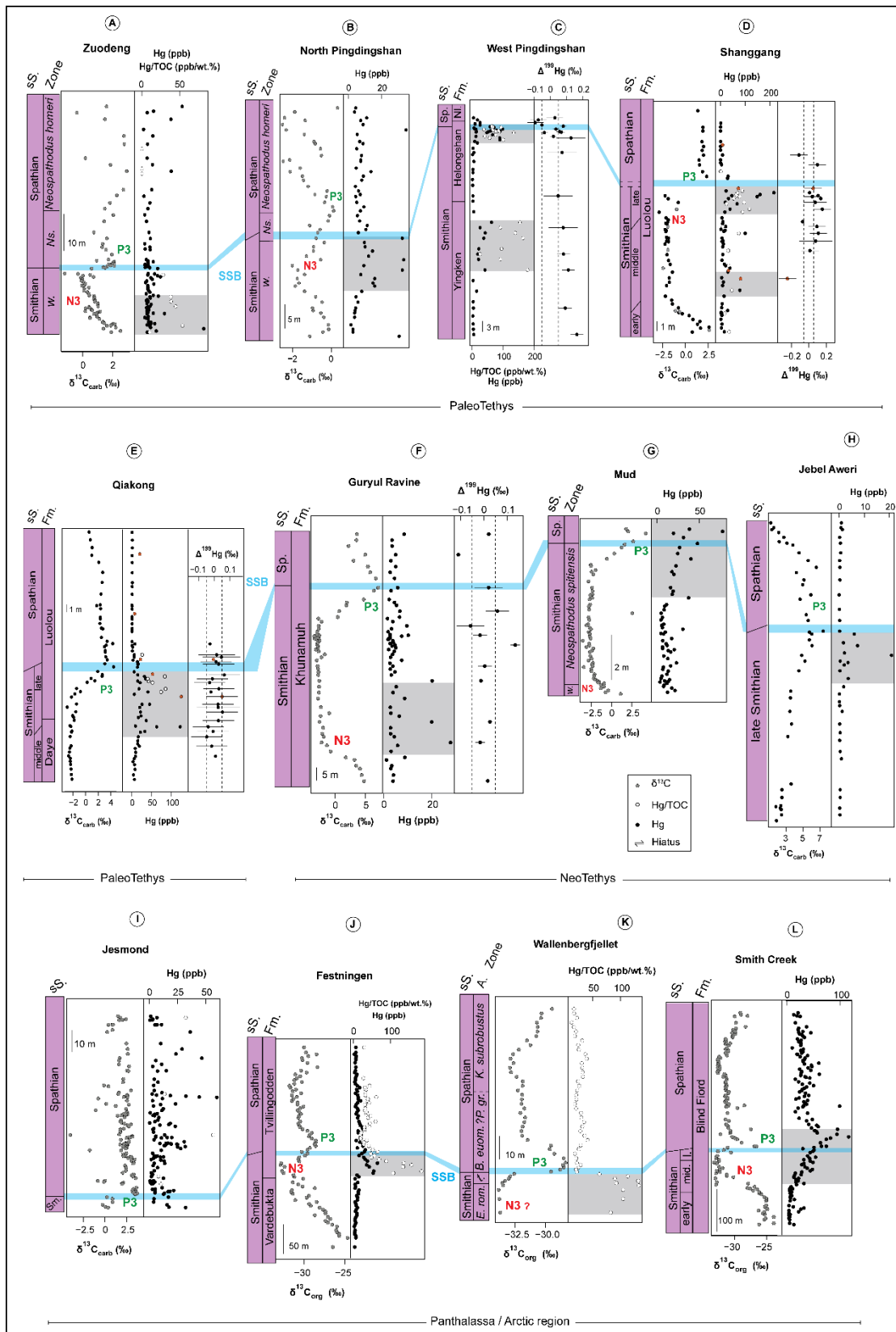


Figure 9. Compilation of Smithian – Spathian mercury and $\delta^{13}\text{C}$ profiles from Tethyan and Boreal sections. A) Zuodeng, B) North Pingdingshan, C) West Pingdingshan, D) Shanggang, E) Qiakong, F) Guryul Ravine, G) Mud, H) Jebel Aweri, I) Jesmond, J) Festningen, K) Wallenbergfjellet, L) Smith

Creek. Hg/TOC profiles are only included where reported Hg/TOC values are > 0.2 wt.%. The sections are correlated using the Smithian-Spathian boundary (SSB) as originally delineated by the authors of the source publications. The horizontal blue band is an uncertainty interval for the placement of the SSB for our correlation. For Festningen, the SSB is delineated by taking the mid-point of the N3 to P3 carbon isotope excursion after Zhang et al. (2019). Data sources are as follows: Guryul Ravine, West Pingdingshan: Wang et al. (2019a); Mud, Zuodeng, North Pingdingshan, Jesmond: Shen et al. (2019a); Wallenbergfjellet: Hammer et al. (2019); Festningen: Grasby et al. (2016); Smith Creek: Grasby et al. (2013a; 2013b). Abbreviations: sS. – sub-Stage, Fm. – Formation, Sp. – Spathian, Sm. – Smithian, mid. – middle, l. – late, Nl. – Nanlinghu, A. – Ammonoid, *w.* – *Novispathodus waageni*, *Ns.* – *Novispathodus pingdingshanensis*, *t.* – *Wasatchites tardus*, *E. rom.* – *Euflemingites romunderi*, *B. euom.* – *Bajarunia euomphala*, *P. gr.* – *Parasibirites grambergi*.

6. Conclusion

The temporally calibrated Hg concentration and Hg-, C-, Sr- and Nd-isotope records and other geochemical data for NeoTethyan and PaleoTethyan successions presented in the current study allows for an assessment of the tempo of global Hg sequestration, as well as an evaluation of Hg input sources to the studied successions during the Olenekian. Based on the presented results, the following conclusions are made:

- 1) The middle Smithian to late Smithian of the Nanpanjiang Basin, South China is characterized by enhanced Hg sequestration recorded by Hg enrichment intervals.
- 2) The Hg enrichment intervals recorded for these PaleoTethyan sections predate the onset of the SSB positive CIE recorded globally.
- 3) The Hg enrichment can be attributed mainly to volcanic Hg input from regional subduction-related arc-volcanism and potential contributions from terrestrial Hg reservoirs to the Nanpanjiang Basin.
- 4) The late Smithian Hg enrichment recorded for the JA succession can be attributed to hydrothermal fluid activity or submarine volcanism proximal to the offshore seamount depositional environment. Thus, the presence of a Hg enrichment interval across both carbonate-poor and carbonate-rich Smithian-aged strata in the PaleoTethys and NeoTethys suggests that although lithology may exert an overarching control on the magnitude of Hg sequestration, marine sedimentary rocks do record primary trends of excess Hg loading to the environment.
- 5) Smithian Hg anomalies recorded for spatially dispersed localities vary in stratigraphic expression, variably coinciding with either a negative or positive CIE and as such, probably record local Hg sequestration patterns. Consequently, Smithian-Spathian Hg anomalies, although recorded in several localities globally, are of variable provenance and cannot be linked to a singular source such as renewed STLIP volcanism during the Smithian to Spathian.

Acknowledgements

This study was funded by a Swiss National Science Foundation Sinergia Grant (project nr. CRSII5_180253). SLH gratefully acknowledges financial support by the University of Geneva (S18173). Field assistance by Kuang Guodun and Ji Cheng is gratefully acknowledged. Jun Shen (CUG, Wuhan) is thanked for providing the raw data for his 2019 Earth Science Reviews paper. We also thank Jorge Spangenberg, Jerome Chmeleff, Massimo Chiaradia, and Sophie Michalet for analytical assistance. The authors wish to thank Sofie Lindström and one anonymous reviewer for their constructive comments which improved the manuscript. Efficient editorial handling of this manuscript by the Editor, Maoyan Zhu, is gratefully acknowledged.

Data Availability

Datasets related to this article can be found at <https://dx.doi.org/10.17632/vg9sy4k8jf.2>, an open-source online data repository hosted at Mendeley Data (Edward et al. 2023a).

References

- Adatte, T., Stinnesbeck, W., Keller, G., 1996. Lithostratigraphic and mineralogic correlations of near K/T boundary clastic sediments in northeastern Mexico: implications for origin and nature of deposition. *Geol. Soc. Am. Spec. Pap* 307, 211-226.
- Augland, L.E., Ryabov, V.V., Vernikovskiy, V.A., Planke, S., Polozov, A., Callegaro, S., Jerram, D.A., Svensen, H., 2019. The main pulse of the Siberian Traps expanded in size and composition. *Scientific Reports* 9, 1-12 DOI: 10.1038/s41598-019-54023-2.
- Bagherpour, B., Bucher, H., Baud, A., Brosse, M., Vennemann, T., Martini, R., Guodun, K., 2017. Onset, development, and cessation of basal Early Triassic microbialites (BETM) in the Nanpanjiang pull-apart Basin, South China Block. *Gondwana Res* 44, 178-204 DOI: 10.1016/j.gr.2016.11.013.
- Bagherpour, B., Bucher, H., Vennemann, T., Schneebeli-Hermann, E., Yuan, D.X., Leu, M., Zhang, C., Shen, S.Z., 2020. Are Late Permian carbon isotope excursions of local or of global significance? *Geological Society of America Bulletin* 132, 521-544 DOI: 10.1130/B31996.1.
- Baud, A., 2013. The Olenekian (early Triassic) Red Ammonoid Limestone, a time-specific facies on the Gondwana margin: Timor-Roof of the World-Oman connection. *Acta Geologica Sinica* 87, 894-931 DOI: https://doi.org/10.1111/1755-6724.12150_2.
- Baud, A., Béchenec, F., Krystyn, L., Le Métour, J., Marcoux, J., Maury, R., Richoz, S., 2001. Permo-Triassic Deposits: from the Platform to the Basin and Seamounts. Conference on the Geology of Oman, Field guidebook, Excursion A01, Conference on the Geology of Oman, Field guidebook, Excursion A01, pp. 1-54 DOI: <https://www.researchgate.net/publication/236624812>.
- Baud, A., Marcoux, J., Guiraud, R., Ricou, L., Gaetani, M., 1993. Late Murgabian (266 to 264 Ma) Paleoenvironment Map, Explanatory Notes. Paris: Gauthier-Villars.
- Baud, A., Richoz, S., Beauchamp, B., Cordey, F., Grasby, S., Henderson, C.M., Krystyn, L., Nicora, A., 2012. The Buday'ah Formation, Sultanate of Oman: A Middle Permian to Early Triassic oceanic record of the Neotethys and the late Induan microsphere bloom. *Journal of Asian Earth Sciences* 43, 130-144 DOI: 10.1016/j.jseas.2011.08.016.
- Behar, F., Beaumont, V., Penteado, H.L.D., 2001. Rock-Eval 6 technology: Performances and developments. *Oil Gas Sci Technol* 56, 111-134 DOI: 10.2516/ogst:2001013.
- Bizimis, M., Scher, H.D., 2016. Neodymium Isotopes, in: White, W.M. (Ed.), *Encyclopedia of Geochemistry: A Comprehensive Reference Source on the Chemistry of the Earth*. Springer International Publishing, Cham, pp. 1-6.
- Blum, J.D., Bergquist, B.A., 2007. Reporting of variations in the natural isotopic composition of mercury. *Anal Bioanal Chem* 388, 353-359 DOI: 10.1007/s00216-007-1236-9.
- Blum, J.D., Sherman, L.S., Johnson, M.W., 2014. Mercury Isotopes in Earth and Environmental Sciences. *Annual Review of Earth and Planetary Sciences*, Vol 42 42, 249-269 DOI: 10.1146/annurev-earth-050212-124107.
- Bowman, K.L., Lamborg, C.H., Agather, A.M., 2020. A global perspective on mercury cycling in the ocean. *Science of The Total Environment* 710, 136166 DOI: <https://doi.org/10.1016/j.scitotenv.2019.136166>.
- Brayard, A., Bucher, H., 2015. Permian-Triassic Extinctions and Rediversifications, in: Klug, C., Korn, D., De Baets, K., Kruta, I., Mapes, R.H. (Eds.), *Ammonoid Paleobiology: From macroevolution to paleogeography*. Springer Netherlands, Dordrecht, pp. 465-473.

Brayard, A., Escarguel, G., Bucher, H., Monnet, C., Brühwiler, T., Goudemand, N., Galfetti, T., Guex, J., 2009. Good Genes and Good Luck: Ammonoid Diversity and the End-Permian Mass Extinction. *Science* 325, 1118-1121 DOI: 10.1126/science.1174638.

Brosse, M., Bucher, H., Baud, A., Frisk, A.M., Goudemand, N., Hagdorn, H., Nutzelt, A., Ware, D., Hautmann, M., 2019. New data from Oman indicate benthic high biomass productivity coupled with low taxonomic diversity in the aftermath of the Permian-Triassic Boundary mass extinction. *Lethaia* 52, 165-187 DOI: 10.1111/let.12281.

Brühwiler, T., Bucher, H., Goudemand, N., Galfetti, T., 2012. Smithian (Early Triassic) ammonoid faunas from Exotic Blocks from Oman: taxonomy and biochronology. *Palaeontographica. Abteilung A: Palaeozoologie-Stratigraphie* 296, 3-107 DOI: 10.1127/pala/296/2012/3.

Caro, G., Bourdon, B., Birck, J.-L., Moorbath, S., 2006. High-precision $^{142}\text{Nd}/^{144}\text{Nd}$ measurements in terrestrial rocks: constraints on the early differentiation of the Earth's mantle. *Geochimica et Cosmochimica Acta* 70, 164-191 DOI: <https://doi.org/10.1016/j.gca.2005.08.015>.

Charbonnier, G., Adatte, T., Föllmi, K.B., Suan, G., 2020. Effect of Intense Weathering and Postdepositional Degradation of Organic Matter on Hg/TOC Proxy in Organic-rich Sediments and its Implications for Deep-Time Investigations. *Geochemistry Geophysics Geosystems* 21, e2019GC008707 DOI: 10.1029/2019GC008707.

Charbonnier, G., Morales, C., Duchamp-Alphonse, S., Westermann, S., Adatte, T., Föllmi, K.B., 2017. Mercury enrichment indicates volcanic triggering of Valanginian environmental change. *Scientific Reports* 7, 1-6 DOI: 10.1038/srep40808.

Chauvet, F., Lapierre, H., Bosch, D., Guillot, S., Mascle, G., Vannay, J.-C., Cotten, J., Brunet, P., Keller, F., 2008. Geochemistry of the Panjal Traps basalts (NW Himalaya): records of the Pangea Permian break-up. *Bulletin de la Société géologique de France* 179, 383-395 DOI: 10.2113/gssgfbull.179.4.383.

Chen, D., Ren, D., Deng, C., Tian, Z., Yin, R., 2022. Mercury loss and isotope fractionation during high-pressure and high-temperature processing of sediments: Implication for the behaviors of mercury during metamorphism. *Geochimica et Cosmochimica Acta* 334, 231-240 DOI: 10.1016/j.gca.2022.08.010.

Chen, Z.-Q., Benton, M.J., 2012. The timing and pattern of biotic recovery following the end-Permian mass extinction. *Nature Geoscience* 5, 375-383 DOI: 10.1038/ngeo1475.

Dai, X., Yuan, Z.W., Brayard, A., Li, M.T., Liu, X.K., Jia, E.H., Du, Y., Song, H.Y., Song, H.J., 2021. Calibrating the late Smithian (Early Triassic) crisis: New insights from the Nanpanjiang Basin, South China. *Global and Planetary Change* 201, 103492 DOI: 10.1016/j.gloplacha.2021.103492.

Du, Y., Zhu, Y., Corso, J.D., Huang, J., Qiu, H., Song, H., Tian, L., Chu, D., Tong, J., Song, H., 2022. New Early Triassic marine $\delta^{13}\text{C}$ record from the northeastern Yangtze Platform: Implications for contemporaneous temperature changes and volcanic eruptions. *Palaeogeography, Palaeoclimatology, Palaeoecology* 607, 111270 DOI: <https://doi.org/10.1016/j.palaeo.2022.111270>.

Duan, L., Christie-Blick, N., Meng, Q.R., Wu, G.L., Yang, Z., Wang, B., 2023. A back-arc transtensional origin for the Nanpanjiang basin in the pre-Norian Triassic, with implications for the broader intracontinental development of South China. *Basin Research* 35, 551-571 DOI: <https://doi.org/10.1111/bre.12722>.

Duan, L., Meng, Q.-R., Wu, G.-L., Yang, Z., Wang, J., Zhan, R., 2020. Nanpanjiang basin: A window on the tectonic development of south China during Triassic assembly of the southeastern and eastern Asia. *Gondwana Res* 78, 189-209 DOI: <https://doi.org/10.1016/j.gr.2019.08.009>.

[Dataset] Edward, Oluwaseun; Bucher, Hugo ; Leu, Marc; Le Houedec, Sandrine; Blattmann, Franziska; V  rard, Christian; Adatte, Thierry; Baud, Aymon; Sonke, Jeroen; Vennemann, Torsten (2023a), "Dataset for "Evidence for Variable Provenance of Mercury Anomalies During the Smithian–Spathian (Olenekian)" ", Mendeley Data, V2, doi: 10.17632/vg9sy4k8jf.2

Edward, O., Paul, A.N., Bucher, H., V  rard, C., Adatte, T., Sonke, J.E., Schaltegger, U., Vennemann, T., 2023b. Timing and Provenance of Volcanic Fluxes Around the Permian-Triassic Boundary Mass Extinction in South China: U-Pb Zircon Geochronology, Volcanic Ash Geochemistry and Mercury Isotopes. *Geochemistry, Geophysics, Geosystems* 24, e2023GC010912 DOI: <https://doi.org/10.1029/2023GC010912>.

Enos, P., Lehrmann, D.J., Jiayong, W., Youyi, Y., Jiafei, X., Chaikin, D.H., Minzoni, M., Berry, A.K., Montgomery, P., 2006. Triassic Evolution of the Yangtze Platform in Guizhou Province, People's Republic of China, in: Enos, P., Lehrmann, D.J., Jiayong, W., Youyi, Y., Jiafei, X., Chaikin, D.H., Minzoni, M., Berry, A.K., Montgomery, P. (Eds.), *Triassic Evolution of the Yangtze Platform in Guizhou Province, People's Republic of China*. Geological Society of America, p. 0.

Erwin, D.H., Bowring, S.A., Yogan, J., 2002. End-Permian mass extinctions: A review, in: Koeberl, C., MacLeod, K.G. (Eds.), *Catastrophic events and mass extinctions: impacts and beyond*. Geological Society of America, p. 0.

Espitali  , J., Deroo, G., Marquis, F., 1985. La pyrolyse Rock-Eval et ses applications. *Rev. Inst. Fr. P  tr* 40, 563-579 DOI: <https://doi.org/10.2516/ogst:1985035>.

Fantasia, A., F  llmi, K.B., Adatte, T., Bern  rdez, E., Spangenberg, J.E., Mattioli, E., 2018. The Toarcian Oceanic Anoxic Event in southwestern Gondwana: an example from the Andean Basin, northern Chile. *Journal of the Geological Society* 175, 883-902 DOI: 10.1144/jgs2018-008.

Foster, W.J., Sebe, K., 2017. Recovery and diversification of marine communities following the late Permian mass extinction event in the western Palaeotethys. *Global and Planetary Change* 155, 165-177 DOI: <https://doi.org/10.1016/j.gloplacha.2017.07.009>.

Friesenbichler, E., Hautmann, M., Bucher, H., 2021. The main stage of recovery after the end-Permian mass extinction: Taxonomic rediversification and ecologic reorganization of marine level-bottom communities during the Middle Triassic. *PeerJ* 9, e11654 DOI: 10.7717/peerj.11654.

Galfetti, T., Bucher, H., Brayard, A., Hochuli, P.A., Weissert, H., Guodun, K., Atudorei, V., Guex, J., 2007a. Late Early Triassic climate change: insights from carbonate carbon isotopes, sedimentary evolution and ammonoid paleobiogeography. *Palaeogeography, Palaeoclimatology, Palaeoecology* 243, 394-411 DOI: <https://doi.org/10.1016/j.palaeo.2006.08.014>.

Galfetti, T., Bucher, H., Martini, R., Hochuli, P.A., Weissert, H., Crasquin-Soleau, S., Brayard, A., Goudemand, N., Br  hwiler, T., Guodun, K., 2008. Evolution of Early Triassic outer platform paleoenvironments in the Nanpanjiang Basin (South China) and their significance for the biotic recovery. *Sedimentary Geology* 204, 36-60 DOI: 10.1016/j.sedgeo.2007.12.008.

Galfetti, T., Bucher, H., Ovtcharova, M., Schaltegger, U., Brayard, A., Br  hwiler, T., Goudemand, N., Weissert, H., Hochuli, P.A., Cordey, F., 2007b. Timing of the Early Triassic carbon cycle perturbations inferred from new U–Pb ages and ammonoid biochronozones. *Earth and Planetary Science Letters* 258, 593-604.

Gilder, S.A., Tan, X., Bucher, H., Kuang, G., Yin, J., 2008. Optimization of apparent polar wander paths: An example from the South China plate. *Physics of the Earth and Planetary Interiors* 169, 166-177 DOI: <https://doi.org/10.1016/j.pepi.2008.07.016>.

- Goudemand, N., Romano, C., Leu, M., Bucher, H., Trotter, J.A., Williams, I.S., 2019. Dynamic interplay between climate and marine biodiversity upheavals during the early Triassic Smithian - Spathian biotic crisis. *Earth-Science Reviews* 195, 169-178 DOI: <https://doi.org/10.1016/j.earscirev.2019.01.013>.
- Grasby, S.E., Beauchamp, B., Bond, D.P., Wignall, P.B., Sanei, H., 2016. Mercury anomalies associated with three extinction events (Capitanian crisis, latest Permian extinction and the Smithian/Spathian extinction) in NW Pangea. *Geological magazine* 153, 285-297 DOI: <https://doi.org/10.1017/S0016756815000436>.
- Grasby, S.E., Beauchamp, B., Embry, A., Sanei, H., 2013a. Recurrent early triassic ocean anoxia. *Geology* 41, 175-178 DOI: 10.1130/G33599.1.
- Grasby, S.E., Sanei, H., Beauchamp, B., Chen, Z., 2013b. Mercury deposition through the Permo-Triassic biotic crisis. *Chemical Geology* 351, 209-216 DOI: <https://doi.org/10.1016/j.chemgeo.2013.05.022>.
- Grasby, S.E., Them II, T.R., Chen, Z., Yin, R., Ardakani, O.H., 2019. Mercury as a proxy for volcanic emissions in the geologic record. *Earth-Science Reviews*, 102880 DOI: <https://doi.org/10.1016/j.earscirev.2019.102880>.
- Hammer, Ø., Jones, M.T., Schneebeli-Hermann, E., Hansen, B.B., Bucher, H., 2019. Are Early Triassic extinction events associated with mercury anomalies? A reassessment of the Smithian/Spathian boundary extinction. *Earth-Science Reviews* 195, 179-190 DOI: 10.1016/j.earscirev.2019.04.016.
- Hauser, M., Martini, R., Matter, A., Krystyn, L., Peters, T., Stampfli, G., Zaninetti, L., 2002. The break-up of East Gondwana along the northeast coast of Oman: evidence from the Batain basin. *Geological Magazine* 139, 145-157 DOI: 10.1017/S0016756801006264.
- Hautmann, M., Bagherpour, B., Brosse, M., Frisk, Å., Hofmann, R., Baud, A., Nützel, A., Goudemand, N., Bucher, H., 2015. Competition in slow motion: the unusual case of benthic marine communities in the wake of the end-Permian mass extinction. *Palaeontology* 58, 871-901 DOI: 10.1111/pala.12186.
- He, B., Zhong, Y.T., Xu, Y.G., Li, X.H., 2014. Triggers of Permo-Triassic boundary mass extinction in South China: The Siberian Traps or Paleo-Tethys ignimbrite flare-up? *Lithos* 204, 258-267 DOI: 10.1016/j.lithos.2014.05.011.
- Hermann, E., Hochuli Peter, A., Bucher, H., Brühwiler, T., Hautmann, M., Ware, D., Weissert, H., Roohi, G., Yaseen, A., Khalil-ur-Rehman, N., 2012. Climatic oscillations at the onset of the Mesozoic inferred from palynological records from the North Indian Margin. *Journal of the Geological Society* 169, 227-237 DOI: 10.1144/0016-76492010-130.
- Hochuli, P.A., Sanson-Barrera, A., Schneebeli-Hermann, E., Bucher, H., 2016. Severest crisis overlooked—Worst disruption of terrestrial environments postdates the Permian-Triassic mass extinction. *Scientific Reports* 6, 28372 DOI: 10.1038/srep28372.
- Hong, H., Algeo, T.J., Fang, Q., Zhao, L., Ji, K., Yin, K., Wang, C., Cheng, S., 2019. Facies dependence of the mineralogy and geochemistry of altered volcanic ash beds: An example from Permian-Triassic transition strata in southwestern China. *Earth-Science Reviews* 190, 58-88 DOI: <https://doi.org/10.1016/j.earscirev.2018.12.007>.
- Immenhauser, A., Schreurs, G., Peters, T., Matter, A., Hauser, M., Dumitrică, P., 1998. Stratigraphy, sedimentology and depositional environments of the Permian to uppermost Cretaceous Batain Group. *Eclogae Geologicae Helvetiae* 91, 217-236 DOI: 10.7892/boris.87096.

Jiskra, M., Heimbürger-Boavida, L.E., Desgranges, M.M., Petrova, M.V., Dufour, A., Ferreira-Araujo, B., Masbou, J., Chmeleff, J., Thyssen, M., Point, D., Sonke, J.E., 2021. Mercury stable isotopes constrain atmospheric sources to the ocean. *Nature* 597, 678-682 DOI: 10.1038/s41586-021-03859-8.

Jiskra, M., Sonke, J.E., Agnan, Y., Helmig, D., Obrist, D., 2019. Insights from mercury stable isotopes on terrestrial-atmosphere exchange of Hg(0) in the Arctic tundra. *Biogeosciences* 16, 4051-4064 DOI: <https://doi.org/10.5194/bg-16-4051-2019>.

Jones, M.T., Percival, L.M.E., Stokke, E.W., Frieling, J., Mather, T.A., Riber, L., Schubert, B.A., Schultz, B., Tegner, C., Planke, S., Svensen, H.H., 2019. Mercury anomalies across the Palaeocene–Eocene Thermal Maximum. *Clim. Past* 15, 217-236 DOI: 10.5194/cp-15-217-2019.

Kübler, B., 1983. Dosage quantitatif des minéraux majeurs des roches sédimentaires par diffraction X. *Cahiers de l'Institut de Géologie Series AX*, 1-13.

Lapierre, H., Samper, A., Bosch, D., Maury, R.C., Béchenec, F., Cotten, J., Demant, A., Brunet, P., Keller, F., Marcoux, J., 2004. The Tethyan plume: geochemical diversity of Middle Permian basalts from the Oman rifted margin. *Lithos* 74, 167-198 DOI: <https://doi.org/10.1016/j.lithos.2004.02.006>.

Lehrmann, D.J., Donghong, P., Enos, P., Minzoni, M., Ellwood, B.B., Orchard, M.J., Jiyan, Z., Jiayong, W., Dillett, P., Koenig, J., 2007. Impact of differential tectonic subsidence on isolated carbonate-platform evolution: Triassic of the Nanpanjiang Basin, south China. *AAPG bulletin* 91, 287-320 DOI: 10.1306/10160606065.

Lehrmann, D.J., Jiayong, W., Enos, P., 1998. Controls on facies architecture of a large Triassic carbonate platform; the Great Bank of Guizhou, Nanpanjiang Basin, South China. *Journal of Sedimentary Research* 68, 311-326 DOI: 10.2110/jsr.68.311.

Leu, M., Bucher, H., Baud, A., Vennemann, T., Luz, Z., Hautmann, M., Goudemand, N., 2023. An expanded Smithian–Spathian (Lower Triassic) boundary from a reefal build-up record in Oman: implications for conodont taxonomy, high-resolution biochronology and the carbon isotope record. *Papers in Palaeontology* 9, e1481 DOI: <https://doi.org/10.1002/spp2.1481>.

Leu, M., Bucher, H., Goudemand, N., 2019. Clade-dependent size response of conodonts to environmental changes during the late Smithian extinction. *Earth-Science Reviews* 195, 52-67 DOI: 10.1016/j.earscirev.2018.11.003.

Leu, M., Bucher, H., Vennemann, T., Bagherpour, B., Ji, C., Brosse, M., Goudemand, N., 2022. A Unitary Association-based conodont biozonation of the Smithian–Spathian boundary (Early Triassic) and associated biotic crisis from South China. *Swiss Journal of Palaeontology* 141, 19 DOI: 10.1186/s13358-022-00259-x.

Lindström, S., Bjerager, M., Alsen, P., Sanei, H., Bojesen-Koefoed, J., 2020. The Smithian–Spathian boundary in North Greenland: implications for extreme global climate changes. *Geological Magazine* 157, 1547-1567 DOI: 10.1017/S0016756819000669.

Lu, J., Zhou, K., Yang, M., Zhang, P., Shao, L., Hilton, J., 2021. Records of organic carbon isotopic composition ($\delta^{13}\text{C}_{\text{org}}$) and volcanism linked to changes in atmospheric $p\text{CO}_2$ and climate during the Late Paleozoic Icehouse. *Global and Planetary Change* 207, 103654 DOI: <https://doi.org/10.1016/j.gloplacha.2021.103654>.

Martin, E.E., Macdougall, J.D., 1995. Sr and Nd isotopes at the Permian/Triassic boundary: A record of climate change. *Chemical Geology* 125, 73-99 DOI: [https://doi.org/10.1016/0009-2541\(95\)00081-V](https://doi.org/10.1016/0009-2541(95)00081-V).

- McArthur, J.M., Howarth, R.J., Bailey, T.R., 2001. Strontium isotope stratigraphy: LOWESS version 3: Best fit to the marine Sr-isotope curve for 0-509 Ma and accompanying look-up table for deriving numerical age. *J Geol* 109, 155-170 DOI: 10.1086/319243.
- Moynier, F., Jackson, M.G., Zhang, K., Cai, H., Halldórsson, S.A., Pik, R., Day, J.M.D., Chen, J., 2021. The Mercury Isotopic Composition of Earth's Mantle and the Use of Mass Independently Fractionated Hg to Test for Recycled Crust. *Geophys Res Lett* 48, e2021GL094301 DOI: <https://doi.org/10.1029/2021GL094301>.
- Orchard, M.J., 2007. Conodont diversity and evolution through the latest Permian and Early Triassic upheavals. *Palaeogeography, Palaeoclimatology, Palaeoecology* 252, 93-117 DOI: <https://doi.org/10.1016/j.palaeo.2006.11.037>.
- Ovtcharova, M., Bucher, H., Schaltegger, U., Galfetti, T., Brayard, A., Guex, J., 2006. New Early to Middle Triassic U-Pb ages from South China: Calibration with ammonoid biochronozones and implications for the timing of the Triassic biotic recovery. *Earth and Planetary Science Letters* 243, 463-475 DOI: 10.1016/j.epsl.2006.01.042.
- Ovtcharova, M., Goudemand, N., Hammer, Ø., Guodun, K., Cordey, F., Galfetti, T., Schaltegger, U., Bucher, H., 2015. Developing a strategy for accurate definition of a geological boundary through radioisotopic and biochronological dating: The Early–Middle Triassic boundary (South China). *Earth-Science Reviews* 146, 65-76 DOI: <https://doi.org/10.1016/j.earscirev.2015.03.006>.
- Paton, M.T., Ivanov, A.V., Fiorentini, M.L., McNaughton, N.J., Mudrovska, I., Reznitskii, L.Z., Demonterova, E.I., 2010. Late Permian and Early Triassic magmatic pulses in the Angara–Taseeva syncline, Southern Siberian Traps and their possible influence on the environment. *Russian Geology and Geophysics* 51, 1012-1020 DOI: <https://doi.org/10.1016/j.rgg.2010.08.009>.
- Payne, J.L., Kump, L.R., 2007. Evidence for recurrent Early Triassic massive volcanism from quantitative interpretation of carbon isotope fluctuations. *Earth and Planetary Science Letters* 256, 264-277 DOI: <https://doi.org/10.1016/j.epsl.2007.01.034>.
- Payne, J.L., Lehrmann, D.J., Wei, J., Orchard, M.J., Schrag, D.P., Knoll, A.H., 2004. Large Perturbations of the Carbon Cycle During Recovery from the End-Permian Extinction. *Science* 305, 506-509 DOI: 10.1126/science.1097023.
- Pearce, J.A., 1982. Trace element characteristics of lavas from destructive plate boundaries, in: Thorpe, R.S. (Ed.), *Orogenic andesites and related rocks*. John Wiley and Sons, Chichester, England, pp. 528-548.
- Pearce, J.A., Baker, P.E., Harvey, P.K., Luff, I.W., 1995. Geochemical evidence for subduction fluxes, mantle melting and fractional crystallization beneath the South Sandwich island arc. *Journal of Petrology* 36, 1073-1109 DOI: 10.1093/petrology/36.4.1073.
- Percival, L.M., Jenkyns, H.C., Mather, T.A., Dickson, A.J., Batenburg, S.J., Ruhl, M., Hesselbo, S.P., Barclay, R., Jarvis, I., Robinson, S.A., 2018. Does large igneous province volcanism always perturb the mercury cycle? Comparing the records of Oceanic Anoxic Event 2 and the end-Cretaceous to other Mesozoic events. *Am J Sci* 318, 799-860 DOI: <https://doi.org/10.2475/08.2018.01>.
- Percival, L.M.E., Bergquist, B.A., Mather, T.A., Sanei, H., 2021. Sedimentary Mercury Enrichments as a Tracer of Large Igneous Province Volcanism, in: Richard E. Ernst, Alexander J. Dickson, Bekker, A. (Eds.), *Large Igneous Provinces*. John Wiley and Sons, Inc., pp. 247-262.

- Pilleveit, A., Marcoux, J., Stampfli, G., Baud, A., 1997. The Oman Exotics: a key to the understanding of the Neotethyan geodynamic evolution. *Geodinamica Acta* 10, 209-238 DOI: <https://doi.org/10.1080/09853111.1997.11105303>.
- Pin, C., Bassin, C., 1992. Evaluation of a strontium-specific extraction chromatographic method for isotopic analysis in geological materials. *Anal Chim Acta* 269, 249-255 DOI: [https://doi.org/10.1016/0003-2670\(92\)85409-Y](https://doi.org/10.1016/0003-2670(92)85409-Y).
- Portnyagin, M.V., Ponomareva, V.V., Zelenin, E.A., Bazanova, L.I., Pevzner, M.M., Plechova, A.A., Rogozin, A.N., Garbe-Schönberg, D., 2020. TephraKam: geochemical database of glass compositions in tephra and welded tuffs from the Kamchatka volcanic arc (northwestern Pacific). *Earth System Science Data* 12, 469-486 DOI: 10.5194/essd-12-469-2020.
- Pyle, D.M., Mather, T.A., 2003. The importance of volcanic emissions for the global atmospheric mercury cycle. *Atmos Environ* 37, 5115-5124 DOI: 10.1016/j.atmosenv.2003.07.011.
- Racki, G., 2020. A volcanic scenario for the Frasnian–Famennian major biotic crisis and other Late Devonian global changes: More answers than questions? *Global and Planetary Change* 189, 103174 DOI: <https://doi.org/10.1016/j.gloplacha.2020.103174>.
- Richoz, S., Baud, A., Beauchamp, B., Grasby, S., Henderson, C., Krystyn, L., 2014. Khuff margin: slope to oceanic deposits (Permian-Triassic Allochthons and Exotics, Oman). *The Khuff Formation: New Perspective: Houten, Netherlands, EAGE Publications* 1, 55-76.
- Richoz, S., Krystyn, L., Baud, A., Brandner, R., Horacek, M., Mohtat-Aghai, P., 2010. Permian–Triassic boundary interval in the Middle East (Iran and N. Oman): Progressive environmental change from detailed carbonate carbon isotope marine curve and sedimentary evolution. *J Asian Earth Sci* 39, 236-253 DOI: <https://doi.org/10.1016/j.jseaes.2009.12.014>.
- Rolison, J., Landing, W., Luke, W., Cohen, M., Salters, V., 2013. Isotopic composition of species-specific atmospheric Hg in a coastal environment. *Chemical Geology* 336, 37-49 DOI: <https://doi.org/10.1016/j.chemgeo.2012.10.007>.
- Romano, C., Goudemand, N., Vennemann, T.W., Ware, D., Schneebeil-Hermann, E., Hochuli, P.A., Brühwiler, T., Brinkmann, W., Bucher, H., 2013. Climatic and biotic upheavals following the end-Permian mass extinction. *Nature Geoscience* 6, 57-60 DOI: 10.1038/ngeo1667.
- Sanei, H., Outridge, P.M., Oguri, K., Stern, G.A., Thamdrup, B., Wenzhöfer, F., Wang, F., Glud, R.N., 2021. High mercury accumulation in deep-ocean hadal sediments. *Scientific Reports* 11, 10970 DOI: 10.1038/s41598-021-90459-1.
- Scaife, J.D., Ruhl, M., Dickson, A.J., Mather, T.A., Jenkyns, H.C., Percival, L.M.E., Hesselbo, S.P., Cartwright, J., Eldrett, J.S., Bergman, S.C., Minisini, D., 2017. Sedimentary Mercury Enrichments as a Marker for Submarine Large Igneous Province Volcanism? Evidence From the Mid-Cenomanian Event and Oceanic Anoxic Event 2 (Late Cretaceous). *Geochemistry, Geophysics, Geosystems* 18, 4253-4275 DOI: <https://doi.org/10.1002/2017GC007153>.
- Scharf, A., Mattern, F., Al-Wardi, M., Frijia, G., Moraetis, D., Pracejus, B., Bauer, W., Callegari, I., 2021. The Geology and Tectonics of the Jabal Akhdar and Saih Hatat Domes, Oman Mountains. *Geological Society of London* DOI: 10.1144/M54.
- Schreurs, G., Immenhauser, A., 1999. West-northwest directed obduction of the Batain Group on the eastern Oman continental margin at the Cretaceous-Tertiary boundary. *Tectonics* 18, 148-160 DOI: <https://doi.org/10.1029/1998TC900020>.

Sedlacek, A.R., Saltzman, M.R., Algeo, T.J., Horacek, M., Brandner, R., Foland, K., Denniston, R.F., 2014. $^{87}\text{Sr}/^{86}\text{Sr}$ stratigraphy from the Early Triassic of Zal, Iran: Linking temperature to weathering rates and the tempo of ecosystem recovery. *Geology* 42, 779-782.

Selin, N.E., 2009. Global Biogeochemical Cycling of Mercury: A Review. *Annu Rev Env Resour* 34, 43-63 DOI: 10.1146/annurev.environ.051308.084314.

Şengör, A.M.C., Yılmaz, Y., Sungurlu, O., 1984. Tectonics of the Mediterranean Cimmerides: nature and evolution of the western termination of Palaeo-Tethys. Geological Society, London, Special Publications 17, 77-112 DOI: 10.1144/GSL.SP.1984.017.01.04.

Shen, J., Algeo, T.J., Planavsky, N.J., Yu, J.X., Feng, Q.L., Song, H.J., Song, H.Y., Rowe, H., Zhou, L., Chen, J.B., 2019a. Mercury enrichments provide evidence of Early Triassic volcanism following the end-Permian mass extinction. *Earth-Science Reviews* 195, 191-212 DOI: 10.1016/j.earscirev.2019.05.010.

Shen, J., Algeo, T.J., Chen, J., Planavsky, N.J., Feng, Q., Yu, J., Liu, J., 2019b. Mercury in marine Ordovician/Silurian boundary sections of South China is sulfide-hosted and non-volcanic in origin. *Earth and Planetary Science Letters* 511, 130-140 DOI: <https://doi.org/10.1016/j.epsl.2019.01.028>

Shen, J., Chen, J., Algeo, T.J., Feng, Q., Yu, J., Xu, Y.-G., Xu, G., Lei, Y., Planavsky, N.J., Xie, S., 2021. Mercury fluxes record regional volcanism in the South China craton prior to the end-Permian mass extinction. *Geology* 49, 452-456 DOI: 10.1130/G48501.1.

Shen, J., Feng, Q.L., Algeo, T.J., Liu, J.L., Zhou, C.Y., Wei, W., Liu, J.S., Them, T.R., Gill, B.C., Chen, J.B., 2020. Sedimentary host phases of mercury (Hg) and implications for use of Hg as a volcanic proxy. *Earth and Planetary Science Letters* 543, 116333 DOI: 10.1016/j.epsl.2020.116333.

Si, M., McLagan, D.S., Mazot, A., Szponar, N., Bergquist, B., Lei, Y.D., Mitchell, C.P.J., Wania, F., 2020. Measurement of Atmospheric Mercury over Volcanic and Fumarolic Regions on the North Island of New Zealand Using Passive Air Samplers. *Acs Earth Space Chem* 4, 2435-2443 DOI: 10.1021/acsearthspacechem.0c00274.

Smith, A.G., Smith, D.G., Funnell, B.M., 2004. Atlas of Mesozoic and Cenozoic coastlines. Cambridge University Press.

Song, H., Tong, J., Algeo, T.J., Horacek, M., Qiu, H., Song, H., Tian, L., Chen, Z.-Q., 2013. Large vertical $\delta^{13}\text{C}_{\text{DIC}}$ gradients in Early Triassic seas of the South China craton: Implications for oceanographic changes related to Siberian Traps volcanism. *Global and Planetary Change* 105, 7-20 DOI: <https://doi.org/10.1016/j.gloplacha.2012.10.023>.

Song, H., Wignall, P.B., Tong, J., Song, H., Chen, J., Chu, D., Tian, L., Luo, M., Zong, K., Chen, Y., Lai, X., Zhang, K., Wang, H., 2015. Integrated Sr isotope variations and global environmental changes through the Late Permian to early Late Triassic. *Earth and Planetary Science Letters* 424, 140-147 DOI: <https://doi.org/10.1016/j.epsl.2015.05.035>.

Song, Q., Hong, H., Algeo, T.J., Fang, Q., Zhao, C., Liu, C., Xu, Y., 2022. Clay mineralogy mediated by pH and chemical weathering intensity of Permian–Triassic boundary K-bentonites at Dongpan (Guangxi, South China). *Chemical Geology*, 121262 DOI: 10.1016/j.chemgeo.2022.121262.

Sonke, J.E., Schafer, J., Chmeleff, J., Audry, S., Blanc, G., Dupre, B., 2010. Sedimentary mercury stable isotope records of atmospheric and riverine pollution from two major European heavy metal refineries. *Chemical Geology* 279, 90-100 DOI: 10.1016/j.chemgeo.2010.09.017.

- Spangenberg, J.E., Herlec, U., 2006. Hydrocarbon biomarkers in the Topla-Mezica zinc-lead deposits, northern Karavanke/Drau range, Slovenia: paleoenvironment at the site of ore formation. *Economic Geology* 101, 997-1021 DOI: <https://doi.org/10.2113/gsecongeo.101.5.997>.
- Stampfli, G., Marcoux, J., Baud, A., 1991. Tethyan margins in space and time. *Palaeogeography, Palaeoclimatology, Palaeoecology* 87, 373-409 DOI: [https://doi.org/10.1016/0031-0182\(91\)90142-E](https://doi.org/10.1016/0031-0182(91)90142-E).
- Stampfli, G.M., 2000. Tethyan oceans. Geological Society, London, Special Publications 173, 1-23 DOI: [doi:10.1144/GSL.SP.2000.173.01.01](https://doi.org/10.1144/GSL.SP.2000.173.01.01).
- Stampfli, G.M., Hochard, C., V  rard, C., Wilhem, C., vonRaumer, J., 2013. The formation of Pangea. *Tectonophysics* 593, 1-19 DOI: <https://doi.org/10.1016/j.tecto.2013.02.037>.
- Stanley, S.M., 2009. Evidence from ammonoids and conodonts for multiple Early Triassic mass extinctions. *Proceedings of the National Academy of Sciences* 106, 15264-15267 DOI: [10.1073/pnas.0907992106](https://doi.org/10.1073/pnas.0907992106).
- Stanley, S.M., 2016. Estimates of the magnitudes of major marine mass extinctions in earth history. *Proceedings of the National Academy of Sciences* 113, E6325-E6334 DOI: [10.1073/pnas.1613094113](https://doi.org/10.1073/pnas.1613094113).
- Sun, R., Enrico, M., Heimbürger, L.E., Scott, C., Sonke, J.E., 2013. A double-stage tube furnace--acid-trapping protocol for the pre-concentration of mercury from solid samples for isotopic analysis. *Anal Bioanal Chem* 405, 6771-6781 DOI: [10.1007/s00216-013-7152-2](https://doi.org/10.1007/s00216-013-7152-2).
- Sun, R., Sonke, J.E., Heimb  rger, L.-E., Belkin, H.E., Liu, G., Shome, D., Cukrowska, E., Liousse, C., Pokrovsky, O.S., Streets, D.G., 2014. Mercury stable isotope signatures of world coal deposits and historical coal combustion emissions. *Environmental science & technology* 48, 7660-7668 DOI: <https://doi.org/10.1021/es501208a>.
- Sun, R., Streets, D.G., Horowitz, H.M., Amos, H.M., Liu, G., Perrot, V., Toutain, J.-P., Hintelmann, H., Sunderland, E.M., Sonke, J.E., 2016. Historical (1850–2010) mercury stable isotope inventory from anthropogenic sources to the atmosphere. *Mercury isotope emission inventory. Elementa: Science of the Anthropocene* 4 DOI: [10.12952/journal.elementa.000091](https://doi.org/10.12952/journal.elementa.000091).
- Sun, R.Y., Jiskra, M., Amos, H.M., Zhang, Y.X., Sunderland, E.M., Sonke, J.E., 2019. Modelling the mercury stable isotope distribution of Earth surface reservoirs: Implications for global Hg cycling. *Geochimica Et Cosmochimica Acta* 246, 156-173 DOI: [10.1016/j.gca.2018.11.036](https://doi.org/10.1016/j.gca.2018.11.036).
- Sun, S.-S., McDonough, W.F., 1989. Chemical and isotopic systematics of oceanic basalts: implications for mantle composition and processes. Geological Society, London, Special Publications 42, 313-345 DOI: [10.1144/GSL.SP.1989.042.01.1](https://doi.org/10.1144/GSL.SP.1989.042.01.1).
- Sun, Y., Joachimski, M.M., Wignall, P.B., Yan, C., Chen, Y., Jiang, H., Wang, L., Lai, X., 2012. Lethally Hot Temperatures During the Early Triassic Greenhouse. *Science* 338, 366-370 DOI: [10.1126/science.1224126](https://doi.org/10.1126/science.1224126).
- Tanaka, T., Togashi, S., Kamioka, H., Amakawa, H., Kagami, H., Hamamoto, T., Yuhara, M., Orihashi, Y., Yoneda, S., Shimizu, H., Kunimaru, T., Takahashi, K., Yanagi, T., Nakano, T., Fujimaki, H., Shinjo, R., Asahara, Y., Tanimizu, M., Dragusanu, C., 2000. JNdi-1: a neodymium isotopic reference in consistency with LaJolla neodymium. *Chemical Geology* 168, 279-281 DOI: [10.1016/S0009-2541\(00\)00198-4](https://doi.org/10.1016/S0009-2541(00)00198-4).
- Them II, T., Jagoe, C., Caruthers, A., Gill, B., Grasby, S., Gr  cke, D., Yin, R., Owens, J., 2019. Terrestrial sources as the primary delivery mechanism of mercury to the oceans across the Toarcian

Oceanic Anoxic Event (Early Jurassic). *Earth and Planetary Science Letters* 507, 62-72 DOI: <https://doi.org/10.1016/j.epsl.2018.11.029>.

Tong, J.N., Zuo, J.X., Chen, Z.Q., 2007. Early Triassic carbon isotope excursions from South China: proxies for devastation and restoration of marine ecosystems following the end-Permian mass extinction. *Geological Journal* 42, 371-389 DOI: 10.1002/gj.1084.

Vérard, C., 2019. Panalexis: towards global synthetic palaeogeographies using integration and coupling of manifold models. *Geological Magazine* 156, 320-330 DOI: 10.1017/S0016756817001042.

Vickers, M.L., Jelby, M.E., Śliwińska, K.K., Percival, L.M., Wang, F., Sanei, H., Price, G.D., Ullmann, C.V., Grasby, S.E., Reinhardt, L., 2023. Volcanism and carbon cycle perturbations in the High Arctic during the Late Jurassic–Early Cretaceous. *Palaeogeography, Palaeoclimatology, Palaeoecology* 613, 111412 DOI: <https://doi.org/10.1016/j.palaeo.2023.111412>.

Wang, X., Cawood, P.A., Zhao, H., Zhao, L., Grasby, S.E., Chen, Z.-Q., Zhang, L., 2019a. Global mercury cycle during the end-Permian mass extinction and subsequent Early Triassic recovery. *Earth and Planetary Science Letters* 513, 144-155 DOI: 10.1016/j.epsl.2019.02.026.

Wang, X., Cawood, P.A., Zhao, L., Chen, Z.-Q., Lyu, Z., Ma, B., 2019b. Convergent continental margin volcanic source for ash beds at the Permian-Triassic boundary, South China: Constraints from trace elements and Hf-isotopes. *Palaeogeography, Palaeoclimatology, Palaeoecology* 519, 154-165 DOI: 10.1016/j.palaeo.2018.02.011.

Wei, H., Shen, J., Schoepfer, S.D., Krystyn, L., Richoz, S., Algeo, T.J., 2015. Environmental controls on marine ecosystem recovery following mass extinctions, with an example from the Early Triassic. *Earth-Science Reviews* 149, 108-135 DOI: <https://doi.org/10.1016/j.earscirev.2014.10.007>.

Widmann, P., Bucher, H., Leu, M., Vennemann, T., Bagherpour, B., Schneebeli-Hermann, E., Goudemand, N., Schaltegger, U., 2020. Dynamics of the largest carbon isotope excursion during the Early Triassic biotic recovery. *Front Earth Sc-Switz*, 196 DOI: <https://doi.org/10.3389/feart.2020.00196>.

Winchester, J.A., Floyd, P.A., 1977. Geochemical discrimination of different magma series and their differentiation products using immobile elements. *Chemical geology* 20, 325-343 DOI: 10.1016/0009-2541(77)90057-2.

Yager, J.A., West, A.J., Thibodeau, A.M., Corsetti, F.A., Rigo, M., Berelson, W.M., Bottjer, D.J., Greene, S.E., Ibarra, Y., Jadoul, F., Ritterbush, K.A., Rollins, N., Rosas, S., Di Stefano, P., Sulca, D., Todaro, S., Wynn, P., Zimmermann, L., Bergquist, B.A., 2021. Mercury contents and isotope ratios from diverse depositional environments across the Triassic-Jurassic Boundary: Towards a more robust mercury proxy for large igneous province magmatism. *Earth-Science Reviews* 223, 103775 DOI: 10.1016/j.earscirev.2021.103775.

Yin, R., Chen, D., Pan, X., Deng, C., Chen, L., Song, X., Yu, S., Zhu, C., Wei, X., Xu, Y., Feng, X., Blum, J.D., Lehmann, B., 2022. Mantle Hg isotopic heterogeneity and evidence of oceanic Hg recycling into the mantle. *Nature Communications* 13, 948 DOI: 10.1038/s41467-022-28577-1.

Yin, R., Feng, X., Hurley, J.P., Krabbenhoft, D.P., Lepak, R.F., Hu, R., Zhang, Q., Li, Z., Bi, X., 2016. Mercury Isotopes as Proxies to Identify Sources and Environmental Impacts of Mercury in Sphalerites. *Sci Rep* 6, 18686 DOI: 10.1038/srep18686.

Yin, R., Feng, X., Li, X., Yu, B., Du, B., 2014. Trends and advances in mercury stable isotopes as a geochemical tracer. *Trends in Environmental Analytical Chemistry* 2, 1-10 DOI: <https://doi.org/10.1016/j.teac.2014.03.001>.

Zambardi, T., Sonke, J.E., Toutain, J.P., Sortino, F., Shinohara, H., 2009. Mercury emissions and stable isotopic compositions at Vulcano Island (Italy). *Earth and Planetary Science Letters* 277, 236-243 DOI: 10.1016/j.epsl.2008.10.023.

Zhang, H., Zhang, F., Chen, J.B., Erwin, D.H., Syverson, D.D., Ni, P., Rampino, M., Chi, Z., Cai, Y.F., Xiang, L., Li, W.Q., Liu, S.A., Wang, R.C., Wang, X.D., Feng, Z., Li, H.M., Zhang, T., Cai, H.M., Zheng, W., Cui, Y., Zhu, X.K., Hou, Z.Q., Wu, F.Y., Xu, Y.G., Planavsky, N., Shen, S.Z., 2021. Felsic volcanism as a factor driving the end-Permian mass extinction. *Sci Adv* 7, eabh1390 DOI: 10.1126/sciadv.abh1390.

Zhang, L., Orchard, M.J., Brayard, A., Algeo, T.J., Zhao, L., Chen, Z.-Q., Lyu, Z., 2019. The Smithian/Spathian boundary (late Early Triassic): a review of ammonoid, conodont, and carbon-isotopic criteria. *Earth-Science Reviews*.

Zhao, Z., Li, S., Wang, G., Gao, J., Yang, T., Li, Y., He, Z., 2021. Provenance of the Permian–Triassic boundary volcanic ash beds in South China. *Geological Journal* 56, 2816-2828 DOI: 10.1002/gj.4072.

Zi, J.-W., Cawood, P.A., Fan, W.-M., Tohver, E., Wang, Y.-J., McCuaig, T.C., Peng, T.-P., 2013. Late Permian-Triassic magmatic evolution in the Jinshajiang orogenic belt, SW China and implications for orogenic processes following closure of the Paleo-Tethys. *Am J Sci* 313, 81-112 DOI: <https://doi.org/10.2475/02.2013.02>.

CHAPTER 3

Author contributions

Oluwaseun Edward: Conceptualization, Formal analysis, Data curation, Investigation, Data Analysis, Data visualization, Writing - original draft, Writing - review and editing.

Jorge E. Spangenberg: Methodology, Investigation, Validation, Resources, Writing - review and editing.

Marc Leu: Validation, Data Curation, Writing - review and editing.

Charline Ragon: Investigation, Software, Writing - review and editing.

Sandrine Le Houedec: Methodology, Investigation, Writing – review and editing

Aymon Baud: Investigation, Validation, Writing – review and editing.

Hugo Bucher: Funding Acquisition, Project Administration, Resources, Writing - review and editing.

Torsten Vennemann: Conceptualization, Funding Acquisition, Project Administration, Resources, Supervision, Writing - review and editing.

Olenekian sulfur isotope records: Deciphering global trends, links to marine redox changes and faunal evolution

Oluwaseun Edward^{a*}, Jorge E. Spangenberg^a, Marc Leu^b, Charline Ragon^c, Sandrine Le Houedec^d,
Aymon Baud^e, Hugo Bucher^b, Torsten Vennemann^a

^a Institute of Earth Surface Dynamics, University of Lausanne, Géopolis, CH-1015 Lausanne, Switzerland

^b Paläontologisches Institut der Universität Zürich, Karl-Schmid-Strasse 4, 8006 Zürich, Switzerland

^c Group of Applied Physics and Institute for Environmental Sciences, University of Geneva, Boulevard Carl Vogt 66, 1205 Geneva, Switzerland

^d Department of Earth Sciences, Université de Genève, Rue des Maraîchers 13, CH-1205 Genève, Switzerland

^e Institute of Earth Sciences, University of Lausanne, Géopolis, CH-1015 Lausanne, Switzerland

*Corresponding author | E-mail: oluwaseun.edward@unil.ch

Abstract

The sulfur (S) isotope composition of carbonate associated sulfate (CAS) in carbonate rocks has been used to assess variations in paleo-oceanographic redox conditions and its relationship to biotic changes in Earth's history, including the Smithian – Spathian transition. However, previous CAS studies of the Olenekian are mostly based on nearshore continental shelf sections and report highly variable $\delta^{34}\text{S}$ values mostly offset from those of contemporaneous evaporites, casting doubt on the utility of the CAS proxy during this interval. The current study presents new CAS isotopic data from three well-dated carbonate successions which were deposited in continental shelf (Qiakong) and offshore marine (Wadi Musjah and Jebel Aweri) environments during the Olenekian (Smithian – Spathian). The aim of the study was to constrain the temporal and spatial variations in sulfur cycling and its relation to marine redox and faunal changes across the Smithian – Spathian transition (ca. 250.5 – 248.8 Ma). The CAS dataset is complemented by rare earth element (REE) concentration data and thin section petrography. Using a suite of optical and geochemical techniques, the preservation of near-primary CAS isotopic information in the studied samples is evaluated. Results indicate that of the three sections investigated, the offshore sections mostly preserve near-primary marine sulfate S-isotope compositions while the continental shelf Qiakong section suffers from post-depositional alteration of CAS. Comparisons of our new, as well as previously published CAS $\delta^{34}\text{S}$ data, with the evaporite $\delta^{34}\text{S}$ record suggests that although Olenekian CAS $\delta^{34}\text{S}$ values may have been modified by diagenetic processes, a global and primary seawater $\delta^{34}\text{S}$ trend can be delineated as follows: seawater $\delta^{34}\text{S}$ values increased across the middle Smithian and Smithian – Spathian boundary (SSB). Based on our new CAS data, this increase was in the order of 9 ‰ over ca. 1.14 million years. Other short-term variability in the CAS $\delta^{34}\text{S}$ record most likely reflects diagenetic processes. The middle Smithian to SSB $\delta^{34}\text{S}$ increase is attributed to a global increase in microbial sulfate reduction and pyrite burial associated with decreasing ocean dissolved oxygen during this time. Calculations of the rate of sulfur cycling and box modeling constraints indicate that Olenekian marine sulfur cycle perturbations occurred while the seawater sulfate reservoir only had between 10 and 25 % of the modern marine sulfate inventory. Furthermore, results from the current study suggest that variations in ocean dissolved oxygen levels, inferred from the $\delta^{34}\text{S}$ and REE data, are not consistently correlated with nektonic faunal changes during the Olenekian in the studied sections. As such, faunal turnover during the Olenekian is unlikely to be explained exclusively by abiotic factors such as ocean-atmosphere oxygenation levels.

Keywords: sulfur isotopes, SSB, sulfur cycle, seawater sulfate, marine redox, CAS

1. Introduction

The sulfur (S) isotope composition of marine sulfate is a widely used proxy for reconstructing changes in the oxygen content of the ocean-atmosphere system, marine redox evolution, and the chemical composition of the ocean (Holser and Kaplan, 1966; Claypool et al., 1980; Berner, 1987; Strauss, 1997; Kampschulte et al., 2001; Bottrell and Newton, 2006; Turchyn and DePaolo, 2019). The sulfate ion (SO_4^{2-}) is the second most abundant anion in seawater (Millero, 2013) and serves as an electron acceptor for the anaerobic breakdown of organic matter (OM) by microbes in marine systems (Habicht and Canfield, 1996; Bottrell and Newton, 2006; Jørgensen et al., 2019). This process, commonly referred to as microbial sulfate reduction (MSR), is the most important anaerobic pathway for OM respiration in the oceans (Jørgensen, 1982). MSR produces reduced sulfur (HS^-), which in the presence of reactive iron, forms pyrite (Strauss, 1997) and together with organic carbon, is subsequently buried in marine sediments. This burial process leaves oxidized products in the ocean-atmosphere system and impacts the oxygen cycle (Berner, 1987; Halevy et al., 2012). As such, the marine sulfur cycle is connected to that of carbon and oxygen and impacts the oxygenation state of the oceans and atmosphere and hence, the ability of Earth's marine environments to support biological function and diversity. Variations in the S-isotope composition of seawater sulfate are governed by relative changes in input and output fluxes of marine sulfur, which involve the transfer of sulfur between different reservoirs (Strauss, 1997; Bottrell and Newton, 2006; Gill et al., 2007). Specifically, the input fluxes of marine sulfur (i.e., sulfide weathering, volcanic degassing) are usually ^{34}S -depleted relative to the marine sulfate pool, resulting in decreased seawater $\delta^{34}\text{S}$ as these input fluxes increase (Wortmann et al., 2001). In contrast, the output fluxes such as sulfide burial and microbial sulfate reduction (MSR) preferentially deplete ^{32}S in the marine sulfate pool, resulting in a ^{34}S enrichment of seawater sulfate (Kah et al., 2004; Stebbins et al., 2019b). Consequently, investigating the variations in the S-isotope composition of marine sulfur may help inform on the causes of ancient environmental and biotic upheavals such as during the Early Triassic (e.g., Payne et al., 2004; Galfetti et al., 2007b; Orchard, 2007; Romano et al., 2013).

Marine barites (Strauss, 1993; Paytan et al., 1998) and evaporites (Claypool et al., 1980; Cortecchi et al., 1981; Strauss, 1997) have been used to reconstruct the marine $\delta^{34}\text{S}$ evolution through geological time. However, these rocks are rare and do not permit high-resolution studies of variations in the marine $\delta^{34}\text{S}$ record (Burdett et al., 1989; Hurtgen et al., 2002; Newton et al., 2004). Marine carbonates are, however, much more common as they occur in a wide range of depositional environments. As such, the S-isotope composition of carbonate associated sulfate (CAS) – trace amounts of sulfate which substitutes for carbonate ions in carbonates (Kaplan et al., 1963) – provides a higher resolution $\delta^{34}\text{S}$ record compared to evaporites and is widely used for investigating the evolution of the marine S cycle (Burdett et al., 1989; Hurtgen et al., 2002). The utility of CAS as a proxy for marine $\delta^{34}\text{S}$ evolution is based on the understanding that CAS is in isotopic equilibrium with seawater sulfate and that there is almost no isotopic fractionation during the incorporation of sulfate into the calcite crystal lattice (Burdett et al.,

1989; Kampschulte et al., 2001; Paris et al., 2014; Barkan et al., 2020). Furthermore, different studies have demonstrated that CAS sulfur is resistant to meteoric and burial diagenesis (e.g., Lyons et al., 2004; Gill et al., 2008; Marengo et al., 2008; Fichtner et al., 2017) and faithfully records seawater S-isotope evolution as recorded by evaporites and barites (Kampschulte and Strauss, 2004; Rennie et al., 2018; Toyama et al., 2020). Nevertheless, this robustness has been challenged by other studies (e.g., Present et al., 2015; Bernasconi et al., 2017; Johnson et al., 2021), which show that compared to evaporites, CAS isotopic data may display considerable scatter/variability within samples and study sites.

The Smithian – Spathian (Olenekian) was a significant interval of the Early Triassic, characterized by notable environmental, climatic, and biotic perturbations. These perturbations are recorded in the biogeochemical cycles of carbon, oxygen, sulfur, mercury, as well as the largest biotic crises for marine nekton during the entire Early Triassic (Payne et al., 2004; Orchard, 2007; Stanley, 2009; Romano et al., 2013; Algeo et al., 2019; Shen et al., 2019; Song et al., 2019; Edward et al., 2024). Different studies have investigated the evolution of marine $\delta^{34}\text{S}$ during this interval (Fig. 1; Song et al., 2014; Zhang et al., 2015; Lyu et al., 2019; Song et al., 2019; Stebbins et al., 2019a; Stebbins et al., 2019b; Thomazo et al., 2019; Du et al., 2022), providing insights on climatic and marine paleoenvironmental conditions which potentially impacted the evolution of marine faunas during the Olenekian. Song et al. (2014) suggested that seawater sulfate was depleted in ^{34}S within the eastern PaleoTethys during the Griesbachian to Smithian, and that Early Triassic marine sulfate variations were probably driven by climate change. Based on a CAS $\delta^{34}\text{S}$ record from a shallow marine section in South China, Zhang et al. (2015) proposed that oceanic upwelling related to circulation changes due to cooling was responsible for a short-lived marine productivity increase and expansion of “thermocline anoxia” at the Smithian – Spathian boundary (SSB). The notion of climatic cooling and enhanced oceanic overturning circulation driving marine $\delta^{34}\text{S}$ perturbations across the SSB has been supported by recent studies of marine sections in South China (Lyu et al., 2019; Song et al., 2019), the northern Gondwanan margin (Stebbins et al., 2019a), and mid Panthalassa (Stebbins et al., 2019b). In contrast, Thomazo et al. (2019) ascribed sulfur isotope variations across the late Smithian to early Spathian in the shallow-water marine Mineral Mountains section, USA, to local sedimentological factors. Finally, a recent study (Du et al., 2022) proposed that sulfur and carbon cycle changes recorded during the late Smithian and across the SSB are related to early to middle Smithian volcanic activity.

However, excepting the Jesmond section (Stebbins et al., 2019b), none of the published Smithian – Spathian $\delta^{34}\text{S}_{\text{CAS}}$ profiles record offshore marine depositional environments, and hence might be influenced by local terrestrial fluxes. Moreover, the Jesmond section only spans the latest Smithian to Spathian (Stebbins et al., 2019b), precluding a comparison of pre-SSB $\delta^{34}\text{S}_{\text{CAS}}$ trends between offshore carbonate and continental shelf successions. In addition, Early Triassic CAS records display large $\delta^{34}\text{S}$ variability in individual sections (Fig. 1) and are often offset to higher values relative to

contemporaneous evaporites (Bernasconi et al., 2017), casting doubt on the reliability of CAS for reconstructing Early Triassic marine sulfur cycle variations.

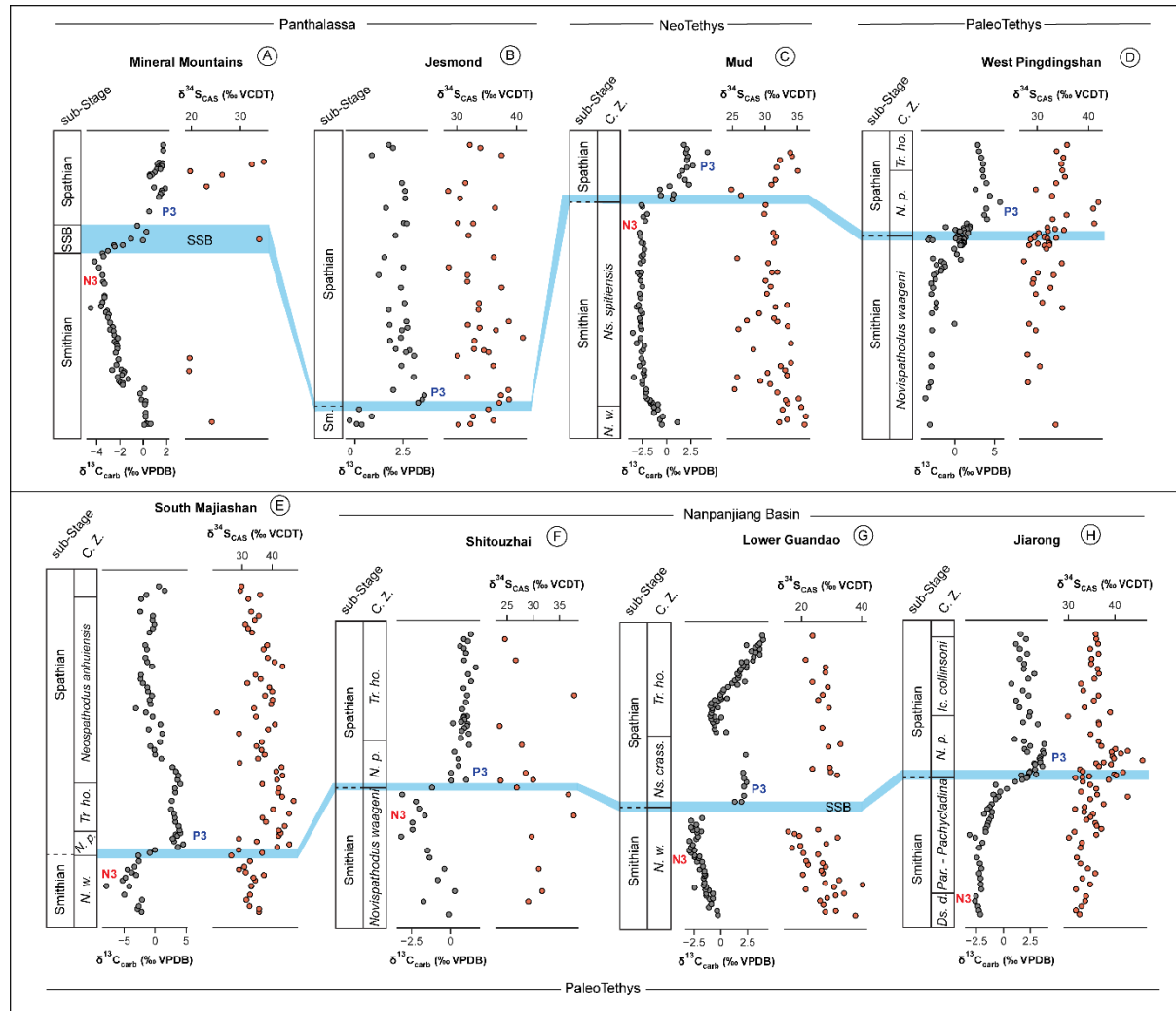


Figure 1. Compilation of published Smithian to Spathian CAS $\delta^{34}\text{S}$ profiles, as well as $\delta^{13}\text{C}$ profiles for a) Mineral Mountains section, USA, b) Jesmond section, Canada, c) Mud section, Spiti Valley, India, d) West Pingdingshan section, South China, e) South Majiashan section, South China, f) Shitouzhai section, South China, g) lower Guandao section, South China, and h) Jiarong section, South China. Data sources are as follows: Mineral Mountains – Thomazo et al. (2019), Mud – Stebbins et al. (2019a), West Pingdingshan and Jiarong – Lyu et al. (2019), South Majiashan – Du et al. (2022), Guandao – Song et al. (2014), Shitouzhai – Zhang et al. (2015), Jesmond – Stebbins et al. (2019b). Sm.= Smithian, C.Z. = conodont zone, N.w.= *Novispathodus waageni*, Ns.=*Neospathodus*, N.p.= *Novispathodus pingdingshanensis*, Tr. Ho.= *Triassospathodus homeri*, Ns. Crass.= *Neospathodus crassatus*, Ds. d.= *Discretella discrete*, Par.= *Parachirognathus*, Ic.= *Icriospathodus*.

In the current study, variations in the marine sulfur cycle during the Olenekian (middle Smithian to Spathian) and its relation to marine redox and faunal changes are investigated based on CAS extracted from three marine successions deposited in the PaleoTethys and NeoTethys oceans. The studied sections

represent deep-water continental shelf (Qiakong section, South China) and shallow- to deep-water offshore (Jebel Aweri and Wadi Musjah sections, Oman) marine environments, respectively (Widmann et al., 2020; Leu et al., 2023). As such, the current study differs from previous studies covering the SSB in that we report CAS isotopic data from both deep-water continental shelf and offshore marine carbonate sections, permitting a more detailed comparison of CAS S-isotope records between these depositional environments during the Olenekian. In addition, the Qiakong section is exceptionally well-constrained by U-Pb zircon absolute ages (Widmann et al., 2020), permitting absolute age-resolved evaluations of the Olenekian marine sulfur cycle. Finally, published Smithian-Spathian CAS $\delta^{34}\text{S}$ records from around the world are compiled within an absolute age framework and compared with the Olenekian evaporite record (as compiled by Present et al., 2020) to assess global secular marine $\delta^{34}\text{S}$ trends during the Olenekian.

2. Sample Localities

Three marine sections: Qiakong (Nanpanjiang Basin, South China), Wadi Musjah and Jebel Aweri (offshore carbonate build-up blocks deposited in the NeoTethys) were studied (Fig. 2). The Qiakong (QIA) section is situated within the Pingtang syncline, in the northeastern edge of the Nanpanjiang Basin of South China (Fig. 2) (Bagherpour et al., 2020; Leu et al., 2022). This section was deposited in deep-water continental shelf environments and comprises an expanded middle Smithian to Spathian marine sedimentary succession belonging to the Daye and Loulou formations, respectively (Widmann et al., 2020; Leu et al., 2022). The Daye Fm. consists of thin-bedded limestone beds that are considered to represent slope deposits (Widmann et al., 2020). In QIA, the Luolou Fm. contains dark mudstones and black shale units interbedded with thin limestone beds within the late Smithian to basal Spathian (unit IVb). Thereafter, a sharp lithological change (indicative of a hiatus) to thicker nodular limestone units characterizes the rest of the Spathian (Widmann et al., 2020; Leu et al., 2022). Volcanic ash beds are found throughout the Smithian and Spathian units of this succession (Widmann et al., 2020).

The QIA section has been extensively studied in terms of its biostratigraphy, U-Pb zircon geochronology, as well as the carbon isotope and mercury record (Widmann et al., 2020; Leu et al., 2022; Edward et al., 2024). As such, this section is chronostratigraphically well-constrained via U-Pb zircon absolute ages and conodont unitary association zones (UAZs) (see Widman et al., 2020 and Leu et al., 2022 for details). The SSB in this section is constrained within the interval of separation between UAZ 7 and UAZ 8 (Leu et al., 2022), with the ash bed within this interval (QIA 7T) having an absolute age of 249.292 ± 0.063 Ma (Widmann et al. 2020). Further details on the facies description and paleodepositional environment of this section are included in the supplementary information. The Wadi Musjah (WMJ) section represents a condensed (4.6 m-thick) Hallstatt-type limestone succession deposited in relatively deep water as an isolated oceanic carbonate build-up on seamounts in the NeoTethys ocean during the Early Triassic (Brühwiler et al., 2012; Baud, 2013; Leu et al., 2023).

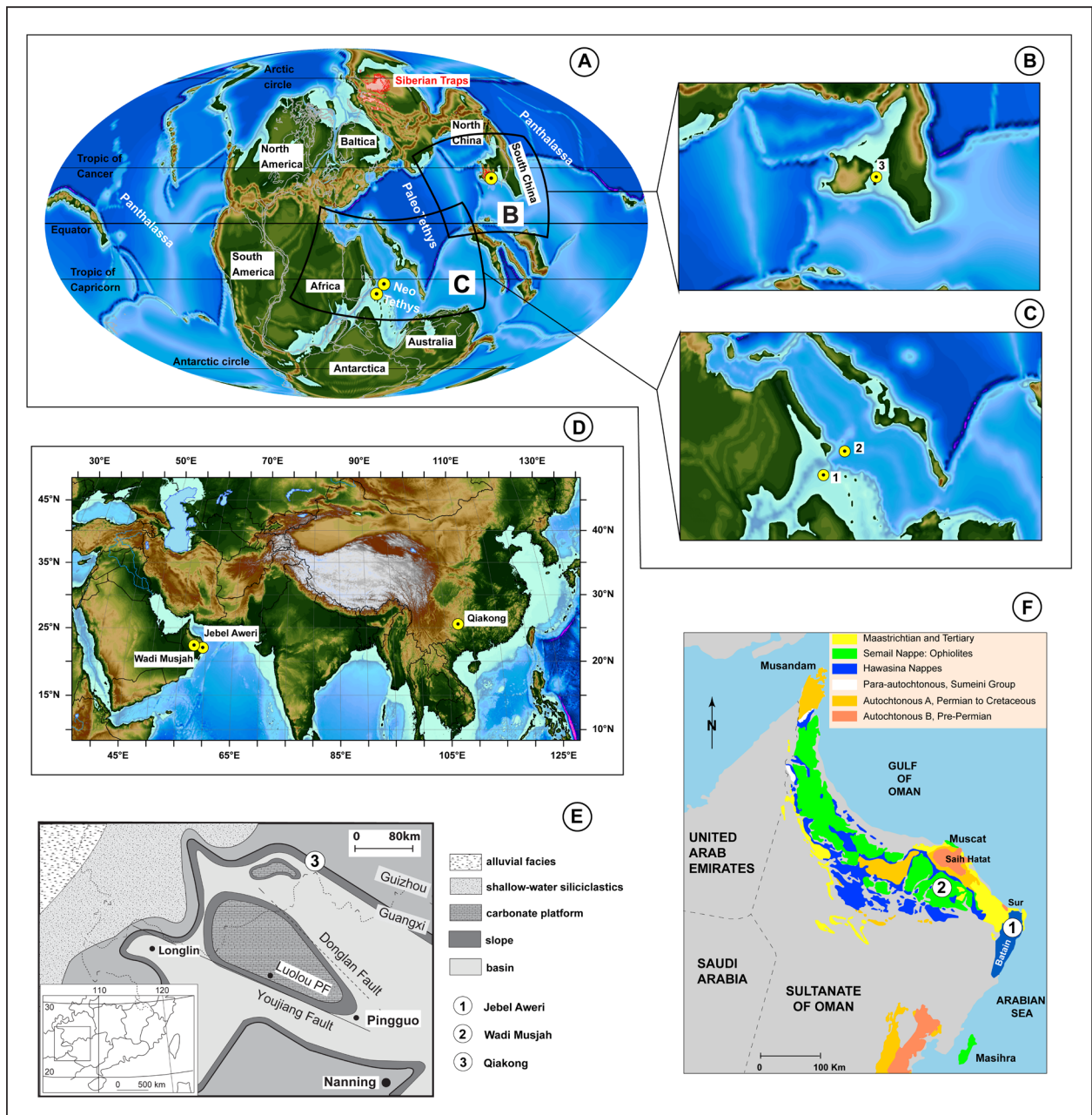


Figure 2. A) Early Triassic paleogeographic map after the Panalesis model (Vérard, 2019), showing the studied successions (yellow circles). Mollweide projection of the B) South China (PaleoTethys) and C) Oman (NeoTethys) areas during the Early Triassic from A. D) Present-day map showing the location of the study sections. Geological map of E) the Nanpanjiang basin after Bagherpour et al. (2017) showing the Qiakong section, and F) Oman with the present-day locations of the offshore carbonate successions, modified after Baud et al. (2001).

The WMJ section spans the middle Smithian to Spathian based on conodont and ammonoid biochronology and in the present-day, is located about 75 km from Muscat, Oman (Brühwiler et al., 2012; Leu et al., 2023). This section contains conodont- and ammonoid-rich carbonate strata that consist of peloidal grainstone and cemented bivalve coquina biostromes, as well as brachiopod biostromes

(Baud et al., 2001). Similarly, the Jebel Aweri (JA) section was deposited as an exotic build-up block on a seamount within the NeoTethys. Today, the JA exotic block is situated within the Batain plains of northeastern Oman (Fig. 2f), having been redeposited as an olistostrome among Middle Jurassic-aged strata of the Guwayza Formation and the Ad Daffah conglomerate (Schreurs and Immenhauser, 1999; Hauser et al., 2001). Unlike WMJ, the JA succession represents an expanded late Smithian to Spathian 30 m-thick sedimentary succession. This exotic block is a shallow water offshore reefal succession containing shell-supported biostrome, cemented lime clasts and microbialite bioherm (Leu et al., 2023). Both the WMJ and JA successions are temporally well-constrained through conodont and ammonoid biostratigraphy (Brühwiler et al., 2012; Leu et al., 2023). As such, the SSB for both successions is also well-constrained, not only based on an intercalibration of conodont and ammonoid biostratigraphy, but also the carbon isotope record, which situates this boundary within the interval of separation between UAZs 3 and 4 (Leu et al., 2023).

3. Methods

Carbon isotope compositions and major and trace element concentrations for the investigated sections were previously analyzed (Leu et al., 2022; 2023; Edward et al., 2024). For the current study, bulk rock samples from 81 carbonate strata from the three studied sections (QIA = 28, WMJ = 21, JA = 32) were processed for CAS extraction and isotope analyses at the University of Lausanne (UNIL).

3.1 CAS and CRS extraction

CAS extraction was based on the extraction protocol used at UNIL (Bagnoud-Velásquez et al., 2013), which was modified following the recommendations of Wotte et al. (2012). Briefly, 50 to 80 g of powdered samples ($n = 99$) were leached with 10 % NaCl solution for at least 8 h to remove NaCl-soluble sulfur. This step was followed by the decantation of the supernatant, after which the leaching step was repeated four times. The samples were then washed with excess Milli-Q water five times to remove any traces of NaCl before dissolution in 37 % HCl to release CAS. Samples were acidified at room temperature within 2 hours, maintaining the pH of the slurry above 3 to avoid pyrite oxidation, and then filtered through 0.45 μm nitrocellulose filters. The pH of the filtrate was lowered to ~ 2 , followed by heating to 95 $^{\circ}\text{C}$ for 3 hours. Subsequently, excess 12 % BaCl_2 solution was added, and the solution left to cool and precipitate BaSO_4 at room temperature over three days. The solution containing the precipitated BaSO_4 was filtered over a 0.2 μm nitrocellulose filter to collect the precipitated BaSO_4 , which was then washed with warm Milli-Q water and dried at 50 $^{\circ}\text{C}$ for 24h. The total amount of recovered BaSO_4 was weighed before isotopic analysis. Further details on the BaSO_4 precipitation process and purification are provided in Spangenberg et al. (2022). CAS concentrations were calculated from the amount of recovered precipitate and its sulfur content determined by EA/IRMS (see supplementary information).

The chromium reducible sulfur (CRS) was extracted from a subset of middle Smithian to Spathian-aged samples which were previously treated for CAS extraction. The solid residue from CAS extraction was washed thoroughly with deionized water until a neutral pH was achieved. Only QIA samples ($n = 16$) were extracted for CRS; JA and WMJ samples, containing generally $> 99\%$ carbonate, did not yield sufficient solid residue for CRS separation after the acid treatment. The washed residues of QIA samples were dried at $50\text{ }^{\circ}\text{C}$ for > 3 days and weighed. CRS (found to be only pyrite) was extracted from $1 - 3$ g of the dried residue using a modified chromium reduction method (Canfield et al., 1986). In short, the sample powder was treated with ethanol to disaggregate the powder and then boiled with freshly prepared acidic chromium (II) chloride 1 M solution under a continuous flow of clean nitrogen, releasing H_2S gas from pyrite. A zinc acetate solution trapped the evolved H_2S gas as ZnS. The ZnS was converted to Ag_2S by adding AgNO_3 to the (ZnS-containing) trapping solution and stored at room temperature in the dark for at least 1 day. The Ag_2S precipitate was filtered through a $0.2\text{ }\mu\text{m}$ nitrocellulose filter, rinsed with 5% ammonia solution and Milli-Q water, and dried at $40\text{ }^{\circ}\text{C}$ for 48 h before isotopic analysis.

3.2 Sulfur and oxygen isotope analyses

Sulfur isotope measurements were performed via elemental analysis-isotope ratio mass spectrometry (EA/IRMS), using a Carlo Erba 1108 elemental analyzer connected to a Thermo Fisher Delta V Plus isotope ratio mass spectrometer following the procedures outlined in Spangenberg et al. (2022). Aliquots of $2 - 3$ mg BaSO_4 (for $\delta^{34}\text{S}_{\text{CAS}}$) or $0.3 - 0.5$ mg Ag_2S (for $\delta^{34}\text{S}_{\text{CRS}}$) were weighed into tin capsules in duplicates and sealed. Analytical precision for $\delta^{34}\text{S}_{\text{CAS}}$ was monitored by repeat analyses of international reference materials (IAEA-SO-5, IAEA-SO-6 and NBS 127) and internal standards (Fx-sulfate and UVA-sulfate, with $\delta^{34}\text{S}_{\text{VCDT}}$ values of $17.82 \pm 0.22\text{ }‰$ and $12.73 \pm 0.21\text{ }‰$, respectively (Spangenberg et al., 2022)). For $\delta^{34}\text{S}_{\text{CRS}}$, analytical precision was monitored by replicate measurements of international reference material: IAEA-S3 (silver sulfide), as well as internal standards: UNIL-Cin (cinnabar) and UNIL-PyE (pyrite). Analytical uncertainty was generally $0.30\text{ }‰$ or better for $\delta^{34}\text{S}$ based on repeat analyses of NBS 127. $\delta^{34}\text{S}_{\text{CAS}}$ and $\delta^{34}\text{S}_{\text{CRS}}$ values are reported as mean values of replicate analyses ($\pm 1\sigma$) in per mille (‰) notation relative to Vienna-Canyon Diablo Troilite (VCDT).

For CAS $\delta^{18}\text{O}$ analysis, $0.25 - 0.3$ mg of extracted BaSO_4 was weighed into silver capsules, alongside 0.15 mg of pulverized graphite and sealed. Isotopic compositions were analyzed using a Thermo Scientific FlashSmart CHNS/O Elemental Analyzer coupled to a Thermo Finnigan MAT 253 isotope ratio mass spectrometer at UNIL. The reactor of the Elemental Analyzer was held at a temperature of $1350\text{ }^{\circ}\text{C}$, and the evolved gas of the samples passed over a gas chromatograph (GC) at $80\text{ }^{\circ}\text{C}$ using a helium flow rate of 100 ml/min . Analytical precision was monitored by replicate measurements of international reference materials: NBS 127 and OGS (barium sulfate), IAEA-601 (benzoic acid), as well as internal standards: SAAS and ANZO (water). Analytical precision was $0.51\text{ }‰$ (1σ) or better based on replicate analysis of IAEA-601. Results are reported as mean values of replicate analyses (\pm

1 σ) in per mille (‰) relative to VSMOW. For samples without replicates, analytical uncertainty is reported using that of the standard material with the highest standard deviation (i.e., IAEA-601: 0.51 ‰).

3.3 Rare earth elements (REE) analysis

Rare earth elements (REE) concentrations of carbonate samples from WMJ (n = 23) were measured by quadrupole ICP-MS (Agilent 7700) at the ICP Centre of the University of Geneva. The samples were digested overnight using concentrated HNO₃ in sealed Teflon vials on a hotplate. Instrumental uncertainty was < 5 % for REE concentrations below 100 ppb. NIST Nd elemental standard was regularly measured at 10 ppb and 100 ppb and yielded relative standard deviation (RSD) of < 3 %. A mixture of Re and Rh was used as internal standards. REE concentrations were normalized relative to Post Archean Australian Shale (PAAS) (Taylor and McLennan, 1985). The cerium (Ce) and europium (Eu) anomalies were calculated based on the PAAS-normalized values as follows:

$$Ce_{anom} = Ce_N / (Pr_N^2 / Nd_N) \text{ (Lawrence et al., 2006)} \quad (1)$$

$$Eu_{anom} = 2 \times Eu_N / (Sm_N + Gd_N) \text{ (De Baar et al., 1985)} \quad (2)$$

Where $_N$ = REE values normalized relative to PAAS

3.4 Thin section petrography

The textural properties of QIA rock samples were investigated by thin section petrography. Thin sections were prepared from hand samples corresponding to strata investigated for CAS extraction and isotopic analyses at the Paleontological Institute, University of Zurich. Thin section petrography for WMJ and JA strata have been published by Leu et al. (2023).

3.5 Stratigraphic correlation framework

The three studied sections (QIA, WMJ, JA) were correlated using the biostratigraphical correlation framework of Leu et al. (2023), which is based on conodont and ammonoid faunas found in Oman and South China (Fig. 3). Absolute age constraints are based on U-Pb zircon ages for conodont unitary association zone boundaries in the QIA section, which is the most expanded U-Pb zircon dated Smithian – Spathian section so far (Widmann et al., 2020). Note that the conodont UAZ numbering for QIA by Widmann et al. (2020) has been updated by Leu et al. (2022), and that the latter UAZ numbering is applied herein.

An absolute age for every sample was estimated based on linear interpolation between the oldest and youngest known ages relative to the stratigraphic position of each sample. For QIA, using the conodont UAZ boundary ages determined by Widmann et al. (2020) as tie-points, the ages of samples between two tie-points were calculated by linear interpolation using a Python script based on the publicly

available NumPy library (Harris et al., 2020) (see supplementary information). To determine an absolute age for the stratigraphically youngest (top of section) and oldest (bottom of section) samples, linear sedimentation rates (LSRs, Shen et al. (2019)) were calculated based on the stratigraphic thickness and duration of the stratigraphically closest interval bracketed by conodont UAZ boundaries with assigned absolute ages.

$$\text{LSR} = \text{stratigraphic thickness/duration (m Myr}^{-1}\text{)} \quad (3)$$

The age of the oldest sample (A_0) (i.e., the sample at the base of the section) and that of the youngest sample (A_1) (i.e., the sample at the top of the section) were calculated as follows:

$$A_0 = T_0 + (sd_0 / \text{LSR}) \quad (4)$$

$$A_1 = T_1 - (sd_1 / \text{LSR}) \quad (5)$$

where T_0 = absolute age of the oldest sample stratigraphically above sample corresponding to A_0 , sd_0 = the difference of the stratigraphic heights of the samples corresponding to A_0 and T_0 , T_1 = absolute age of the youngest sample stratigraphically below sample corresponding to A_1 , and sd_1 = the difference of the stratigraphic heights of the samples corresponding to A_1 and T_1 .

In addition to the biostratigraphical correlation framework for Oman and South China (Fig. 3), the globally recognized carbon isotope excursions (CIEs): N3, P3 and N4 (Song et al., 2013) spanning the middle Smithian and Spathian, were used to further refine the stratigraphic correlation between QIA, WMJ and JA, as well as correlations to other sections in the literature. To ensure consistency in the delineation of the SSB between the current study and previously published CAS $\delta^{34}\text{S}$ records (Fig. 1), the midpoint of the transition from the N3 to P3 CIE was used to correlate the SSB (as suggested by Zhang et al. (2019b)). However, it should be noted that the P3 peak is usually associated with a hiatus of variable duration (Widmann et al. 2020). The SSB was assigned the absolute age of 249.29 Ma after Widmann et al. (2020) and the N3 minimum was assigned the absolute age of 250.038 Ma based on its correlation to the base of UAZ 5 in QIA (Fig. 4). Based on the tie-points and the reported stratigraphic heights in the relevant literature, LSRs, A_0 and A_1 were calculated for each section, as well as linearly interpolated ages for samples between each tie-point.

Series	(sub)Stage	sub (sub)Stage	Ammonoid faunas		Conodont faunas		Conodont UA zones		U-Pb zircon ages			
			Oman	South China	Oman	South China	Oman	South China				
Early Triassic	Spathian	late Spathian								247.2		
		middle Spathian		<i>Neo. haugi</i>								
					<i>Hellenites</i>							248.846
		early Spathian										
	Smithian	late Smithian										
		middle Smithian										
		early Smithian										

Figure 3. Biostratigraphic correlation framework based on ammonoid and conodont faunas of Olenekian marine successions of Oman and South China modified after Leu et al. (2023). Vertical blue lines indicate the stratigraphic extent of sporadic occurrences of the associated conodont faunas in some successions of the study region. Abbreviations are as follows: Ic: *Icriospathodus*, Eu: *Eurygnathodus*, Gu: *Guanxidella*, Neo: *Neospathodus*, Nv: *Novispathodus*, Sc: *Scythogondolella*, Tr: *Triassospathodus*, Ur: *Urdyella*, UA: Unitary Association. U-Pb zircon ages in blue correspond to the ages of the Induan – Olenekian boundary and Olenekian – Anisian boundary, which are taken from the International Chronostratigraphic Chart 2023 (Cohen et al., 2013; updated). Other U-Pb ages are based on Widmann et al. (2020). See main text for details.

4 Results

The CAS concentration and isotopic data ($\delta^{34}\text{S}_{\text{CAS}}$, $\delta^{34}\text{S}_{\text{CRS}}$, and $\delta^{18}\text{O}_{\text{CAS}}$), as well as REE data generated for this study are presented in the supplementary data file (Edward et al., 2024b) and visualized in Figures 4 to 6.

4.1 Sulfur isotopes

The exceptional age control available for the studied sections (Widmann et al., 2020; Leu et al., 2022; Leu et al., 2023) enables the current CAS $\delta^{34}\text{S}$ results to be evaluated within a precise chronostratigraphic framework. $\delta^{34}\text{S}_{\text{CAS}}$ values within the studied interval have a wide range for QIA (21 – 39 ‰) relative to WMJ (22 – 28 ‰) and JA (24 – 31 ‰). CAS $\delta^{34}\text{S}$ within the middle to upper Smithian of QIA show an overall decreasing trend. However, a positive excursion is recorded across the SSB (Fig. 4). This positive $\delta^{34}\text{S}_{\text{CAS}}$ excursion is also observed in $\delta^{34}\text{S}_{\text{CRS}}$ and coincides with the globally recorded P3 positive CIE (Song et al., 2013). Difference in the $\delta^{34}\text{S}$ values of co-occurring CAS and CRS ($\Delta^{34}\text{S}_{\text{CAS-CRS}}$), assumed to be pyrite, has a range between 25 and 54 ‰. $\Delta^{34}\text{S}_{\text{CAS-CRS}}$ values increase in tandem with $\delta^{34}\text{S}_{\text{CAS}}$ across the SSB (Fig. 4f) and have a positive correlation with $\delta^{34}\text{S}_{\text{CAS}}$ (Spearman's $r = 0.76$, $p = 0.00$), suggesting that $\Delta^{34}\text{S}_{\text{CAS-CRS}}$ variation is mainly driven by $\delta^{34}\text{S}_{\text{CAS}}$.

For JA, which has the most expanded late Smithian record (~ 20 m) and no apparent SSB unconformity (Leu et al., 2023), a gradual change of about + 7 ‰ for $\delta^{34}\text{S}_{\text{CAS}}$ is recorded within the entire late Smithian (UAZ 1 to UAZ 3; Fig. 5). Here, maximum values (ca. 31 ‰) are recorded within the SSB interval of separation (Fig. 5). This late Smithian to SSB positive trend is succeeded by a 3 ‰ decrease in the basal Spathian (UAZ 4 to base of UAZ 5). Thereafter, $\delta^{34}\text{S}_{\text{CAS}}$ values remain around 27 ‰ for the rest of the JA Spathian record. The WMJ section records a gradual overall 6 ‰ increase in $\delta^{34}\text{S}_{\text{CAS}}$ values across the middle Smithian to SSB, also reaching maximum values within the SSB interval of separation (Fig. 6). This increasing trend is interrupted by a ca. 4 ‰ $\delta^{34}\text{S}_{\text{CAS}}$ decline at the basal Spathian (i.e., within UAZ 4). Afterwards, a return to SSB $\delta^{34}\text{S}_{\text{CAS}}$ values of ca. 27 ‰ is recorded before a final decline to lower values (ca. 22 ‰) at the top of UAZ 7.

4.2 Oxygen isotopes

For QIA, CAS $\delta^{18}\text{O}$ values have a range between 11 and 20 ‰, whereas JA and WMJ have a range between 14 – 25 ‰ and 12 – 26 ‰, respectively. CAS $\delta^{18}\text{O}$ values prior to the SSB for QIA (Fig. 4d) are relatively constant between 15 and 17 ‰ (except sample Q133 with $\delta^{18}\text{O}$ value of ca. 20 ‰) and display an increasing trend across the SSB. Subsequently, a decrease in values by 4 ‰ is recorded in the early Spathian (Fig. 4d), followed by a recovery to background values of about 16 ‰ as noted prior to the SSB. Both WMJ and JA display an overall $\delta^{18}\text{O}_{\text{CAS}}$ increase during the Smithian towards the SSB similar to the $\delta^{34}\text{S}_{\text{CAS}}$ record. Also, both sections show a general decrease in $\delta^{18}\text{O}$ in the early Spathian, similar to the decrease in $\delta^{18}\text{O}_{\text{CAS}}$ values for QIA, albeit somewhat further above the SSB.

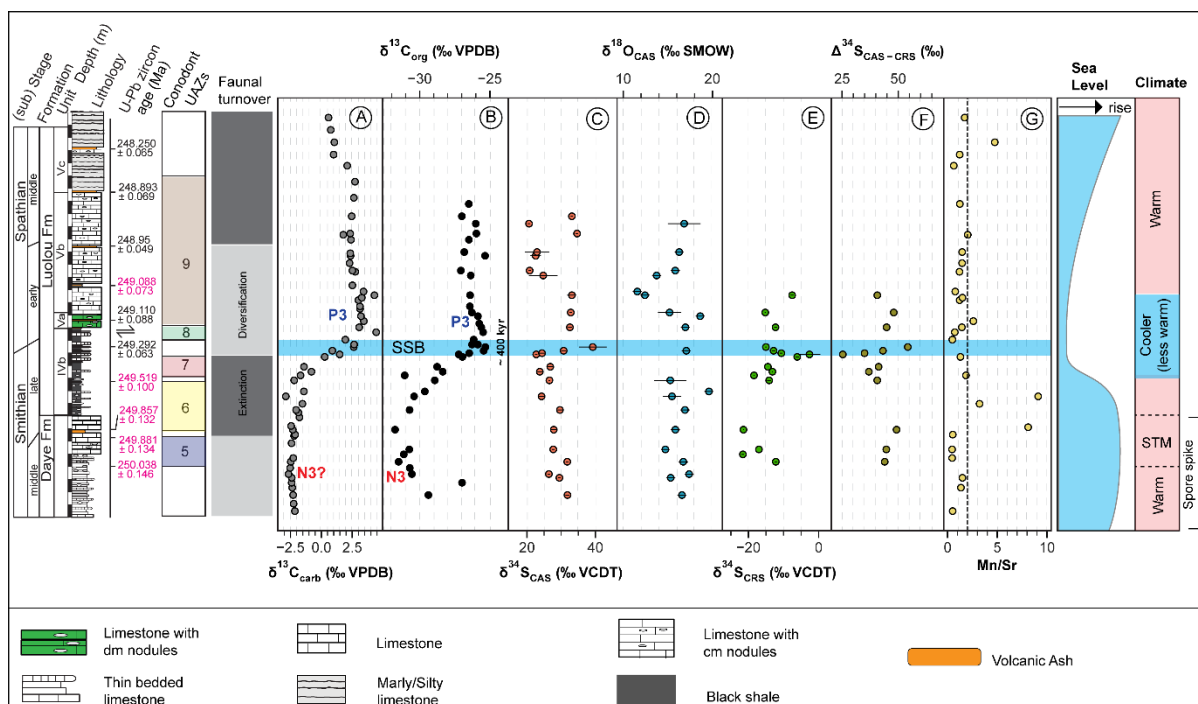


Figure 4. Geochemical profile showing the A) $\delta^{13}\text{C}_{\text{carb}}$, B) $\delta^{13}\text{C}_{\text{org}}$, C) $\delta^{34}\text{S}_{\text{CAS}}$, D) $\delta^{18}\text{O}_{\text{CAS}}$, E) $\delta^{34}\text{S}_{\text{CRS}}$ F) $\Delta^{34}\text{S}_{\text{CAS-CRS}}$, G) Mn/Sr profiles for the Qiakong section. UAZ = unitary association zone. Lithostratigraphic log, U-Pb zircon ages and $\delta^{13}\text{C}_{\text{carb}}$ values are from Widmann et al. (2020). The ages denoted in pink represent those interpolated by Bayesian age-depth modelling (Widmann et al., 2020). $\delta^{13}\text{C}_{\text{org}}$ values and Mn, and Sr values are from Edward et al. (2024). Conodont UAZs and faunal turnover (based on conodonts) are from Leu et al. (2022). Climate depiction and timing is after Goudemand et al. (2019) and Widmann et al. (2020). The spore spike interval is after Herman et al. (2011). Relative sea level changes depiction is after Zhang et al. (2015). STM = Smithian thermal maximum.

4.3 CAS concentrations

CAS concentrations were stoichiometrically calculated from the amount of recovered precipitate following CAS extraction. The calculated CAS content was then normalized to total sulfur (TS) content determined by EA/IRMS (e.g., Witts et al., 2018), as pure barite has 13.74 wt.% S. The TS content of recovered CAS- BaSO_4 was on average 8.83 wt. %, indicating that not all recovered precipitate was indeed barite. We tentatively attribute this discrepancy between expected and measured TS content to BaCl_2 reprecipitation due to the excess 12 % BaCl_2 solution used for CAS extraction. However, this requires further study. Calculated CAS concentrations for QIA, JA and WMJ have a range between 85 and 423 ppm, 2 and 2283 ppm, and 2 and 2089 ppm, respectively. These CAS contents show no correlation to either CAS $\delta^{34}\text{S}$ or $\delta^{18}\text{O}$ (Fig. 7, Fig. S15), suggesting that CAS concentrations have no measurable influence on CAS isotopic compositions in the present study.

4.4 REE concentrations

Analyzed samples have a REE pattern consistent with that of modern seawater, displaying a prominent negative Ce anomaly (Fig. 8A), and a mean Eu_{anom} value of 1.01 (German and Elderfield, 1990; Alibo and Nozaki, 1999). Total REE concentrations are between 0.2 and 5.8 ppm, except for sample WMJ 17C (303.4 ppm) and are generally lower in the Smithian relative to the Spathian. Ce_{anom} values have a range between 0.21 and 1.09 ppm, with the Smithian being characterized by higher values (between 0.7 and 1 ppm) relative to the Spathian (< 0.7 ppm).

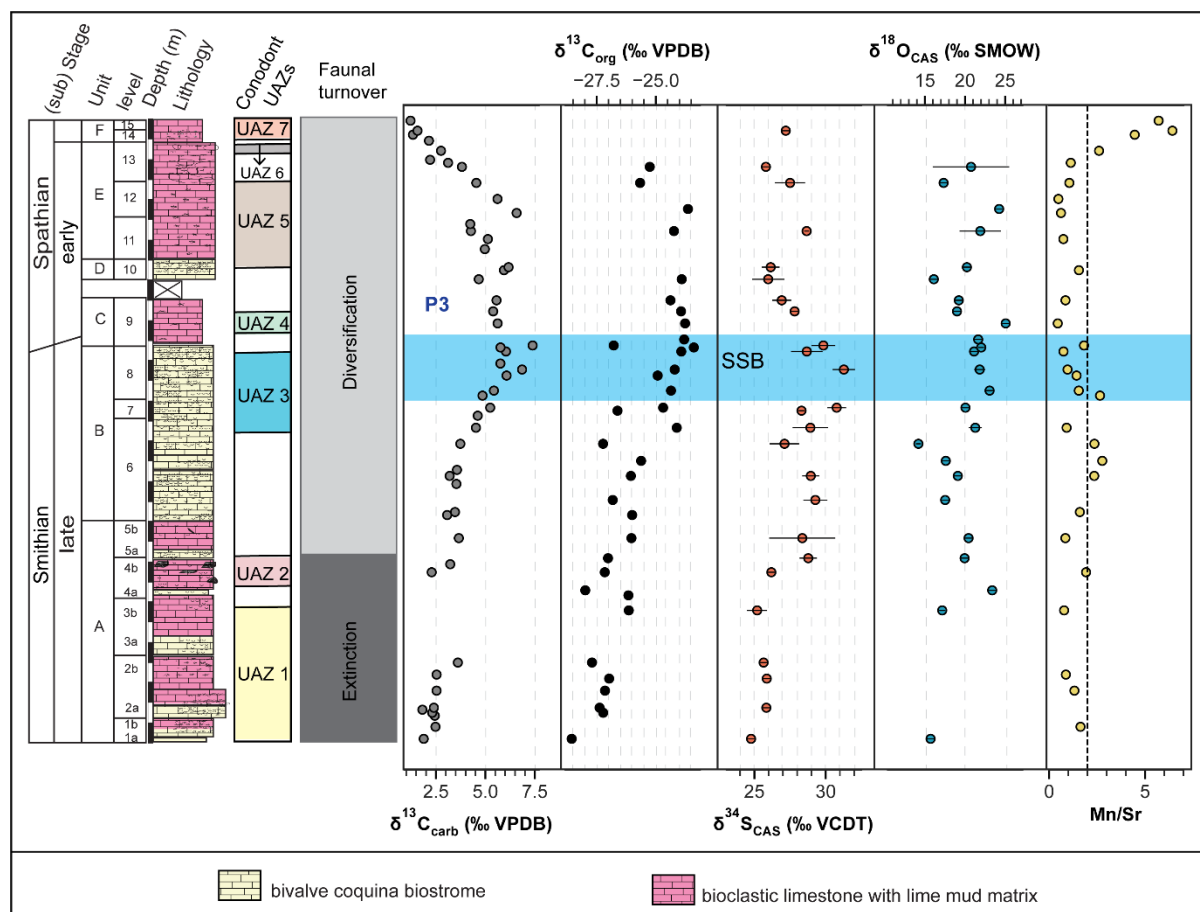


Figure 5. Geochemical profiles of the Jebel Aweri section showing the $\delta^{13}C_{carb}$, $\delta^{13}C_{org}$, $\delta^{34}S_{CAS}$, $\delta^{18}O_{CAS}$ and Mn/Sr record for the late Smithian to Spathian interval. The SSB is defined as the interval of separation between UAZs 3 and 4 (Leu et al., 2023). $\delta^{13}C_{carb}$ and conodont faunal turnover data are from Leu et al. (2023). Mn/Sr and $^{87}Sr/^{86}Sr$ data are from Edward et al. (2024). The vertical black dashed line depicts the Mn/Sr preservation limit applied (2).

5 Discussion

5.1 Assessing the preservation of primary CAS isotopic information

Primary marine CAS $\delta^{34}S$ and $\delta^{18}O$ values have the potential to be altered by post-depositional diagenetic processes (e.g., increasing sedimentary burial, dolomitization, carbonate dissolution and recrystallization in diagenetic pore fluids) or sample contamination during laboratory CAS extraction

(Marenco et al., 2008; Wotte et al., 2012; Present et al., 2015; Fichtner et al., 2017). Different techniques are commonly applied in assessing the preservation of primary CAS compositions. These include the evaluation of Mn/Sr ratios and cross-plots of CAS isotope and geochemical data (e.g., Hurtgen et al., 2002; Gill et al., 2008; Marenco et al., 2008; Johnson et al., 2021; Du et al., 2022; Kwon et al., 2022), as well as statistical smoothing of CAS isotope curves to elucidate overall trends and attenuate the impact of outliers (e.g., Kampschulte and Strauss, 2004; Song et al., 2014). Furthermore, significant heterogeneity of $\delta^{34}\text{S}_{\text{CAS}}$ values ($> 5 \text{ ‰}$) within individual bulk carbonate samples may result from diagenetic alteration and/or the mixing of CAS from different carbonate components such as micrite, skeletal fragments and calcite cements (Present et al., 2015; Johnson et al., 2021). In addition, diagenetic modification of CAS $\delta^{34}\text{S}$ may be expressed by an inverse relationship between CAS concentrations and $\delta^{34}\text{S}$ values (Johnson et al., 2021).

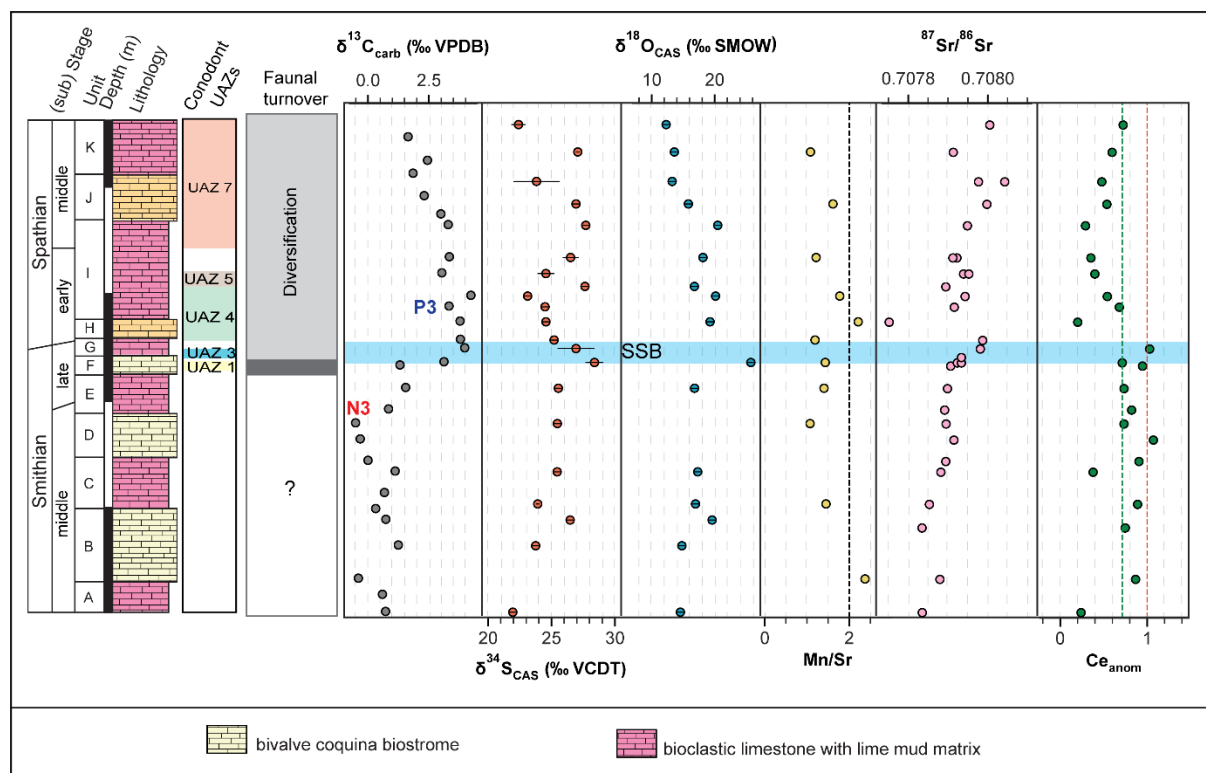


Figure 6. Geochemical profiles of the Wadi Musjah (WMJ) section showing the $\delta^{13}\text{C}_{\text{carb}}$, $\delta^{34}\text{S}_{\text{CAS}}$, $\delta^{18}\text{O}_{\text{CAS}}$, Mn/Sr, $^{87}\text{Sr}/^{86}\text{Sr}$ and Cerium anomaly (Ce_{anom}) record for the middle Smithian to Spathian interval. The Smithian – Spathian boundary is defined after Leu et al. (2023). $\delta^{13}\text{C}_{\text{carb}}$ and conodont faunal turnover data are from Leu et al. (2023). Mn/Sr and $^{87}\text{Sr}/^{86}\text{Sr}$ data are from Edward et al. (2024). The vertical dashed red line depicts the typical Ce anomaly value (Ce_{anom}) for anoxic seawater (i.e., 1, Liu et al., 2021), the red dashed line depicts the median Ce_{anom} value (0.71), and the black dashed line depicts the Mn/Sr preservation limit applied.

Mn/Sr ratios for most strata in the present study are < 2 and have no correlation to $\delta^{34}\text{S}_{\text{CAS}}$ values (Fig. 7c, 7e). Also, Mg/Ca ratios are < 0.1 and have no correlation to $\delta^{34}\text{S}_{\text{CAS}}$ nor $\delta^{18}\text{O}_{\text{CAS}}$, and no correlation

is observed between CAS concentrations (depicted as $1/[CAS]$) and $\delta^{34}S_{CAS}$ (Fig. 7c). Furthermore, $\delta^{34}S$ and $\delta^{18}O$ values determined by multiple analyses of individual samples are similar, mostly varying by $< 4 \text{ ‰}$. However, three samples: Q146, Q148, and JA C34 show differences as large as 7.2 ‰ (for $\delta^{18}O_{CAS}$) and 9.5 ‰ (for $\delta^{34}S_{CAS}$), suggesting that non-primary CAS isotopic values are also recorded by these samples.

Although of very limited stratigraphic resolution, existing evaporite data indicate that the Olenekian was characterized by $\delta^{34}S$ values between 24 and 32 ‰, although lower values of ca. 17 ‰ are recorded at the Olenekian – Anisian boundary (Claypool et al., 1980; Cortecci et al., 1981; Insalaco et al., 2006; Marengo et al., 2008; Horacek et al., 2010; Bernasconi et al., 2017). The main Smithian – Spathian range of evaporite $\delta^{34}S$ values (24 – 32 ‰) is similar to $\delta^{34}S_{CAS}$ values recorded for JA (24 – 31 ‰) and WMJ (22 – 28 ‰) (Figs. 5 – 6), suggesting that these two sections preserve near-primary Olenekian seawater $\delta^{34}S$ values. Furthermore, the WMJ section displays REE characteristics similar to that of modern seawater (Fig. 8A; section 4.4) and the Sr isotope records of WMJ and JA are consistent with the global Sr isotope trend and absolute values for the Early Triassic (Edward et al., 2024). In addition, WMJ and JA strata mostly consist of biogenic calcite components (Fig. 9), a carbonate phase known to reliably record seawater S-isotope compositions (Kampschulte and Strauss, 2004). These considerations strongly support the inference that the Oman offshore sections preserve near-primary seawater geochemical information.

In contrast, QIA samples have a wider range of absolute $\delta^{34}S$ values (21 – 39 ‰) relative to the evaporite record, suggesting that $\delta^{34}S$ trends recorded for this section may not all be near-primary. Also, thin section photos indicate that unlike WMJ and JA, QIA samples have a low biogenic calcite component and instead are occasionally composed of a combination of carbonate and clastic material (Fig. 9D, supplementary information). Also, partial dissolution of the carbonate and replacement with clastic material or sparry calcite is evident in many QIA samples (see facies description in the supplementary information). Hence, QIA samples are likely to incorporate sulfate from both seawater and terrestrial sources, consistent with the wider range of CAS $\delta^{34}S$ values for this section.

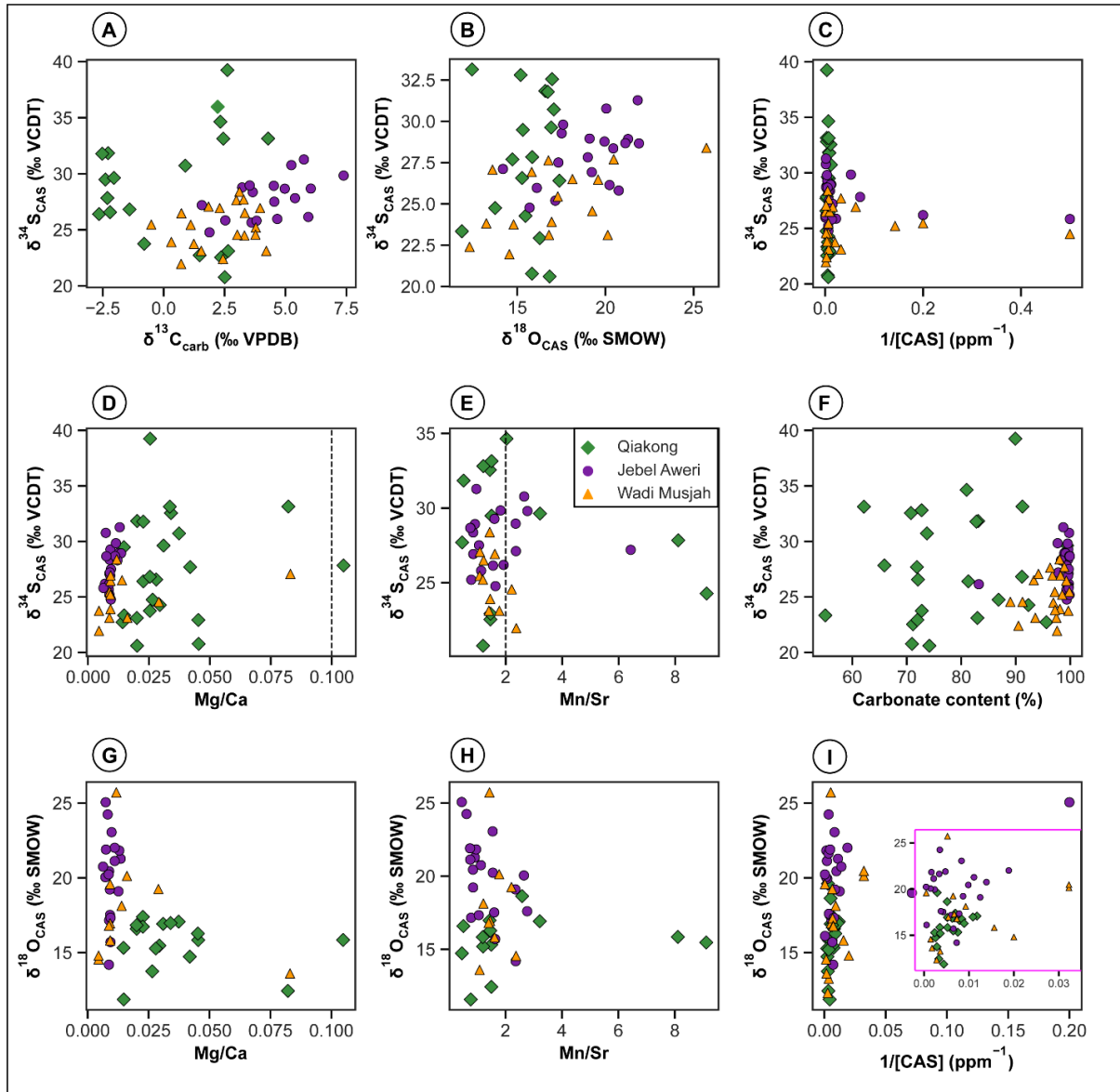


Figure 7. Cross-plots of $\delta^{34}\text{S}_{\text{CAS}}$ vs A) $\delta^{13}\text{C}_{\text{carb}}$, B) $\delta^{18}\text{O}_{\text{CAS}}$, C) inverse of CAS concentration ($1/[\text{CAS}]$), D) Mg/Ca ratio, E) Mn/Sr ratio, F) carbonate content, for samples for Qiakong, Jebel Aweri and Wadi Musjah. Cross plots of $\delta^{18}\text{O}_{\text{CAS}}$ vs G) Mg/Ca, H) Mn/Sr, I) $1/[\text{CAS}]$. Inset in pink rectangle plots $\delta^{18}\text{O}_{\text{CAS}}$ vs $1/[\text{CAS}]$ excluding the 2 Jebel Aweri samples with the highest $1/[\text{CAS}]$ values. Mg, Ca, Mn and Sr data are from Edward et al. (2024).

5.2 Comparison of global Olenekian CAS $\delta^{34}\text{S}$ records

A compilation of previously published CAS $\delta^{34}\text{S}$ records spanning the Smithian – Spathian enables an assessment of the general CAS $\delta^{34}\text{S}$ trend during the Olenekian (Fig. 10). The compiled data indicates that Olenekian CAS $\delta^{34}\text{S}$ values have a wide range (i.e., between 15 and 47 ‰; Fig. 8B; Fig. 10A), which is a factor of 4 higher than that of the relatively sparse evaporite record (24 – 32 ‰; Present et al., 2020 and references therein). Offset between evaporite and CAS $\delta^{34}\text{S}$ values have previously been reported for the late Changhsingian to Induan (Permian – Triassic transition), as well as other intervals

of the Phanerozoic (Bernasconi et al., 2017; Present et al., 2020; Johnson et al., 2021). The offset between these two archives, as well as observed $\delta^{34}\text{S}$ variability between coeval CAS samples (Fig. 8B) have been attributed to post-depositional alteration and/or an effect of different constituents (e.g., micrite, skeletal allochems, cements) of individual carbonate samples having different $\delta^{34}\text{S}$ values (Marenco et al., 2008; Present et al., 2015; 2020; Bernasconi et al., 2017). Considering thin section petrography observations from QIA samples (Fig. 9D) and the discordance between CAS $\delta^{34}\text{S}$ values for QIA relative to the offshore WMJ and JA successions, we endorse this interpretation.

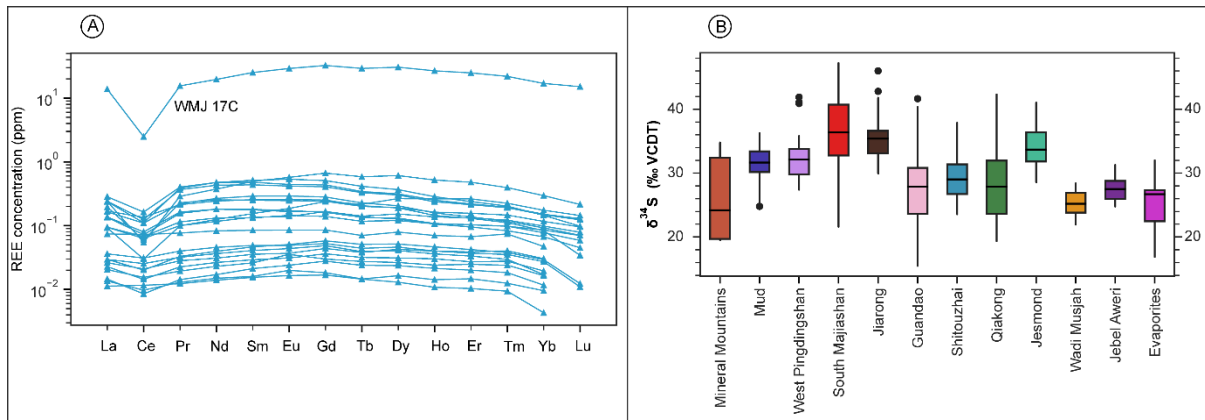


Figure 8. A) Post Archean Australian Shale (PAAS)-normalized spider diagram comparing the rare earth element concentrations for Olenekian carbonate samples from Wadi Musjah (WMJ). PAAS values are from Taylor and McLennan (1985). B) Box plots showing the distribution of CAS $\delta^{34}\text{S}$ values for Olenekian bulk carbonates and evaporites. Data sources are the same as for Figure 1 and evaporite data is from the $\delta^{34}\text{S}$ compilation of Present et al. (2020).

Nevertheless, a spatially consistent $\delta^{34}\text{S}$ trend discernible from the Olenekian CAS record upon (i) comparison of $\delta^{34}\text{S}$ records from individual sections (Fig. 1) or (ii) fitting a locally weighted scatter plot smoothing (LOWESS) model to the compiled CAS data (Fig. 10A) is that $\delta^{34}\text{S}$ values increase across the middle Smithian to SSB, followed by a gradual decrease during the Spathian. Also, a positive correlation between carbonate $\delta^{13}\text{C}$ and CAS $\delta^{34}\text{S}$ trends between the Smithian and early Spathian interval is observable. Hence, the increase in $\delta^{34}\text{S}_{\text{CAS}}$ values across the Smithian – Spathian transition is considered a primary global $\delta^{34}\text{S}$ trend during the Olenekian. Notably, this pattern is consistent with the sparse Olenekian evaporite record, which seems to indicate an increase in $\delta^{34}\text{S}$ between the middle and late Smithian followed by a Spathian decline towards the Anisian (Fig. 10B; see also Fig. 5 of Bernasconi et al., 2017). Furthermore, an increasing trend in Early Triassic evaporite $\delta^{34}\text{S}$ was previously documented by earlier workers, although with lower resolution age calibration (e.g., Holser, 1977; Claypool et al., 1980; Holser et al., 1988). Consequently, it is proposed that although some Olenekian CAS $\delta^{34}\text{S}$ values may have been altered by late diagenetic processes, primary global trends in seawater $\delta^{34}\text{S}$ evolution over the Olenekian are still preserved by this archive. Our JA and WMJ

$\delta^{34}\text{S}_{\text{CAS}}$ records are overall consistent with the inferred global trend for the Olenekian (Fig. 5, Fig. 6). Similarly, the QIA section records a trend of increasing $\delta^{34}\text{S}_{\text{CAS}}$ values across the SSB.

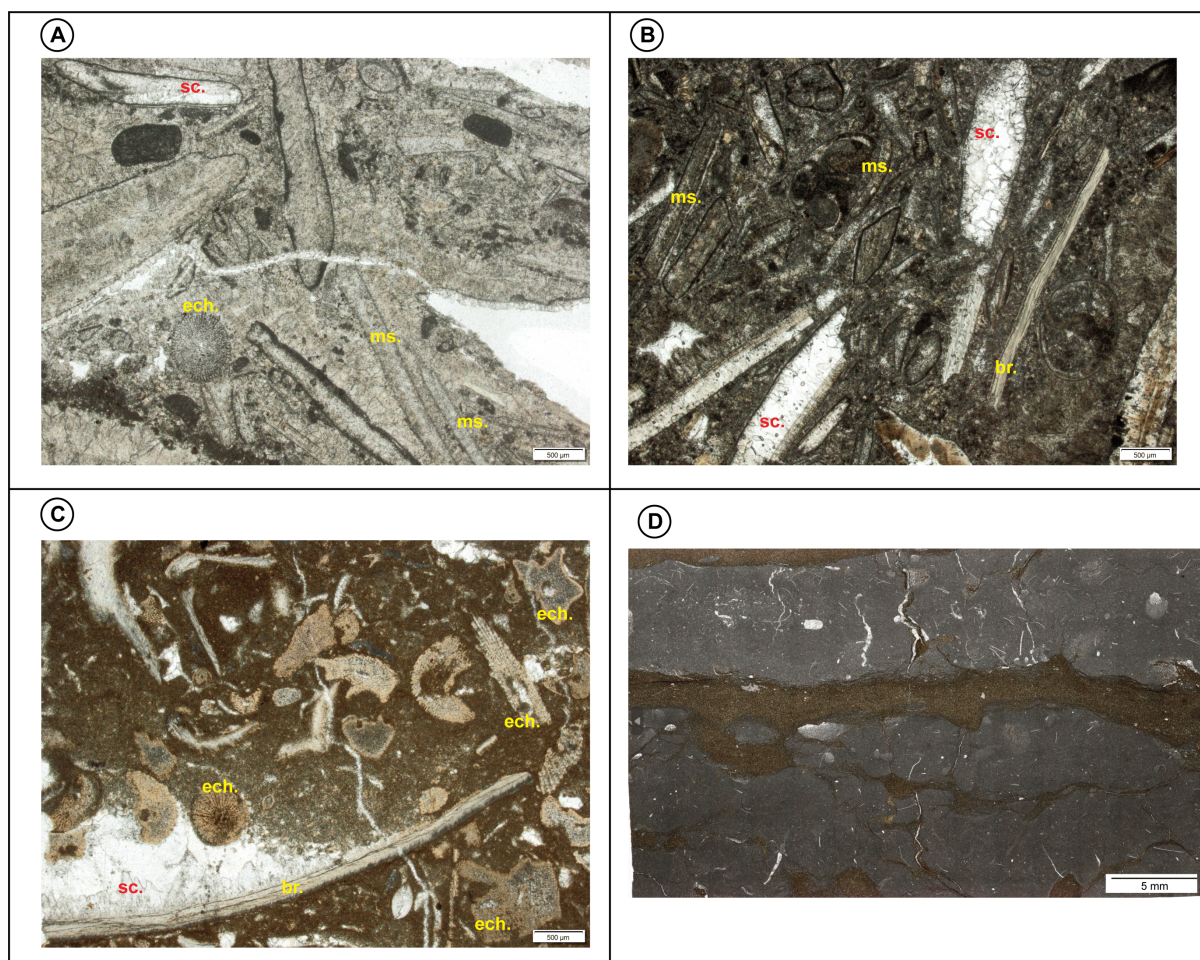


Figure 9. Representative thin section images of hand samples from the studied sections. A) Sample 13C, Jebel Aweri, late Smithian – early Spathian. Shell-supported biostrome sample with various skeletal fragments. B) Sample 29C, Jebel Aweri, late Smithian. Shell-supported biostrome sample with densely packed skeletal fragments. C) Sample 13C, Wadi Musjah, middle Smithian. Bivalve coquina biostrome sample with abundant echinoderm shell fragments. D) Sample 145C, Qiakong, Spathian. Nodular marly limestone with sponge spicules and brown silty-clay seams. Abbreviations – sc. = sparry calcite, ech. = echinoderm shell, br. = brachiopod shell, ms. = mollusc shell.

5.3 Interpretation of the Olenekian CAS isotopic records

Given the long residence time of seawater sulfate in the modern oceans, i.e., 13 – 20 Myr (Claypool et al., 1980; Walker, 1986), primary changes in seawater S-isotope compositions can be expected to only be observable within this temporal resolution. However, very rapid changes (< 10 Myr) in seawater $\delta^{34}\text{S}$ have been documented for different intervals of geologic time including the Devonian and Early Triassic (e.g., Holser, 1977; Claypool et al., 1980; Kampschulte and Strauss, 2004). As such, it has been suggested (e.g., Bottrell and Newton, 2006) that the oceanic residence time of sulfate was shorter in the

geologic past. This suggestion is supported by different evaporite fluid inclusion studies (e.g., Horita et al., 2002; Lowenstein et al., 2003), which indicate that ancient oceans had lower sulfate concentrations than is the case for modern oceans.

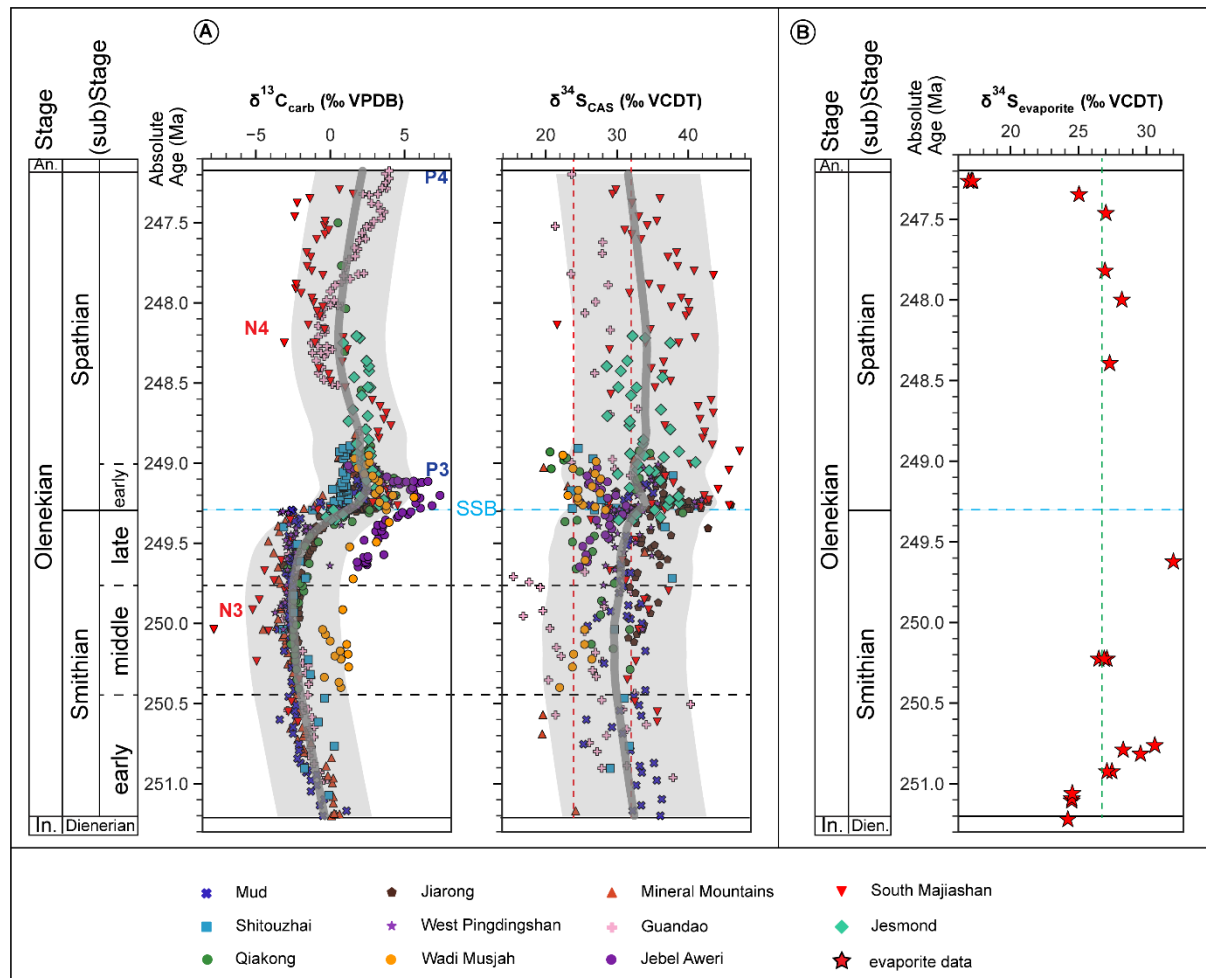


Figure 10. A) Absolute age calibrated compilation of previously published Olenekian $\delta^{13}\text{C}$ and $\delta^{34}\text{S}$ records and data from the current study. Literature $\delta^{13}\text{C}$ and $\delta^{34}\text{S}$ values are taken from the same sources given in Figure 1. B) Olenekian evaporite $\delta^{34}\text{S}$ record as compiled by Present et al. (2020). Absolute ages for the Smithian and Spathian are based on Widmann et al. (2020), Induan – Olenekian boundary and Olenekian – Anisian boundary ages are taken from the International Chronostratigraphic Chart 2023 (Cohen et al., 2013; updated). The nomenclature: N3, N4, P3, P4 depicts globally recognizable carbon isotope excursions after Song et al. (2013). In. = Induan, An. = Anisian. Dashed red lines on the CAS $\delta^{34}\text{S}$ record depict the range of Olenekian evaporite $\delta^{34}\text{S}$ values (Present et al., 2020 and references therein). The thick grey lines represent a Lowess regression fit to the data, and the associated grey band represents the 95 % confidence interval of the Lowess fit (see supplementary information for details on the implementation of the Lowess fit). The green vertical dashed line in B) depicts the median evaporite $\delta^{34}\text{S}$ value for the Olenekian (26.7 ‰).

Changes towards lower marine $\delta^{34}\text{S}_{\text{CAS}}$ values can be explained by increased inputs of sulfide-derived sulfur from weathering of continental sediments (typically $\delta^{34}\text{S}$ values of 0 to 10 ‰; Paytan et al. 1998) and/or of magmatic rocks or even direct volcanic sulfur inputs ($\delta^{34}\text{S}$ values: 0 to 3.5 ‰; Paytan et al., 1998). In addition, upwelling and oxidation of H_2S -rich bottom waters have been invoked to explain decreasing $\delta^{34}\text{S}_{\text{CAS}}$ trends (e.g., Zhang et al., 2015; Song et al., 2019). Alternatively, a decrease in the burial of reduced sulfur species in sediments or decreasing MSR rates may account for a trend towards lower $\delta^{34}\text{S}_{\text{CAS}}$ values (Bottrell and Newton, 2006; Halevy et al., 2012; Schobben et al., 2016). Primary CAS isotopic compositions can be altered via the reoxidation of reduced sulfate produced by MSR during early diagenesis, as well as the mixing of different CAS phases in an individual sample (Bottrell and Newton, 2006; Johnson et al., 2021).

The short-term $\delta^{34}\text{S}$ variability recorded for QIA prior to and after the SSB (Fig. 4), at odds with the global increasing CAS $\delta^{34}\text{S}$ trend (Fig. 10), may be explained by post-depositional incorporation of terrestrial sulfide-derived sulfur or the reoxidation of reduced sulfur species during early or late diagenesis. Inferred alteration of primary seawater CAS S-isotope compositions by the incorporation of terrestrial reduced sulfur species during diagenesis is also compatible with the nearshore continental shelf paleo-depositional environment of the QIA succession (Widmann et al., 2020; Leu et al., 2022) as well as enhanced continental weathering fluxes during the Olenekian (Sedlacek et al., 2014; Edward et al., 2024). Previous studies indicate that the SSB in the PaleoTethys was associated with a ca. 10 ‰ CAS $\delta^{34}\text{S}$ increase over 500 – 600 kyr (Lyu et al., 2019; Stebbins et al., 2019b; Du et al., 2022). However, the SSB of the QIA succession is characterized by a rapid increase in $\delta^{34}\text{S}$ values of 17 ‰ within ca. 55 kyr if the most extreme values around the SSB are considered (i.e., Q136C: 22.70 ‰, Q51: 24.40 ‰ and Q53: 39.25 ‰). Although consistent with an overall increase in $\delta^{34}\text{S}$ across the Smithian – Spathian transition, the magnitude and speed of the QIA $\delta^{34}\text{S}$ increase is very unlikely to represent a primary seawater $\delta^{34}\text{S}$ change. However, if the extreme $\delta^{34}\text{S}$ values at the SSB are not considered, an increase in $\delta^{34}\text{S}$ values is still recorded (i.e., 9 ‰ increase within ~ 400 kyr) which is more consistent with CAS records from other Tethyan localities. Nevertheless, the wide $\delta^{34}\text{S}$ range of the QIA succession (up to 20 ‰), as well as the rapid short-term changes in the CAS record of this section point to a significant influence of diagenetic processes on this CAS record. As such, the QIA section may be unsuitable for reliable interpretations of global $\delta^{34}\text{S}$ changes during the studied interval.

In contrast with the QIA section, the WMJ and JA $\delta^{34}\text{S}_{\text{CAS}}$ records, considered together, indicate a trend of increasing marine $\delta^{34}\text{S}_{\text{CAS}}$ values from the middle Smithian to SSB (Fig. 5, Fig. 6, Fig. S14B), consistent with the inferred global trend (Fig. 10). The middle Smithian to SSB $\delta^{34}\text{S}_{\text{CAS}}$ increasing trend can be explained by a decrease in continental weathering of sulfides, or by globally increased rates of net MSR and pyrite burial in Olenekian oceans (e.g., Stebbins et al., 2019a). Considering that the middle to early late Smithian was characterized by a warm climate regime (Hermann et al., 2011; Goudemand et al., 2019), elevated continental weathering fluxes (Sedlacek et al., 2014) and hence, an increase in

nutrient and organic carbon delivery to the oceans (Widmann et al., 2020), the preferred interpretation for the middle Smithian to SSB $\delta^{34}\text{S}_{\text{CAS}}$ trend is an increase in net marine MSR. Increased marine productivity over this interval likely facilitated dissolved oxygen depletion in the water column and increase in MSR. This inference is consistent with the Ce anomaly record for WMJ (Fig. 6), which shows that relative to the Spathian, the Smithian is characterized by higher Ce_{anom} values (i.e., close to 1), indicative of a poorly oxygenated water column (Liu et al., 2021). In addition, the inference of low dissolved oxygen in Smithian oceans is consistent with previous suggestions of expanded middle to late Smithian oceanic anoxia based on uranium isotope data (Zhang et al., 2018; Zhang et al., 2019), although it should be noted that there is no evidence for oceanic anoxia during the deposition of the Oman offshore carbonates themselves (Leu et al., 2023). Increase in MSR usually results in higher $\delta^{18}\text{O}$ values, albeit to a lower extent compared to $\delta^{34}\text{S}$ (Mizutani and Rafter, 1973; Fichtner et al., 2017). Enhanced MSR rates across the middle Smithian to SSB is thus, also supported by the $\delta^{18}\text{O}_{\text{CAS}}$ record, which displays an increasing trend during this interval in the studied sections.

The WMJ $\delta^{34}\text{S}_{\text{CAS}}$ profile (Fig. 6) is thus, at odds with previous suggestions that the middle Smithian negative CIE (N3) was associated with a trend towards lower $\delta^{34}\text{S}$ values due to causes related to climatic warming (e.g., Song et al., 2014). Similarly, the positive middle Smithian to SSB $\delta^{34}\text{S}$ trend for WMJ indicates that an increasing $\delta^{34}\text{S}_{\text{CAS}}$ trend during the Olenekian is not restricted to an interval of climatic cooling e.g., across the SSB. Enhanced nutrient delivery to marine environments across the middle to late Smithian resulted in increased accumulation and burial of OM on continental shelves, as evidenced by black shale deposition during the late Smithian (Widmann et al., 2020; Leu et al., 2022). However, increased OM accumulation and burial during the latest Smithian occurred within a cooling climate regime. As such, increased marine productivity across the SSB was probably facilitated by enhanced oceanic circulation and upwelling of nutrients from deeper ocean waters (Song et al., 2019). The consequent increased oxygen demand for OM respiration resulted in less oxygenated waters and would have favored increased MSR and pyrite burial in the oceans, as can be inferred from the global positive $\delta^{13}\text{C}$ and $\delta^{34}\text{S}$ excursions across the SSB (Fig. 10; Stebbins et al., 2019b).

The SSB increasing $\delta^{34}\text{S}$ trend for JA and WMJ was followed by a sharp $\delta^{34}\text{S}$ decrease at the base of the Spathian (UAZ 4) followed by a muted recovery (to higher values but still lower than during the SSB positive excursion) in UAZ 5 (Figs. 5, 6). Based on correlations with the QIA section, the WMJ and JA basal Spathian $\delta^{34}\text{S}$ decrease is estimated to have spanned ca. 180 kyr and predates the eventual $\delta^{34}\text{S}$ decrease recorded for other sections during the early Spathian (Fig. 1; Fig. 10). Two hypotheses may explain this negative $\delta^{34}\text{S}$ trend: 1) localized upwelling of H_2S -rich cold waters in the NeoTethys around the SSB or 2) Post-depositional alteration of the CAS S-isotope compositions of these samples. Several studies have suggested that the SSB was characterized by climatic cooling-mediated oceanic overturning circulation in contrast to the relatively stagnant ocean circulation of the middle Smithian (Lyu et al., 2019; Song et al., 2019; Zhang et al., 2015). Both WMJ and JA successions were deposited

on offshore topographic highs (i.e., seamounts) (Brühwiler et al., 2012; Leu et al., 2023). As such, the disruption of the flow of offshore currents as they encountered submarine topographic features like seamounts or ridges may have resulted in the upwelling of nutrient- and H₂S-rich deep waters to the surface during the earliest Spathian. Moreover, the C_{e_{anom}} record for WMJ (Fig. 6) strongly supports an early Spathian ocean oxygenation event, consistent with an inference of oxidation of upwelled H₂S-rich waters producing the δ³⁴S decline recorded. A similar scenario was proposed by Zhang et al. (2015) to explain the negative δ³⁴S excursion recorded at the SSB for the Shitouzhai section. However, this interpretation is argued against by the fact that the basal Spathian δ³⁴S decline is not recorded in other sections (except perhaps, Mud; Fig. 1), which should be the case considering that Early Triassic seawater sulfate concentrations are considered to have been much lower than that of the present day (e.g., Song et al., 2014; Bernasconi et al., 2017; Stebbins et al., 2019b). Hence, it is probably more likely that this negative trend reflects post-depositional alteration of CAS (e.g., via sulfide oxidation or incorporation of different CAS phases during late diagenesis; Johnson et al., 2021). Regardless of the actual explanation of this negative basal Spathian δ³⁴S trend, what is clear is that it is not a global marine δ³⁴S trend.

5.4 Seawater sulfate concentrations during the Olenekian

Quantitative estimates of ancient oceanic sulfate concentrations can be obtained by considering the fractionation between sulfate and sulfide ($\Delta^{34}\text{S}_{\text{sulfate-sulfide}}$) during MSR (the MSR-trend method), as well as the rate of change of sulfate δ³⁴S over a time interval of interest (the rate method; Song et al., 2014; Algeo et al., 2015). The rate method allows for an estimate of the maximum likely [SO₄²⁻]_{sw} concentration within a time interval of interest, whereas the MSR-trend method enables an estimate of mean [SO₄²⁻]_{sw} values (Algeo et al., 2015). An estimate of ancient seawater sulfate concentrations based on $\Delta^{34}\text{S}_{\text{sulfate-sulfide}}$ (MSR-trend method), however, requires an evaluation of the origin of the analyzed pyrite contained in the bulk rock (i.e., whether pyrite is cogenetic or not, and if its isotopic composition is of only local significance). In addition, $\Delta^{34}\text{S}_{\text{sulfate-sulfide}}$ is dependent on factors other than sulfate concentrations such as organic matter type, sulfate reduction rates and variability between sulfate reducing microbes (Song et al., 2014 and references therein). Alternatively, sulfate concentrations in ancient seawater can be estimated from fluid inclusions in evaporite rocks (e.g., Horita et al., 2002; Lowenstein et al., 2003; see also Turchyn and DePaolo; 2019).

Based on the rate method, Griesbachian – Smithian [SO₄²⁻]_{sw} concentration within the eastern PaleoTethys was estimated to be between 0.5 and 4.2 mM (Song et al., 2014), with the upper limit of this range being identical to previous estimates for the Permian – Triassic transition (Luo et al., 2010). Using Griesbachian – Dienerian evaporite δ³⁴S data, [SO₄²⁻]_{sw} values between 2 and 6 mM were estimated for the Early Triassic using the rate method (Bernasconi et al., 2017). More recently, mean [SO₄²⁻]_{sw} values between 2.5 and 9.1 mM based on the MSR-trend method have been proposed for the Smithian – Spathian transition using CAS δ³⁴S data for the Jesmond section (Stebbins et al., 2019b).

The absolute age constraint available for our studied sections (Widmann et al., 2020; Leu et al., 2023) permits an estimate of the rates of change of marine $\delta^{34}\text{S}$ values during the Olenekian. The WMJ and JA dataset considered together (Fig. S14), indicate a $\delta^{34}\text{S}$ change of ca. +9 ‰ within 1.14 Myr (i.e., between the middle Smithian to SSB), implying a rate of $\delta^{34}\text{S}$ change of ca. 8 ‰ Myr⁻¹. As there are no $\delta^{34}\text{S}_{\text{CRS}}$ measurements for these sections, a $\Delta^{34}\text{S}_{\text{CAS-CRS}}$ value of ca. 25 ‰ is assumed based on data for the Jesmond section, considering that this section was deposited in similar paleo-depositional environments as JA and WMJ (i.e., on offshore seamounts, Stebbins et al., 2019b). Based on the estimated rate of $\delta^{34}\text{S}$ change (8 ‰ Myr⁻¹) and a $\Delta^{34}\text{S}_{\text{CAS-CRS}}$ value of 25 ‰, the rate method is applied to reconstruct Olenekian $[\text{SO}_4^{2-}]_{\text{SW}}$ values. Using a pyrite burial flux (F_{PY}) of 4×10^{13} g yr⁻¹ (Song et al., 2014; Algeo et al., 2015) and 1×10^{14} g yr⁻¹ (Kah et al., 2004), we obtain $[\text{SO}_4^{2-}]_{\text{SW}}$ values between 2.8 mM and 7.0 mM, respectively for Olenekian seawater. Consequently, it is estimated that Olenekian seawater sulfate concentrations were between 2.8 and 7 mM or between 10 and 25 % of the modern $[\text{SO}_4^{2-}]_{\text{SW}}$ value. This estimated $[\text{SO}_4^{2-}]_{\text{SW}}$ range is identical to that previously proposed for the Early Triassic based on evaporite S-isotope data and using the rate method (2 – 6 mM; Bernasconi et al., 2017). The similarity between the CAS- and evaporite-based estimates strengthens the robustness of our estimated Olenekian $[\text{SO}_4^{2-}]_{\text{SW}}$ concentrations.

Reliable evaporite fluid inclusion estimates of Early Triassic $[\text{SO}_4^{2-}]_{\text{SW}}$ concentrations are so far lacking (Horita et al., 2002), precluding a direct comparison of our CAS-based Olenekian $[\text{SO}_4^{2-}]_{\text{SW}}$ concentration estimates with those from coeval evaporite fluid inclusion data. However, estimates of $[\text{SO}_4^{2-}]_{\text{SW}}$ concentration based on SO_4^{2-} content of fluid inclusions in halite deposits suggest that Middle Triassic (Ladinian) and Late Triassic (upper Carnian) seawater had minimum $[\text{SO}_4^{2-}]_{\text{SW}}$ concentrations of 14 and 13 mM, respectively (Horita et al., 2002; Lowenstein et al., 2003). Considering the upper threshold of our Olenekian $[\text{SO}_4^{2-}]_{\text{SW}}$ concentration estimate (7 mM), $[\text{SO}_4^{2-}]_{\text{SW}}$ concentrations may have doubled between the Early Triassic (early Spathian, ca. 249 Ma) and Middle Triassic (Ladinian, ca. 240 Ma).

A question that arises given low Olenekian $[\text{SO}_4^{2-}]_{\text{SW}}$ estimates is whether there would have been enough sulfate in Olenekian oceans to sustain MSR and pyrite burial over the middle Smithian to SSB, an interval of ca. 1.1 Myr. However, Olenekian Sr isotope records as well as increased clastic deposition during the middle to late Smithian (Sedlacek et al., 2014; Song et al., 2015; Widmann et al., 2020) suggest that sulfate input fluxes via continental weathering likely increased during this interval. Also, mercury records (Shen et al., 2019; Edward et al., 2024) and volcanic ash occurrence (Ovtcharova et al., 2006; Galfetti et al., 2007a; Widmann et al., 2020) are consistent with a scenario of increased volcanic sulfur input to the ocean-atmosphere system across the Smithian – Spathian transition. Furthermore, it has been suggested that the rate of change of oceanic S-isotope composition need not necessarily be coupled to sulfate concentrations if open ocean environments are the locus of pyrite burial instead of shelf settings (Rennie et al., 2018). However, it is currently unclear if this was the case

during the Early Triassic. In addition, $\Delta^{34}\text{S}_{\text{CAS-CRS}}$ data from the open ocean Jesmond section suggest that $[\text{SO}_4^{2-}]_{\text{SW}}$ concentrations remained constant across the SSB (Stebbins et al., 2019b). Based on these considerations, we suggest that seawater sulfate depletion due to MSR and pyrite burial was probably offset by sustained sulfate input fluxes during this interval.

5.5 Sulfur cycle box modeling constraints

To quantitatively constrain potential controls on the Olenekian marine sulfur cycle variations as recorded in the current study, simple sulfur cycle box model experiments were conducted to 1) explore the magnitude of change in the input and output fluxes of the sulfur cycle that are compatible with the magnitude and duration of the Olenekian $\delta^{34}\text{S}$ changes recorded, 2) evaluate the extent of sulfate-sulfide fractionation ($\Delta^{34}\text{S}_{\text{sulfate-sulfide}}$) that is compatible with the recorded CAS $\delta^{34}\text{S}$ trend and 3) assess the seawater sulfate concentrations that are consistent with the $\delta^{34}\text{S}$ variations. The box model used is a simple time-dependent sulfur cycle model described in Witts et al. (2018), which solves a system of two differential equations for the concentration and isotopic composition of marine sulfate as follows:

$$\frac{\partial S}{\partial t} = W_{\text{PYR}} + W_{\text{GYP}} - B_{\text{PYR}} - B_{\text{GYP}} \quad (6)$$

$$\frac{\partial(S \times \delta S)}{\partial t} = W_{\text{PYR}} \delta_{\text{PYR}} + W_{\text{GYP}} \delta_{\text{GYP}} - B_{\text{PYR}} (\delta_S - \Delta S) - B_{\text{GYP}} \delta_S \quad (7)$$

W_{PYR} is the weathering flux of pyrite (0.7×10^{12} mol/yr; He et al., 2020), W_{GYP} is the weathering flux of gypsum (1×10^{12} mol/yr; He et al., 2020), B_{PYR} is the burial flux of pyrite (varied in experiments, initial set to W_{PYR} value), B_{GYP} is the burial rate of gypsum ($W_{\text{GYP}} \left(\frac{S}{S_{\text{steady}}} \right)$), S_{steady} is the oceanic sulphate concentration at equilibrium (varied in experiments), δ_{PYR} and δ_{GYP} are the respective isotopic compositions of pyrite and gypsum ($\delta_{\text{PYR}} = -20$ ‰, Paytan et al. (1998); $\delta_{\text{GYP}} = 20$ ‰, Holser and Kaplan, 1966), and ΔS is the sulfur enrichment factor (varied in experiments).

Equation (6) represents the input and output fluxes of marine sulfate via burial and weathering. The S-isotope composition of seawater sulfate is resolved by computing $\delta S = \frac{(S \times \delta S)}{S}$ (Witts et al., 2018). Equations (6) and (7) are solved in Python using a 4th order Runge-Kutta method. In the model experiments, we use $\Delta^{34}\text{S}_{\text{CAS-CRS}}$ to represent the fractionation between sulfate and sulfide (i.e., ΔS in the model). Two scenarios are tested, using $\Delta S = 25$ ‰ (Stebbins et al., 2019b) and $\Delta S = 44$ ‰ (median $\Delta^{34}\text{S}_{\text{CAS-CRS}}$ value for the QIA dataset). Seawater sulfate concentrations (the model parameter: S_{steady}) were varied between 2.8 mM and 14 mM (i.e., the lower limit from our rate method calculations and the Middle Triassic evaporite fluid inclusion estimate). Results from the model experiments are presented in Figure 11.

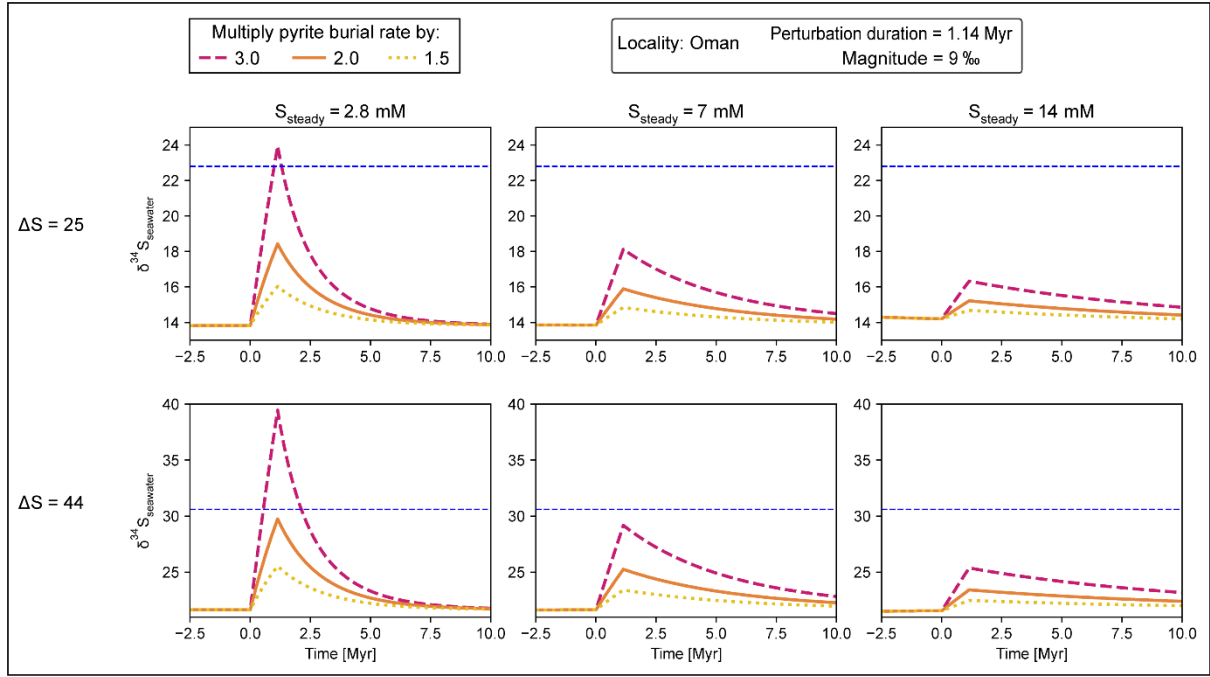


Figure 11. Sulfur cycle box modeling results showing the changes in pyrite burial fluxes required to reproduce the middle Smithian to Smithian – Spathian boundary (SSB) $\delta^{34}\text{S}$ increase recorded. The horizontal, blue, dashed lines mark the $\delta^{34}\text{S}$ peak value relative to equilibrium $\delta^{34}\text{S}$ values predicted by the model for $\Delta\text{S} = 25 \text{ ‰}$ (13.8 ‰) and $\Delta\text{S} = 44 \text{ ‰}$ (21.6 ‰).

We also estimated the expected increase in organic carbon burial during the late Smithian using the $\delta^{13}\text{C}$ record after Kump and Arthur (1999) based on the following equation:

$$f_{org} = \frac{\delta_w - \delta_{carb}}{\Delta_B} \quad (8)$$

f_{org} = fraction of buried organic carbon, δ_w = mantle $\delta^{13}\text{C}$ (-5 ‰; Kump and Arthur, 1999), δ_{carb} = carbonate $\delta^{13}\text{C}$, and Δ_B = difference between organic and carbonate $\delta^{13}\text{C}$ (for QIA = -29 ‰; Widmann, 2019). Based on the 6 ‰ positive CIE across the late Smithian to early Spathian (Widmann et al., 2020), organic carbon burial can be estimated to have increased by 200 % by the SSB. Considering that the rates of organic carbon and pyrite burial in non-euxinic marine sediments (such as those herein studied) have a constant ratio (Bernier and Raiswell, 1983), pyrite burial would have increased at most by a factor of 3 during the late Smithian.

In this case, model simulations indicate that an overall 9 ‰ $\delta^{34}\text{S}$ increase over 1.14 Myr recorded for the Oman offshore sections within the middle Smithian to SSB are only compatible with seawater sulfate concentrations around 2.8 mM and ΔS of 25 ‰ considering pyrite burial rate increase of 200 % as estimated during this interval (Fig. 11). Alternatively, sulfate concentrations closer to 7 mM are required for ΔS of 44 ‰ with the same rate of pyrite burial increase. As such, modeling constraints indicate that with either estimated $\Delta^{34}\text{S}_{\text{sulfate-sulfide}}$ of 25 ‰ or values closer to that of average modern

seawater (i.e., around 40 ‰; Bernasconi et al., 2017 and references therein), a much lower marine sulfate reservoir (in this case, 2.8 – 7 mM) is required for the magnitude and duration of the observed $\delta^{34}\text{S}$ increase. Consequently, given the compatibility of the rate method seawater sulfate concentration estimates with results from box model simulations, we propose that seawater sulfate concentrations during the Olenekian in the Tethys were at maximum ~ 7 mM or < 25 % of the modern seawater value. This $[\text{SO}_4^{2-}]_{\text{SW}}$ value is similar to the upper limit of the $[\text{SO}_4^{2-}]_{\text{SW}}$ range (2 – 6 mM) proposed for the Early Triassic based on evaporite $\delta^{34}\text{S}$ data (Bernasconi et al., 2017).

5.6 Implications for Olenekian marine faunal perturbations

Previous studies have suggested a causal link between faunal extinction around the SSB and the development of oceanic anoxia (e.g., Sun et al., 2015; Song et al., 2019). However, nekto-pelagic organisms, like conodonts and ammonoids, seem to have been less affected by late Smithian extinction than benthic communities (Stanley, 2007, 2008). Even marine level-bottom communities were likely not primarily impacted by marine environmental perturbations during the Early Triassic. Instead, the diversification pattern of most taxa and guilds shows an initial Early Triassic lag phase followed by a hyperbolic diversity increase during the early middle Anisian and was mainly driven by the intensity of biotic interactions (Friesenbichler et al., 2021).

Comparison of the current $\delta^{34}\text{S}$ record with the most recent analysis of conodont diversity in the studied successions (Leu et al., 2022; Leu et al., 2023) indicates that phases of increased nektonic faunal extinction and diversification alike coincide with the global middle Smithian to SSB $\delta^{34}\text{S}$ increase (interpreted as reflecting continuous depletion of water column dissolved oxygen, Figs. 4 – 6). Also, black shale deposition (suggestive of more reducing conditions) in QIA and coeval sections in the Nanpanjiang Basin, South China (Widmann et al., 2020; this study) coincides with both a conodont extinction phase and the onset of a diversification pulse at the end of the black shale interval (Fig. 4; Leu et al., 2022). Furthermore, the middle Smithian was marked by climatic warming followed by cooling at the SSB, as evidenced by sea surface temperature records (Romano et al., 2013; Goudemand et al., 2019). However, the warm middle Smithian interval was also characterized by a peak in Early Triassic ammonoid diversity (Brayard et al., 2006; Brühwiler et al., 2010; Brosse et al., 2013). These observations are at variance with the notion that oceanic anoxia or seawater temperature changes alone can explain faunal turnover during the Olenekian. Although, faunal diversification in the earliest Spathian did coincide with ocean oxygenation (Fig. 6) and seawater temperature decrease (Goudemand et al., 2019). It is important to note that various abiotic (and biotic) factors apart from dissolved oxygen levels, can act as stressors and impact the diversification rates of conodonts and their paleobiogeographic distribution (Goudemand et al., 2019; Leu et al., 2019). A recent study by Herrmann et al. (2015) indicates that the distribution of conodont biofacies was influenced by more physico-chemical properties than dissolved oxygen levels, such as salinity and nutrients. Furthermore,

it has been suggested that Early Triassic conodont biodiversity changes were predominantly impacted by both sea level and sea temperature fluctuations (Leu et al., 2019; Ginot and Goudemand, 2020). Additionally, Jattiot et al. (2018) proposed that sedimentary facies and depositional environment (i.e., vertically diverse graben-horst structures vs. vertically homogenous continental shelf areas) were the main influencers of the taxonomic composition of Smithian ammonoid assemblages. Taken together, the above enumerated considerations, as well as our data, suggest that marine dissolved oxygen levels alone are unlikely to explain the faunal perturbations that characterized the Smithian to Spathian transition. Instead, a combination of biotic and abiotic factors (such as nutrients, predation stress, intraspecific competition, and sea-level changes) probably influenced the Smithian – Spathian transition marine faunal perturbations, in agreement with previous similar suggestions (e.g., Herrmann et al., 2015; Jattiot et al., 2018; Goudemand et al. 2019).

6. Conclusions

The evolution of marine $\delta^{34}\text{S}$ across the middle Smithian to Spathian (Olenekian) are documented in the current study from continental shelf (QIA) and offshore (WMJ and JA) carbonate successions. Detailed assessments of the preservation of primary CAS isotopic information within the studied successions as well as comparisons with the sparse evaporite $\delta^{34}\text{S}$ record, allow us to conclude that the CAS isotopic compositions for the QIA section suffer from post-depositional alteration. However, near primary marine S-isotope compositions are mostly preserved by the offshore carbonates. In addition, an assessment of published Olenekian CAS $\delta^{34}\text{S}$ records relative to contemporaneous evaporite data suggests that the Olenekian CAS record only partially reflects primary seawater $\delta^{34}\text{S}$ values. The CAS record nonetheless preserves a primary global trend of increasing seawater $\delta^{34}\text{S}$ values across the middle Smithian to SSB followed by a gradual $\delta^{34}\text{S}$ decline during the Spathian. The middle Smithian – SSB global increasing $\delta^{34}\text{S}$ trend, observed also in our studied sections, is consistent with a global decrease in ocean dissolved oxygen and an increase in microbial sulfate reduction and pyrite burial. Other short-term variability in the CAS isotopic data, including a sharp $\delta^{34}\text{S}$ decrease at the basal Spathian observed for WMJ and JA, are interpreted as most likely reflective of post-depositional alteration of CAS. Based on sulfur cycling rate calculations and box modeling experiments, the inferred global sulfur cycle perturbations occurred within the context of a Olenekian seawater sulfate inventory that was between 10 and 25 % (2.8 – 7 mM) of that of modern seawater. Furthermore, results from the current study suggest that variations in oceanic dissolved oxygen levels, inferred from the $\delta^{34}\text{S}$ and REE data, are not consistently correlated to nektonic faunal changes during the Smithian to Spathian interval in the studied sections.

Data Availability

The dataset generated for this article is available at <https://dx.doi.org/10.17632/p5238ks2m5.3>, an open-source online data repository hosted at Mendeley Data (Edward et al., 2024b).

Acknowledgements

The authors thank Claudia Baumgartner, Laetitia Monbaron, Maxime Siegenthaler and Jessica Chaves (UNIL) for laboratory support. This study was funded by a Swiss National Science Foundation Sinergia Grant (Project Number: CRSII5_180253). SLH acknowledges financial support by the University of Geneva (S18173). Three anonymous reviewers are thanked for their constructive comments which improved the manuscript.

References

- Alibo, D.S., Nozaki, Y., 1999. Rare earth elements in seawater: particle association, shale-normalization, and Ce oxidation. *Geochimica et Cosmochimica Acta* 63, 363-372 DOI: [https://doi.org/10.1016/S0016-7037\(98\)00279-8](https://doi.org/10.1016/S0016-7037(98)00279-8).
- Algeo, T.J., Brayard, A., Richoz, S., 2019. The Smithian-Spathian boundary: A critical juncture in the Early Triassic recovery of marine ecosystems. *Earth-Science Reviews* 195, 1-6 DOI: <https://doi.org/10.1016/j.earscirev.2019.102877>.
- Algeo, T.J., Luo, G.M., Song, H.Y., Lyons, T.W., Canfield, D.E., 2015. Reconstruction of secular variation in seawater sulfate concentrations. *Biogeosciences* 12, 2131-2151 DOI: 10.5194/bg-12-2131-2015.
- Bagherpour, B., Bucher, H., Baud, A., Brosse, M., Vennemann, T., Martini, R., Guodun, K., 2017. Onset, development, and cessation of basal Early Triassic microbialites (BETM) in the Nanpanjiang pull-apart Basin, South China Block. *Gondwana Res* 44, 178-204 DOI: 10.1016/j.gr.2016.11.013.
- Bagherpour, B., Bucher, H., Vennemann, T., Schneebeli-Hermann, E., Yuan, D.X., Leu, M., Zhang, C., Shen, S.Z., 2020. Are Late Permian carbon isotope excursions of local or of global significance? *Geological Society of America Bulletin* 132, 521-544 DOI: 10.1130/B31996.1.
- Bagnoud-Velásquez, M., Spangenberg, J.E., Poiré, D.G., Gómez Peral, L.E., 2013. Stable isotope (S, C) chemostratigraphy and hydrocarbon biomarkers in the Ediacaran upper section of Sierras Bayas Group, Argentina. *Precambrian Research* 231, 388-400 DOI: <https://doi.org/10.1016/j.precamres.2013.04.001>.
- Barkan, Y., Paris, G., Webb, S.M., Adkins, J.F., Halevy, I., 2020. Sulfur isotope fractionation between aqueous and carbonate-associated sulfate in abiotic calcite and aragonite. *Geochimica et Cosmochimica Acta* 280, 317-339 DOI: <https://doi.org/10.1016/j.gca.2020.03.022>.
- Baud, A., Béchenec, F., Krystyn, L., Le Métour, J., Marcoux, J., Maury, R., Richoz, S., 2001. Permo-Triassic Deposits: from the Platform to the Basin and Seamounts. Conference on the Geology of Oman, Field guidebook, Excursion A01, Conference on the Geology of Oman, Field guidebook, Excursion A01, pp. 1-54 DOI: <https://www.researchgate.net/publication/236624812>.
- Baud, A., 2013. The Olenekian (early Triassic) Red Ammonoid Limestone, a time-specific facies on the Gondwana margin: Timor-Roof of the World-Oman connection. *Acta Geologica Sinica* 87, 894-931 DOI: https://doi.org/10.1111/1755-6724.12150_2.
- Bernasconi, S.M., Meier, I., Wohlwend, S., Brack, P., Hochuli, P.A., Bläsi, H., Wortmann, U.G., Ramseyer, K., 2017. An evaporite-based high-resolution sulfur isotope record of Late Permian and Triassic seawater sulfate. *Geochimica et Cosmochimica Acta* 204, 331-349.
- Berner, R.A., 1987. Models for carbon and sulfur cycles and atmospheric oxygen; application to Paleozoic geologic history. *Am J Sci* 287, 177-196 DOI: <https://dx.doi.org/10.2475/ajs.287.3.177>.
- Berner, R.A., Raiswell, R., 1983. Burial of organic carbon and pyrite sulfur in sediments over Phanerozoic time: a new theory. *Geochimica et Cosmochimica Acta* 47, 855-862 DOI: [https://doi.org/10.1016/0016-7037\(83\)90151-5](https://doi.org/10.1016/0016-7037(83)90151-5).
- Bottrell, S.H., Newton, R.J., 2006. Reconstruction of changes in global sulfur cycling from marine sulfate isotopes. *Earth-Science Reviews* 75, 59-83 DOI: <https://doi.org/10.1016/j.earscirev.2005.10.004>.
- Brayard, A., Bucher, H., Escarguel, G., Fluteau, F., Bourquin, S., Galfetti, T., 2006. The Early Triassic ammonoid recovery: Paleoclimatic significance of diversity gradients. *Palaeogeography, Palaeoclimatology, Palaeoecology* 239, 374-395 DOI: <https://doi.org/10.1016/j.palaeo.2006.02.003>.

Brosse, M., Brayard, A., Fara, E., Neige, P., 2013. Ammonoid recovery after the Permian–Triassic mass extinction: a re-exploration of morphological and phylogenetic diversity patterns. *Journal of the Geological Society* 170, 225-236 DOI: doi:10.1144/jgs2012-084.

Brühwiler, T., Bucher, H., Brayard, A., Goudemand, N., 2010. High-resolution biochronology and diversity dynamics of the Early Triassic ammonoid recovery: the Smithian faunas of the Northern Indian Margin. *Palaeogeography, Palaeoclimatology, Palaeoecology* 297, 491-501 DOI: <https://doi.org/10.1016/j.palaeo.2010.09.001>.

Brühwiler, T., Bucher, H., Goudemand, N., Galfetti, T., 2012. Smithian (Early Triassic) ammonoid faunas from Exotic Blocks from Oman: taxonomy and biochronology. *Palaeontographica. Abteilung A: Palaeozoologie-Stratigraphie* 296, 3-107 DOI: 10.1127/pala/296/2012/3.

Burdett, J.W., Arthur, M.A., Richardson, M., 1989. A Neogene seawater sulfur isotope age curve from calcareous pelagic microfossils. *Earth and Planetary Science Letters* 94, 189-198 DOI: 10.1016/0012-821x(89)90138-6.

Canfield, D.E., Raiswell, R., Westrich, J.T., Reaves, C.M., Berner, R.A., 1986. The use of chromium reduction in the analysis of reduced inorganic sulfur in sediments and shales. *Chemical Geology* 54, 149-155 DOI: [https://doi.org/10.1016/0009-2541\(86\)90078-1](https://doi.org/10.1016/0009-2541(86)90078-1).

Claypool, G.E., Holser, W.T., Kaplan, I.R., Sakai, H., Zak, I., 1980. The age curves of sulfur and oxygen isotopes in marine sulfate and their mutual interpretation. *Chemical Geology* 28, 199-260 DOI: [https://doi.org/10.1016/0009-2541\(80\)90047-9](https://doi.org/10.1016/0009-2541(80)90047-9).

Cohen, K.M., Finney, S.C., Gibbard, P.L., Fan, J.X., 2013; updated. The ICS International Chronostratigraphic Chart. *International Union of Geological Sciences* 36, 199-204 DOI: 10.18814/epiiugs/2013/v36i3/002.

Cortecci, G., Reyes, E., Berti, G., Casati, P., 1981. Sulfur and oxygen isotopes in Italian marine sulfates of Permian and Triassic ages. *Chemical Geology* 34, 65-79 DOI: [https://doi.org/10.1016/0009-2541\(81\)90072-3](https://doi.org/10.1016/0009-2541(81)90072-3).

De Baar, H.J.W., Bacon, M.P., Brewer, P.G., Bruland, K.W., 1985. Rare earth elements in the Pacific and Atlantic Oceans. *Geochimica et Cosmochimica Acta* 49, 1943-1959 DOI: [https://doi.org/10.1016/0016-7037\(85\)90089-4](https://doi.org/10.1016/0016-7037(85)90089-4).

Du, Y., Song, H., Algeo, T.J., Song, H., Tian, L., Chu, D., Shi, W., Li, C., Tong, J., 2022. A massive magmatic degassing event drove the Late Smithian Thermal Maximum and Smithian–Spathian boundary mass extinction. *Global and Planetary Change* 215, 103878 DOI: <https://doi.org/10.1016/j.gloplacha.2022.103878>.

[Dataset] Edward, Oluwaseun; Spangenberg, Jorge; Leu, Marc; Ragon, Charline; Le Houedec, Sandrine; Baud, Aymon; Bucher, Hugo; Vennemann, Torsten (2024b), “CAS isotopic and rare earth element concentration data for Olenekian carbonate rocks from Qiakong, Wadi Musjah and Jebel Aweri sections”, Mendeley Data, V3, doi: 10.17632/p5238ks2m5.3

Edward, O., Leu, M., Bucher, H., Le Houedec, S., Blattmann, F., Vérard, C., Adatte, T., Baud, A., Sonke, J.E., Vennemann, T., 2024. Evidence for variable provenance of Mercury anomalies during the Smithian–Spathian (Olenekian). *Global and Planetary Change* 232, 104343 DOI: 10.1016/j.gloplacha.2023.104343.

Fichtner, V., Strauss, H., Immenhauser, A., Buhl, D., Neuser, R.D., Niedermayr, A., 2017. Diagenesis of carbonate associated sulfate. *Chemical Geology* 463, 61-75 DOI: <https://doi.org/10.1016/j.chemgeo.2017.05.008>.

Friesenbichler, E., Hautmann, M., Bucher, H., 2021. The main stage of recovery after the end-Permian mass extinction: Taxonomic rediversification and ecologic reorganization of marine level-bottom communities during the Middle Triassic. *PeerJ* 9, e11654 DOI: 10.7717/peerj.11654.

- Galfetti, T., Bucher, H., Ovtcharova, M., Schaltegger, U., Brayard, A., Brühwiler, T., Goudemand, N., Weissert, H., Hochuli, P.A., Cordey, F., 2007a. Timing of the Early Triassic carbon cycle perturbations inferred from new U–Pb ages and ammonoid biochronozones. *Earth and Planetary Science Letters* 258, 593-604.
- Galfetti, T., Hochuli, P.A., Brayard, A., Bucher, H., Weissert, H., Vigran, J.O., 2007b. Smithian-Spathian boundary event: Evidence for global climatic change in the wake of the end-Permian biotic crisis. *Geology* 35, 291-294 DOI: <https://doi.org/10.1130/G23117A.1>.
- German, C.R., Elderfield, H., 1990. Application of the Ce anomaly as a paleoredox indicator: The ground rules. *Paleoceanography* 5, 823-833 DOI: <https://doi.org/10.1029/PA005i005p00823>.
- Gill, B.C., Lyons, T.W., Frank, T.D., 2008. Behavior of carbonate-associated sulfate during meteoric diagenesis and implications for the sulfur isotope paleoproxy. *Geochimica et Cosmochimica Acta* 72, 4699-4711 DOI: <https://doi.org/10.1016/j.gca.2008.07.001>.
- Gill, B.C., Lyons, T.W., Saltzman, M.R., 2007. Parallel, high-resolution carbon and sulfur isotope records of the evolving Paleozoic marine sulfur reservoir. *Palaeogeography, Palaeoclimatology, Palaeoecology* 256, 156-173 DOI: <https://doi.org/10.1016/j.palaeo.2007.02.030>.
- Genot, S., Goudemand, N., 2020. Global climate changes account for the main trends of conodont diversity but not for their final demise. *Global and Planetary Change* 195, 103325 DOI: <https://doi.org/10.1016/j.gloplacha.2020.103325>.
- Goudemand, N., Romano, C., Leu, M., Bucher, H., Trotter, J.A., Williams, I.S., 2019. Dynamic interplay between climate and marine biodiversity upheavals during the early Triassic Smithian - Spathian biotic crisis. *Earth-Science Reviews* 195, 169-178 DOI: <https://doi.org/10.1016/j.earscirev.2019.01.013>.
- Habicht, K.S., Canfield, D.E., 1996. Sulphur isotope fractionation in modern microbial mats and the evolution of the sulphur cycle. *Nature* 382, 342-343 DOI: 10.1038/382342a0.
- Halevy, I., Peters, S.E., Fischer, W.W., 2012. Sulfate Burial Constraints on the Phanerozoic Sulfur Cycle. *Science* 337, 331-334 DOI: [doi:10.1126/science.1220224](https://doi.org/10.1126/science.1220224).
- Harris, C.R., Millman, K.J., van der Walt, S.J., Gommers, R., Virtanen, P., Cournapeau, D., Wieser, E., Taylor, J., Berg, S., Smith, N.J., Kern, R., Picus, M., Hoyer, S., van Kerkwijk, M.H., Brett, M., Haldane, A., del Río, J.F., Wiebe, M., Peterson, P., Gérard-Marchant, P., Sheppard, K., Reddy, T., Weckesser, W., Abbasi, H., Gohlke, C., Oliphant, T.E., 2020. Array programming with NumPy. *Nature* 585, 357-362 DOI: 10.1038/s41586-020-2649-2.
- Hauser, M., Martini, R., Burns, S., Dumitrica, P., Krystyn, L., Matter, A., Peters, T., Zaninetti, L., 2001. Triassic stratigraphic evolution of the Arabian-Greater India embayment of the southern Tethys margin. *Eclogae Geologicae Helveticae* 94, 29-62 DOI: 10.5169/seals-168876.
- He, T., Dal Corso, J., Newton, R.J., Wignall, P.B., Mills, B.J.W., Todaro, S., Di Stefano, P., Turner, E.C., Jamieson, R.A., Randazzo, V., Rigo, M., Jones, R.E., Dunhill, A.M., 2020. An enormous sulfur isotope excursion indicates marine anoxia during the end-Triassic mass extinction. *Sci Adv* 6, eabb6704 DOI: 10.1126/sciadv.abb6704.
- Hermann, E., Hochuli, P.A., Bucher, H., Brühwiler, T., Hautmann, M., Ware, D., Roohi, G., 2011. Terrestrial ecosystems on North Gondwana following the end-Permian mass extinction. *Gondwana Res* 20, 630-637 DOI: <https://doi.org/10.1016/j.gr.2011.01.008>.
- Herrmann, A.D., Barrick, J.E., Algeo, T.J., 2015. The relationship of conodont biofacies to spatially variable water mass properties in the Late Pennsylvanian Midcontinent Sea. *Paleoceanography* 30, 269-283 DOI: <https://doi.org/10.1002/2014PA002725>.
- Holser, W.T., Kaplan, I.R., 1966. Isotope geochemistry of sedimentary sulfates. *Chemical Geology* 1, 93-135 DOI: [https://doi.org/10.1016/0009-2541\(66\)90011-8](https://doi.org/10.1016/0009-2541(66)90011-8).

Holser, W.T., 1977. Catastrophic chemical events in the history of the ocean. *Nature* 267, 403-408 DOI: 10.1038/267403a0.

Holser, W.T., Schidlowski, M., Mackenzie, F., Maynard, J., 1988. Geochemical cycles of carbon and sulfur, in: Gregor, C.B., Garrels, R.M., Mackenzie, F., Maynard, J.B. (Eds.), *Chemical Cycles in the Evolution of the Earth*. John Wiley & Sons, New York, pp. 105-173.

Horacek, M., Brandner, R., Richoz, S., Povoden-Karadeniz, E., 2010. Lower Triassic sulphur isotope curve of marine sulphates from the Dolomites, N-Italy. *Palaeogeography, Palaeoclimatology, Palaeoecology* 290, 65-70 DOI: <https://doi.org/10.1016/j.palaeo.2010.02.016>.

Horita, J., Zimmermann, H., Holland, H.D., 2002. Chemical evolution of seawater during the Phanerozoic: Implications from the record of marine evaporites. *Geochimica et Cosmochimica Acta* 66, 3733-3756 DOI: [https://doi.org/10.1016/S0016-7037\(01\)00884-5](https://doi.org/10.1016/S0016-7037(01)00884-5).

Hurtgen, M.T., Arthur, M.A., Suits, N.S., Kaufman, A.J., 2002. The sulfur isotopic composition of Neoproterozoic seawater sulfate: implications for a snowball Earth? *Earth and Planetary Science Letters* 203, 413-429 DOI: [https://doi.org/10.1016/S0012-821X\(02\)00804-X](https://doi.org/10.1016/S0012-821X(02)00804-X).

Insalaco, E., Virgone, A., Courme, B., Gaillot, J., Kamali, M., Moallemi, A., Lotfpour, M., Monibi, S., 2006. Upper Dalan Member and Kangan Formation between the Zagros Mountains and offshore Fars, Iran: depositional system, biostratigraphy and stratigraphic architecture. *GeoArabia* 11, 75-176 DOI: 10.2113/geoarabia110275.

Jattiot, R., Brayard, A., Bucher, H., Vennin, E., Caravaca, G., Jenks, J.F., Bylund, K.G., Escarguel, G., 2018. Palaeobiogeographical distribution of Smithian (Early Triassic) ammonoid faunas within the western USA basin and its controlling parameters. *Palaeontology* 61, 881-904 DOI: <https://doi.org/10.1111/pala.12375>.

Johnson, D.L., Present, T.M., Li, M., Shen, Y., Adkins, J.F., 2021. Carbonate associated sulfate (CAS) $\delta^{34}\text{S}$ heterogeneity across the End-Permian Mass Extinction in South China. *Earth and Planetary Science Letters* 574, 117172 DOI: 10.1016/j.epsl.2021.117172.

Jørgensen, B.B., 1982. Mineralization of organic matter in the sea bed—the role of sulphate reduction. *Nature* 296, 643-645 DOI: 10.1038/296643a0.

Jørgensen, B.B., Findlay, A.J., Pellerin, A., 2019. The Biogeochemical Sulfur Cycle of Marine Sediments. *Frontiers in Microbiology* 10 DOI: 10.3389/fmicb.2019.00849.

Kah, L.C., Lyons, T.W., Frank, T.D., 2004. Low marine sulphate and protracted oxygenation of the Proterozoic biosphere. *Nature* 431, 834-838 DOI: 10.1038/nature02974.

Kampschulte, A., Bruckschen, P., Strauss, H., 2001. The sulphur isotopic composition of trace sulphates in Carboniferous brachiopods: implications for coeval seawater, correlation with other geochemical cycles and isotope stratigraphy. *Chemical Geology* 175, 149-173 DOI: Doi 10.1016/S0009-2541(00)00367-3.

Kampschulte, A., Strauss, H., 2004. The sulfur isotopic evolution of Phanerozoic seawater based on the analysis of structurally substituted sulfate in carbonates. *Chemical Geology* 204, 255-286 DOI: <https://doi.org/10.1016/j.chemgeo.2003.11.013>.

Kaplan, I.R., Emery, K.O., Rittenberg, S.C., 1963. The Distribution and Isotopic Abundance of Sulphur in Recent Marine Sediments Off Southern California. *Geochimica Et Cosmochimica Acta* 27, 297-& DOI: Doi 10.1016/0016-7037(63)90074-7.

Kump, L.R., Arthur, M.A., 1999. Interpreting carbon-isotope excursions: carbonates and organic matter. *Chemical Geology* 161, 181-198 DOI: [https://doi.org/10.1016/S0009-2541\(99\)00086-8](https://doi.org/10.1016/S0009-2541(99)00086-8).

- Kwon, H., Woo, J., Oh, J.-R., Joo, Y.J., Lee, S., Nakrem, H.A., Sim, M.S., 2022. Responses of the biogeochemical sulfur cycle to Early Permian tectonic and climatic events. *Earth and Planetary Science Letters* 591, 117604 DOI: [10.1016/j.epsl.2022.117604](https://doi.org/10.1016/j.epsl.2022.117604).
- Lawrence, M.G., Greig, A., Collerson, K.D., Kamber, B.S., 2006. Rare Earth Element and Yttrium Variability in South East Queensland Waterways. *Aquatic Geochemistry* 12, 39-72 DOI: [10.1007/s10498-005-4471-8](https://doi.org/10.1007/s10498-005-4471-8).
- Leu, M., Bucher, H., Baud, A., Vennemann, T., Luz, Z., Hautmann, M., Goudemand, N., 2023. An expanded Smithian–Spathian (Lower Triassic) boundary from a reefal build-up record in Oman: implications for conodont taxonomy, high-resolution biochronology and the carbon isotope record. *Papers in Palaeontology* 9, e1481 DOI: <https://doi.org/10.1002/spp2.1481>.
- Leu, M., Bucher, H., Goudemand, N., 2019. Clade-dependent size response of conodonts to environmental changes during the late Smithian extinction. *Earth-Science Reviews* 195, 52-67 DOI: [10.1016/j.earscirev.2018.11.003](https://doi.org/10.1016/j.earscirev.2018.11.003).
- Leu, M., Bucher, H., Vennemann, T., Bagherpour, B., Ji, C., Brosse, M., Goudemand, N., 2022. A Unitary Association-based conodont biozonation of the Smithian–Spathian boundary (Early Triassic) and associated biotic crisis from South China. *Swiss Journal of Palaeontology* 141, 19 DOI: [10.1186/s13358-022-00259-x](https://doi.org/10.1186/s13358-022-00259-x).
- Liu, X.-M., Kah, L.C., Knoll, A.H., Cui, H., Wang, C., Bekker, A., Hazen, R.M., 2021. A persistently low level of atmospheric oxygen in Earth's middle age. *Nature Communications* 12, 351 DOI: [10.1038/s41467-020-20484-7](https://doi.org/10.1038/s41467-020-20484-7).
- Lowenstein, T.K., Hardie, L.A., Timofeeff, M.N., Demicco, R.V., 2003. Secular variation in seawater chemistry and the origin of calcium chloride basinal brines. *Geology* 31, 857-860 DOI: [10.1130/G19728R.1](https://doi.org/10.1130/G19728R.1).
- Luo, G., Kump, L.R., Wang, Y., Tong, J., Arthur, M.A., Yang, H., Huang, J., Yin, H., Xie, S., 2010. Isotopic evidence for an anomalously low oceanic sulfate concentration following end-Permian mass extinction. *Earth and Planetary Science Letters* 300, 101-111 DOI: <https://doi.org/10.1016/j.epsl.2010.09.041>.
- Lyons, T.W., Walter, L.M., Gellatly, A.M., Martini, A.M., Blake, R.E., 2004. Sites of anomalous organic remineralization in the carbonate sediments of South Florida, USA: The sulfur cycle and carbonate-associated sulfate, in: Amend, J.P., Edwards, K.J., Lyons, T.W. (Eds.), *Sulfur Biogeochemistry - Past and Present*. Geological Society of America, p. 0.
- Lyu, Z., Zhang, L., Algeo, T.J., Zhao, L., Chen, Z.-Q., Li, C., Ma, B., Ye, F., 2019. Global-ocean circulation changes during the Smithian–Spathian transition inferred from carbon-sulfur cycle records. *Earth-Science Reviews* 195, 114-132 DOI: <https://doi.org/10.1016/j.earscirev.2019.01.010>.
- Marenco, P.J., Corsetti, F.A., Kaufman, A.J., Bottjer, D.J., 2008. Environmental and diagenetic variations in carbonate associated sulfate: An investigation of CAS in the Lower Triassic of the western USA. *Geochimica et Cosmochimica Acta* 72, 1570-1582 DOI: <https://doi.org/10.1016/j.gca.2007.10.033>.
- Millero, F.J., 2013. *Chemical oceanography* (4th ed.). CRC press.
- Mizutani, Y., Rafter, T.A., 1973. Isotopic behaviour of sulphate oxygen in the bacterial reduction of sulphate. *GEOCHEMICAL JOURNAL* 6, 183-191 DOI: [10.2343/geochemj.6.183](https://doi.org/10.2343/geochemj.6.183).
- Newton, R.J., Pevitt, E.L., Wignall, P.B., Bottrell, S.H., 2004. Large shifts in the isotopic composition of seawater sulphate across the Permo–Triassic boundary in northern Italy. *Earth and Planetary Science Letters* 218, 331-345 DOI: [https://doi.org/10.1016/S0012-821X\(03\)00676-9](https://doi.org/10.1016/S0012-821X(03)00676-9).

- Orchard, M.J., 2007. Conodont diversity and evolution through the latest Permian and Early Triassic upheavals. *Palaeogeography, Palaeoclimatology, Palaeoecology* 252, 93-117 DOI: <https://doi.org/10.1016/j.palaeo.2006.11.037>.
- Ovtcharova, M., Bucher, H., Schaltegger, U., Galfetti, T., Brayard, A., Guex, J., 2006. New Early to Middle Triassic U-Pb ages from South China: Calibration with ammonoid biochronozones and implications for the timing of the Triassic biotic recovery. *Earth and Planetary Science Letters* 243, 463-475 DOI: [10.1016/j.epsl.2006.01.042](https://doi.org/10.1016/j.epsl.2006.01.042).
- Paris, G., Fehrenbacher, J.S., Sessions, A.L., Spero, H.J., Adkins, J.F., 2014. Experimental determination of carbonate-associated sulfate $\delta^{34}\text{S}$ in planktonic foraminifera shells. *Geochemistry, Geophysics, Geosystems* 15, 1452-1461 DOI: <https://doi.org/10.1002/2014GC005295>.
- Payne, J.L., Lehrmann, D.J., Wei, J., Orchard, M.J., Schrag, D.P., Knoll, A.H., 2004. Large Perturbations of the Carbon Cycle During Recovery from the End-Permian Extinction. *Science* 305, 506-509 DOI: [10.1126/science.1097023](https://doi.org/10.1126/science.1097023).
- Paytan, A., Kastner, M., Campbell, D., Thiemens, M.H., 1998. Sulfur Isotopic Composition of Cenozoic Seawater Sulfate. *Science* 282, 1459-1462 DOI: [doi:10.1126/science.282.5393.1459](https://doi.org/10.1126/science.282.5393.1459).
- Present, T.M., Paris, G., Burke, A., Fischer, W.W., Adkins, J.F., 2015. Large Carbonate Associated Sulfate isotopic variability between brachiopods, micrite, and other sedimentary components in Late Ordovician strata. *Earth and Planetary Science Letters* 432, 187-198 DOI: [10.1016/j.epsl.2015.10.005](https://doi.org/10.1016/j.epsl.2015.10.005).
- Present, T.M., Adkins, J.F., Fischer, W.W., 2020. Variability in Sulfur Isotope Records of Phanerozoic Seawater Sulfate. *Geophys Res Lett* 47, e2020GL088766 DOI: <https://doi.org/10.1029/2020GL088766>.
- Rennie, V.C.F., Paris, G., Sessions, A.L., Abramovich, S., Turchyn, A.V., Adkins, J.F., 2018. Cenozoic record of $\delta^{34}\text{S}$ in foraminiferal calcite implies an early Eocene shift to deep-ocean sulfide burial. *Nature Geoscience* 11, 761-765 DOI: <https://doi.org/10.1038/s41561-018-0200-y>.
- Romano, C., Goudemand, N., Vennemann, T.W., Ware, D., Schneebeil-Hermann, E., Hochuli, P.A., Brühwiler, T., Brinkmann, W., Bucher, H., 2013. Climatic and biotic upheavals following the end-Permian mass extinction. *Nature Geoscience* 6, 57-60 DOI: [10.1038/ngeo1667](https://doi.org/10.1038/ngeo1667).
- Schobben, M., Stebbins, A., Ghaderi, A., Strauss, H., Korn, D., Korte, C., 2016. Eutrophication, microbial-sulfate reduction and mass extinctions. *Commun Integr Biol* 9, e1115162 DOI: [10.1080/19420889.2015.1115162](https://doi.org/10.1080/19420889.2015.1115162).
- Schreurs, G., Immenhauser, A., 1999. West-northwest directed obduction of the Batain Group on the eastern Oman continental margin at the Cretaceous-Tertiary boundary. *Tectonics* 18, 148-160 DOI: <https://doi.org/10.1029/1998TC900020>.
- Sedlacek, A.R., Saltzman, M.R., Algeo, T.J., Horacek, M., Brandner, R., Foland, K., Denniston, R.F., 2014. $^{87}\text{Sr}/^{86}\text{Sr}$ stratigraphy from the Early Triassic of Zal, Iran: Linking temperature to weathering rates and the tempo of ecosystem recovery. *Geology* 42, 779-782.
- Shen, J., Algeo, T.J., Planaysky, N.J., Yu, J.X., Feng, Q.L., Song, H.J., Song, H.Y., Rowe, H., Zhou, L., Chen, J.B., 2019. Mercury enrichments provide evidence of Early Triassic volcanism following the end-Permian mass extinction. *Earth-Science Reviews* 195, 191-212 DOI: [10.1016/j.earscirev.2019.05.010](https://doi.org/10.1016/j.earscirev.2019.05.010).
- Song, H., Du, Y., Algeo, T.J., Tong, J., Owens, J.D., Song, H., Tian, L., Qiu, H., Zhu, Y., Lyons, T.W., 2019. Cooling-driven oceanic anoxia across the Smithian/Spathian boundary (mid-Early Triassic). *Earth-Science Reviews* 195, 133-146 DOI: [10.1016/j.earscirev.2019.01.009](https://doi.org/10.1016/j.earscirev.2019.01.009).
- Song, H., Tong, J., Algeo, T.J., Horacek, M., Qiu, H., Song, H., Tian, L., Chen, Z.-Q., 2013. Large vertical $\delta^{13}\text{C}_{\text{DIC}}$ gradients in Early Triassic seas of the South China craton: Implications for oceanographic changes related to Siberian Traps volcanism. *Global and Planetary Change* 105, 7-20 DOI: <https://doi.org/10.1016/j.gloplacha.2012.10.023>.

- Song, H., Tong, J., Algeo, T.J., Song, H., Qiu, H., Zhu, Y., Tian, L., Bates, S., Lyons, T.W., Luo, G., Kump, L.R., 2014. Early Triassic seawater sulfate drawdown. *Geochimica et Cosmochimica Acta* 128, 95-113 DOI: <https://doi.org/10.1016/j.gca.2013.12.009>.
- Song, H., Wignall, P.B., Tong, J., Song, H., Chen, J., Chu, D., Tian, L., Luo, M., Zong, K., Chen, Y., Lai, X., Zhang, K., Wang, H., 2015. Integrated Sr isotope variations and global environmental changes through the Late Permian to early Late Triassic. *Earth and Planetary Science Letters* 424, 140-147 DOI: <https://doi.org/10.1016/j.epsl.2015.05.035>.
- Spangenberg, J.E., Saintilan, N.J., Palinkas, S.S., 2022. Safe, accurate, and precise sulfur isotope analyses of arsenides, sulfarsenides, and arsenic and mercury sulfides by conversion to barium sulfate before EA/IRMS. *Anal Bioanal Chem* 414, 2163-2179 DOI: 10.1007/s00216-021-03854-y.
- Stanley, S.M., 2007. An Analysis of the History of Marine Animal Diversity. *Paleobiology* 33, 1-55.
- Stanley, S.M., 2008. Predation defeats competition on the seafloor. *Paleobiology* 34, 1-21 DOI: 10.1666/07026.1.
- Stanley, S.M., 2009. Evidence from ammonoids and conodonts for multiple Early Triassic mass extinctions. *Proceedings of the National Academy of Sciences* 106, 15264-15267 DOI: 10.1073/pnas.0907992106.
- Stebbins, A., Algeo, T.J., Krystyn, L., Rowe, H., Brookfield, M., Williams, J., Nye Jr, S.W., Hannigan, R., 2019a. Marine sulfur cycle evidence for upwelling and eutrophic stresses during Early Triassic cooling events. *Earth-Science Reviews* 195, 68-82 DOI: <https://doi.org/10.1016/j.earscirev.2018.09.007>.
- Stebbins, A., Algeo, T.J., Olsen, C., Sano, H., Rowe, H., Hannigan, R., 2019b. Sulfur-isotope evidence for recovery of seawater sulfate concentrations from a PTB minimum by the Smithian-Spathian transition. *Earth-Science Reviews* 195, 83-95 DOI: <https://doi.org/10.1016/j.earscirev.2018.08.010>.
- Strauss, H., 1993. The sulfur isotopic record of Precambrian sulfates: new data and a critical evaluation of the existing record. *Precambrian Research* 63, 225-246 DOI: [https://doi.org/10.1016/0301-9268\(93\)90035-Z](https://doi.org/10.1016/0301-9268(93)90035-Z).
- Strauss, H., 1997. The isotopic composition of sedimentary sulfur through time. *Palaeogeography, Palaeoclimatology, Palaeoecology* 132, 97-118 DOI: [https://doi.org/10.1016/S0031-0182\(97\)00067-9](https://doi.org/10.1016/S0031-0182(97)00067-9).
- Sun, Y.D., Wignall, P.B., Joachimski, M.M., Bond, D.P.G., Grasby, S.E., Sun, S., Yan, C.B., Wang, L.N., Chen, Y.L., Lai, X.L., 2015. High amplitude redox changes in the late Early Triassic of South China and the Smithian–Spathian extinction. *Palaeogeography, Palaeoclimatology, Palaeoecology* 427, 62-78 DOI: <https://doi.org/10.1016/j.palaeo.2015.03.038>.
- Taylor, S.R., McLennan, S.M., 1985. The continental crust: its composition and evolution.
- Thomazo, C., Brayard, A., Elmeknassi, S., Vennin, E., Olivier, N., Caravaca, G., Escarguel, G., Fara, E., Bylund, K.G., Jenks, J.F., Stephen, D.A., Killingsworth, B., Sansjofre, P., Cartigny, P., 2019. Multiple sulfur isotope signals associated with the late Smithian event and the Smithian/Spathian boundary. *Earth-Science Reviews* 195, 96-113 DOI: <https://doi.org/10.1016/j.earscirev.2018.06.019>.
- Toyama, K., Paytan, A., Sawada, K., Hasegawa, T., 2020. Sulfur isotope ratios in co-occurring barite and carbonate from Eocene sediments: A comparison study. *Chemical Geology* 535, 119454 DOI: <https://doi.org/10.1016/j.chemgeo.2019.119454>.
- Turchyn, A.V., DePaolo, D.J., 2019. Seawater Chemistry Through Phanerozoic Time. *Annual Review of Earth and Planetary Sciences* 47, 197-224 DOI: 10.1146/annurev-earth-082517-010305.
- Vérard, C., 2019. Panalexis: towards global synthetic palaeogeographies using integration and coupling of manifold models. *Geological Magazine* 156, 320-330 DOI: 10.1017/S0016756817001042.

Walker, J.C.G., 1986. Global geochemical cycles of carbon, sulfur and oxygen. *Marine Geology* 70, 159-174 DOI: [https://doi.org/10.1016/0025-3227\(86\)90093-9](https://doi.org/10.1016/0025-3227(86)90093-9).

Widmann, P., Bucher, H., Leu, M., Vennemann, T., Bagherpour, B., Schneebeli-Hermann, E., Goudemand, N., Schaltegger, U., 2020. Dynamics of the largest carbon isotope excursion during the Early Triassic biotic recovery. *Front Earth Sc-Switz*, 196 DOI: <https://doi.org/10.3389/feart.2020.00196>.

Widmann, P.A., 2019. Temporal calibration and quantification of Early Triassic climatic disturbances through high-precision U-Pb zircon dating and an improved chemical abrasion procedure, Département des sciences de la Terre. Université de Genève, Genève DOI: [10.13097/archive-ouverte/unige:121676](https://doi.org/10.13097/archive-ouverte/unige:121676).

Witts, J.D., Newton, R.J., Mills, B.J.W., Wignall, P.B., Bottrell, S.H., Hall, J.L.O., Francis, J.E., Alistair Crame, J., 2018. The impact of the Cretaceous–Paleogene (K–Pg) mass extinction event on the global sulfur cycle: Evidence from Seymour Island, Antarctica. *Geochimica et Cosmochimica Acta* 230, 17-45 DOI: <https://doi.org/10.1016/j.gca.2018.02.037>.

Wortmann, U.G., Bernasconi, S.M., Böttcher, M.E., 2001. Hypersulfidic deep biosphere indicates extreme sulfur isotope fractionation during single-step microbial sulfate reduction. *Geology* 29, 647-650 DOI: [https://doi.org/10.1130/0091-7613\(2001\)029<0647:HDBIES>2.0.CO;2](https://doi.org/10.1130/0091-7613(2001)029<0647:HDBIES>2.0.CO;2).

Wotte, T., Shields-Zhou, G.A., Strauss, H., 2012a. Carbonate-associated sulfate: Experimental comparisons of common extraction methods and recommendations toward a standard analytical protocol. *Chemical Geology* 326-327, 132-144 DOI: <https://doi.org/10.1016/j.chemgeo.2012.07.020>.

Zhang, F., Algeo, T.J., Cui, Y., Shen, J., Song, H., Sano, H., Rowe, H.D., Anbar, A.D., 2019. Global-ocean redox variations across the Smithian-Spathian boundary linked to concurrent climatic and biotic changes. *Earth-Science Reviews* 195, 147-168.

Zhang, F., Romaniello, S.J., Algeo, T.J., Lau, K.V., Clapham, M.E., Richoz, S., Herrmann, A.D., Smith, H., Horacek, M., Anbar, A.D., 2018. Multiple episodes of extensive marine anoxia linked to global warming and continental weathering following the latest Permian mass extinction. *Science Advances* 4, e1602921 DOI: [doi:10.1126/sciadv.1602921](https://doi.org/10.1126/sciadv.1602921).

Zhang, L., Zhao, L., Chen, Z.Q., Algeo, T.J., Li, Y., Cao, L., 2015. Amelioration of marine environments at the Smithian-Spathian boundary, Early Triassic. *Biogeosciences* 12, 1597-1613 DOI: [10.5194/bg-12-1597-2015](https://doi.org/10.5194/bg-12-1597-2015).

CHAPTER 4

Author contributions

Oluwaseun Edward: Conceptualization, Formal analysis, Data curation, Investigation, Data Analysis, Data visualization, Writing - original draft, Writing - review and editing.

Sandrine Le Houedec: Investigation, Validation, Data Curation.

Aymon Baud: Investigation, Resources, Validation, Writing - review and editing.

Thomas Brühwiler: Investigation, Resources, Validation.

Hugo Bucher: Funding Acquisition, Project Administration, Resources.

Torsten Vennemann: Conceptualization, Funding Acquisition, Project Administration, Resources, Supervision, Writing - review and editing.

Carbonate Clumped Isotope Constraints on Early Triassic NeoTethyan Seawater Oxygen Isotope Compositions and Temperatures

Oluwaseun Edward^{1*}, Sandrine Le Houedec², Aymon Baud³, Thomas Brühwiler⁴, Hugo Bucher⁴,
Torsten Vennemann¹

¹Institute of Earth Surface Dynamics, Géopolis, University of Lausanne, CH-1015 Lausanne, Switzerland

²Department of Earth Sciences, Université de Genève, Rue des Maraîchers 13, CH-1205 Genève, Switzerland

³Institute of Earth Sciences, Géopolis, University of Lausanne, CH-1015 Lausanne, Switzerland

⁴Paläontologisches Institut der Universität Zürich, Karl-Schmid-Strasse 4, 8006 Zürich, Switzerland

*Corresponding author | E-mail: oluwaseun.edward@unil.ch

Keywords: Early Triassic, brachiopods, clumped isotopes, oxygen isotope compositions

Abstract

Carbonate clumped isotope thermometry is a valuable tool to estimate past seawater temperatures and hence, oxygen isotope compositions ($\delta^{18}\text{O}_{\text{sw}}$). Both these parameters are valuable for examining marine faunal evolution in the context of changing climate during the geological past. The current study reconstructs NeoTethyan $\delta^{18}\text{O}_{\text{sw}}$ and temperatures during the Early Triassic using clumped isotope analysis of articulate brachiopod fossils and micritic whole rock carbonates. Diagenetic alteration of the analyzed material is assessed by means of a suite of optical, geochemical, and statistical techniques, which together, suggest that both near-primary and diagenetically altered fossilized carbonate is present. Based on replicate analysis of the best-preserved brachiopod calcite and whole rock carbonate samples, NeoTethyan seawater $\delta^{18}\text{O}_{\text{sw}}$ is interpreted to have had values of between 0.5 ± 1.1 ‰ VSMOW during the Dienerian (Induan) and -0.7 ± 0.8 ‰ during the Smithian – Spathian (Olenekian). Furthermore, during the early to middle Dienerian, seawater temperatures probably increased, congruent with previously published conodont $\delta^{18}\text{O}$ values. In contrast, during the latest Smithian to earliest Spathian, temperatures were relatively lower (ca. 25 °C), as also indicated by coeval conodont paleotemperature records. These results are compatible with the notion that biotic turnover at the Smithian-Spathian boundary was associated with climatic cooling and suggest that seawater $\delta^{18}\text{O}$ values during the Early Triassic were within the expected range for an ice-free world (ca. -1 ‰ VSMOW).

1. Introduction

Reconstructions of past seawater temperatures are a crucial part of paleoclimate research, which enables scientists to track periods of climatic warming or cooling throughout Earth's history, and to investigate the links between climate change and biotic events (e.g., Veizer and Hoefs, 1976; Veizer et al., 1986; Veizer et al., 1999; Trotter et al., 2008; Joachimski et al., 2012; Romano et al., 2013; Scotese et al., 2021; Grossman and Joachimski, 2022). One of the most common methods of such a reconstruction is based on oxygen isotope paleothermometry applied to fossilized marine carbonates (e.g., Epstein et al., 1951; Urey et al., 1951; Emiliani, 1955). This paleothermometer leverages the temperature dependence of oxygen isotope fractionation between ambient water and authigenic minerals such as carbonates and phosphates (Grossman, 2012). As an example of such an application, the latest Permian to Early Triassic interval (252 – 247.2 Ma), marked by the largest mass extinction of the Phanerozoic and subsequent biotic perturbations, conodont oxygen isotope studies indicate a general “hothouse” climate and large seawater surface temperature fluctuations (Korte et al., 2010; Joachimski et al., 2012; Sun et al., 2012; Romano et al., 2013; Goudemand et al., 2019; Joachimski et al., 2022). However, the reliability of inferred Early Triassic seawater temperature changes is complicated by the need to assume the oxygen isotope composition of ambient seawater ($\delta^{18}\text{O}_{\text{sw}}$), necessary for deriving absolute seawater temperatures from conodont $\delta^{18}\text{O}$ values.

Carbonate clumped isotope thermometry enables a direct estimate of marine carbonate precipitation temperatures without the need for knowledge of the O-isotope composition of the ambient seawater. In turn, seawater $\delta^{18}\text{O}$ values can be calculated from a clumped isotope-derived temperature and the O-isotope composition of the analyzed carbonate mineral (Ghosh et al., 2006; Schauble et al., 2006; Eiler, 2007; Eiler, 2011; Huntington and Lechler, 2015). This technique is based on the thermodynamically controlled occurrence of carbonate ions that contain both the heavy carbon (^{13}C) and oxygen (^{18}O) isotopes relative to a stochastic distribution of all isotopes in the carbonate lattice. This so-called clumping of the heavy isotopes within the carbonate lattice is thermodynamically favored at lower temperatures (Schauble et al., 2006) and is transferred to the CO_2 extracted from the mineral by acid digestion as an anomalously high abundance of the mass 47 isotopologue of CO_2 , the Δ_{47} composition of carbonates (Ghosh et al., 2006). A growing number of studies have utilized carbonate clumped isotope thermometry for reconstructing seawater temperatures and oxygen isotope compositions in the geologic past with success (e.g., Came et al., 2007; Price and Passey, 2013; Bergmann et al., 2018a; de Winter et al., 2021; Goldberg et al., 2021). The utility of carbonate Δ_{47} compositions for paleoenvironmental studies can be hindered by thermally induced solid state reordering of the C-O bonds in the carbonate crystal lattice, which resets the carbonate Δ_{47} composition (Passey and Henkes, 2012; Stolper and Eiler, 2015; Looser et al., 2023). However, under certain circumstances, Δ_{47} compositions affected by reordering may still preserve records of paleotemperature change (Lawson et al., 2017; Fernandez et al., 2021). Also, some studies have shown that Δ_{47} temperature estimates for

material deposited within the same sedimentary bed can be variable due to different degrees of carbonate recrystallization or solid-state reordering (Winkelstern and Lohmann, 2016; Bergmann et al., 2018b), highlighting the need for rigorous assessments of the preservation state of carbonate material being used for clumped isotope analysis.

The current study attempts to determine seawater oxygen isotope compositions through clumped isotope thermometry of marine carbonates precipitated during the Early Triassic. Our study is based on rare preserved articulate brachiopod fossils, complemented by micritic whole rock carbonates that were deposited in the NeoTethys Ocean during the Early Triassic (Dienerian to Spathian) but today occur as exotic blocks in eastern Oman (Baud et al., 2012; Souquet and Goudemand, 2020; Leu et al., 2023). We evaluate the preservation of the analyzed carbonates using a suite of optical, geochemical, and statistical methods, and test the utility of whole rock material recovered from Induan-aged lime mud strata to preserve near-primary seawater compositions.

2. Sample localities

Investigated fossil brachiopod and whole rock samples originate from four carbonate exotic blocks that were deposited in the NeoTethys Ocean during the Early Triassic. These are: Ras al Jin 2 block (RAJ2), Wadi ad Daffah 2 block (WAD2), Wadi Musjah block (WMJ) and Jebel Aweri block (JA) (Fig. 1). Except for RAJ2, the sample localities and geological setting of the studied carbonate successions have been described in previous studies: WAD2: (Souquet and Goudemand, 2020), WMJ and JA (Brühwiler et al., 2012; Luz, 2022; Leu et al., 2023). As such, only the RAJ2 succession is described herein. The RAJ2 succession is an exotic block *sensu* Pillevuit et al. (1997), which is situated within the Batain Plain of eastern Oman, about 25 km South of Ras al Hadd at GPS coordinates: 22°25'59.7" N, 59°45'35.0" E. Similar to the WMJ and JA successions, RAJ2 is found alongside rock successions of the Middle Jurassic Guwayza Formation. The RAJ2 block represents one of many exotic blocks originating from the partial destruction of the proximal Triassic Batain Basin during the Late Jurassic, which resulted in the redeposition of Permian to Triassic rocks within Middle Jurassic rock successions (Hauser et al., 2002; Baud et al., 2012; Souquet and Goudemand, 2020). The Guwayza Formation comprises Late Bajocian to Early Bathonian radiolarian chert beds, containing up to 4 m-thick oolitic turbidites at the base. About 21 m above the base of the Guwayza Fm., debris flow units of two to tens of meters thickness occur. These rock units comprise large boulders – the Ad Daffah facies of Hauser et al. (2001; 2002) – containing Early Triassic fossiliferous limestones which outcrop in many localities within the Batain Plain, Oman (e.g., Brühwiler et al., 2012; Brosse et al., 2019; Souquet and Goudemand, 2020; Leu et al., 2023). The RAJ2 succession is one of such boulders. It is condensed, being ca. 1 m-thick and contains early Dienerian to early Smithian ammonoids (Fig. 2).

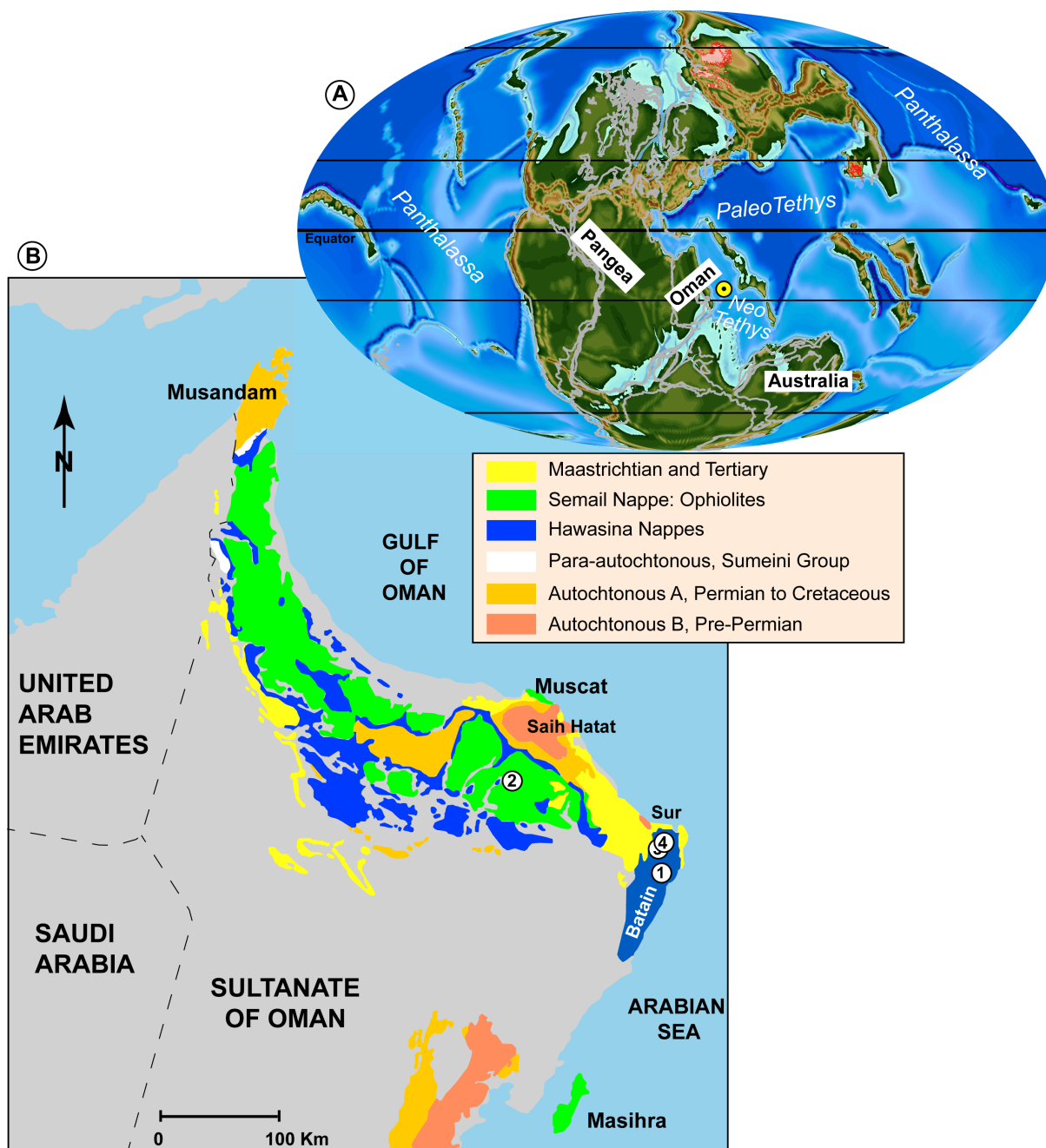


Figure 1. A) Global paleogeographical map of the Early Triassic based on the Panalesis model (Vérard, 2019), with the paleo-location of Oman denoted (yellow circle), and B) geological map of the Oman area showing the present-day location of the sections studied. 1 – Jebel Aweri section, 2 – Wadi Musjah, 3 – Wadi ad Daffah, 4 – Ras al Jin.

RAJ2 includes macrofossil-rich and macrofossil-depleted strata alike, varying in thickness from a few to several centimetres (Fig. 2). In the macrofossil-depleted succession, both microspheres and silty debris lime wackestone occur. The macrofossil-rich accumulation varies from transported graded crushed shells to unabraded and well-sorted molluscs with ammonoid and/or bivalve concentrations (Fig. 3). Fossil preservation and the sediment grain size variation, as noted from thin sections (Fig. 3)

indicate a large range of depositional energies, suggestive of a distal offshore deep-shelf (seamount) depositional environment above fair weather wave base with proximal to distal tempestites and bottom currents. Within Unit A of RAJ2 (Fig. 2) and beds M and P of WAD2 (Fig. 2C of Souquet & Goudemand, (2020); Fig. S4), layers of very fine-grained laminated lime mud termed “couche caramel” occur (Fig. 3). These strata comprise very fine (~ 20 μm) equigranular, porous micrite (Fig. 3). Based on laboratory experiments, these usually precipitate in cool waters (around 15 °C, Nicolas Meisser, personal communication).

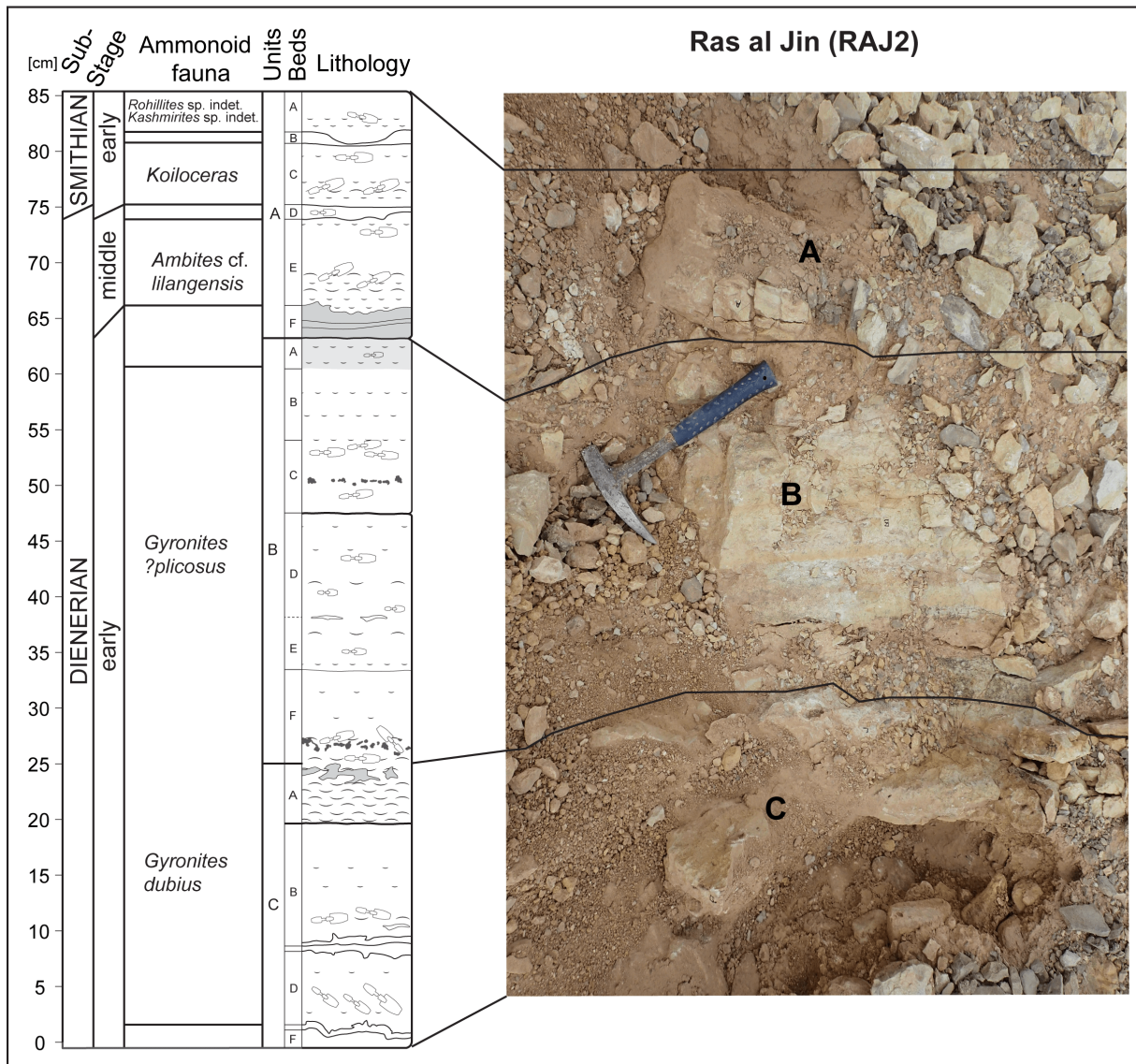


Figure 2. Lithological log and field photograph of the RAJ2 succession. The “couche caramel” bed corresponds to Unit AF. Geological hammer for scale.

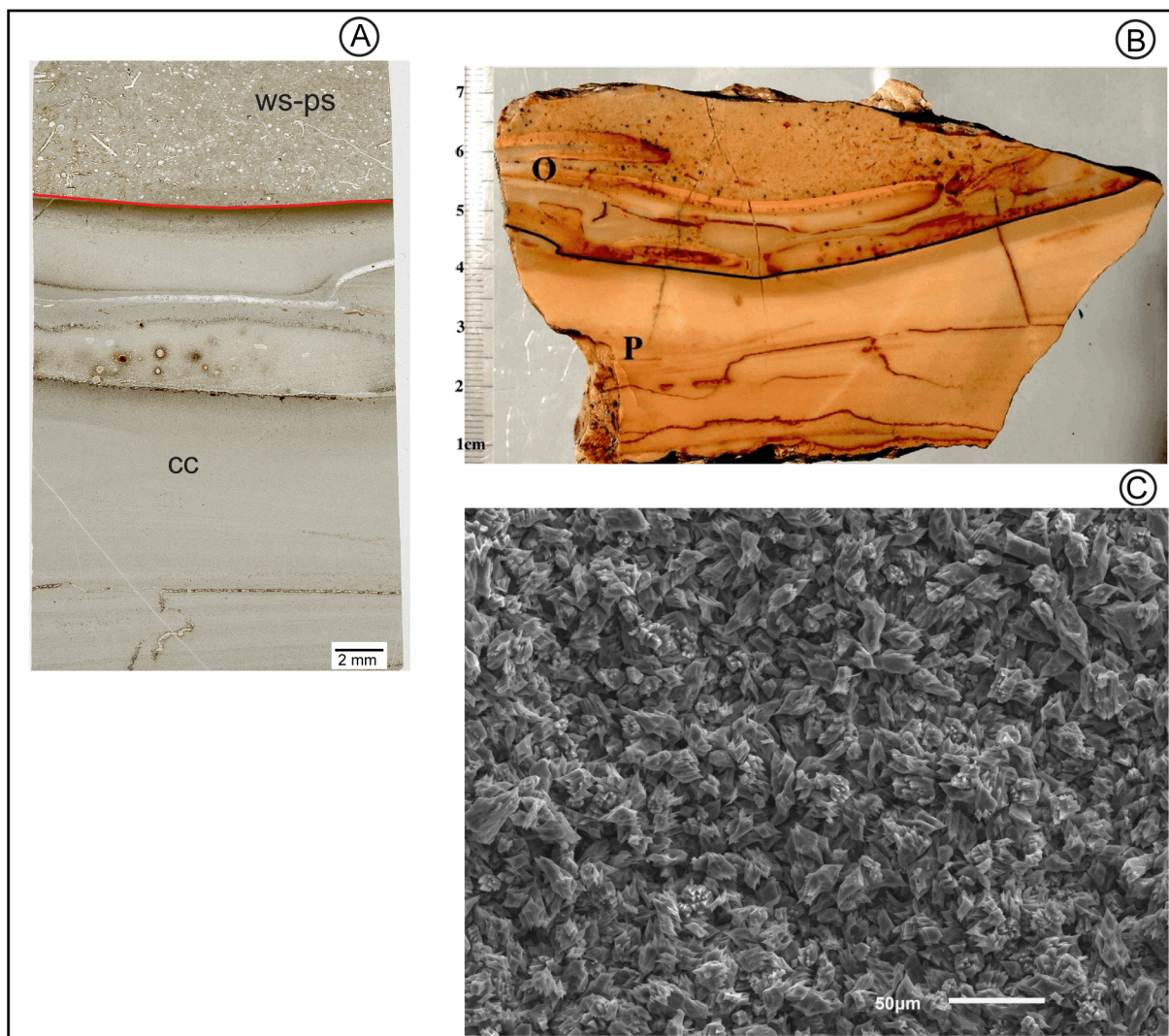


Figure 3. A) Thin section photomicrograph, B) polished section and C) scanning electron image of sample WAD2 P – the “couche caramel” layer in the Wadi ad Daffah 2 section. cc: “couche caramel”, ws-ps: wackestone – packstone.

3. Methods

Samples analyzed include fossil brachiopod calcite shell splinters and bulk rock carbonates, the latter including the micritic whole rock material from the “couche caramel” beds of WAD2 and RAJ2, which are of Dienerian (Induan) age. Fossil brachiopods from the WMJ and JA sections are Smithian – Spathian (Olenekian). The Olenekian biogenic calcite samples are complemented by micritic bulk carbonate material from the same beds. In addition, calcite veins and sparry calcite samples were analyzed for comparison. For samples other than biogenic calcite, material for analysis ($n = 77$) was extracted from cut and polished hand samples using a microdrill with a 1 mm diamond drill bit. For every brachiopod-bearing bed (Table 1), several brachiopod fossils were sampled. Using a scalpel, brachiopod calcite shell material was extracted i) across the entire fossil shell and ii) separately from brachial and pedicle valves of individual fossil shells. This sampling strategy enabled the extraction of

several subsamples for replicate analysis, facilitating the measurement of the range of precipitation temperatures recorded within each brachiopod fossil.

3.1 Clumped isotope analysis

About 500 μg (for small samples) or 4500 μg (for big samples) of material was weighed into 2 ml glass vials for clumped isotope (Δ_{47}) analysis. Measurements were conducted over several analytical sessions between 2018 and 2022 at the Institute of Earth Surface Dynamics, University of Lausanne (UNIL) using a Nu Perspective isotope ratio mass spectrometer fitted with a NuCarb sample preparation device (see supplementary information). Precision was monitored by repeated measurements of carbonate reference materials: ETH-1, -2, and -3 (Bernasconi et al., 2018; 2021), as well as our in-house Carrara Marble standard (CM2) used for routine carbon and oxygen isotope analyses. Within-run analytical precision is reported conservatively using the ETH standard with the highest standard deviation (1 sd) and was on average 0.022 ‰ for the individual sequences. However, over the course of all analytical sessions between 2018 and 2022, analytical uncertainty was 0.015 ‰ for large sample aliquots (ca. 4500 μg) and on average 0.020 ‰ for small (ca. 500 μg) sample aliquots (see supplementary data). Final Δ_{47} values are reported with respect to the interlaboratory carbon dioxide equilibration scale (I-CDES) (Bernasconi et al., 2021). Δ_{47} values were calculated by normalization against accepted Δ_{47} values for ETH-1, -2, and -3 (Bernasconi et al., 2021) projected to a 90 °C acid reaction and applying an acid correction factor of 0.088 ‰ (Petersen et al., 2019; Bernasconi et al., 2021). Subsequent Δ_{47} temperatures were calculated using the recently proposed unified Δ_{47} -T calibration: $\Delta_{47(\text{I-CDES})} = 0.0391 (\pm 0.0004) \times 10^6/T^2 + 0.154 (\pm 0.004)$, which is applicable to a wide range of temperatures (0.5 to 1100 °C) and carbonate mineralogies (Anderson et al., 2021). Water oxygen isotope compositions that are tentatively considered to be seawater or exchanged seawater ($\delta^{18}\text{O}_{\text{sw}}$), were calculated using the calcite-water fractionation equations of Kim and O'Neil (1997) (corrected for CO_2 -calcite acid fractionation factor of 1.01025 (Kim et al., 2007)).

3.2 REE geochemistry and Element/Ca ratios

Fossil brachiopods and whole rock samples were analyzed for Sr/Ca and Mg/Ca ratios, as well as rare earth element (REE) concentrations at the ICP Centre of the University of Geneva. For REE analysis, samples were digested in sealed Teflon vials overnight in concentrated HNO_3 on a hotplate. REE concentrations were measured by quadrupole ICP-MS (Agilent 7700) using a microflow injector. The instrumental uncertainty was < 5 % for elemental concentrations below 100 ppb. NIST Nd elemental standard was regularly measured at 10 ppb and 100 ppb for quality control with a relative standard deviation (RSD) of < 3 % and a mixture of Re and Rh was used as internal standards. REE concentrations were normalized relative to Post Archean Australian Shale (PAAS) (Taylor and McLennan, 1985). As the abundance of Ce and Eu in seawater can vary due to redox variations (De Baar et al., 1985), the concentrations of these elements are usually normalized relative to their

neighbouring REEs, a measure regarded as the Ce and Eu anomaly (German and Elderfield, 1990; Alibo and Nozaki, 1999). The Ce and Eu anomalies were calculated as follows:

$$Ce_{anom} = Ce_n / (Pr_n^2 / Nd_n) \text{ (Lawrence et al., 2006)} \quad (1)$$

$$Eu_{anom} = 2 \times Eu_n / (Sm_n + Gd_n) \text{ (De Baar et al., 1985)} \quad (2)$$

Where n refers to REE values normalized relative to PAAS.

Around 1 to 7 mg of material was used for Sr/Ca and Mg/Ca measurements. The element/Ca ratios were measured on an iCAP 6000 ICP-OES. Mg and Ca were radially measured on 280.270 and 317.933 nm, respectively and Sr was measured on 216.596 nm. Each Mg/Ca and Sr/Ca ratio presented is the average of three measurements from which the analytical errors are also deduced (see supplementary information). Both element/Ca ratios were normalized to the JCP-1 certified reference material (Okai et al., 2002). The external reproducibility was monitored with multiple JCP-1 standard solutions measurements at concentrations similar to those of the measured samples, giving Mg/Ca = 4.199 ± 0.02 mmol/mol (2sd, n = 42) and Sr/Ca = 8.838 ± 0.12 mmol/mol (2sd, n = 42).

3.3 Optical screening

To evaluate the textural preservation of brachiopod shell material, high resolution scanning electron microscope (SEM) images were obtained on a subset of fossil brachiopods (JA C2, W18, W30) at UNIL using a Tescan Mira II Field Emission SEM. SEM images were taken at between 120 \times and 430 \times magnification under high vacuum mode at 20 kV and a working distance of between 12 and 14 mm. Thin-section photomicrographs of whole rock samples were made at the Institute of Earth Sciences, UNIL (WMJ and JA samples) and at the Paleontological Institute, University of Zurich (WAD2 samples).

4. Results

Results of clumped isotope analysis as well as estimated Δ_{47} temperatures and $\delta^{18}O_{sw}$ values are presented in the supplementary information (Edward et al., 2024a) and graphically presented in Figures 4, 5 and 7. In Table 1, Δ_{47} temperatures and $\delta^{18}O_{sw}$ estimates from fossil brachiopod and “couche caramel” samples are presented grouped by sampling locality.

Fossil brachiopod samples from individual beds, as well as shell material extracted from the same brachiopod samples record a relatively wide range of precipitation temperatures (Fig. 4). For JA, brachiopod samples recovered from bed C2 record Δ_{47} temperatures between 21 ± 4 °C and 48 ± 2 °C, and for WMJ bed 18C, estimated Δ_{47} temperatures are between 20 ± 2 °C and 56 ± 6 °C. For analyzed micritic whole rock material, estimated Δ_{47} temperatures for JA are lower (range: 33 ± 6 – 58 ± 10 °C) relative to WMJ (range: 41 ± 5 – 68 ± 7 °C). Replicate measurements for the Dienerian-aged “couche caramel” samples yield a smaller range of Δ_{47} temperatures for RAJ2 (between 13 ± 10 °C and 25 ± 12

°C), relative to the WAD2 section (between 25 ± 12 °C and 70 ± 18 °C). Furthermore, analyzed sparry calcite material yields Δ_{47} temperatures between 41 ± 2 and 69 ± 7 °C, whereas calcite veins yield Δ_{47} temperatures between 45 ± 5 and 68 ± 20 °C.

Table 1. Summary of the estimated average Δ_{47} temperatures and $\delta^{18}\text{O}_{\text{sw}}$ values for fossil brachiopod and whole rock samples having replicates analyzed in the current study. Abbreviations: n = number of samples, T = temperature, JA = Jebel Aweri, WMJ = Wadi Musjah, RAJ2 = Ras al Jin2, WAD2 = Wadi ad Daffah2, BR = brachiopod, WR = whole rock micrite.

Locality	Bed	Sample Name	Material	Age	n	$\Delta_{47}\text{-T}$ (°C)	$\Delta_{47}\text{-T}$ 2SE (±)	$\delta^{18}\text{O}_{\text{sw}}$ (‰ VSMOW)	$\delta^{18}\text{O}_{\text{s}}$ w 2SE (±)
JA	C2	C2	BR	late Smithian	2	35	3	-0.6	0.5
JA	C2	C2 A	BR	late Smithian	4	30	7	0.0	1.3
JA	C2	C2 BM	BR	late Smithian	2	28	9	-0.9	0.1
JA	C2	C2 BV	BR	late Smithian	2	39	1	-0.1	0.5
JA	C2	C2 DR	BR	late Smithian	2	33	4	1.2	0.9
JA	C2	C2 S	BR	late Smithian	2	36	4	-0.2	0.8
JA	C2	C2 X	BR	late Smithian	2	36	3	-1.1	1.1
JA	C2	C2B PV	BR	late Smithian	2	36	18	-1.2	3.9
JA	C2	C2B X	BR	late Smithian	3	24	4	-1.3	1.2
JA	C13	JA C13	WR	SSB	3	56	3	4.6	0.6
JA	C11	JA C11	WR	late Smithian	2	38	7	1.3	1.3
JA	C15	JA C15	WR	Spathian	8	48	2	1.6	0.5
JA	C19	JA C19	WR	late Smithian	3	41	8	1.7	1.9
JA	C21	C21	WR	late Smithian	2	42	6	1.4	0.8
JA	C25	C25	WR	late Smithian	3	37	1	1.4	0.3
JA	C27	C27	WR	late Smithian	2	41	9	1.7	1.7
JA	C28	C28	WR	late Smithian	3	36	3	1.1	0.5
JA	C29	C29	WR	late Smithian	2	40	8	2.0	1.3
JA	C2	C2	WR	late Smithian	4	47	8	2.7	1.6
JA	C3	C3	WR	SSB	3	49	4	3.2	0.6
JA	C31	C31	WR	Spathian	3	47	5	2.9	1
JA	C32	C32	WR	Spathian	2	45	11	2.5	1.9
JA	C36	C36	WR	Spathian	3	49	6	3.1	0.9
RAJ2	AF	RAJ2AF	WR	early Dienerian	5	19	5	0.5	1.1
WMJ	18C	W18 M	BR	early Spathian	3	39	19	0.7	3.3
WMJ	18C	W18X	BR	early Spathian	7	45	4	1.7	0.7

WMJ	18C	W18Y	BR	early Spathian	5	31	6	-0.7	1.8
WMJ	26C	W26	BR	middle Spathian	6	40	8	1.1	0.8
WMJ	30 iso	W30 MX	BR	middle Spathian	2	47	8	2.5	0.6
WAD2	MC	WAD2MC	WR	middle Dienerian	6	41	3	2.3	1.0
WAD2	P	WAD2P	WR	middle Dienerian	5	41	15	2.3	2.8
WMJ	20C	WM20	BR	early Spathian	3	48	9	1.7	1.7
WMJ	25C	W25C	BR	middle Spathian	3	40	4	1.4	1.5
WMJ	15C	WMJ15	BR	late Smithian	4	48	4	2.1	0.9
WMJ	18C	WMJ18	BR	early Spathian	7	42	7	1.0	0.7
WMJ	30 iso	WMJ30	BR	middle Spathian	4	48	9	2.4	0.8

PAAS-normalized REE results (Fig. 5) indicate that fossil brachiopods record a prominent negative Ce anomaly, consistent with modern seawater (Alibo and Nozaki, 1999). The calculated mean Eu_{anom} value for WMJ and JA fossil brachiopods are 1.10 and 1.11, respectively. Whole rock samples are characterized by generally lower Sr/Ca and higher Mg/Ca ratios relative to fossil brachiopods. Sr/Ca ratios for fossil brachiopods are between 0.2 and 1.2 mmol/mol, whereas values for Mg/Ca are between 3.5 and 20 mmol/mol, which are Mg/Ca values within the threshold of low-magnesium calcite (LMC) fossils (< 40 mmol/mol, Ullmann and Korte, 2015). Sr/Ca ratios for whole rock samples have a range between 0.1 and 0.8 mmol/mol, whereas for Mg/Ca, the ratios are between 4.4 and 29.5 mmol/mol. Cross-plots of both element/Ca ratios reveal a moderate negative covariation between Sr/Ca and Mg/Ca for brachiopods (Fig. 4d). In contrast, whole rock samples are characterized by a strong positive covariation between these two ratios ($r = 0.74$, p -value = 0.00, $n = 25$).

SEM images indicate that brachiopod calcite shells have variable levels of preservation, with individual calcite shell splinters comprising both texturally well-preserved zones, as well as dissolution and recrystallization features (Fig. 6).

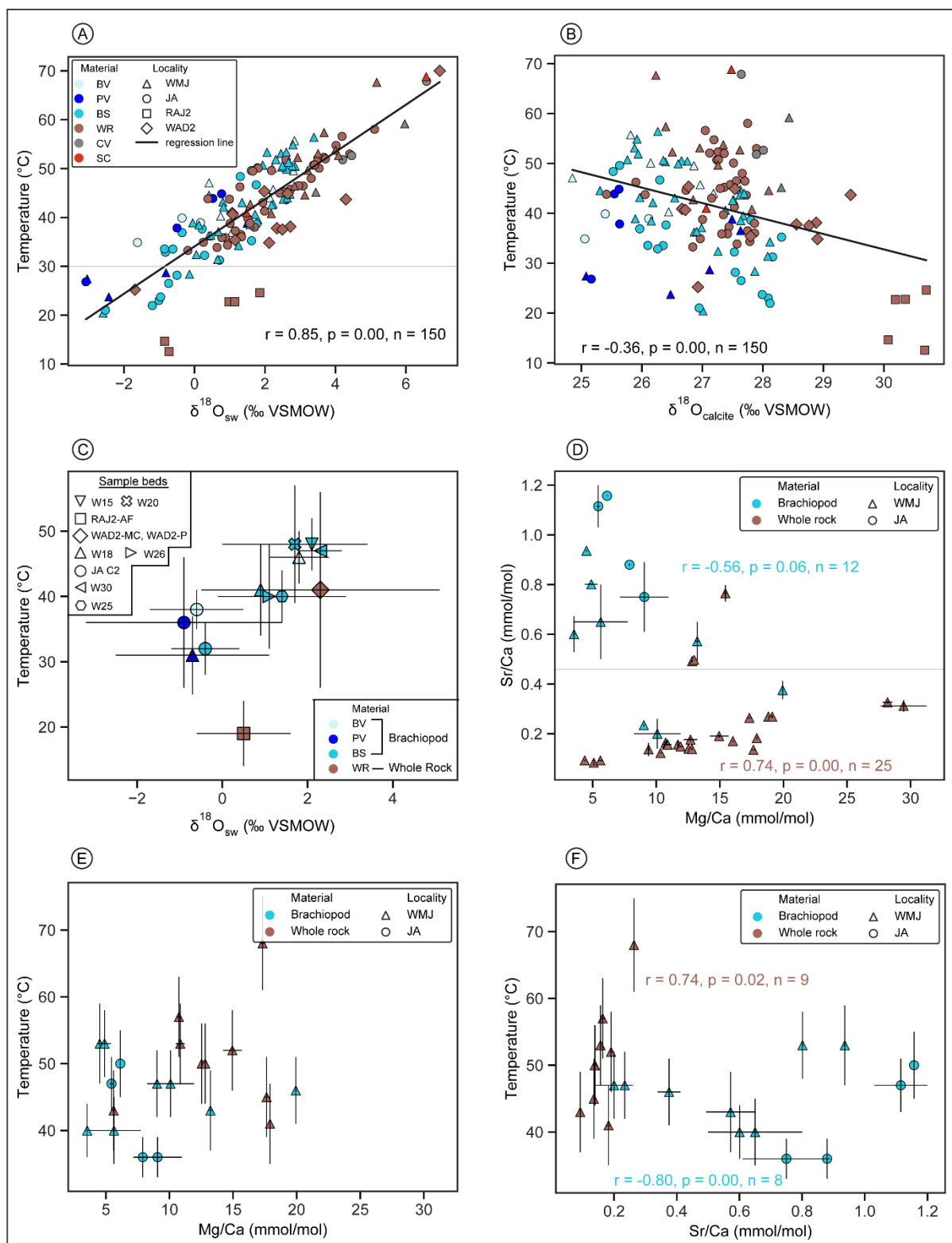


Figure 4. Cross-plots of A) Δ_{47} temperatures vs. estimated $\delta^{18}\text{O}_{\text{sw}}$ based on the calcite paleothermometry equation of Kim and O’Neil (1997) modified after Kim et al. (2007), B) Δ_{47} temperatures vs. calcite $\delta^{18}\text{O}$ values for all analyzed samples, C) mean Δ_{47} temperatures vs. mean estimated $\delta^{18}\text{O}_{\text{sw}}$ values for brachiopod and whole rock (“couche caramel”) subsamples. Brachiopod subsamples are categorized by extraction strategy (i.e., bulk shell extraction or separate pedicle and brachial valve sampling), D) Sr/Ca

vs Mg/Ca ratios for brachiopods and whole rock samples. The horizontal line represents the Sr/Ca lower limit for well-preserved Triassic fossil brachiopods according to Korte et al. (2003; 2005). Abbreviations: BV – brachial valve, PV – pedicle valve, BS – bulk shell, WR – whole rock, CV – calcite vein, SC – sparry calcite, BR – brachiopod, JA – Jebel Aweri, WMJ – Wadi Musjah, WAD2 – Wadi ad Daffah 2, RAJ2 – Ras al Jin 2.

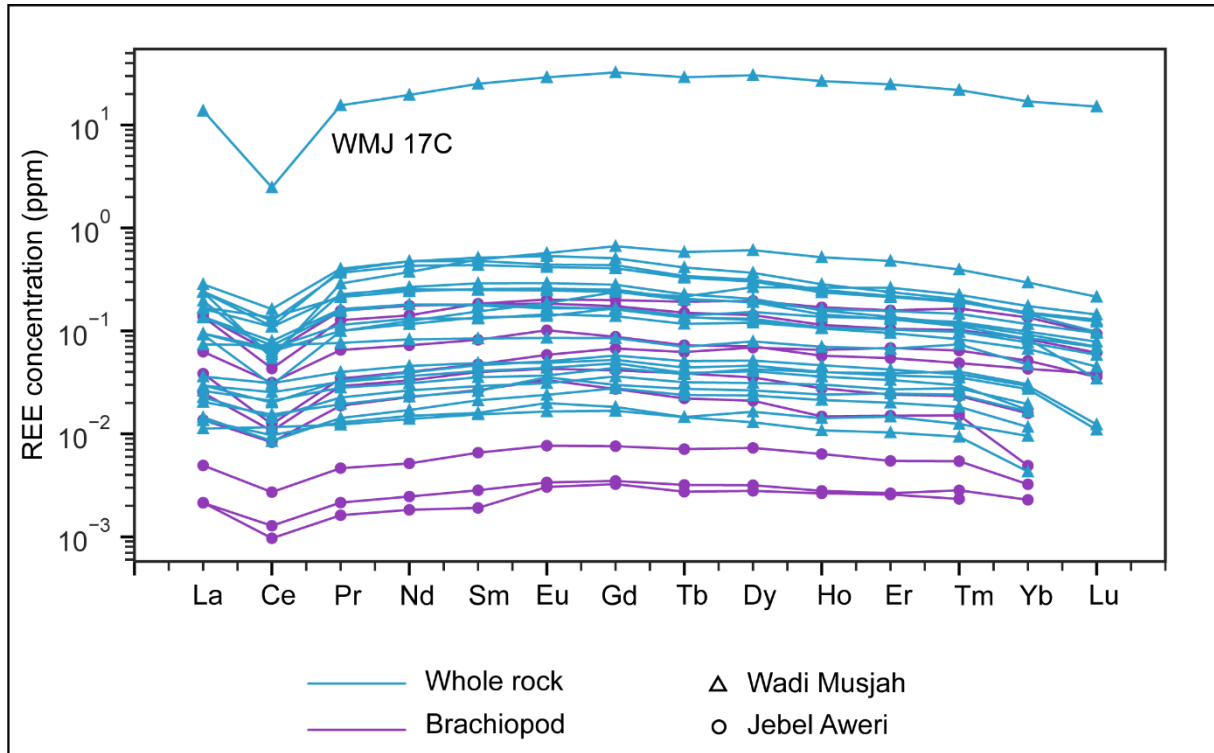


Figure 5. PAAS-normalized rare earth element concentrations of whole rock and fossil brachiopod samples. PAAS values are after Taylor and McLennan (1985). Whole rock REE data are from Edward et al. (2024b).

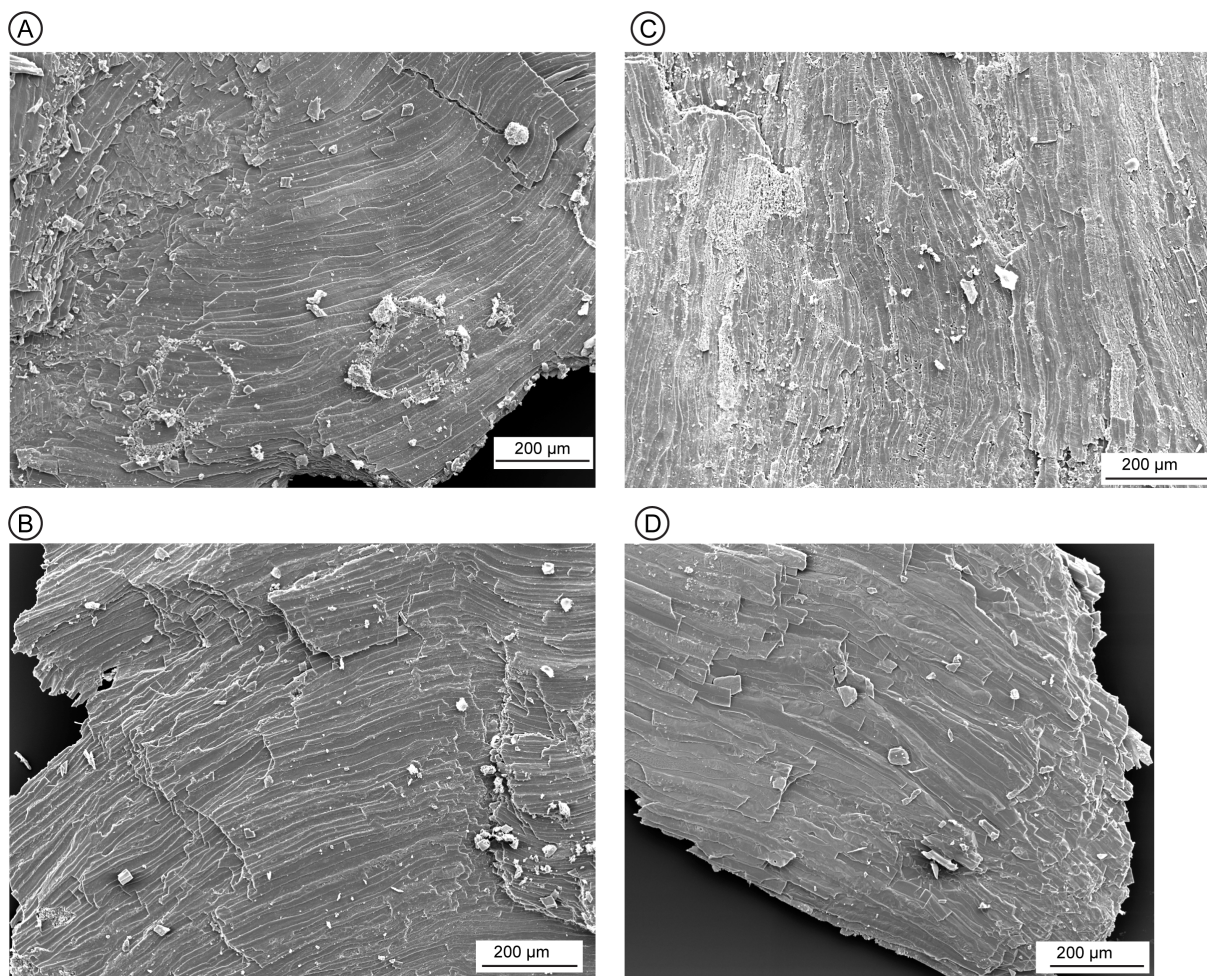


Figure 6. SEM images showing the variability in fossil brachiopod shell ultrastructure preservation for samples JA C2 (A, B) and sample WMJ 18 (C, D). Note the nucleus of dissolution and recrystallization visible in the bottom middle of A) and the pervasive recrystallization for a sample from WMJ 18 shown in C).

5. Discussion

5.1 Assessing the preservation of primary geochemical information

The preservation of near-primary geochemical information by the analyzed samples is assessed based using a combination of optical (SEM and thin section petrography), geochemical (element/Ca ratios, REE concentrations), and statistical criteria.

Sr/Ca and Mg/Ca ratios are commonly used to evaluate shell preservation of calcitic fossils as the concentration of both Sr and Mg in calcitic fossils may be modified during diagenetic stabilization of sediments (Brand and Veizer, 1980; Korte et al., 2003; Pérez-Huerta et al., 2008; Ullmann and Korte, 2015). The applied suite of preservation assessment criteria provides evidence both for good preservation and diagenetic alteration of the analyzed carbonate material. Negative covariation observed between Sr/Ca and Mg/Ca, as well as between Δ_{47} temperatures and Sr/Ca ratios for brachiopods suggests that progressive incorporation of Mg in shell calcite during diagenetic

stabilization in the sediment was associated with Sr loss. This interpretation is congruent with previous observations that diagenetic alteration would result in the depletion of Sr from the brachiopod shell (Brand and Veizer, 1980; Ullmann and Korte, 2015), and is also compatible with an inverse correlation between seawater Sr/Ca and Mg/Ca ratios (Steuber and Veizer, 2002). Hence, if Sr depletion is indeed indicative of diagenetic alteration, then the best preserved/least altered brachiopod samples would be those with the highest Sr/Ca ratios. However, the validity of such an interpretation is challenged by the observation that samples which have relatively high Sr/Ca ratios (i.e., higher than the proposed lower limit of 0.46 mmol/mol for well-preserved Triassic brachiopods according to Korte et al. (2003; 2005)), do not yield Δ_{47} temperatures that can be taken as primary crystallization temperatures in seawater (Fig. 4F). For example, samples JA C10 and C13 have the highest Sr/Ca ratios recorded (~ 1.1 mmol/mol) but nonetheless yield Δ_{47} temperatures of about 50 °C, which is very unlikely to be a primary crystallization temperature in seawater. In contrast with brachiopods, the positive covariation between Mg/Ca and Sr/Ca for whole rock micrite suggests that both Sr and Mg concentrations are modified in the same direction during diagenesis. These opposing covariation patterns for brachiopods and whole rock samples (Fig. 4D) make the use of element/Ca for assessing preservation of near-primary geochemical properties in the studied samples inconclusive. Similar complications in utilizing element/Ca ratios for assessing diagenetic alteration patterns are documented in the literature (e.g., Harlou et al., 2016; Schobben et al., 2016).

The variability in textural features within individual calcite shell fragments (Fig. 6), as well as the wide range of estimated temperatures for samples extracted from the same brachiopod specimen (occasionally up to 20 °C), indicates that individual fossil brachiopods record both diagenetic recrystallization temperatures and near-primary calcite precipitation temperatures. Thus, estimates of precipitation temperatures using calcitic macrofossils such as brachiopods are likely to differ between structurally and/or geochemically distinct zones of the original biogenic carbonate. Nevertheless, the potential that at least some fossil calcitic brachiopods record near-primary shell growth temperatures is given by the REE profile for these samples (Fig. 5). Specifically, analyzed samples display a prominent negative Ce anomaly and have Eu_{anom} values of around 1.10, similar to modern seawater (German and Elderfield, 1990; Alibo and Nozaki, 1999).

5.1.1. Variable preservation of fossil brachiopods

Previous studies using modern brachiopod shells and other biogenic calcites indicate that sampling of distinct parts of the same biogenic calcite shell affects the results obtained for geochemical analysis, as different parts of these shells preserve variable geochemical characteristics (e.g., Brand et al., 2003; Romanin et al., 2018; Cisneros-Lazaro et al., 2022). This phenomenon is observed in the current study. For example, in the WMJ section, which yields a wider Δ_{47} temperature range, material extracted from the pedicle valve of samples from bed WMJ 18C yield lower (and statistically distinct) Δ_{47} temperatures (i.e., mean \pm 2SE) relative to material extracted from the brachial valve (Fig. 4C). However, the Δ_{47}

temperatures for subsamples of brachiopod specimens from bed JA C2 are statistically indistinguishable from one another (Fig. 4C). The WMJ section is in the present-day, overlain by Semail nappe ophiolites and subaerially exposed through a “tectonic window” reaching into the Hawasina nappes of Oman (c.f. Leu et al., 2023). As such, WMJ samples have likely experienced some degree of post-depositional thermal stress, as also suggested by the higher Δ_{47} temperatures for WMJ whole rock samples relative to JA. However, it should be noted that conodonts from this section show no evidence of thermal alteration, having a conodont alteration index (CAI) of 1 (Leu et al., 2023). Consequently, considering the depositional context of the WMJ succession, the observed difference in Δ_{47} temperatures depending on sampling site for WMJ probably indicates variable preservation of near-primary calcite crystallization temperatures by WMJ samples. These considerations suggest that sampling and analysis of shell calcite from different parts of individual fossil brachiopods is required to extract the full range of temperatures recorded in brachiopod fossils that may have experienced post-depositional thermal modification.

5.2. Seawater oxygen isotope compositions and temperatures during the Early Triassic

Samples with lower Δ_{47} temperatures (i.e., < 30 °C, Fig. 4A) yield fluid $\delta^{18}\text{O}$ values that are comparable to the expected seawater $\delta^{18}\text{O}$ values for an ice-free world (-1 to -1.4 ‰ VSMOW, Shackleton and Kennett, 1975; Lear et al., 2000; Lhomme et al., 2005), and within the range of modern seawater $\delta^{18}\text{O}$ (-1.5 to 1.8 ‰ VSMOW, Jaffrés et al., 2007). The correspondence of high fluid $\delta^{18}\text{O}$ values with high Δ_{47} temperatures may be attributed to rock-buffered low-temperature alteration of the investigated samples (c.f. Bergmann et al., 2018a; Goldberg et al., 2021). This inference is supported by the observation that the highest fluid $\delta^{18}\text{O}$ values are recorded by calcite vein and sparry calcite samples (Fig. 4a). Similarly, a negative and statistically significant correlation between Δ_{47} temperatures and calcite $\delta^{18}\text{O}$ values is observed ($r = -0.36$, $p\text{-value} = 0.00$, $n = 150$), indicating that lower calcite $\delta^{18}\text{O}$ values are associated with higher temperatures. Consequently, within a given set of subsamples, those which yield the lowest Δ_{47} temperatures can be considered as the best preserved/least altered samples (e.g., Finnegan et al., 2011; Bergmann et al., 2018b; Goldberg et al., 2021). Modern day measurements indicate that annual mean equatorial seawater surface temperatures have an upper range of 30 °C (Boyer et al., 2018), and that brachiopod shell precipitation may occur at temperatures up to 25 °C (Letulle et al. 2023). Based on these considerations and the average within-run Δ_{47} analytical uncertainty (i.e., ± 0.022 ‰ or 9 °C), samples with replicate analysis yielding Δ_{47} temperature ≤ 30 °C and no replicate yielding > 39 °C were considered in estimating Early Triassic seawater $\delta^{18}\text{O}$ (Table 2). Admittedly, the applied selection criteria assumes that ocean temperatures during the Early Triassic were comparable to those of the present day. However, such an assumption is reasonable considering that brachiopods are an extant Fossil Group with a vital temperature limit of -2 °C to 38 °C (Giles, 2012), and temperatures higher than 35 °C are intolerable for most invertebrates (Brock, 1985).

From the Dienerian “couche caramel” beds, only samples from Ras al Jin2 (bed RAJ2-AF) yield suitable and replicable Δ_{47} temperatures (i.e., $< 30 \pm 9$ °C, $n = 5$). Based on these samples, a mean $\delta^{18}\text{O}_{\text{sw}}$ value of 0.5 ± 1.1 ‰ VSMOW is estimated for the Dienerian. For the Olenekian interval, only brachiopod calcite subsamples from beds JA C2 and WMJ 18C ($n = 14$) meet the selection criteria (Table 2). These samples have a mean $\delta^{18}\text{O}$ value of -0.7 ± 0.8 ‰ VSMOW.

Table 2. Clumped isotope data and calculated temperature and $\delta^{18}\text{O}_{\text{sw}}$ values for Early Triassic fossil brachiopods and whole rock samples deemed to be the best-preserved.

Age	Sample Bed	Sample Name	Number of samples	Replicates	Material	$\delta^{13}\text{C}$ (VPDB)	$\delta^{15}\text{O}$ (VPDB)	$\delta^{18}\text{O}$ (SMOW)	Δ_{47}	Δ_{48}	Δ_{49}	$\Delta_{47}(\text{t-CDES80})$	$\Delta_{47} 1\sigma$	$\Delta_{47}\text{-T } 1\sigma$	$\Delta_{47}\text{-Temperature (°C)}$	$\delta^{18}\text{O}_{\text{sw}}$ (‰ VSMOW)	
Spathian	WMJ 18C	W18Y	5	W18Y B	Brachiopod	4.17	-4.30	26.47	-0.454	0.443	-32.576	0.598	0.005	± 2	24	-2.4	
				W18Y B	Brachiopod	4.36	-3.68	27.12	-0.461	-0.654	-35.744	0.583	0.013	± 5	29	-0.8	
				W18Y C	Brachiopod	3.33	-3.32	27.49	-0.492	-0.740	-45.382	0.556	0.005	± 2	39	1.5	
				W18Y C	Brachiopod	3.36	-3.18	27.63	-0.480	-0.742	-39.740	0.562	0.013	± 5	37	1.2	
				W18Y D	Brachiopod	5.65	-5.66	25.08	-0.464	0.950	-29.671	0.587	0.005	± 2	27	-3.0	
late Smithian	JA C2	C2 A	4	C2 A	Brachiopod	5.71	-2.71	28.12	-0.334	-0.118	0.024	0.603	0.035	± 14	22	-1.2	
				C2 A	Brachiopod	5.59	-3.28	27.53	-0.384	-0.739	-17.587	0.573	0.005	± 2	32	0.3	
				C2 A-OS	Brachiopod	5.70	-3.02	27.80	-0.4851	-0.7909	-42.834	0.556	0.013	± 5	39	1.8	
				C2 A-OS	Brachiopod	5.66	-3.17	27.64	-0.4615	-0.831	-40.829	0.589	0.005	± 2	27	-0.7	
		C2B X 1	Brachiopod	5.46	-3.84	26.95	-0.441	-0.582	-37.793	0.606	0.013	± 4	21	-2.5			
		C2B X 2	Brachiopod	4.00	-2.74	28.09	-0.446	-0.744	-39.576	0.600	0.013	± 4	23	-1.0			
		C2B X 3	Brachiopod	5.69	-3.27	27.54	-0.460	-0.774	-40.383	0.585	0.013	± 5	28	-0.5			
		C2 BM	Brachiopod	7.36	-2.83	27.99	-0.448	-0.760	-43.952	0.598	0.013	± 4	24	-1.0			
	C2 BM	Brachiopod	4.24	-4.51	26.26	-0.471	-0.713	-42.378	0.572	0.013	± 5	33	-0.8				
														Mean	29	-0.7	
														st.dev.	6	1.5	
														2SE	3	0.8	
	early Dienerian	RAJ2 AF	RAJ2 AF	5	RAJ2AF	couche caramel	2.54	-0.81	30.07	-0.290	-0.239	-12.565	0.626	0.043	± 17	15	-0.8
					RAJ2AF-A	couche caramel	2.52	-0.23	30.68	-0.336	-0.511	-25.280	0.633	0.035	± 14	13	-0.7
RAJ2AF-A					couche caramel	2.21	-0.70	30.19	-0.312	-0.516	-15.592	0.601	0.035	± 14	23	1.0	
RAJ2AF-B					couche caramel	2.51	-0.20	30.70	-0.366	-0.510	-37.537	0.595	0.035	± 14	25	1.9	
RAJ2AF-B					couche caramel	2.37	-0.54	30.36	-0.312	-0.430	-14.296	0.601	0.035	± 14	23	1.1	
													Mean	19	0.5		
													st.dev.	5	1.2		
													2SE	5	1.1		

Consequently, it is inferred that the mean $\delta^{18}\text{O}$ value of NeoTethyan seawater during the Olenekian was ca. -1 ‰ VSMOW, congruent with previously proposed seawater $\delta^{18}\text{O}$ values for an ice-free world (Shackleton and Kennett, 1975; Lhomme et al., 2005). The estimated $\delta^{18}\text{O}$ values for the Dienerian and Smithian – Spathian, similar within uncertainty, suggest that NeoTethyan seawater $\delta^{18}\text{O}$ values were similar throughout the Early Triassic. Furthermore, our estimated Early Triassic seawater $\delta^{18}\text{O}$ compositions for the NeoTethys are compatible with results from other clumped isotope studies (e.g., Came et al., 2007; Finnegan et al., 2011; Dennis et al., 2013; Bergmann et al., 2018b; Price et al., 2020; Goldberg et al., 2021), which indicate that the $\delta^{18}\text{O}$ value of seawater has not varied by more than 2 ‰ or less throughout the Phanerozoic.

The remainder of analyzed whole rocks and fossil brachiopods, with relatively higher Δ_{47} temperatures (i.e., > 39 °C), have fluid $\delta^{18}\text{O}$ values between -1.8 and 5 ‰ VSMOW. These samples are interpreted as having experienced low-temperature alteration but may offer insights into the temperature and fluid O-isotope compositions during diagenetic stabilization of the carbonate (Bergmann et al., 2018a). The highest calculated Δ_{47} temperature for analyzed samples is ca. 70 °C, suggestive of relatively shallow burial conditions for the analyzed successions. Considering a geothermal gradient of 25 °C km⁻¹ (DiPietro, 2013; Criss, 2020), the studied successions have potentially experienced less than 3 km of sedimentary burial. Although the conditions under which carbonate clumped isotope compositions (Δ_{47})

are altered are not fully known (Eiler, 2011), it is apparent that fluid-driven carbonate recrystallization, as well as solid state reordering (which does not necessarily require textural modification to the carbonate), can reset primary Δ_{47} values (Henkes et al., 2014; Winkelstern and Lohmann, 2016; Looser et al., 2023). Experimental studies indicate that the resetting of Δ_{47} compositions by solid state reordering occurs at temperatures > 100 °C (Passey and Henkes, 2012; Henkes et al., 2014; Stolper and Eiler, 2015; Chen et al., 2019; Perez-Beltran et al., 2023). Consequently, solid state reordering of the C-O bonds in the samples herein considered for estimating Early Triassic seawater ^{18}O composition (having Δ_{47} temperatures < 40 °C) is deemed unlikely.

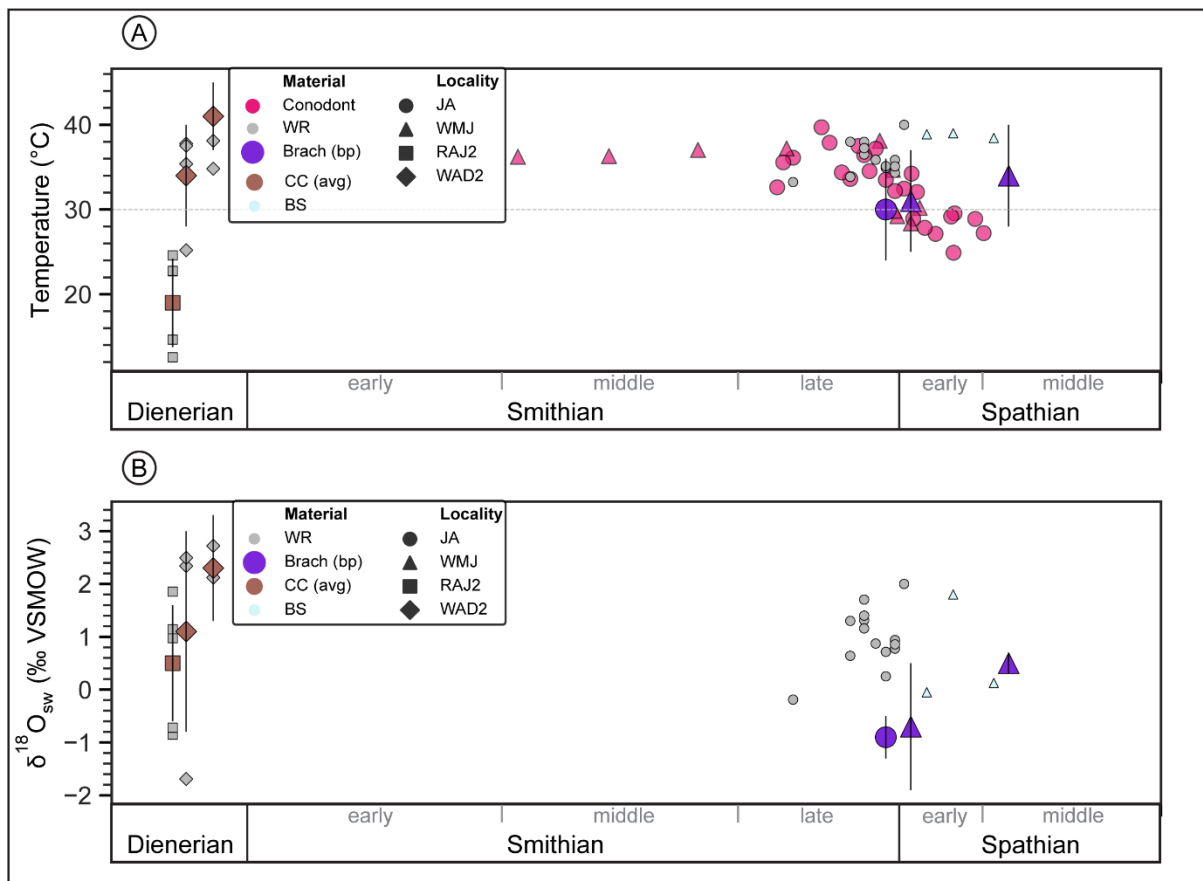


Figure 7. Estimated A) temperature and B) water $\delta^{18}\text{O}$ values based on Δ_{47} compositions of whole rock carbonates and fossil brachiopods. The horizontal grey line on A) represents the upper limit of the mean annual modern equatorial sea surface temperature (i.e., 30 °C, Boyer et al., 2018). Conodont temperature data is based on $\delta^{18}\text{O}$ values from Luz (2022) and calculated using the paleotemperature equation of Lécuyer et al. (2013). Abbreviations: avg – average, bp – best preserved. Others are the same as in Figure 4. Absolute age constraint is based on the International Chronostratigraphic Chart 2022 (Cohen et al., 2013; updated) and Widmann et al. (2020) and Leu et al. (2023) (for the Smithian to Spathian).

Studies of seawater temperature evolution during the Early Triassic indicate that the middle Dienerian to earliest Smithian of the NeoTethys was characterized by increasing sea surface temperatures (SSTs)

(Romano et al., 2013), although another study (Sun et al., 2012) based on the PaleoTethys suggested the opposite. Although the paleotemperature record from the current study is of limited temporal resolution, data from the Dienerian “couche caramel” beds support a general SST increase during the Dienerian (Fig. 7A). However, the magnitude of temperature increase suggested by the WAD2 “couche caramel” clumped isotope data (ca. 20 °C) is very unlikely to be primary and is probably affected by post-depositional alteration. Nevertheless, the general trend of increasing temperatures indicated by these samples is likely to be primary, as supported by conodont oxygen isotope data (Romano et al., 2013). In the case of the Smithian and Spathian, previous studies (Sun et al., 2012; Romano et al., 2013; Goudemand et al., 2019; Luz, 2022) indicate that the latest Smithian to earliest Spathian interval was characterized by a decrease in seawater temperatures, attributed to climatic cooling. The current clumped isotope data for coeval best-preserved brachiopods accords with these previous records. Notably, applying the O-isotope composition for Olenekian seawater inferred from the current study (i.e., ca. -1 ‰ VSMOW), the temperatures calculated from phosphate $\delta^{18}\text{O}$ for JA conodonts (Luz, 2022) are similar to the Δ_{47} temperatures derived for the best-preserved late Smithian whole rock carbonates from JA (i.e., sample replicates with Δ_{47} temperatures ≤ 39 °C, Fig. 7A). Converting the WMJ and JA conodont $\delta^{18}\text{O}$ values (Luz, 2022) into absolute temperatures suggests that NeoTethyan seawater temperatures decreased from around 36 °C during the middle Smithian to around 28 °C across the SSB (Fig. 7). In addition, Δ_{47} temperatures recorded for the best-preserved SSB fossil brachiopod samples are similar to temperatures derived from coeval conodonts for WMJ and JA (Fig. 7A). Consequently, the SSB brachiopod Δ_{47} temperatures further strengthen the inference that some of the analyzed fossil brachiopods record near-primary seawater chemical and isotopic compositions. Furthermore, the SSB carbonate Δ_{47} temperature record is compatible with the notion that faunal turnover during the Smithian – Spathian transition occurred during a regime of climatic cooling (Romano et al., 2013; Goudemand et al., 2019).

6. Conclusions

Clumped isotope analysis of Early Triassic fossil brachiopods and whole rock carbonates deposited in the NeoTethys demonstrates that ancient marine carbonates, although having undergone some degree of diagenetic modification, have the potential to preserve near-primary paleoenvironmental information. Dienerian Δ_{47} temperatures indicate a warming SST trend during this interval, in agreement with previous conodont-based paleotemperature data for the NeoTethys. Results based on the best-preserved carbonate samples indicate that Early Triassic NeoTethyan seawater had mean $\delta^{18}\text{O}$ values between 0.5 ± 1.1 ‰ and -0.7 ± 0.8 ‰ VSMOW, comparable to expected seawater oxygen isotope compositions for an ice-free world. Furthermore, Δ_{47} temperatures recorded during the SSB support previous conodont paleotemperature records, which indicate that faunal turnover at this time coincided with cooler seawater temperatures.

Data Availability

The dataset generated for this article can be found on an open-source online data repository hosted at Zenodo (Edward et al., 2024a) using the following link: <https://doi.org/10.5281/zenodo.10630039>

Acknowledgements

The authors thank Claudia Baumgartner and Laetitia Monbaron for laboratory support. This study was funded by a Swiss National Science Foundation Sinergia Grant (Project Number: CRSII5_180253). SLH acknowledges financial support by the University of Geneva (S18173).

References

- Alibo, D.S., Nozaki, Y., 1999. Rare earth elements in seawater: particle association, shale-normalization, and Ce oxidation. *Geochimica et Cosmochimica Acta* 63, 363-372 DOI: [https://doi.org/10.1016/S0016-7037\(98\)00279-8](https://doi.org/10.1016/S0016-7037(98)00279-8).
- Anderson, N.T., Kelson, J.R., Kele, S., Daeron, M., Bonifacie, M., Horita, J., Mackey, T.J., John, C.M., Kluge, T., Petschnig, P., Jost, A.B., Huntington, K.W., Bernasconi, S.M., Bergmann, K.D., 2021. A Unified Clumped Isotope Thermometer Calibration (0.5-1,100 degrees C) Using Carbonate-Based Standardization. *Geophys Res Lett* 48, e2020GL092069 DOI: <https://doi.org/10.1029/2020GL092069>.
- Baud, A., Richoz, S., Beauchamp, B., Cordey, F., Grasby, S., Henderson, C.M., Krystyn, L., Nicora, A., 2012. The Buday'ah Formation, Sultanate of Oman: A Middle Permian to Early Triassic oceanic record of the Neotethys and the late Induan microsphere bloom. *J Asian Earth Sci* 43, 130-144 DOI: <https://doi.org/10.1016/j.jseae.2011.08.016>.
- Bergmann, K.D., Al Balushi, S.A.K., Mackey, T.J., Grotzinger, J.P., Eiler, J.M., 2018a. A 600-Million-Year Carbonate Clumped-Isotope Record from the Sultanate of Oman. *Journal of Sedimentary Research* 88, 960-979 DOI: 10.2110/jsr.2018.51.
- Bergmann, K.D., Finnegan, S., Creel, R., Eiler, J.M., Hughes, N.C., Popov, L.E., Fischer, W.W., 2018b. A paired apatite and calcite clumped isotope thermometry approach to estimating Cambro-Ordovician seawater temperatures and isotopic composition. *Geochimica et Cosmochimica Acta* 224, 18-41 DOI: <https://doi.org/10.1016/j.gca.2017.11.015>.
- Bernasconi, S.M., Daëron, M., Bergmann, K.D., Bonifacie, M., Meckler, A.N., Affek, H.P., Anderson, N., Bajnai, D., Barkan, E., Beverly, E., Blamart, D., Burgener, L., Calmels, D., Chaduteau, C., Clog, M., Davidheiser-Kroll, B., Davies, A., Dux, F., Eiler, J., Elliott, B., Fetrow, A.C., Fiebig, J., Goldberg, S., Hermoso, M., Huntington, K.W., Hyland, E., Ingalls, M., Jaggi, M., John, C.M., Jost, A.B., Katz, S., Kelson, J., Kluge, T., Kocken, I.J., Laskar, A., Leutert, T.J., Liang, D., Lucarelli, J., Mackey, T.J., Mangenot, X., Meinicke, N., Modestou, S.E., Müller, I.A., Murray, S., Neary, A., Packard, N., Passey, B.H., Pelletier, E., Petersen, S., Piasecki, A., Schauer, A., Snell, K.E., Swart, P.K., Tripathi, A., Upadhyay, D., Vennemann, T., Winkelstern, I., Yarian, D., Yoshida, N., Zhang, N., Ziegler, M., 2021. InterCarb: A Community Effort to Improve Interlaboratory Standardization of the Carbonate Clumped Isotope Thermometer Using Carbonate Standards. *Geochemistry, Geophysics, Geosystems* 22, e2020GC009588 DOI: <https://doi.org/10.1029/2020GC009588>.
- Bernasconi, S.M., Muller, I.A., Bergmann, K.D., Breitenbach, S.F.M., Fernandez, A., Hodell, D.A., Jaggi, M., Meckler, A.N., Millan, I., Ziegler, M., 2018. Reducing Uncertainties in Carbonate Clumped Isotope Analysis Through Consistent Carbonate-Based Standardization. *Geochem Geophys Geosy* 19, 2895-2914 DOI: 10.1029/2017GC007385.
- Boyer, T.P., Garcia, H.E., Locarnini, R.A., Zweng, M.M., Mishonov, A.V., Reagan, J.R., Weathers, K.A., Baranova, O.K., Seidov, D.R., Smolyar, I.V., 2018. World Ocean Atlas 2018.[Temperature], NOAA Atlas NESDIS 68. Volume, Silver Spring, Maryland.
- Brand, U., Logan, A., Hiller, N., Richardson, J., 2003. Geochemistry of modern brachiopods: applications and implications for oceanography and paleoceanography. *Chemical Geology* 198, 305-334 DOI: [https://doi.org/10.1016/S0009-2541\(03\)00032-9](https://doi.org/10.1016/S0009-2541(03)00032-9).
- Brand, U., Veizer, J., 1980. Chemical diagenesis of a multicomponent carbonate system--1: Trace elements. *Journal of Sedimentary Research* 50, 1219-1236 DOI: <https://doi.org/10.1306/212F7BB7-2B24-11D7-8648000102C1865D>.

Brock, T.D., 1985. Life at High Temperatures. *Science* 230, 132-138 DOI: <https://doi.org/10.1126/science.230.4722.132>.

Brosse, M., Bucher, H., Baud, A., Frisk, Å.M., Goudemand, N., Hagdorn, H., Nützel, A., Ware, D., Hautmann, M., 2019. New data from Oman indicate benthic high biomass productivity coupled with low taxonomic diversity in the aftermath of the Permian–Triassic Boundary mass extinction. *Lethaia* 52, 165-187 DOI: <https://doi.org/10.1111/let.12281>.

Brühwiler, T., Bucher, H., Goudemand, N., Galfetti, T., 2012. Smithian (Early Triassic) ammonoid faunas from Exotic Blocks from Oman: taxonomy and biochronology. *Palaeontographica. Abteilung A: Palaeozoologie-Stratigraphie* 296, 3-107 DOI: [10.1127/pala/296/2012/3](https://doi.org/10.1127/pala/296/2012/3).

Came, R.E., Eiler, J.M., Veizer, J., Azmy, K., Brand, U., Weidman, C.R., 2007. Coupling of surface temperatures and atmospheric CO₂ concentrations during the Palaeozoic era. *Nature* 449, 198-201 DOI: [10.1038/nature06085](https://doi.org/10.1038/nature06085).

Chen, S., Ryb, U., Piasecki, A., Lloyd, M., Baker, M., Eiler, J., 2019. Mechanism of Solid-State Clumped Isotope Reordering in Carbonate Minerals from Aragonite Heating Experiments. *Geochimica et Cosmochimica Acta* 258 DOI: [10.1016/j.gca.2019.05.018](https://doi.org/10.1016/j.gca.2019.05.018).

Cisneros-Lazaro, D., Adams, A., Guo, J., Bernard, S., Baumgartner, L.P., Daval, D., Baronnet, A., Grauby, O., Vennemann, T., Stolarski, J., Escrig, S., Meibom, A., 2022. Fast and pervasive diagenetic isotope exchange in foraminifera tests is species-dependent. *Nat Commun* 13, 113 DOI: [10.1038/s41467-021-27782-8](https://doi.org/10.1038/s41467-021-27782-8).

Cohen, K.M., Finney, S.C., Gibbard, P.L., Fan, J.X., 2013; updated. The ICS International Chronostratigraphic Chart. *International Union of Geological Sciences* 36, 199-204 DOI: [10.18814/epiiugs/2013/v36i3/002](https://doi.org/10.18814/epiiugs/2013/v36i3/002).

Criss, R.E., 2020. Chapter 6 - Thermal models of the continental lithosphere, in: Hofmeister, A.M. (Ed.), *Heat Transport and Energetics of the Earth and Rocky Planets*. Elsevier, pp. 151-174.

De Baar, H.J.W., Bacon, M.P., Brewer, P.G., Bruland, K.W., 1985. Rare earth elements in the Pacific and Atlantic Oceans. *Geochimica et Cosmochimica Acta* 49, 1943-1959 DOI: [https://doi.org/10.1016/0016-7037\(85\)90089-4](https://doi.org/10.1016/0016-7037(85)90089-4).

de Winter, N.J., Müller, I.A., Kocken, I.J., Thibault, N., Ullmann, C.V., Farnsworth, A., Lunt, D.J., Claeys, P., Ziegler, M., 2021. Absolute seasonal temperature estimates from clumped isotopes in bivalve shells suggest warm and variable greenhouse climate. *Communications Earth & Environment* 2, 121 DOI: [10.1038/s43247-021-00193-9](https://doi.org/10.1038/s43247-021-00193-9).

Dennis, K.J., Cochran, J.K., Landman, N.H., Schrag, D.P., 2013. The climate of the Late Cretaceous: New insights from the application of the carbonate clumped isotope thermometer to Western Interior Seaway macrofossil. *Earth and Planetary Science Letters* 362, 51-65 DOI: <https://doi.org/10.1016/j.epsl.2012.11.036>.

DiPietro, J.A., 2013. Chapter 20 - Keys to the Interpretation of Geological History, in: DiPietro, J.A. (Ed.), *Landscape Evolution in the United States*. Elsevier, Boston, pp. 327-344.

Edward, O., Le Houedec, S., & Vennemann, T. (2024a). Supplementary dataset for: Carbonate Clumped Isotope Constraints on Early Triassic NeoTethyan Seawater Oxygen Isotope Compositions and Temperatures [Data set]. In *Evaluating Environmental Drivers of Late Permian to Early Triassic Marine Biotic Events Using Multiple Geochemical and Isotopic Proxies (version 2)*. Zenodo. <https://doi.org/10.5281/zenodo.10630038>

- Edward, O., Spangenberg, J.E., Leu, M., Ragon, C., Le Houedec, S., Baud, A., Bucher, H., Vennemann, T., 2024b. Olenekian sulfur isotope records: Deciphering global trends, links to marine redox changes and faunal evolution. *Chemical Geology*, 121984 DOI: <https://doi.org/10.1016/j.chemgeo.2024.121984>.
- Eiler, J.M., 2007. “Clumped-isotope” geochemistry—The study of naturally-occurring, multiply-substituted isotopologues. *Earth and Planetary Science Letters* 262, 309-327 DOI: <https://doi.org/10.1016/j.epsl.2007.08.020>.
- Eiler, J.M., 2011. Paleoclimate reconstruction using carbonate clumped isotope thermometry. *Quaternary Science Reviews* 30, 3575-3588 DOI: 10.1016/j.quascirev.2011.09.001.
- Emiliani, C., 1955. Pleistocene Temperatures. *The Journal of Geology* 63, 538-578 DOI: 10.1086/626295.
- Epstein, S., Buchsbaum, R., Lowenstam, H., Urey, H., 1951. CARBONATE-WATER ISOTOPIC TEMPERATURE SCALE. *Bulletin of the Geological Society of America* 62, 417-426 DOI: 10.1130/0016-7606(1951)62[417:CITS]2.0.CO;2.
- Fernandez, A., Korte, C., Ullmann, C.V., Looser, N., Wohlwend, S., Bernasconi, S.M., 2021. Reconstructing the magnitude of Early Toarcian (Jurassic) warming using the reordered clumped isotope compositions of belemnites. *Geochimica et Cosmochimica Acta* 293, 308-327 DOI: <https://doi.org/10.1016/j.gca.2020.10.005>.
- Finnegan, S., Bergmann, K., Eiler, J.M., Jones, D.S., Fike, D.A., Eisenman, I., Hughes, N.C., Tripathi, A.K., Fischer, W.W., 2011. The Magnitude and Duration of Late Ordovician–Early Silurian Glaciation. *Science* 331, 903-906 DOI: 10.1126/science.1200803.
- German, C.R., Elderfield, H., 1990. Application of the Ce anomaly as a paleoredox indicator: The ground rules. *Paleoceanography* 5, 823-833 DOI: <https://doi.org/10.1029/PA005i005p00823>.
- Ghosh, P., Adkins, J., Affek, H., Balta, B., Guo, W., Schauble, E.A., Schrag, D., Eiler, J.M., 2006. ^{13}C – ^{18}O bonds in carbonate minerals: a new kind of paleothermometer. *Geochimica et Cosmochimica Acta* 70, 1439-1456.
- Giles, P.S., 2012. Low-latitude Ordovician to Triassic brachiopod habitat temperatures (BHTs) determined from $\delta^{18}\text{O}$ [brachiopod calcite]: A cold hard look at ice-house tropical oceans. *Palaeogeography, Palaeoclimatology, Palaeoecology* 317-318, 134-152 DOI: <https://doi.org/10.1016/j.palaeo.2012.01.002>
- Goldberg, S.L., Present, T.M., Finnegan, S., Bergmann, K.D., 2021. A high-resolution record of early Paleozoic climate. *Proc Natl Acad Sci U S A* 118 DOI: 10.1073/pnas.2013083118.
- Goudemand, N., Romano, C., Leu, M., Bucher, H., Trotter, J.A., Williams, I.S., 2019. Dynamic interplay between climate and marine biodiversity upheavals during the early Triassic Smithian - Spathian biotic crisis. *Earth-Science Reviews* 195, 169-178 DOI: <https://doi.org/10.1016/j.earscirev.2019.01.013>.
- Grossman, E.L., 2012. Applying Oxygen Isotope Paleothermometry in Deep Time. *The Paleontological Society Papers* 18, 39-68 DOI: 10.1017/S1089332600002540.
- Grossman, E.L., Joachimski, M.M., 2022. Ocean temperatures through the Phanerozoic reassessed. *Scientific Reports* 12, 8938 DOI: 10.1038/s41598-022-11493-1.

Harlou, R., Ullmann, C.V., Korte, C., Lauridsen, B.W., Schovsbo, N.H., Surlyk, F., Thibault, N., Stemmerik, L., 2016. Geochemistry of Campanian–Maastrichtian brachiopods from the Rørdal-1 core (Denmark): Differential responses to environmental change and diagenesis. *Chemical Geology* 442, 35-46 DOI: <https://doi.org/10.1016/j.chemgeo.2016.08.039>.

Hauser, M., Martini, R., Burns, S., Dumitrica, P., Krystyn, L., Matter, A., Peters, T., Zaninetti, L., 2001. Triassic stratigraphic evolution of the Arabian-Greater India embayment of the southern Tethys margin. *Eclogae Geologicae Helvetiae* 94, 29-62 DOI: 10.5169/seals-168876.

Hauser, M., Martini, R., Matter, A., Krystyn, L., Peters, T., Stampfli, G., Zaninetti, L., 2002. The break-up of East Gondwana along the northeast coast of Oman: evidence from the Batain basin. *Geological Magazine* 139, 145-157 DOI: 10.1017/S0016756801006264.

Henkes, G.A., Passey, B.H., Grossman, E.L., Shenton, B.J., Pérez-Huerta, A., Yancey, T.E., 2014. Temperature limits for preservation of primary calcite clumped isotope paleotemperatures. *Geochimica et Cosmochimica Acta* 139, 362-382 DOI: <https://doi.org/10.1016/j.gca.2014.04.040>.

Huntington, K.W., Lechler, A.R., 2015. Carbonate clumped isotope thermometry in continental tectonics. *Tectonophysics* 647-648, 1-20 DOI: <https://doi.org/10.1016/j.tecto.2015.02.019>.

Jaffrés, J., Shields, G., Wallmann, K., 2007. The oxygen isotope evolution of seawater: A critical review of a long-standing controversy and an improved geological water cycle model for the past 3.4 billion years. Elsevier Sequoia S.A., Amsterdam, p. 83 DOI: 10.1016/j.earscirev.2007.04.002.

Joachimski, M.M., Lai, X.L., Shen, S.Z., Jiang, H.S., Luo, G.M., Chen, B., Chen, J., Sun, Y.D., 2012. Climate warming in the latest Permian and the Permian-Triassic mass extinction. *Geology* 40, 195-198 DOI: 10.1130/G32707.1.

Joachimski, M.M., Müller, J., Gallagher, T.M., Mathes, G., Chu, D.L., Mouraviev, F., Silantiev, V., Sun, Y.D., Tong, J.N., 2022. Five million years of high atmospheric CO₂ in the aftermath of the Permian-Triassic mass extinction. *Geology* 50, 650-654 DOI: 10.1130/G49714.1.

Kim, S.-T., Mucci, A., Taylor, B.E., 2007. Phosphoric acid fractionation factors for calcite and aragonite between 25 and 75 °C: Revisited. *Chemical Geology* 246, 135-146 DOI: <https://doi.org/10.1016/j.chemgeo.2007.08.005>.

Kim, S.T., O'Neil, J.R., 1997. Equilibrium and nonequilibrium oxygen isotope effects in synthetic carbonates. *Geochimica Et Cosmochimica Acta* 61, 3461-3475 DOI: [https://doi.org/10.1016/S0016-7037\(97\)00169-5](https://doi.org/10.1016/S0016-7037(97)00169-5).

Korte, C., Kozur, H.W., Bruckschen, P., Veizer, J., 2003. Strontium isotope evolution of Late Permian and Triassic seawater. *Geochimica et Cosmochimica Acta* 67, 47-62 DOI: [https://doi.org/10.1016/S0016-7037\(02\)01035-9](https://doi.org/10.1016/S0016-7037(02)01035-9).

Korte, C., Kozur, H.W., Veizer, J., 2005. $\delta^{13}\text{C}$ and $\delta^{18}\text{O}$ values of Triassic brachiopods and carbonate rocks as proxies for coeval seawater and palaeotemperature. *Palaeogeography, Palaeoclimatology, Palaeoecology* 226, 287-306 DOI: <https://doi.org/10.1016/j.palaeo.2005.05.018>.

Korte, C., Pande, P., Kalia, P., Kozur, H.W., Joachimski, M.M., Oberhänsli, H., 2010. Massive volcanism at the Permian–Triassic boundary and its impact on the isotopic composition of the ocean and atmosphere. *J Asian Earth Sci* 37, 293-311 DOI: <https://doi.org/10.1016/j.jseaes.2009.08.012>.

Lawrence, M.G., Greig, A., Collerson, K.D., Kamber, B.S., 2006. Rare Earth Element and Yttrium Variability in South East Queensland Waterways. *Aquatic Geochemistry* 12, 39-72 DOI: 10.1007/s10498-005-4471-8.

- Lawson, M., Shenton, B.J., Stolper, D.A., Eiler, J.M., Rasbury, E.T., Becker, T.P., Phillips-Lander, C.M., Buono, A.S., Becker, S.P., Pottorf, R., Gray, G.G., Yurewicz, D., Gournay, J., 2017. Deciphering the diagenetic history of the El Abra Formation of eastern Mexico using reordered clumped isotope temperatures and U-Pb dating. *GSA Bulletin* 130, 617-629 DOI: 10.1130/B31656.1.
- Lear, C.H., Elderfield, H., Wilson, P.A., 2000. Cenozoic Deep-Sea Temperatures and Global Ice Volumes from Mg/Ca in Benthic Foraminiferal Calcite. *Science* 287, 269-272 DOI: 10.1126/science.287.5451.269.
- Lécuyer, C., Amiot, R., Touzeau, A., Trotter, J., 2013. Calibration of the phosphate $\delta^{18}\text{O}$ thermometer with carbonate–water oxygen isotope fractionation equations. *Chemical Geology* 347, 217-226 DOI: <https://doi.org/10.1016/j.chemgeo.2013.03.008>.
- Letulle, T., Gaspard, D., Daëron, M., Arnaud-Godet, F., Vinçon-Laugier, A., Suan, G., Lécuyer, C., 2023. Multi-proxy assessment of brachiopod shell calcite as a potential archive of seawater temperature and oxygen isotope composition. *Biogeosciences* 20, 1381-1403 DOI: <https://doi.org/10.5194/bg-20-1381-2023>.
- Leu, M., Bucher, H., Baud, A., Vennemann, T., Luz, Z., Hautmann, M., Goudemand, N., 2023. An expanded Smithian–Spathian (Lower Triassic) boundary from a reefal build-up record in Oman: implications for conodont taxonomy, high-resolution biochronology and the carbon isotope record. *Papers in Palaeontology* 9, e1481 DOI: <https://doi.org/10.1002/spp2.1481>.
- Lhomme, N., Clarke, G.K.C., Ritz, C., 2005. Global budget of water isotopes inferred from polar ice sheets. *Geophys Res Lett* 32 DOI: <https://doi.org/10.1029/2005GL023774>.
- Looser, N., Petschnig, P., Hemingway, J.D., Fernandez, A., Morales Grafulha, L., Perez-Huerta, A., Vickers, M.L., Price, G.D., Schmidt, M.W., Bernasconi, S.M., 2023. Thermally-induced clumped isotope resetting in belemnite and optical calcites: Towards material-specific kinetics. *Geochimica et Cosmochimica Acta* DOI: <https://doi.org/10.1016/j.gca.2023.03.030>.
- Luz, Z., 2022. Characterizing conodont bioapatite from the Early-Triassic: an analytical and palaeoclimatological approach, *Faculté des géosciences et de l'environnement. Université de Lausanne, Lausanne*, p. 154 DOI: [urn:nbn:ch:serval-BIB_8C8763A96DE22](https://nbn-resolving.org/urn:nbn:ch:serval-BIB_8C8763A96DE22).
- Okai, T., Suzuki, A., Kawahata, H., Terashima, S., Imai, N., 2002. Preparation of a New Geological Survey of Japan Geochemical Reference Material: Coral JcP-1. *Geostandards Newsletter* 26, 95-99 DOI: <https://doi.org/10.1111/j.1751-908X.2002.tb00627.x>.
- Passey, B.H., Henkes, G.A., 2012. Carbonate clumped isotope bond reordering and geospeedometry. *Earth and Planetary Science Letters* 351-352, 223-236 DOI: <https://doi.org/10.1016/j.epsl.2012.07.021>.
- Perez-Beltran, S., Zaheer, W., Sun, Z., Defliese, W.F., Banerjee, S., Grossman, E.L., 2023. Density functional theory and ab initio molecular dynamics reveal atomistic mechanisms for carbonate clumped isotope reordering. *Science Advances* 9, eadf1701 DOI: 10.1126/sciadv.adf1701.
- Pérez-Huerta, A., Cusack, M., Jeffries, T.E., Williams, C.T., 2008. High resolution distribution of magnesium and strontium and the evaluation of Mg/Ca thermometry in Recent brachiopod shells. *Chemical Geology* 247, 229-241 DOI: <https://doi.org/10.1016/j.chemgeo.2007.10.014>.
- Petersen, S.V., Defliese, W.F., Saenger, C., Daëron, M., Huntington, K.W., John, C.M., Kelson, J.R., Bernasconi, S.M., Colman, A.S., Kluge, T., Olack, G.A., Schauer, A.J., Bajnai, D., Bonifacie, M., Breitenbach, S.F.M., Fiebig, J., Fernandez, A.B., Henkes, G.A., Hodell, D., Katz, A., Kele, S., Lohmann, K.C., Passey, B.H., Peral, M.Y., Petrizzo, D.A., Rosenheim, B.E., Tripathi, A., Venturelli, R.,

Young, E.D., Winkelstern, I.Z., 2019. Effects of Improved ^{17}O Correction on Interlaboratory Agreement in Clumped Isotope Calibrations, Estimates of Mineral-Specific Offsets, and Temperature Dependence of Acid Digestion Fractionation. *Geochemistry, Geophysics, Geosystems* 20, 3495-3519 DOI: <https://doi.org/10.1029/2018GC008127>.

Pilleveit, A., Marcoux, J., Stampfli, G., Baud, A., 1997. The Oman Exotics: a key to the understanding of the Neotethyan geodynamic evolution. *Geodinamica Acta* 10, 209-238 DOI: <https://doi.org/10.1080/09853111.1997.11105303>.

Price, G.D., Bajnai, D., Fiebig, J., 2020. Carbonate clumped isotope evidence for latitudinal seawater temperature gradients and the oxygen isotope composition of Early Cretaceous seas. *Palaeogeography, Palaeoclimatology, Palaeoecology* 552, 109777 DOI: <https://doi.org/10.1016/j.palaeo.2020.109777>.

Price, G.D., Passey, B.H., 2013. Dynamic polar climates in a greenhouse world: Evidence from clumped isotope thermometry of Early Cretaceous belemnites. *Geology* 41, 923-926 DOI: [10.1130/G34484.1](https://doi.org/10.1130/G34484.1).

Romanin, M., Crippa, G., Ye, F., Brand, U., Bitner, M.A., Gaspard, D., Häussermann, V., Laudien, J., 2018. A sampling strategy for recent and fossil brachiopods: selecting the optimal shell segment for geochemical analyses. *Rivista Italiana di Paleontologia e Stratigrafia* 124, 343-359 DOI: <https://doi.org/10.13130/2039-4942/10193>.

Romano, C., Goudemand, N., Vennemann, T.W., Ware, D., Schneebeli-Hermann, E., Hochuli, P.A., Brühwiler, T., Brinkmann, W., Bucher, H., 2013. Climatic and biotic upheavals following the end-Permian mass extinction. *Nature Geoscience* 6, 57-60 DOI: [10.1038/ngeo1667](https://doi.org/10.1038/ngeo1667).

Schauble, E.A., Ghosh, P., Eiler, J.M., 2006. Preferential formation of ^{13}C - ^{18}O bonds in carbonate minerals, estimated using first-principles lattice dynamics. *Geochimica et Cosmochimica Acta* 70, 2510-2529 DOI: <https://doi.org/10.1016/j.gca.2006.02.011>.

Schobben, M., Ullmann, C., Leda, L., Korn, D., Struck, U., Reimold, W., Ghaderi, A., Algeof, T., Korte, C., 2016. Discerning primary versus diagenetic signals in carbonate carbon and oxygen isotope records: An example from the Permian-Triassic boundary of Iran. *Chem. Geol.* 422, 94-107 DOI: [10.1016/j.chemgeo.2015.12.013](https://doi.org/10.1016/j.chemgeo.2015.12.013).

Scotese, C.R., Song, H.J., Mills, B.J.W., van der Meer, D.G., 2021. Phanerozoic paleotemperatures: The earth's changing climate during the last 540 million years. *Earth-Science Reviews* 215, 103503 DOI: <https://doi.org/10.1016/j.earscirev.2021.103503>.

Shackleton, N.J., Kennett, J.P., 1975. Paleotemperature history of the Cenozoic and the initiation of Antarctic glaciation: oxygen and carbon isotope analyses in DSDP Sites 277, 279, and 281. *Initial Reports Deep Sea Drilling Project* 29, 743-755 DOI: [10.2973/dsdp.proc.29.117.1975](https://doi.org/10.2973/dsdp.proc.29.117.1975).

Souquet, L., Goudemand, N., 2020. Exceptional basal-body preservation in some Early Triassic conodont elements from Oman. *Palaeogeography, Palaeoclimatology, Palaeoecology* 549, 109066 DOI: <https://doi.org/10.1016/j.palaeo.2019.01.028>.

Steuber, T., Veizer, J., 2002. Phanerozoic record of plate tectonic control of seawater chemistry and carbonate sedimentation. *Geology* 30, 1123-1126 DOI: [https://doi.org/10.1130/0091-7613\(2002\)030<1123:PROPTC>2.0.CO;2](https://doi.org/10.1130/0091-7613(2002)030<1123:PROPTC>2.0.CO;2).

Stolper, D.A., Eiler, J.M., 2015. The Kinetics of Solid-State Isotope-Exchange Reactions for Clumped Isotopes: A Study of Inorganic Calcites and Apatites from Natural and Experimental Samples. *Am J Sci* 315, 363-411 DOI: [10.2475/05.2015.01](https://doi.org/10.2475/05.2015.01).

Sun, Y., Joachimski, M.M., Wignall, P.B., Yan, C., Chen, Y., Jiang, H., Wang, L., Lai, X., 2012. Lethally Hot Temperatures During the Early Triassic Greenhouse. *Science* 338, 366-370 DOI: 10.1126/science.1224126.

Taylor, S.R., McLennan, S.M., 1985. The continental crust: its composition and evolution.

Trotter, J.A., Williams, I.S., Barnes, C.R., Lécuyer, C., Nicoll, R.S., 2008. Did Cooling Oceans Trigger Ordovician Biodiversification? Evidence from Conodont Thermometry. *Science* 321, 550-554 DOI: 10.1126/science.1155814.

Ullmann, C.V., Korte, C., 2015. Diagenetic alteration in low-Mg calcite from microfossils: a review. 2015 59 DOI: <https://doi.org/10.7306/gq.1217>.

Urey, H.C., Lowenstam, H.A., Epstein, S., McKinney, C.R., 1951. Measurement of paleotemperatures and temperatures of the Upper Cretaceous of England, Denmark, and the southeastern United States. *GSA Bulletin* 62, 399-416 DOI: 10.1130/0016-7606(1951)62[399:Mopato]2.0.Co;2.

Veizer, J., Ala, D., Azmy, K., Bruckschen, P., Buhl, D., Bruhn, F., Carden, G.A.F., Diener, A., Ebner, S., Godderis, Y., Jasper, T., Korte, C., Pawellek, F., Podlaha, O.G., Strauss, H., 1999. $^{87}\text{Sr}/^{86}\text{Sr}$, $\delta^{13}\text{C}$ and $\delta^{18}\text{O}$ evolution of Phanerozoic seawater. *Chemical Geology* 161, 59-88 DOI: 10.1016/S0009-2541(99)00081-9.

Veizer, J., Fritz, P., Jones, B., 1986. Geochemistry of brachiopods: Oxygen and carbon isotopic records of Paleozoic oceans. *Geochimica et Cosmochimica Acta* 50, 1679-1696 DOI: 10.1016/0016-7037(86)90130-4.

Veizer, J., Hoefs, J., 1976. The nature of $\text{O}^{18}/\text{O}^{16}$ and $\text{C}^{13}/\text{C}^{12}$ secular trends in sedimentary carbonate rocks. *Geochimica et Cosmochimica Acta* 40, 1387-1395 DOI: [https://doi.org/10.1016/0016-7037\(76\)90129-0](https://doi.org/10.1016/0016-7037(76)90129-0).

Vérard, C., 2019. Panalexis: towards global synthetic palaeogeographies using integration and coupling of manifold models. *Geological Magazine* 156, 320-330 DOI: 10.1017/S0016756817001042.

Widmann, P., Bucher, H., Leu, M., Vennemann, T., Bagherpour, B., Schneebeli-Hermann, E., Goudemand, N., Schaltegger, U., 2020. Dynamics of the largest carbon isotope excursion during the Early Triassic biotic recovery. *Front Earth Sc-Switz*, 196 DOI: <https://doi.org/10.3389/feart.2020.00196>.

Winkelstern, I.Z., Lohmann, K.C., 2016. Shallow burial alteration of dolomite and limestone clumped isotope geochemistry. *Geology* 44, 467-470 DOI: 10.1130/G37809.1.

General Conclusions and Recommendations

Using a wide array of geochemical and isotopic proxies, environmental perturbations associated with biotic events in the Tethys Ocean across the latest Permian to Early Triassic have been investigated. The studies documented in this thesis demonstrate that the record of volcanic activity across the PTB in South China varies across localities, with enhanced volcanic Hg emissions recorded several hundreds of thousand years before and after the mass extinction event. This spatial and temporal heterogeneity in enhanced volcanic Hg fluxes to Tethyan paleoenvironments was also the case during the Smithian to Spathian. In addition, elevated volcanic Hg fluxes to Tethyan depositional environments across the PTB and Smithian – Spathian cannot be confidently linked to STLIP magmatism. Instead, more proximal subduction-related arc volcanism was the likeliest source of volcanic Hg fluxes to South China across the PTB and Early Triassic, although Hg emissions from the STLIP across the PTB cannot be ruled out. Therefore, regional arc volcanism may have played a larger role in causing environmental deterioration in Tethyan paleoenvironments across the studied interval than previously thought. Consequently, further work is necessary to better constrain the role of regional volcanism in environmental deterioration and faunal extinction across the PTB. This can be achieved for example, by comparing the faunal records of regions characterized by regional volcanism across the PTB (e.g., eastern PaleoTethys and southwest Gondwana) with those of regions with no regional volcanic activity (e.g., eastern Gondwana). In addition, higher resolution absolute dating of STLIP rocks via precise U-Pb zircon geochronology is necessary to better understand links between STLIP intrusive magmatism and the PTBME.

The CAS S-isotope record demonstrates that the Early Triassic was characterized by a low seawater sulfate inventory, estimated to have been between 10 and 25 % of that of present-day oceans, permitting geologically rapid marine sulfur cycle perturbations at this time. In addition, the CAS S-isotope record indicates that relative to offshore carbonates, CAS extracted from continental shelf successions may be significantly offset from primary seawater S-isotope compositions as recorded by evaporites. Hence, offshore marine successions are better suited for deciphering global marine paleoenvironmental trends during the Early Triassic. Future work should therefore focus on offshore carbonates in investigating the record of Early Triassic marine redox variations. Furthermore, based on carbonate clumped isotope analyses, which yield seawater $\delta^{18}\text{O}$ values of ca. -1 ‰, it is estimated that seawater temperatures during the middle Smithian were about 36 °C but dropped to ca. 28 °C across the SSB. However, the middle Smithian to earliest Spathian was characterized by decreasing water column oxygenation in the global ocean. This redox trend coincided with both increased diversification and extinction rates in conodonts and ammonoids, as well as relatively warmer and cooler seawater temperatures. Hence, there is no consistent correlation between oceanic anoxia, seawater temperature changes and faunal turnover across the middle Smithian to early Spathian. Therefore, it is difficult to single out one environmental factor as the trigger for the biotic upheavals of the Smithian – Spathian transition. Consequently, synergies

between environmental and biotic factors (e.g., predation stress and intra-specific competition) during the SSB biotic crises require further investigation.

APPENDIX A

Supplementary information for Chapter 2:

Evidence for Variable Provenance of Mercury Anomalies During the Smithian – Spathian (Olenekian)

Oluwaseun Edward^{1*}, Hugo Bucher², Sandrine Le Houedec³, Christian V  rard³, Marc Leu², Aymon Baud⁴, Jeroen E. Sonke⁵, Franziska Blattmann¹, Thierry Adatte⁴, Torsten Vennemann¹

Text S1: Biostratigraphic age control between Wadi Musjah, Jebel Aweri, Shanggang, and Qiakong

A biostratigraphic correlation can be easily calibrated between the four studied sections although major differences exist with regards to the paleogeographical deposition, the latitudinal location, the lithology and the paleo bathymetrical depth. The biostratigraphic age control include inter alia ammonoid zones and conodont faunas.

Early Smithian

Of all 4 above-mentioned sections, only Shanggang covers the Early Triassic. The section includes the so called ‘‘Flemingites limestone’’ at the base, which is known to encompass the early Smithian stage. Concretely, the Flemingites limestone (within the Luolou Formation) includes the *Flemingites rursiradiatus* ammonoid zone, a well-established early Smithian zone (Brayard and Bucher, 2008). Furthermore, iconic early Smithian conodonts such as *Eurygnathodus costatus* and *Eurygnathodus hamadai* were recovered from these Flemingites limestone beds in Shanggang (Leu et al., 2022), clearly identifying this part of the Shanggang section as early Smithian in age.

Middle Smithian

In Wadi Musjah, conodonts are rare in the levels A-D, but specimens belonging to *Urduyella unicorna* n. gen. n. sp. were found (Leu et al., 2022). This species can also be found in Qiakong and Shanggang, South China in the middle Smithian Daye Formation and Luolou Formation, respectively (Leu et al., 2022). In other sections from South China, this species can be found in the *Owenites koeni* beds (e.g., Laren), a typical middle Smithian ammonoid fauna (Widmann et al. 2020). Furthermore, typical Smithian species (e.g., *Novispathodus ex gr. waageni* and *Discretella* sp.) co-occur in Wadi Musjah in levels B-D.

Within the uppermost part of level D in the Wadi Musjah section, *Inyoites oweni* was recovered. The *Inyoites* fauna is a typical ammonoid association from the late middle Smithian (within the *Owenites koeneni* beds). In the same bed (WM12C) we also found the conodont species *Discretella robusta*, a typical middle Smithian conodont species recorded also from *Owenites koeneni* beds in Vietnam (Shigeta et al. 2014) and the *Guangxidella bransoni* subzone (within the *Nv. ex. gr. waageni* zone) in Japan (Maekawa et al. 2018).

With this biostratigraphic age control, we can confidently state that levels A-D in Wadi Musjah and the Daye Formation in Qiakong are of middle Smithian age. Similarly, the middle part of the Luolou Formation in Shanggang is also of middle Smithian age with the co-occurrence of *Guangxidella bransoni*, *Neospathodus bevelledi* and *Urdyella unicorna* (Leu et al., 2022).

Late Smithian

Biostratigraphically, the late Smithian begins with the *Anasibirites multiformis* ammonoid fauna. Intercalibrated with this fauna, conodont fauna including *Hadrodontina aequabilis* and *Scythogondolella milleri* can be associated (Orchard 2008, Orchard and Zonneveld 2009). In Wadi Musjah, *Anasibirites multiformis*, *Scythogondolella milleri* and *Hadrodontina aequabilis* are found in levels F and G, respectively. Furthermore *Nv. pingdingshanensis* co-occurs with *Sc. milleri* in level G but ranges until level I, making *Nv. pingdingshanensis* an unsuitable candidate for the beginning of the Spathian. Nonetheless, for its restricted occurrence of late Smithian to early Spathian age, *Nv. pingdingshanensis* is of important biostratigraphic value as it can also co-occur with the ammonoid *Tirolites cassianus* (Shigeta et al. 2014). *Hadrodontina aequabilis* is recorded from Jebel Aweri in level A and in Qiakong in the lower part of level IVb.

The second ammonoid beds within the late Smithian, the *Xenoceltites/Glyptophiceras* beds, are associated with the conodont *Nv. pingdingshanensis/Nv.abruptus* beds (Shigeta et al. 2014, Widmann et al. 2020). *Xenoceltites* was found in the uppermost part of level A in Jebel Aweri. The conodont fauna *Nv. pingdingshanensis/Nv.abruptus* was retrieved from the middle part of level IVb in Qiakong, from level B in Jebel Aweri and from the upper part of level G in Wadi Musjah. Chemostratigraphically, these faunas are within the worldwide recognized positive C-isotope excursion during the late Smithian.

Therefore, levels F and G in Wadi Musjah, levels A and B in Jebel Aweri and the lower half of unit IVb in Qiakong are definitely associated with late Smithian faunas.

Early Spathian

One of the earliest Spathian conodont faunas (among others) consists of the co-occurrence of *Ic. crassatus* and *Nv. pingdingshanensis* (Orchard & Tozer 1997, Komatsu et al 2016). This faunal composition can be found in level D and E in Jebel Aweri and in level I in Wadi Musjah. In Qiakong, *Ic. crassatus* could not be recovered, but *Nv. pingdingshanensis* ranges to the uppermost carbonate beds within the black shale unit IVb, where it co-occurs with *Nv. brevissimus*, another typical early Spathian conodont species (Orchard, 1995). Chemostratigraphically, the earliest Spathian conodont fauna coincides with the positive C-isotope peak which can be observed in all four studied localities (except for Shanggang where the peak coincides with a hiatus).

Level C in Jebel Aweri is here also considered to be of earliest Spathian age, primarily based on the co-occurrence of *Nv. pingdingshanensis*, *Is. zaksi* and neogondolellids, typical of early Spathian age (Orchard, 2022).

Text S2: Expressing Nd isotope compositions in $\epsilon_{Nd(t)}$

Obtained Nd isotope ratios, $^{143}\text{Nd}/^{144}\text{Nd}$, were converted to $\epsilon_{Nd(t)}$ as follows:

$$^{143}\text{Nd}/^{144}\text{Nd}_{(t)} = ^{143}\text{Nd}/^{144}\text{Nd}_{(0)} - ^{147}\text{Sm}/^{144}\text{Nd}_{(0)} \times [\exp^{(\lambda t)} - 1] \quad (\text{Martin and Macdougall, 1995}) \quad (1)$$

Where t = age of the sample, λ = decay constant for ^{147}Sm - ^{143}Nd , i.e., $6.54 \times 10^{-12} \text{ yr}^{-1}$, and

$$^{147}\text{Sm}/^{144}\text{Nd} = \text{Sm}/\text{Nd}_{(\text{avg})} \times \text{Sm}/\text{Nd isotopic factor} \quad (2)$$

Where Sm/Nd isotopic factor = isotopic abundance/atomic mass of $^{147}\text{Sm}/^{144}\text{Nd}$ i.e., $(14.99/23.8) / (150.36/144.24) = 0.604$, and $\text{Sm}/\text{Nd}_{(\text{avg})}$ = Average Sm/Nd ratio for analyzed bioapatite samples (0.2123 ± 0.0160 ppm, $n = 7$).

$$\epsilon_{Nd(t)} = [^{143}\text{Nd}/^{144}\text{Nd}_{(t)} / ^{143}\text{Nd}/^{144}\text{Nd}_{(\text{CHUR})(t)} - 1] \times 10^4. \quad (3)$$

$$^{143}\text{Nd}/^{144}\text{Nd}_{(\text{CHUR})(t)} = ^{143}\text{Nd}/^{144}\text{Nd}_{(\text{CHUR})(0)} - ^{147}\text{Sm}/^{144}\text{Nd}_{(\text{CHUR})(0)} \times [\exp^{(\lambda t)} - 1] \quad (4)$$

where $^{143}\text{Nd}/^{144}\text{Nd}_{(\text{CHUR})(0)} = 0.512638$ and $^{147}\text{Sm}/^{144}\text{Nd}_{(\text{CHUR})(0)} = 0.1967$ (Jacobsen and Wasserburg, 1980).

Absolute ages were calculated by linear interpolation using a Python script (see python file named “age_interpolation.py” in the dataset repository). For Qiakong (QIA) and Shanggang (SHA), linear interpolation was done based on the published U-Pb zircon ages for samples from these sections (Widmann et al., 2020). For Jebel Aweri (JA) and Wadi Musjah (WMJ), the ages of the Smithian – Spathian boundary (249.29 Ma, Widmann et al., 2020), as well as Unitary Association Zone boundaries for QIA biostratigraphically correlated with JA and WMJ (Widmann et al. 2020; Leu et al. 2023; Fig. 8 of main text), were used as tie-points for age interpolation.

Table S1: Spearman's correlation coefficient (ρ) and p-values (p) for the statistical correlation between Hg and TOC, Al, Fe, Mo, and U for the studied successions.

	Locality	n		Strength (ρ)	Significance (p)	Correlation
TOC	SHA	58		0.57	0.00	moderate, significant
	QIA	36		0.72	0.00	strong, significant
	JA	18		0.17	0.49	none
	WMJ	16		0.19	0.48	none
Al	SHA	19		0.50	0.03	moderate, significant
	QIA	26		-0.15	0.46	none
	JA	34		-0.06	0.75	none
	WMJ	11		0.01	0.98	none
Fe	SHA	19		0.39	0.10	none
	QIA	26		-0.04	0.84	none
	JA	34		0.24	0.19	none
	WMJ	11		-0.04	0.91	none
U	SHA	19		0.57	0.01	moderate, significant
	QIA	27		0.65	0.00	moderate, significant
	JA	11		-0.03	0.94	none
Mo	SHA	7		0.57	0.18	moderate, insignificant
	QIA	13		0.29	0.33	none
	JA	24		0.26	0.23	none
	WMJ	11		0.06	0.86	none

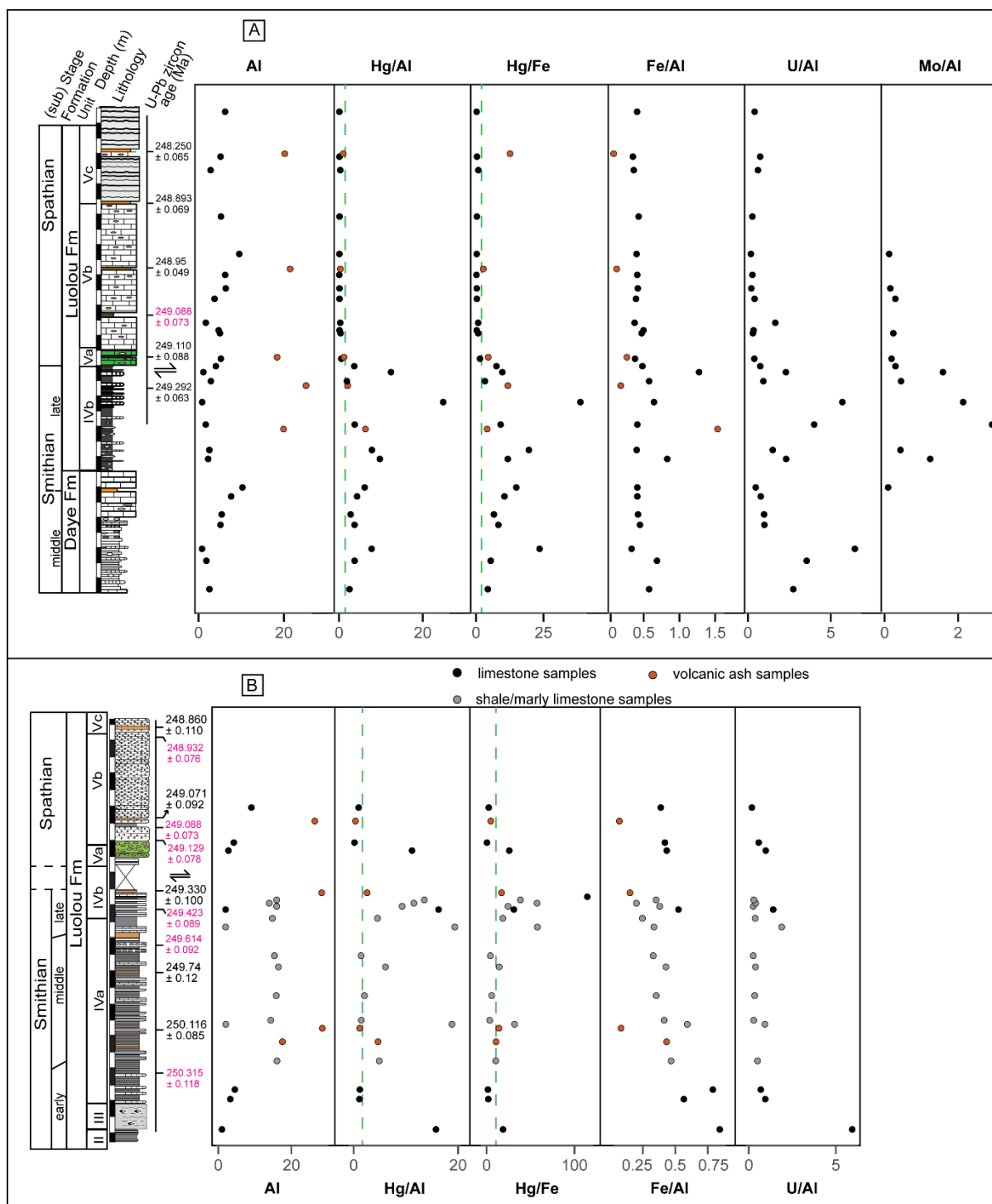


Figure S1. Geochemical profile showing Al, Hg/Al, Hg/Fe, Fe/Al, U/Al and Mo/Al records for A) the Qiakong section and B) Al, Hg/Al, Hg/Fe, Fe/Al, and U/Al records for the Shanggang section. Vertical dashed green lines represent background values. Normalized Hg concentrations indicate that both the middle and late Smithian were characterized by elevated Hg sequestration.

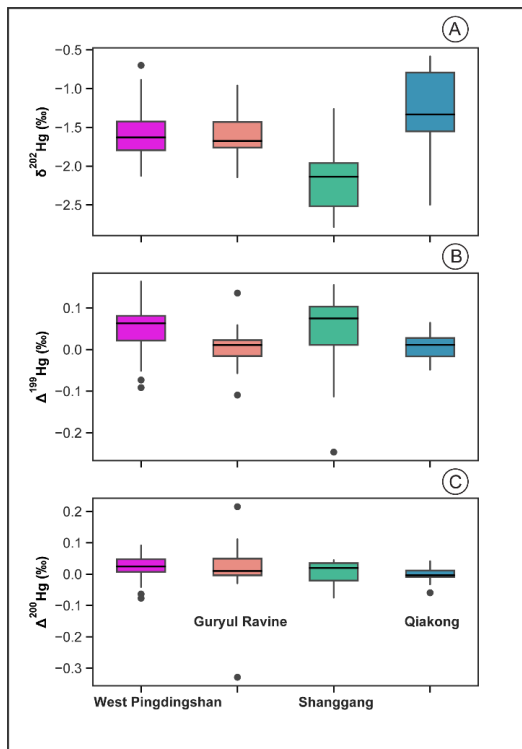


Figure S2. Box and whisker plots of Hg isotope compositions for Smithian to Spathian samples from Tethyan marine successions. A) $\delta^{202}\text{Hg}$, b) $\Delta^{199}\text{Hg}$ and c) $\Delta^{200}\text{Hg}$ values recorded from the studied sections – Qiakong and Shanggang, compared with published values from Chaohu, South China and Guryul Ravine, India. Data for Chaohu and Guryul Ravine are from Wang et al. (2019).

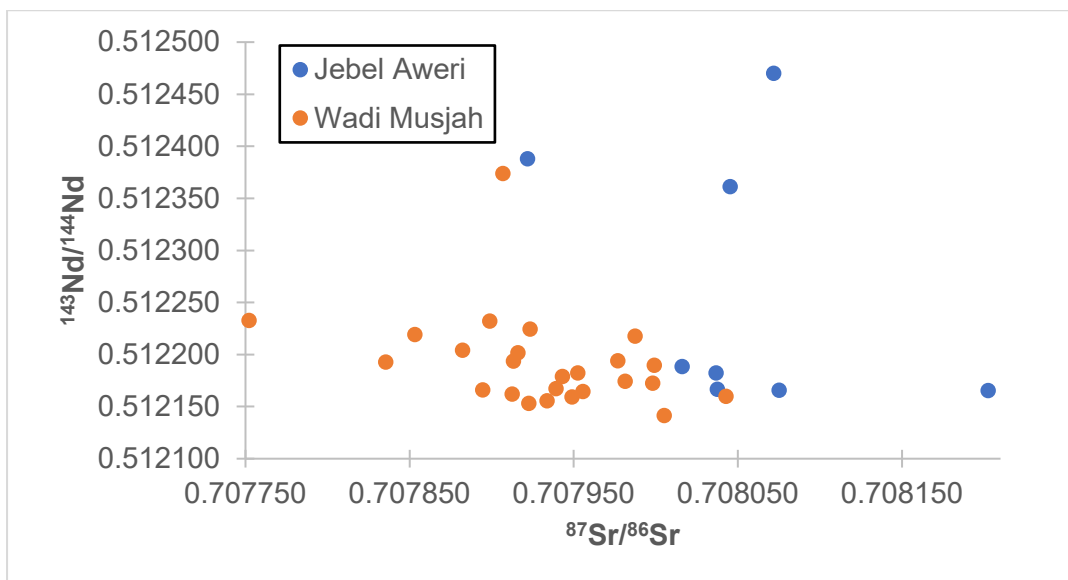


Fig. S3. Cross-plot of Strontium and Neodymium isotope compositions. Nd and Sr isotope compositions have a moderate negative correlation, $r = -0.49$, $n = 29$.

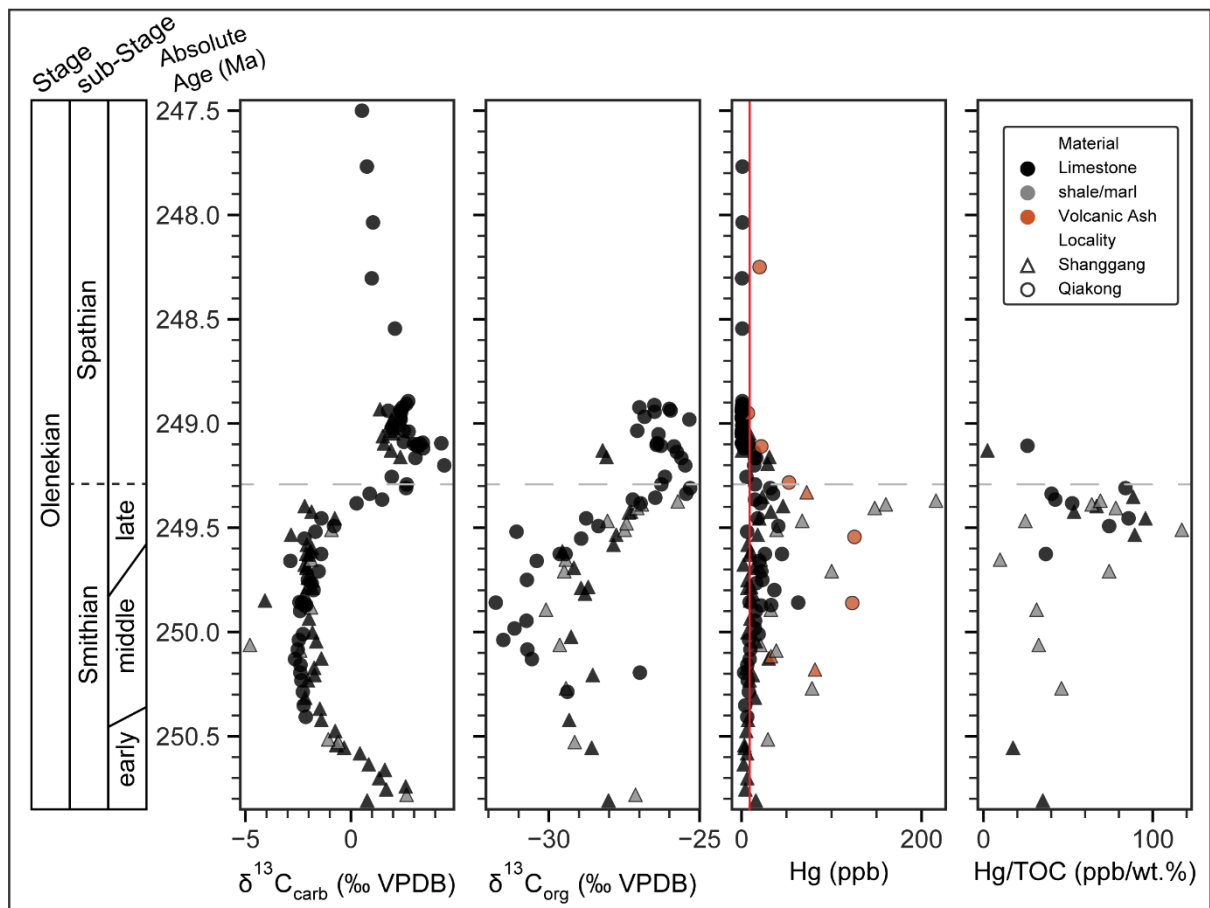


Figure S4. Carbon isotope (carbonate and organic carbon), mercury (Hg) and Hg/TOC ratios for Shanggang (SHA) and Qiakong (QIA) samples plotted relative to interpolated absolute ages. Absolute ages are interpolated after Widmann et al. (2020). Vertical red line denotes background Hg concentrations (10 ppb) and horizontal grey dashed line denotes the SSB absolute age (249.29 Ma) after Widmann et al. (2020).

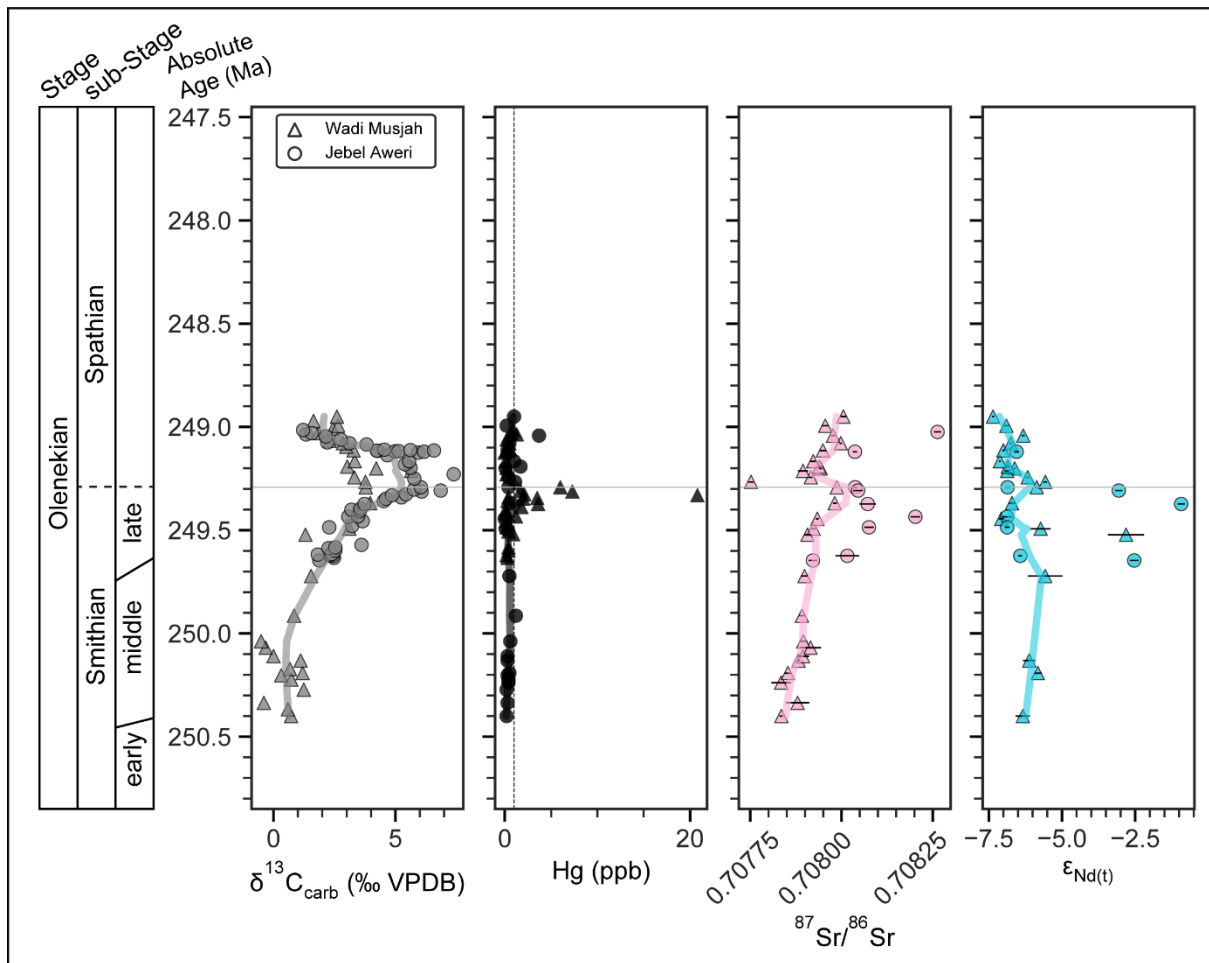


Figure S5. Carbon isotope, mercury concentration, $^{87}\text{Sr}/^{86}\text{Sr}$ ratios, and $\epsilon_{\text{Nd}(t)}$ values for Wadi Musjah (WMJ) and Jebel Aweri (JA) samples plotted according to absolute age. Absolute ages for WMJ and JA are derived based on biostratigraphic correlation of unitary association zones (UAZs) of WMJ and JA (Fig. 8 of main text; Leu et al. 2023). The estimated absolute ages of UAZ boundaries for QIA (correlated to WMJ and JA) and that of the Smithian-Spathian boundary (Widmann et al., 2020) were used as tie-points for linear absolute age interpolation.

References

- Brayard, A., Bucher, H., 2008. Smithian (Early Triassic) ammonoid faunas from northwestern Guangxi (South China): taxonomy and biochronology. Wiley-Blackwell Chichester (UK).
- Jacobsen, S.B., Wasserburg, G.J., 1980. Sm-Nd isotopic evolution of chondrites. *Earth and Planetary Science Letters* 50, 139-155 DOI: [https://doi.org/10.1016/0012-821X\(80\)90125-9](https://doi.org/10.1016/0012-821X(80)90125-9).
- Komatsu, T., Takashima, R., Shigeta, Y., Maekawa, T., Tran, H. D., Cong, T. D., ... & Takahashi, O. (2016). Carbon isotopic excursions and detailed ammonoid and conodont biostratigraphies around Smithian–Spathian boundary in the Bac Thuy Formation, Vietnam. *Palaeogeography, Palaeoclimatology, Palaeoecology*, 454, 65-74.
- Leu, M., Bucher, H., Vennemann, T., Bagherpour, B., Ji, C., Brosse, M., Goudemand, N., 2022. A Unitary Association-based conodont biozonation of the Smithian–Spathian boundary (Early Triassic) and associated biotic crisis from South China. *Swiss Journal of Palaeontology* 141, 19 DOI: 10.1186/s13358-022-00259-x.
- Leu, M., Bucher, H., Baud, A., Vennemann, T., Luz, Z., Hautmann, M., Goudemand, N., 2023. An expanded Smithian–Spathian (Lower Triassic) boundary from a reefal build-up record in Oman: implications for conodont taxonomy, high-resolution biochronology and the carbon isotope record. *Papers in Palaeontology* 9, e1481 DOI: <https://doi.org/10.1002/spp2.1481>
- Maekawa, T., Komatsu, T., & Koike, T. (2018). Early Triassic conodonts from the Tahogawa Member of the Taho Formation, Ehime Prefecture, Southwest Japan. *Paleontological Research*, 22(s1), 1-62.
- Martin, E.E., Macdougall, J.D., 1995. Sr and Nd isotopes at the Permian/Triassic boundary: A record of climate change. *Chemical Geology* 125, 73-99 DOI: [https://doi.org/10.1016/0009-2541\(95\)00081-V](https://doi.org/10.1016/0009-2541(95)00081-V).
- Orchard, M. J. (1995). Taxonomy and correlation of Lower Triassic (Spathian) segminate conodonts from Oman and revision of some species of Neospathodus. *Journal of Paleontology*, 110-122.
- Orchard, M. J. (2008). Lower Triassic conodonts from the Canadian Arctic, their intercalibration with ammonoid-based stages and a comparison with other North American Olenekian faunas. *Polar Research*, 27(3), 393-412.
- Orchard, M.J., 2022. North American Spathian (upper Olenekian, Lower Triassic) neogondolellin conodonts. *Papers in Palaeontology* 8, e1409 DOI: <https://doi.org/10.1002/spp2.1409>.
- Orchard, M. J., & Tozer, E. T. (1997). Triassic conodont biochronology, its calibration with the ammonoid standard, and a biostratigraphic summary for the Western Canada Sedimentary Basin. *Bulletin of Canadian Petroleum Geology*, 45(4), 675-692.
- Orchard, M. J., & Zonneveld, J. P. (2009). The Lower Triassic Sulphur Mountain Formation in the Wapiti Lake area: lithostratigraphy, conodont biostratigraphy, and a new biozonation for the lower Olenekian (Smithian) Earth Science Sector (ESS) Contribution 20080714. *Canadian Journal of Earth Sciences*, 46(10), 757-790.
- Shigeta, Y. (Ed.). (2014). *Olenekian (Early Triassic) stratigraphy and fossil assemblages in northeastern Vietnam* (No. 45). National Museum of Nature and Science.
- Wang, X., Cawood, P.A., Zhao, H., Zhao, L., Grasby, S.E., Chen, Z.-Q., Zhang, L., 2019. Global mercury cycle during the end-Permian mass extinction and subsequent Early Triassic recovery. *Earth and Planetary Science Letters* 513, 144-155 DOI: 10.1016/j.epsl.2019.02.026.
- Widmann, P., Bucher, H., Leu, M., Vennemann, T., Bagherpour, B., Schneebeli-Hermann, E., ... & Schaltegger, U. (2020). Dynamics of the Largest Carbon Isotope Excursion During the Early Triassic Biotic Recovery. *Frontiers in Earth Science*, 8, 196.

APPENDIX B

Supplementary information for Chapter 3:

Olenekian sulfur isotope records: Deciphering global trends, links to marine redox changes and faunal evolution

Oluwaseun Edward^{a*}, Jorge E. Spangenberg^a, Marc Leu^b, Charline Ragon^c, Sandrine Le Houedec^d,
Aymon Baud^e, Hugo Bucher^b, Torsten Vennemann^a

Calculation of CAS concentrations

CAS concentrations were calculated as follows:

Step 1: CAS concentration (g/g) =

$$\left[\frac{\text{Weight of precipitated BaSO}_4 \text{ (in grams)} \times \text{atomic weight ratio}}{\text{weight of carbonate in treated sample (in grams)}} \right]$$

where atomic weight ratio = molecular weight of SO₄ / molecular weight of BaSO₄ = 0.4116,

weight of carbonate in treated sample = initial weight of treated sample – weight after acid treatment

Step 2: CAS concentration (μg/g) = CAS concentration (g/g) × 10⁶

Step 3: Final CAS concentration (μg/g) = CAS concentration (μg/g) × (Total Sulfur content from Elemental Analysis (in wt. %) / 13.74)

where 13.74 = the percentage of sulfur in BaSO₄

Calculation of sample absolute age using linear interpolation.

Absolute ages were calculated for all samples by linear interpolation using a Python script based on the publicly available Python library, Numpy. A simplified version of the relevant code, which can be modified to suit much larger datasets, is provided below.

```

1 import numpy as np
2
3 # Create a dictionary that contains samples with known ages,
4 # as well as their stratigraphic heights, like so.
5 known_data = {
6     'age': [251.1, 249.292, 249.088, 248.25, 248],
7     'height': [101.2, 150.6, 158.1, 189.8, 224.6]
8 }
9
10 # Then create a list with the stratigraphic heights of the interbedded samples
11 # for which absolute ages are not known.
12 unknown_height = [103.4, 103.9, 106.5, 108.1, 109.4,
13                  110.5, 111.3, 113.1, 114.2, 115.1,
14                  115.8, 117.1, 119.5, 120.1]
15
16 # Then using the numpy interp method, you can calculate the corresponding ages
17 # for these interbedded samples using linear interpolation
18
19 interpolated_ages = np.interp(unknown_height, known_data["height"], known_data["age"])
20
21 interpolated_ages

```

Figure S1. Example python code with which linear interpolation of absolute ages can be achieved. Relevant explanations are included in the code snippet.

Lowess regression model

A locally weighted scatterplot smoothing (LOWESS) model, which uses a moving window to fit local linear regressions to data, was applied to the CAS global data compilation (Fig. 8 of the main text). The model assigns more weight to nearby data points and less weight to distant ones. The Lowess model was implemented in Python using the Statsmodels module (version 0.13.5) which is publicly available at: <https://www.statsmodels.org/stable/index.html>. The main parameter controlling the smoothness of the Lowess fit in the statsmodels Python module herein applied is the parameter: “frac”. This parameter determines the size of the local window used for estimating each y-value in the smoothed curve (however, it should be noted that the smoothed data in this study relates to the x-axis). This parameter (frac) takes a value between 0 and 1. More details on the parameters of the Lowess function in statsmodels can be found in the official user guide available at https://www.statsmodels.org/devel/generated/statsmodels.nonparametric.smoothers_lowess.lowess.html. Effectively, the choice of local window selected (frac) enables one to control the tradeoff between smoothness of the fit and the fit’s responsiveness to local fluctuations in the data. In this study, different values of frac between 0.1 and 0.5 were tested to determine an optimal value considering this tradeoff (Fig. S2).

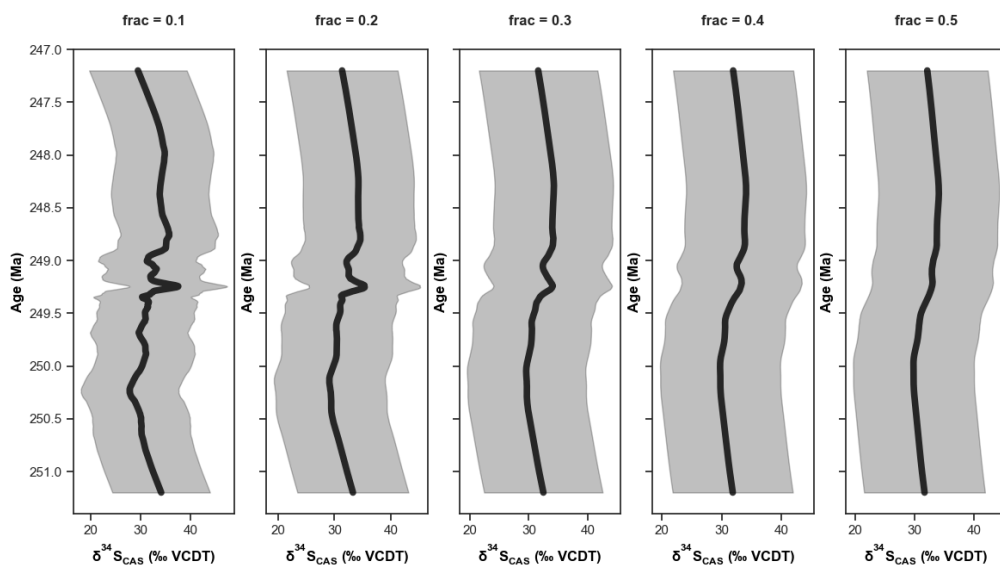


Figure S2. Plot showing the output of LOWESS model iterations of the Python statsmodels LOWESS smoothing function applying different ‘frac’ values (0.1 – 0.5). The data used in this instance is the compilation of published CAS $\delta^{34}\text{S}$ values for the Olenekian as well as the new data generated for the current study (Figure 8 in the main text).

Based on these tests, we use $\text{frac}=0.3$ for the global CAS $\delta^{34}\text{S}$ compilation presented in the main text, as it balances both the smoothness of the fit and its responsiveness to the fluctuations in the data. Importantly, regardless of which frac value is used, the overall trend of the Lowess fit remains consistent (i.e., a decrease in $\delta^{34}\text{S}$ values from 251.2 Ma, followed by an increasing trend which peaks close to 249.3 Ma, and then a gradual decline to ca. 247 Ma). An example of the python code used to implement the Lowess fit, and its 95% confidence interval is included below (Figure S3).

```

1 def plot_smoothed_with_ci(x_data, y_data, ax, color, frac=0.3, is_sorted=True):
2     """
3     This function carries out lowess smoothing using the statsmodels lowess function,
4     calculates a 95% confidence interval for the lowess smoothed data and plots both
5     the lowess fits and confidence interval on specified axes in a scatter plot.
6     For the code to successfully run, the following package dependencies are required:
7     pandas, numpy, matplotlib pyplot and statsmodels. Upon installation of these packages,
8     the following code needs to be run in order to satisfy the package dependencies as follows:
9
10    import pandas as pd
11    import numpy as np
12    import matplotlib.pyplot as plt
13    from statsmodels.nonparametric.smoothers_lowess import lowess
14    """
15
16    # Fit lowess smoother
17    smoothed_data = lowess(x_data, y_data, frac=frac, is_sorted=True)
18
19    # Calculate residuals
20    residuals = x_data - smoothed_data[:, 1]
21
22    # Calculate degrees of freedom
23    dof = len(residuals) - 1
24
25    # Calculate mean squared error (MSE)
26    mse = np.sum(residuals**2) / dof
27
28    # Calculate standard error of residuals
29    se = np.sqrt(mse)
30    # se = np.std(residuals)
31
32    # specify the z-score
33    z_score = 1.96 # For a 95% confidence interval & assuming a normal distribution.
34
35    # Calculate margin of error
36    margin_of_error = z_score * se
37
38    # Calculate confidence interval
39    lower_bound = smoothed_data[:, 1] - margin_of_error
40    upper_bound = smoothed_data[:, 1] + margin_of_error
41
42    # Plot the smoothed values and the 95% confidence interval
43    ax.plot(smoothed_data[:, 1], smoothed_data[:, 0], c=color, linewidth=5.5, alpha=0.8)
44    ax.fill_betweenx(smoothed_data[:, 0], lower_bound, upper_bound, color=color, alpha=0.25)
45
46
47 # Call the function using the requisite parameters
48 plot_smoothed_with_ci(d13C_df['d13C'], d13C_df['Age'], ax0, color[0], frac=0.3)

```

Figure S3. Snapshot of Python code used to implement LOWESS smoothing with 95% confidence interval for the CAS isotopic data.

Facies description: Qiakong (QIA) section

Thin section photomicrographs for QIA enable the delineation of six main microfacies in this section (Fig. S4).

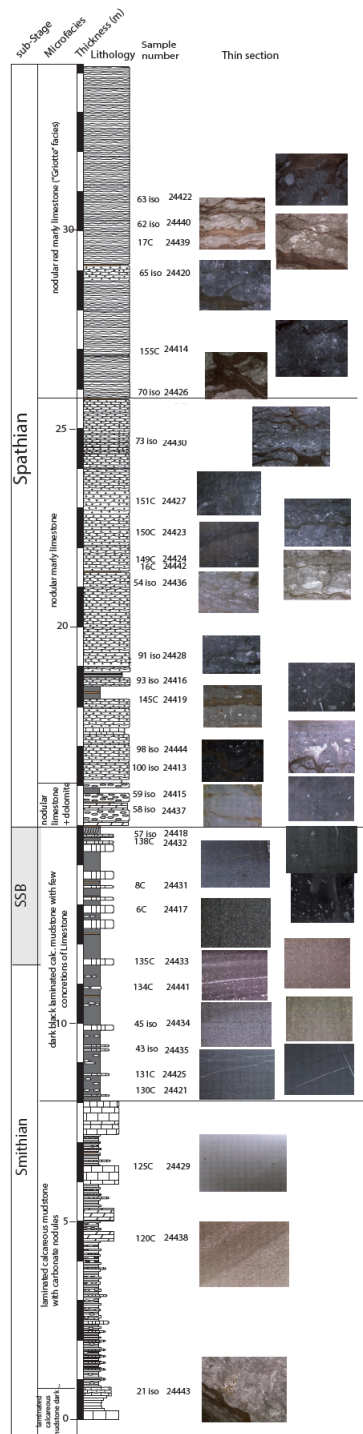


Figure S4: Lithological log of the Qiakong section (after Leu et al., 2022) with microfacies annotated.

The microfacies consist of carbonates deposited on distal outer ramp part of the continental margin with fine to silty terrigenous input. The microfacies are described from the base to the top of the QIA section.

Microfacies 1

This consists of dark laminated calcareous mudstone and is 0.7 m thick. It shows abundant calcispheres, possibly calcitized radiolarians in a micritic matrix. There is sharp, undulatory contact between calcisphere wackestone and dark lime mudstone with thin shelled fragmented flat valves (Fig. S5).



Figure S5. Representative thin section photo (no. 24443) of microfacies 1 – dark laminated calcareous mudstone.

Microfacies 2

This microfacies encompasses an interval of 7.2 m and is made up of both laminated calcareous mudstone with carbonate nodules, as well as laminated high-energy lime silty arenite with calcisphere phantom and thin-shelled fragmented flat valves (Fig. S6).



Figure S6. Thin section photo (no. 24438) of microfacies 2 showing a laminated lime silty arenite.

Microfacies 3

This microfacies covers the next ca. 7 m of the QIA section and consists of a combination of black shales and dark limestone and limestone concretions. This microfacies likely marks an oxygen depletion event during the Smithian – Spathian transition, as well as input of terrigenous material rich in organic matter (Unit IV of Galfetti et al., 2008). The microfacies of the lower 4 m show high energy deposition as seen in the thin section no. 24435 (Fig. S7). The limestone microfacies of the upper 3m as seen in thin section no. 24417 (Fig. S8) are characterized by low energy dark lime mudstone - wackestone with unsorted calcispheres.



Figure S7. Thin section photo (no. 24435) showing laminated reworked lime packstone made of broken flat thin-shelled bivalve micro-debris.

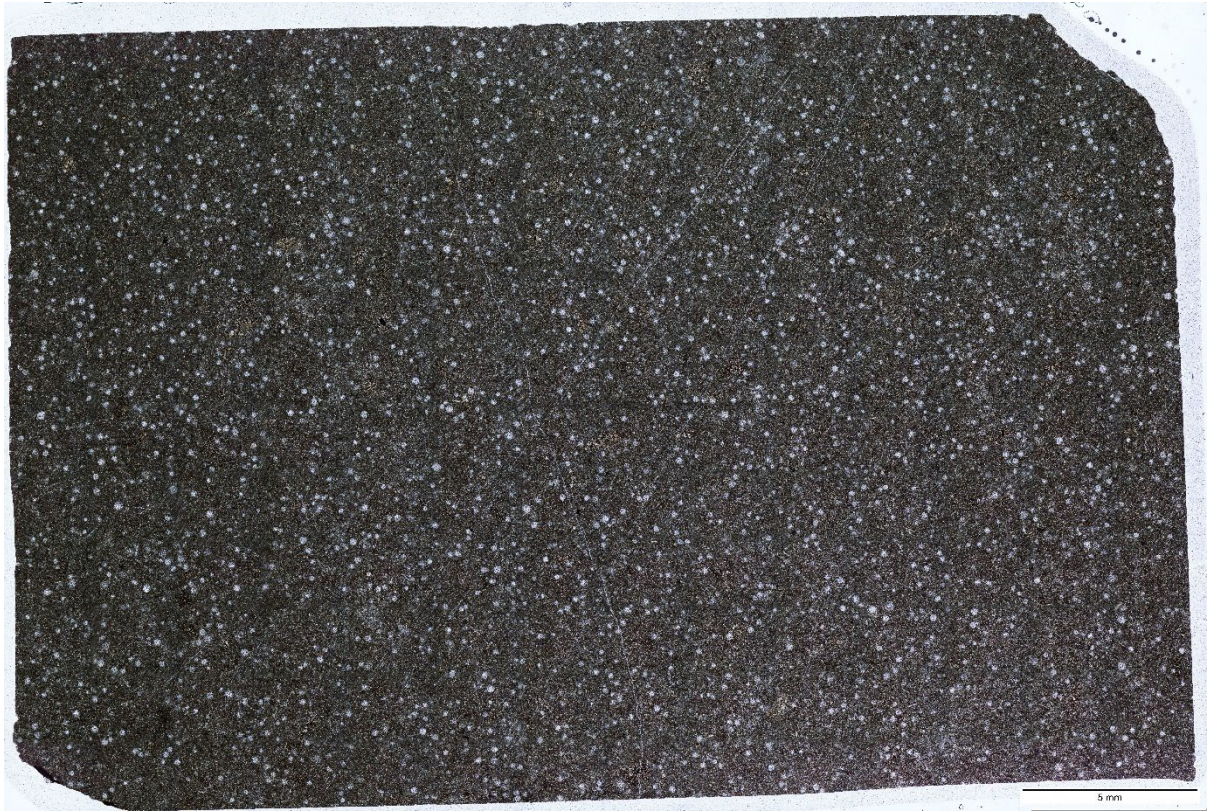


Figure S8. Thin section (no. 24417) photo showing dark lime mudstone-wackestone with unsorted calcispheres of 0.1 to 0.3 mm diameter and broken, flat thin-shelled bivalve micro-debris with possible sponge spicules.

Microfacies 4

This microfacies consists of nodular limestone with few dolomite beds and covers a 1.2 m interval. It is characterized by sponge spicule-containing dark lime mudstone with rare calcisphere in centimetric nodules (Fig. S9). Samples comprising this microfacies show evidence of dissolution and fracture-filling by brown silty material.

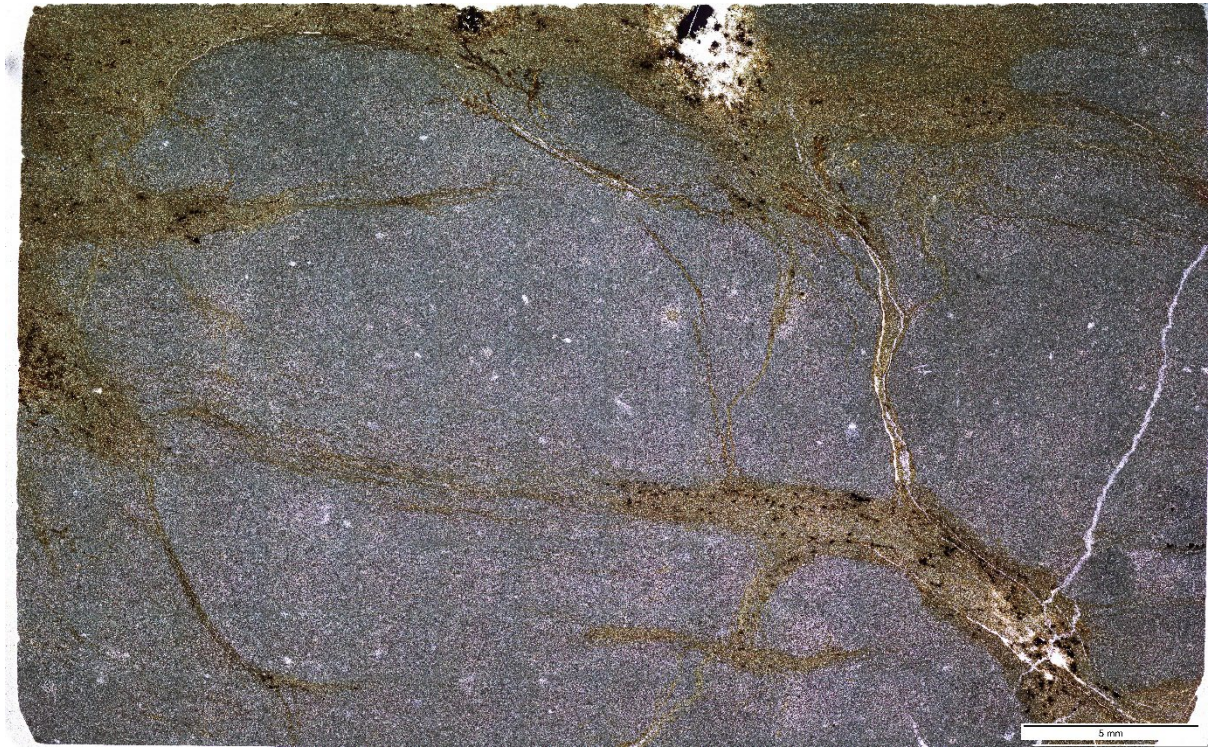


Figure S9. Photo of thin section no. 24437 showing dark mudstone with sponge spicules and rare calcisphere, surrounded by brown silty-clay seam.

Microfacies 5

This microfacies covers a 10 m thick interval and consists of nodular marly limestone. Based on 11 thin sections, this microfacies is characterized by nodules of dark lime mudstone to dark silty-lime-wackestone with stromatactis. These nodules usually contain sponge spicules, thin bivalve shells, ostracods, and micro-calcisphere surrounded by brown silty-clay seams (Fig. S10, Fig. S11).

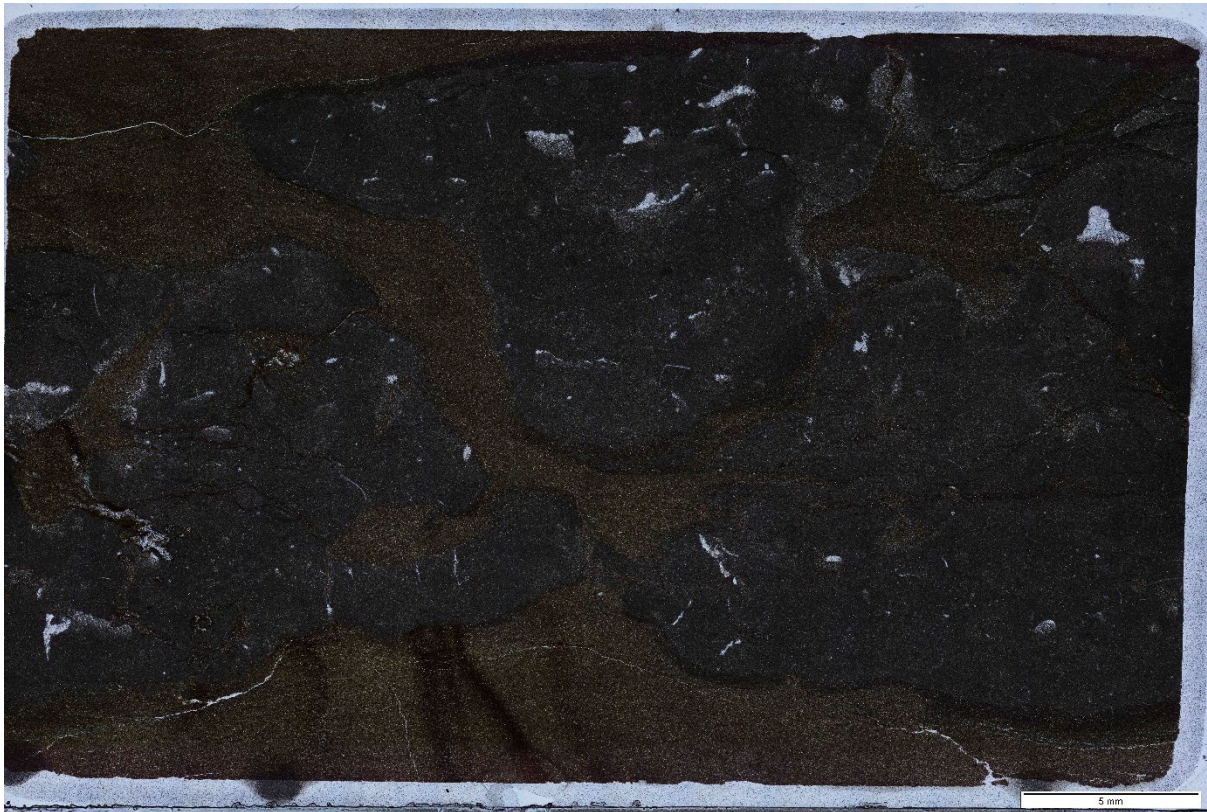


Figure S10. Photo of thin section no. 24413 showing microfacies 5 with nodules of dark lime mudstone with stromatactis, sponge tissue and spicules, rare ostracods, surrounded by brown silty-clay seams.



Figure S11. Photo of thin section no. 24442 showing microfacies 5 with nodules of dark silty-lime-wackestone with some package of thin bivalve shells, ostracodes, rare micro-calcisphere surrounded by brown silty-clay seams.

Microfacies 6

This microfacies marks the onset of a Spathian red nodular marly limestone also known as the “griotte facies” in the Nanpanjiang Basin (Sun et al., 2015). This facies is well known in the Himalaya region and has been described in Tulong by Brühwiler et al. (2009). Based on six thin sections, this microfacies in the QIA section is characterized by nodular red silty-lime wackestone-packstone with thin bivalve shells, crinoids and calcispheres, as well as nodular red wackestone with thin bivalve shells and calcispheres interlaced by red silty-clay seams (Fig. S12, Fig. S13).

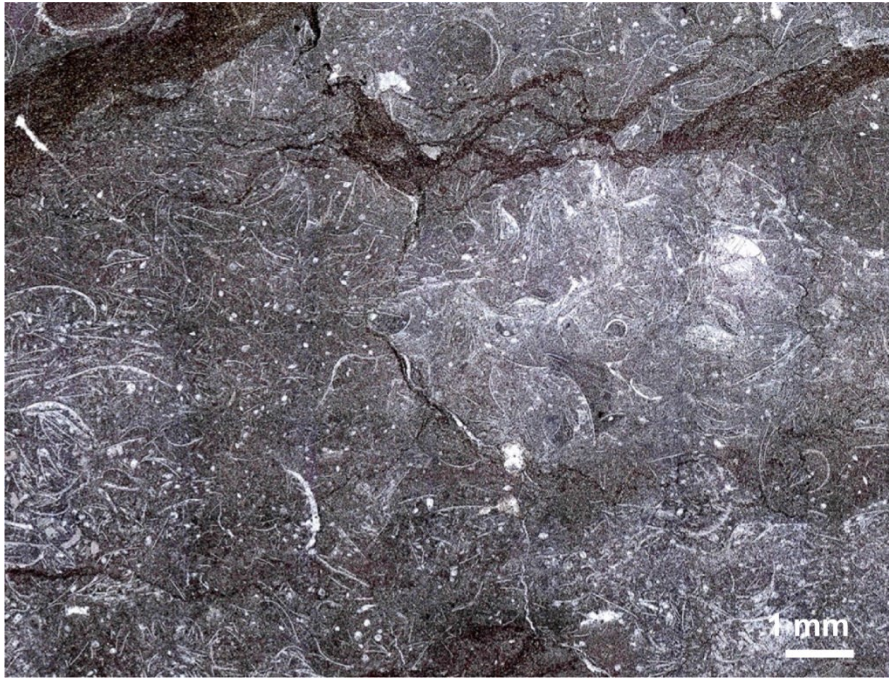


Figure S12. Photo of thin section no. 24414 (microfacies 6) showing nodular red wackestone-packstone with thin bivalve shells, crinoids and calcispheres.



Figure S13. Photo of thin section no. 24440 (microfacies 6) showing nodular red lime wackestone with thin bivalve shells and calcispheres interlaced by red silty-clay seams.

In summary, the deep-water shelf QIA succession starts with some high energy deposition due to bottom currents reworking small sized debris. Part of these debris are thin shelled fragmented flat

valves and calcispheres. The complete thin bivalve shells with convexity oriented upwards and geopetal structures are present in low energy environment. The local presence of stromatactis is linked with sponge tissue or sponge spicules. The lower Spathian nodular succession start with mainly dark facies within the lower 10 m. The following red nodular marly limestone is a well-known part of the Loulou Formation in South China and widespread in Himalaya and in Western Tethys, called “Ammonitico-rosso” or “Han-Bulog” (Brühwiler et al., 2009; Sun et al., 2015).

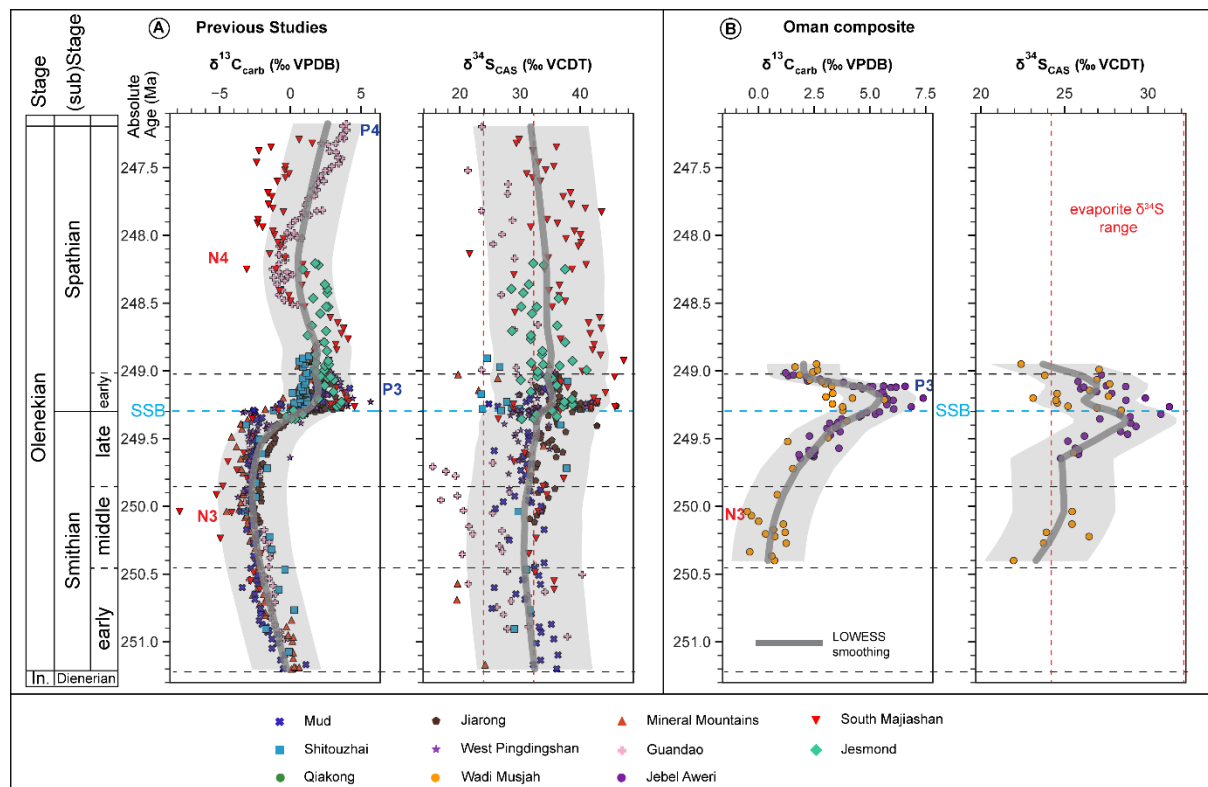


Figure S14. A) Absolute age calibrated comparison of A) previously published Olenekian $\delta^{13}\text{C}$ and $\delta^{34}\text{S}$ records with. B) composite data from Oman sections: Wadi Musjah and Jebel Aweri. $\delta^{13}\text{C}$ and $\delta^{34}\text{S}$ values are taken from the same sources given in Figure 1 of the main text. Absolute ages for the Smithian and Spathian are based on Widmann et al. (2020), Induan – Olenekian boundary and Olenekian – Anisian boundary ages are taken from the International Chronostratigraphic Chart 2023 (Cohen et al., 2013; updated). The nomenclature: N3, N4, P3, P4 depicts globally recognizable carbon isotope excursions after Song et al. (2013). In. = Induan, An. = Anisian. The SSB absolute age (249.29 Ma) is after Widmann et al. (2020). Dashed red lines on the $\delta^{34}\text{S}_{\text{CAS}}$ record depict the range of Olenekian evaporite $\delta^{34}\text{S}$ values (Present et al., 2020 and references therein). The thick grey lines represent a Lowess regression fit to the data, and the associated grey band represents the 95 % confidence interval of the Lowess fit.

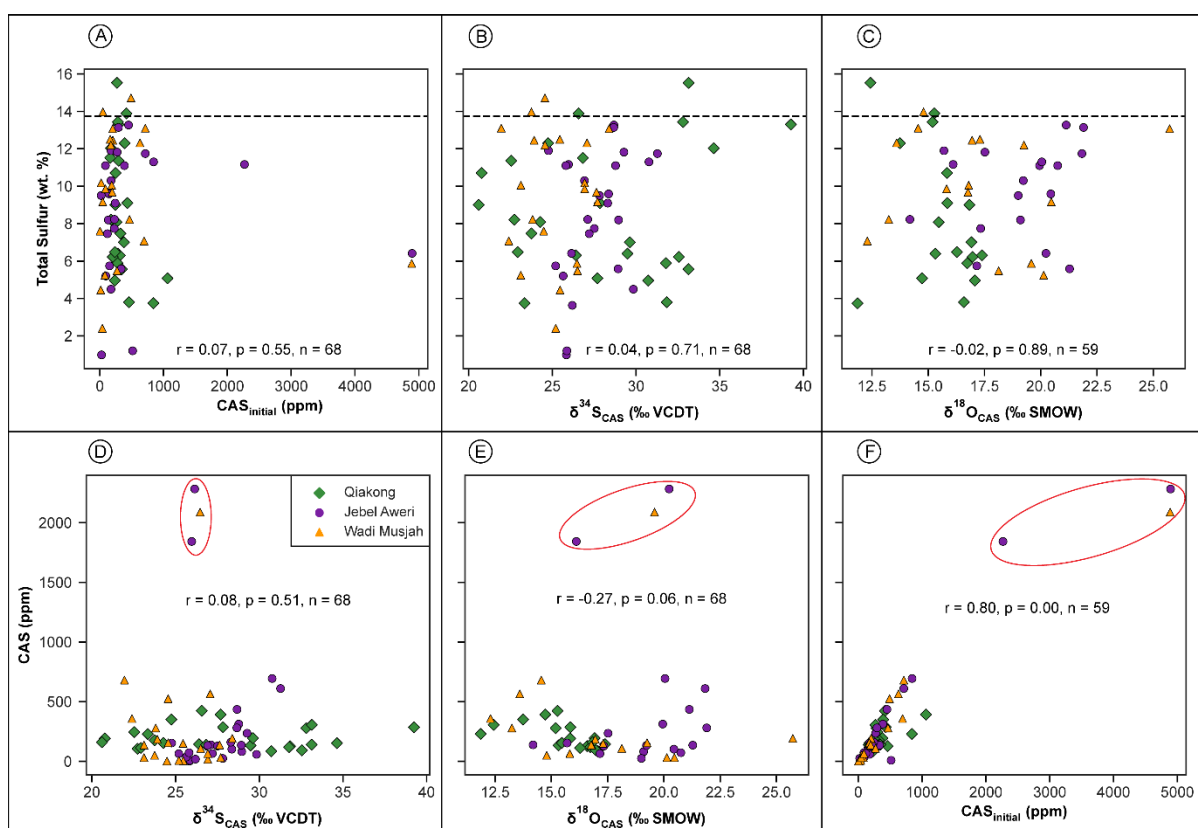


Figure S15. Cross-plots of Total Sulfur (TS) content determined by EA/IRMS vs A) initial CAS concentrations, B) CAS $\delta^{34}\text{S}$, C) CAS $\delta^{18}\text{O}$. Dashed black lines depict the expected TS content of pure barite - 13.74 wt. %. Cross-plots of final CAS concentrations vs. D) CAS $\delta^{34}\text{S}$, E) CAS $\delta^{18}\text{O}$, and F) CAS concentrations prior to normalization against TS content. Calculated values for r (Spearman's correlation coefficient) and p (p-value) do not consider samples with unusually high CAS concentrations (marked with the red oval). No correlation is observed between TS content and CAS concentration prior to TS normalization, nor between final CAS concentration and CAS isotopic compositions. The lack of correlation suggests that CAS concentration (and measured TS content) have little to no influence on CAS isotopic compositions (Gill et al., 2008).

References

- Brühwiler, T., Goudemand, N., Galfetti, T., Bucher, H., Baud, A., Ware, D., Hermann, E., Hochuli, P.A., Martini, R., 2009. The Lower Triassic sedimentary and carbon isotope records from Tulong (South Tibet) and their significance for Tethyan palaeoceanography. *Sedimentary Geology* 222, 314-332 DOI: <https://doi.org/10.1016/j.sedgeo.2009.10.003>.
- Cohen, K.M., Finney, S.C., Gibbard, P.L., Fan, J.X., 2013; updated. The ICS International Chronostratigraphic Chart. *International Union of Geological Sciences* 36, 199-204 DOI: 10.18814/epiiugs/2013/v36i3/002.
- Galfetti, T., Bucher, H., Martini, R., Hochuli, P.A., Weissert, H., Crasquin-Soleau, S., Brayard, A., Goudemand, N., Bruehwiler, T., Guodun, K., 2008. Evolution of Early Triassic outer platform paleoenvironments in the Nanpanjiang Basin (South China) and their significance for the biotic recovery. *Sedimentary Geology* 204, 36-60 DOI: 10.1016/j.sedgeo.2007.12.008.
- Gill, B.C., Lyons, T.W., Frank, T.D., 2008. Behavior of carbonate-associated sulfate during meteoric diagenesis and implications for the sulfur isotope paleoproxy. *Geochimica et Cosmochimica Acta* 72, 4699-4711 DOI: <https://doi.org/10.1016/j.gca.2008.07.001>.
- Leu, M., Bucher, H., Vennemann, T., Bagherpour, B., Ji, C., Brosse, M., Goudemand, N., 2022. A Unitary Association-based conodont biozonation of the Smithian–Spathian boundary (Early Triassic) and associated biotic crisis from South China. *Swiss Journal of Palaeontology* 141, 19 DOI: 10.1186/s13358-022-00259-x.
- Present, T.M., Adkins, J.F., Fischer, W.W., 2020. Variability in Sulfur Isotope Records of Phanerozoic Seawater Sulfate. *Geophys Res Lett* 47, e2020GL088766 DOI: <https://doi.org/10.1029/2020GL088766>.
- Song, H., Tong, J., Algeo, T.J., Horacek, M., Qiu, H., Song, H., Tian, L., Chen, Z.-Q., 2013. Large vertical $\delta^{13}\text{C}_{\text{DIC}}$ gradients in Early Triassic seas of the South China craton: Implications for oceanographic changes related to Siberian Traps volcanism. *Global and Planetary Change* 105, 7-20 DOI: <https://doi.org/10.1016/j.gloplacha.2012.10.023>.
- Sun, Y.D., Wignall, P.B., Joachimski, M.M., Bond, D.P.G., Grasby, S.E., Sun, S., Yan, C.B., Wang, L.N., Chen, Y.L., Lai, X.L., 2015. High amplitude redox changes in the late Early Triassic of South China and the Smithian–Spathian extinction. *Palaeogeography, Palaeoclimatology, Palaeoecology* 427, 62-78 DOI: <https://doi.org/10.1016/j.palaeo.2015.03.038>.
- Widmann, P., Bucher, H., Leu, M., Vennemann, T., Bagherpour, B., Schneebeli-Hermann, E., Goudemand, N., Schaltegger, U., 2020. Dynamics of the largest carbon isotope excursion during the Early Triassic biotic recovery. *Front Earth Sc-Switz*, 196 DOI: <https://doi.org/10.3389/feart.2020.00196>.

APPENDIX C

Supplementary information for Chapter 4:
**Carbonate Clumped Isotope Constraints on Early Triassic NeoTethyan Seawater
Oxygen Isotope Compositions and Temperatures**

Oluwaseun Edward^{1*}, Sandrine Le Houedec², Aymon Baud³, Thomas Brühwiler⁴, Hugo Bucher⁴,
Torsten Vennemann¹

Text S1: Clumped isotope analytical protocol at UNIL

Clumped isotope measurements at UNIL are done using an analytical setup composed of a NuCarb sample preparation device coupled to a NuPerspective mass spectrometer (Fig. S1). For carbonate samples, material between 400 and 5000 μg is weighed into 2 ml glass vials that are then placed in a sample carousel. The sample carousel is housed in the vacuum based NuCarb sample preparation device held at 70 °C. During analysis, a piston raises each sample vial against the O-ring for vacuum evacuation for a period of 240 seconds before the vial is automatically infused with 110 μl of H_3PO_4 with specific gravity of 1.95 using a Teflon-plunger micro-syringe. The acid reaction with the carbonate in the vial takes place for 300 seconds, after which evolved CO_2 gas is expanded for 300 seconds into a water trap held at -80 °C using liquid nitrogen. The CO_2 then passes in vacuum for 1500 seconds across a PoraPakTM Q adsorption trap to a first cold finger at -160 °C. Here, a pressure reading occurs with the P-transducer at -70 °C. If a large pressure reading is attained, the sample passes into the bellows for analysis, otherwise the sample is frozen at -160 °C for 180 seconds into a second cold finger. Before isotopic analyses in the mass spectrometer, automatic pressure balancing occurs if needed. Analysis takes place in 3 or 4 blocks of 20 aliquot measurements. Clumped isotope analysis takes about 80 minutes per sample. Typical Δ_{47} precision for small samples (300 – 500 μg) is 0.015 ‰, while for large samples, precision is typically better than 0.007 ‰.



Figure S1. NuCarb sample preparation device coupled to a Nu Perspective isotope ratio mass spectrometer at the stable isotope laboratory of the University of Lausanne (UNIL).

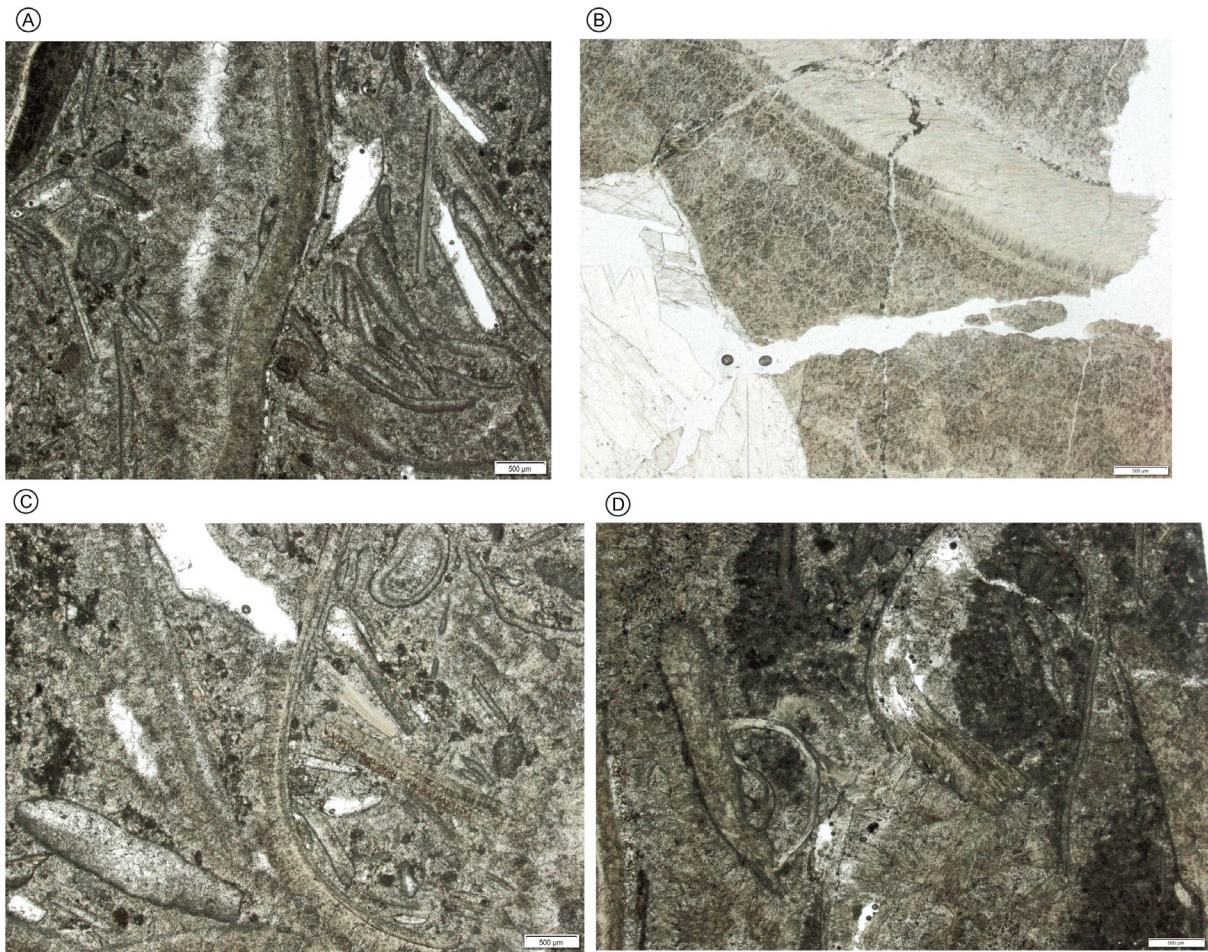


Figure S2. Thin section photomicrographs of whole rock samples from Jebel Aweri (JA). A) Sample JA C28, b) Sample JA C2, c) Sample JA C28, d) Sample JA C11. These photomicrographs show the abundant skeletal parts which comprise the strata of the JA succession.



Figure S3. Polished section showing the inorganic carbonate “couche caramel” lime mud facies of the Ras al Jin section (RAJ2). These fine lime mud beds are characterized by very fine lamina and yield Δ_{47} temperatures which suggest carbonate deposition in cool waters of ca. 15 °C.

Wadi ad Daffa (WAD2)

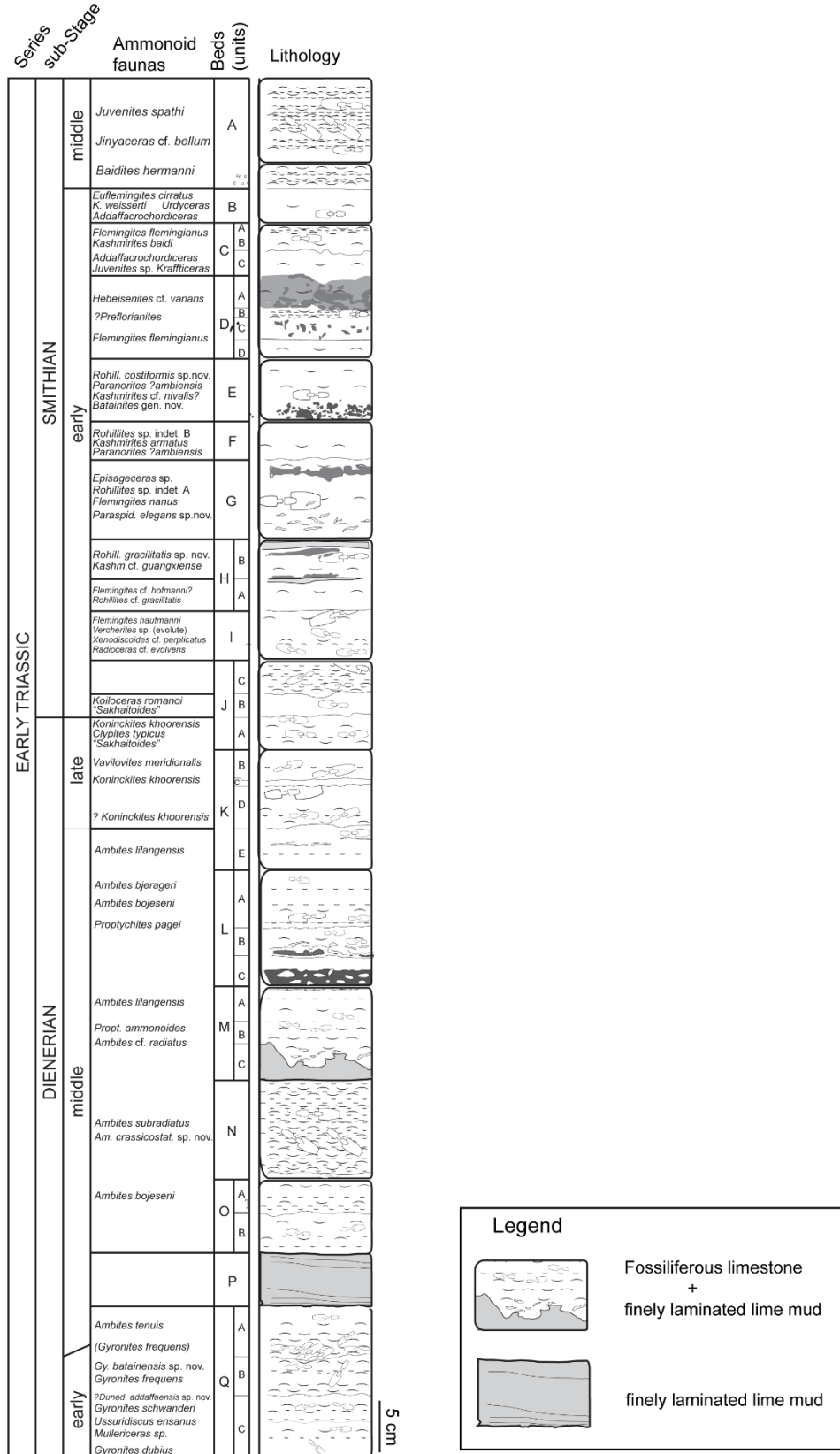


Figure S4. Lithological log of the Wadi ad Daffah (WAD2) succession.

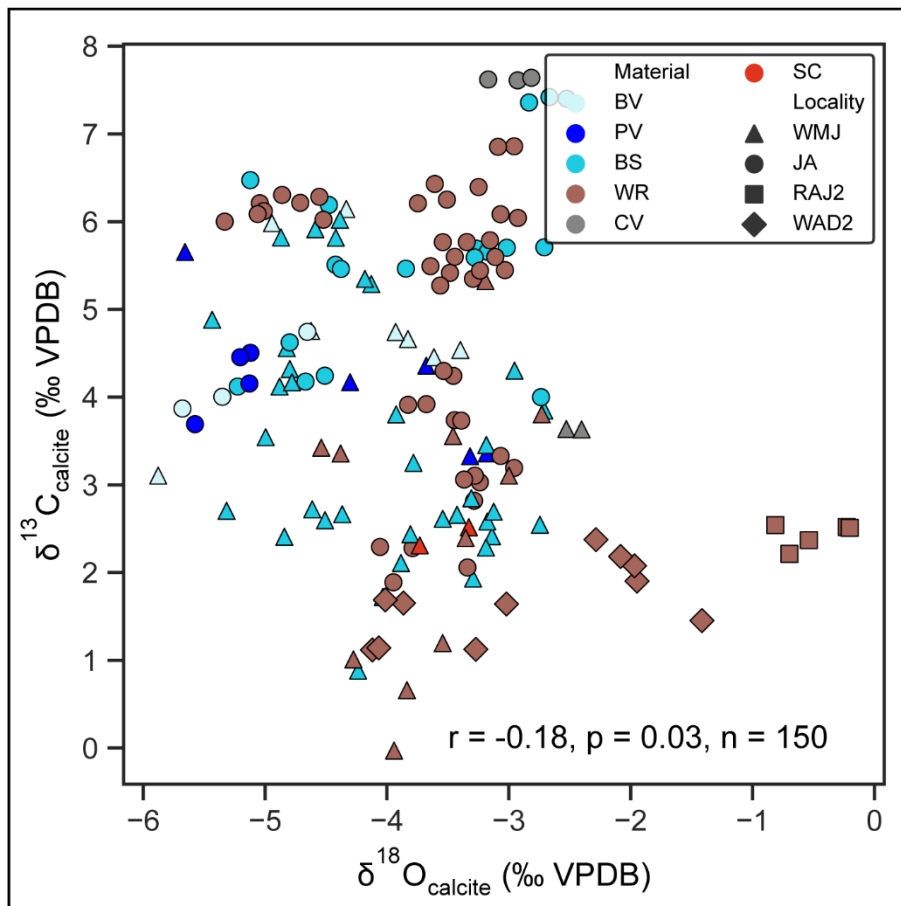


Figure S5. Cross-plot of carbon and oxygen isotope data for all analyzed samples. Abbreviations in the figure legend are the same as in Figure 4 of the main text.

APPENDIX D

Curriculum Vitae

Name: Oluwaseun Edward

Date of birth: 25/02/1991

Nationality: Nigerian

Address: La Mottaz 23, 1143 Apples

Email: olu.edward@outlook.com

Education:

2019 – 2023: Ph.D in Earth Sciences (in-view), University of Lausanne, Switzerland

2015 – 2017: MSc. Geoscience, University of Copenhagen, Denmark

2008 – 2013: BSc. Geology, Olabisi Onabanjo University, Nigeria

Languages:

English: Native proficiency

Danish: Level C1 (Prøve i dansk 3)

Yoruba: Native proficiency

French: Level A1

List of publications

Published First-Author Papers:

Edward, Oluwaseun; Korte, Christoph; Ullmann, Clemens V.; Colmenar, Jorge; Thibault, Nicolas; Bagnoli, Gabriella; Stouge, Svend; Rasmussen, Christian M. Ø. 2022. A Baltic Perspective on the Early to Early Late Ordovician $\delta^{13}\text{C}$ and $\delta^{18}\text{O}$ Records and Its Paleoenvironmental Significance. *Paleoceanography and Paleoclimatology* Vol. 37 Issue 3, pp.26.

<https://doi.org/10.1029/2021PA004309>

Edward, O., Paul, A.N., Bucher, H., V  rard, C., Adatte, T., Sonke, J.E., Schaltegger, U., Vennemann, T., 2023. Timing and Provenance of Volcanic Fluxes Around the Permian-Triassic Boundary Mass Extinction in South China: U-Pb Zircon Geochronology, Volcanic Ash Geochemistry and Mercury Isotopes. *Geochemistry, Geophysics, Geosystems* 24, e2023GC010912 DOI:

<https://doi.org/10.1029/2023GC010912>.

Edward, O., Leu, M., Bucher, H., Le Houedec, S., Blattmann, F., V  rard, C., Adatte, T., Baud, A., Sonke, J.E., Vennemann, T., 2024. Evidence for variable provenance of Mercury anomalies during the Smithian–Spathian (Olenekian). *Global and Planetary Change* 232, 104343.

<https://doi.org/10.1016/j.gloplacha.2023.104343>

Edward, O., Spangenberg, J.E., Leu, M., Ragon, C., Le Houedec, S., Baud, A., Bucher, H., Vennemann, T., 2024b. Olenekian sulfur isotope records: Deciphering global trends, links to marine

redox changes and faunal evolution. *Chemical Geology*, 121984 DOI:

<https://doi.org/10.1016/j.chemgeo.2024.121984>.

Conference Abstracts:

Oluwaseun Edward, Zoneibe Luz, Hugo Bucher, Torsten Vennemann. Carbonate clumped isotope thermometry in deep time: Insights from Early Triassic brachiopods and bulk carbonates. *Goldschmidt Virtual 2020*. Oral presentation. DOI: 10.46427/gold2020.646

Oluwaseun Edward, Hugo Bucher, Marc Leu, Thierry Adatte, Aymon Baud, Torsten Vennemann. Do Tethyan mercury anomalies reflect a global volcanic trigger for the Smithian/Spathian boundary climatic and biotic crisis? *18th Swiss Geoscience Meeting, Zurich 2020*. Oral presentation

Oluwaseun Edward, André Navin Paul, Hugo Bucher, Borhan Bagherpour, Aymon Baud, Thierry Adatte, Jeroen Sonke, Urs Schaltegger, Torsten Vennemann. Mercury isotope evidence for sustained regional volcanism in South China before and after the Permian-Triassic boundary. *EGU General Assembly 2022*. Oral presentation. <https://doi.org/10.5194/egusphere-egu22-8013>.

Oluwaseun Edward, André Navin Paul, Hugo Bucher, Thierry Adatte, Urs Schaltegger, Torsten Vennemann. Mercury (Hg) anomalies and carbon isotope excursions as a stratigraphic marker for the Permian – Triassic mass extinction. *EGU General Assembly 2023*. Oral presentation. <https://doi.org/10.5194/egusphere-egu23-11420>

Oluwaseun Edward, Jorge Spangenberg, Charline Ragon, Marc Leu, Hugo Bucher, Torsten Vennemann. Marine sulfur isotope records and environmental changes during the Smithian-Spathian transition: Insights from nearshore and offshore Tethyan successions. *Across the End Permian “Great Extinction” : From field studies to scientific results conference, Lausanne 2023*. Oral presentation

Edward O., Leu M., Dudit L., Le Houedec, S., Bucher H., Baud A., Vérard C., Vennemann T. Latest Permian to Early Triassic (Spathian) integrated carbon, strontium, and neodymium isotope chemostratigraphy from Oman exotic blocks. *20th Swiss Geoscience Meeting, Lausanne 2022*. Poster presentation

Verard C., Baud A., Bucher H., **Edward O.** Tracking back Permian–Triassic sections from Oman over the Mesozoic –Cenozoic: Geodynamic and paleogeographic implications. *20th Swiss Geoscience Meeting, Lausanne 2022*. Poster presentation

Luz Z., Leu M., **Edward O.**, Baud A., Bucher H., Vennemann T. Climate cooling event in the Early Triassic subtropics. *20th Swiss Geoscience Meeting, Lausanne 2022*. Poster presentation

Vennemann, T.; **Edward, O.**; Luz, Z. and Bucher, H. 2020. Tracing temperature and oxygen isotope compositions of Early Triassic seawater with clumped isotope thermometry. *Goldschmidt Virtual 2020*. DOI: 10.46427/gold2020.2674

Luz, Z.; Leu, M.; **Edward, O.**; Baumgartner, L. P.; Bucher, H. and Vennemann, T. 2020. Deciphering the Early Triassic paleocean using stable oxygen isotopes in conodont bioapatite. *Goldschmidt Virtual 2020*. DOI: 10.46427/gold2020.1665

Co-authored papers-in-prep

Franziska R. Blattmann, Federica Tamburini, Thierry Adatte, **Oluwaseun Edward**, Zoneibe Luz, Hugo Bucher, Christian Vérard, Torsten Vennemann, 2023. Marine Productivity in the Smithian and Spathian: New Insights from SEDEX Data.

Zoneibe Luz, Marc Leu, **Oluwaseun Edward**, Aymon Baud, Hugo Bucher, Torsten Vennemann, 2023. Climatic cooling in the Early Triassic subtropics.